Technische Universität München
Fakultät für Physik

Neutrino-Mass Analysis with sub-eV Sensitivity and Search for Light Sterile Neutrinos with the KATRIN Experiment

---

Lisa Schlüter

Vollständiger Abdruck der von der Fakultät für Physik der
Technischen Universität München zur Erlangung des akademischen Grades
einer
Doktorin der Naturwissenschaften (Dr. rer. nat.)
genehmigten Dissertation.

Vorsitzender: apl. Prof. Dr. Norbert Kaiser

Prüfer der Dissertation:
1. Prof. Dr. Susanne Mertens
2. Dr. Thierry Lasserre

Die Dissertation wurde am 21.06.2022 bei der Technischen Universität
München eingereicht und durch die Fakultät für Physik am 19.07.2022
angenommen.

Contents

Introduction 1

1 Neutrino physics 3
  1.1 Postulation and discovery of the neutrino . . . 3
    1.1.1 Postulation . . . 3
    1.1.2 Discovery of the electron neutrino . . . 3
    1.1.3 Discovery of muon and tau neutrinos . . . 4
  1.2 Neutrino oscillations . . . 4
    1.2.1 Theoretical description . . . 5
    1.2.2 Solar neutrino problem . . . 6
  1.3 Neutrino mass . . . 8
    1.3.1 Cosmology . . . 8
    1.3.2 Neutrinoless double β-decay . . . 8
    1.3.3 Single β-decay . . . 9
  1.4 Sterile neutrinos . . . 11
    1.4.1 Signature of sterile neutrinos . . . 11
    1.4.2 Sterile-neutrino anomalies . . . 12

2 The KATRIN experiment 17
  2.1 Experimental setup . . . 17
    2.1.1 Rear section . . . 17
    2.1.2 Windowless gaseous tritium source . . . 19
    2.1.3 Transport section . . . 19
    2.1.4 Forward beam monitor . . . 20
    2.1.5 Spectrometer section . . . 20
    2.1.6 Focal plane detector . . . 22
  2.2 Model of the experimental spectrum . . . 23
    2.2.1 Differential energy spectrum for molecular tritium β-decay . . . 23
    2.2.2 Experimental response function . . . 25
    2.2.3 Signal normalization . . . 31
    2.2.4 Background model . . . 31
    2.2.5 Measurement time distribution . . . 32

3 Analysis strategy 33
  3.1 Analysis software . . . 33
  3.2 Data combination . . . 33
    3.2.1 Scan combination . . . 34
    3.2.2 Pixel combination . . . 34
    3.2.3 Model of combined spectrum . . . 35
  3.3 Statistical methods . . . 35
    3.3.1 Parameter inference . . . 35
    3.3.2 Confidence belts . . . 37
    3.3.3 Systematic uncertainty propagation . . . 40

4 Systematic effects in KATRIN 43
4.1 Theoretical corrections . . . 43
4.2 Final-state distribution . . . 44
4.3 Source potential . . . 45
  4.3.1 Longitudinal homogeneity . . . 45
  4.3.2 Radial homogeneity . . . 46
  4.3.3 Long-term stability . . . 47
4.4 Source activity . . . 47
  4.4.1 Uncertainty on absolute value . . . 47
  4.4.2 Scan fluctuations . . . 47
4.5 Molecular gas composition . . . 48
4.6 Number of scatterings . . . 48
4.7 Energy-loss function . . . 49
4.8 Magnetic fields . . . 50
4.9 Retarding potential . . . 50
4.10 Background . . . 50
  4.10.1 Steady-state background: Non-Poisson over-dispersion . . . 51
  4.10.2 Scan-step-time-dependent background rate . . . 51
  4.10.3 Retarding-potential-dependent background rate . . . 51
4.11 Detector efficiency . . . 52

5 First measurement campaign 53
5.1 Measurement time distribution . . . 53
5.2 Data selection . . . 54
  5.2.1 Golden pixels . . . 54
  5.2.2 Golden scans . . . 54
5.3 Molecular gas composition . . . 55
5.4 Column density . . . 56
5.5 Source activity stability within a scan . . . 56
5.6 Source potential . . . 57
5.7 Retarding potentials . . . 58
  5.7.1 Pre-spectrometer . . . 58
  5.7.2 Main spectrometer . . . 58
5.8 Magnetic fields . . . 59
5.9 Detector efficiency . . . 59
5.10 Background . . . 59
  5.10.1 Steady-state background: Radial distribution . . . 60
  5.10.2 Steady-state background: Non-Poisson over-dispersion . . . 60
  5.10.3 Steady-state background: Signal-to-background ratio . . . 61
  5.10.4 Retarding-potential-dependent background . . . 61
  5.10.5 Scan-step-time dependent background . . . 62

6 Second measurement campaign 63
6.1 Measurement time distribution . . . 63
6.2 Data selection . . . 64
  6.2.1 Golden pixels . . . 64
  6.2.2 Golden scans . . . 65
6.3 Molecular gas composition . . . 65
6.4 Column density . . . 66
6.5 Source activity stability within a scan . . . 66
6.6 Source potential . . . 67
  6.6.1 Longitudinal homogeneity . . . 67
  6.6.2 Long-term potential variations . . . 68

6.6.3 Radial homogeneity . . . 71
6.6.4 Effective source potential model . . . 72
6.7 Retarding potentials . . . 72
6.7.1 Pre-spectrometer . . . 72
6.7.2 Main spectrometer . . . 72
6.8 Magnetic fields . . . 73
6.9 Detector efficiency . . . 74
6.10 Background . . . 74
6.10.1 Steady-state background: Radial distribution . . . 74
6.10.2 Steady-state background: Non-Poisson over-dispersion . . . 75
6.10.3 Steady-state background: Signal-to-background ratio . . . 75
6.10.4 Retarding-potential-dependent background . . . 76
6.10.5 Scan-step-time dependent background . . . 77

7 Blinding procedure 79
7.1 Monte Carlo twins . . . 79
7.2 Blinding protocol . . . 79

8 Neutrino-mass analysis of KNM1 81
8.1 Monte Carlo twins . . . 81
8.2 Data combination . . . 81
8.2.1 Scan combination . . . 81
8.2.2 Pixel combination . . . 82
8.3 Spectral model configuration . . . 83
8.4 Scan-wise analysis: Nuisance parameter stability . . . 83
8.4.1 Effective tritium endpoint . . . 85
8.4.2 Steady-state background rate . . . 85
8.4.3 Signal normalization . . . 85
8.4.4 Goodness-of-fit . . . 85
8.5 Baseline neutrino-mass analysis . . . 86
8.5.1 Best-fit result . . . 86
8.5.2 Profile chi-squared . . . 87
8.5.3 Confidence belt and upper limit . . . 87
8.5.4 Fit parameter correlations . . . 88
8.6 Systematic uncertainty breakdown . . . 89
8.7 Radial fit parameter dependencies . . . 90
8.8 Extended fit interval . . . 92
8.8.1 Fit-interval-dependent neutrino-mass sensitivity . . . 92
8.8.2 Retarding-potential fit parameter dependencies . . . 92
8.9 Alternative scan selection . . . 94
8.10 Alternative pixel selection . . . 95
8.10.1 Alternative half pixel lists . . . 95
8.10.2 Azimuthal position . . . 96
8.11 Statistical tests with CATS . . . 96
8.11.1 Cook’s distance . . . 96
8.11.2 Fits with excluded data points . . . 97
8.12 Reanalysis with updated model configuration . . . 99

9 Neutrino-mass analysis of KNM2 101
9.1 Monte Carlo Twins . . . 101
9.2 Data combination . . . 101
9.2.1 Scan combination . . . 101
9.2.2 Pixel combination . . . 101

9.3 Spectral model configuration . . . 102
9.4 Scan-wise analysis: Nuisance parameter stability . . . 102
  9.4.1 Effective tritium endpoint . . . 102
  9.4.2 Steady-state background rate . . . 103
  9.4.3 Signal normalization . . . 103
  9.4.4 Goodness-of-fit . . . 103
9.5 Baseline neutrino-mass analysis . . . 104
  9.5.1 Best-fit result . . . 105
  9.5.2 Profile chi-squared . . . 106
  9.5.3 Confidence belt and upper limit . . . 107
  9.5.4 Fit parameter correlations . . . 108
9.6 Comparison of pixel combination strategies . . . 109
9.7 Systematic uncertainty breakdown . . . 109
9.8 Radial-dependent neutrino mass . . . 110
9.9 Alternative treatment of retarding-potential-dependent background rate . . . 111
9.10 Extended fit interval . . . 112
  9.10.1 Fit-interval-dependent neutrino-mass sensitivity . . . 112
  9.10.2 Retarding-potential fit parameter dependencies . . . 113
9.11 Alternative scan selection . . . 114
9.12 Alternative pixel selection . . . 114
9.13 Statistical tests with CATS . . . 115
  9.13.1 Cook's distance . . . 115
  9.13.2 Fits with excluded data points . . . 115

10 Combined neutrino-mass analysis of KNM1 and KNM2 **117**
10.1 Multi-campaign model . . . 117
10.2 Combination method . . . 117
  10.2.1 Combined fit . . . 118
  10.2.2 Combination of chi-squared profiles . . . 118
10.3 Combined sensitivity . . . 119
10.4 Combined neutrino-mass constraint . . . 119
10.5 Data set compatibility: Parameter goodness-of-fit . . . 121

11 Sterile-neutrino search of the first two measurement campaigns **123**
11.1 Data combination, model configuration and blinding . . . 123
11.2 Sterile-neutrino analysis methods . . . 124
  11.2.1 Fit parameters . . . 124
  11.2.2 Grid search . . . 124
  11.2.3 Choice of grid . . . 125
  11.2.4 Combined analysis . . . 125
11.3 Correlation between active and sterile neutrino branches . . . 126
11.4 Sensitivity contours: Results on simulation . . . 127
  11.4.1 Structure of sensitivity contours . . . 127
  11.4.2 Comparison of data sets . . . 127
  11.4.3 Comparison of analysis cases . . . 127
11.5 Exclusion contours: Results on data . . . 128
  11.5.1 Analysis case I) $m_\nu^2 = 0\,\mathrm{eV}^2$ . . . 129
  11.5.2 Analysis case II) with m_ν^2 free . . . 130
  11.5.3 Comparison of exclusion and sensitivity contours . . . 131
  11.5.4 Comparison to other experiments . . . 132
11.6 Neutrino-mass sensitivity in $3\nu + 1$ framework . . . 133
11.7 Influence of systematic uncertainties . . . 134
11.8 Extension of the fit interval . . . 137

11.9 Nonphysical parameter space . . . 138
11.10 Test of Wilks's theorem . . . 138

12 Summary and Conclusion **141**

A KATRIN Experiment **145**
A.1 Energy-dependent scattering cross section . . . 145
A.2 Energy-loss function parameter . . . 146

B Pixel combination **147**

C Overview Tables of KNM1 and KNM2 Campaigns **151**

D First measurement campaign **153**
D.1 Golden scan list . . . 153
D.2 Alternative scan lists . . . 153
D.3 Golden pixel list . . . 156
D.4 Pseudo-ring statistics . . . 157
D.5 Covariance matrices . . . 157

E Second measurement campaign **161**
E.1 Golden scan list . . . 161
E.2 Alternative scan lists . . . 161
E.3 Golden pixel list . . . 163
E.4 Rate monitor analysis . . . 163
E.5 Retarding potential . . . 164
E.6 Background . . . 164
E.7 Covariance matrices . . . 164

F Neutrino-mass analysis of KNM1 **169**
F.1 Retarding potential fit parameter dependencies . . . 169
F.2 Azimuthal fit parameter dependencies . . . 170
F.3 Neutrino-mass imprint in the integral spectrum . . . 171

G Neutrino-mass analysis of KNM2 **173**
G.1 Signal normalization in multi-ring fit . . . 173
G.2 Fit result using uniform pixel segmentation . . . 173
G.3 Radial fit parameter dependencies . . . 173
G.4 Alternative treatment of retarding-potential-dependent background rate . . . 174
G.5 Retarding potential fit parameter dependencies . . . 176

H Sterile Neutrino Search **177**
H.1 Influence of background level on sterile-neutrino search . . . 177
H.2 Comparison of exclusion and sensitivity contour . . . 177
H.3 Neutrino-mass sensitivity in $3\nu+1$ framework . . . 179
H.4 Influence of systematic uncertainties . . . 179
H.5 Extension of the fit interval . . . 180
H.6 Test of Wilks's theorem . . . 181
H.7 Nonphysical parameter space . . . 184

Introduction

The discovery of neutrino oscillations was a revolutionary milestone in the history of particle physics. Requiring neutrinos to carry a mass, neutrino oscillations are not foreseen in the widely successful standard model of particle physics. Even though neutrino oscillations are not sensitive to the absolute neutrino mass scale, they provide a lower limit of 0.01 eV[1]. Moreover, it is known from β-decay experiments, that the neutrino mass must be tiny. As of today, an upper bound of 0.8 eV could be determined, which is already more than five orders of magnitude smaller than the mass of the next lightest fermion. The lightness of the neutrino brings up the fundamental question of how neutrinos obtain their mass, since the associated mass generation mechanism appears to be different from all other fermions in the standard model. The exact knowledge of the neutrino mass is of uttermost importance to identify the mass generation model that is realized in nature. Moreover, the neutrino mass is a crucial input parameter in cosmology. Neutrinos are the most abundant massive particles in our universe: Each cm^3 of the universe is penetrated by 336 neutrinos from the big bang. Despite their small mass, neutrinos have a large influence on the structure formation in the early universe due to their vast abundance.

The Karlsruhe Tritium Neutrino (KATRIN) experiment is designed to determine the absolute neutrino-mass scale via the kinematics of molecular tritium β-decay with an unprecedented sensitivity of 0.2 eV at 90 % confidence level after five calendar years. This is achieved in a neutrino-mass model independent way by measuring the integrated β-electron spectrum in the close vicinity of the tritium endpoint at $E_0 = 18.57\,\mathrm{keV}$. The effective electron antineutrino mass m_ν^2 leads to a reduction of the maximal available electron energy and to a slight distortion of the spectral shape, that is most prominent in the endpoint region. To obtain a considerable m_ν^2 sensitivity, two cruxes have to be addressed: First, only a small fraction of β-electrons are emitted at the highest energies. Second, the imprint of m_ν^2 in the experimental spectrum is minuscule. The KATRIN experiment tackles these challenges by employing an ultra-stable high-luminosity windowless gaseous tritium source in combination with a spectrometer with an eV-scale energy resolution at a low background level $\mathcal{O}(0.1\,\mathrm{cps})$. Additionally, a comprehensive understanding of the experimental functionality and of all systematic uncertainties is required.

Furthermore, the KATRIN experiment is sensitive to sterile neutrinos with an associated fourth mass eigenstate m_4 at the eV mass scale. Sterile neutrinos are a minimal extension of the standard model, forming the right-handed counterpart to the known left-handed neutrino flavors. Due to their handiness, sterile neutrinos do not participate in any fundamental interaction except for gravitation. Thanks to their mixing with the known active neutrinos, their existence can be probed in laboratory experiments. Experimentally, eV-scale sterile neutrinos are well motivated by several anomalies observed in short-baseline neutrino oscillation experiments. The signature of a sterile neutrino in β-decay experiments is a kink-like spectral distortion at electron energies around $E_0 - m_4$.

In spring and fall 2019, the KATRIN experiment recorded its first two science runs, already collecting more than five million signal electrons in the region of interest. The objective of this thesis is a comprehensive analysis of the first two measurement campaigns in terms of the neutrino mass and the existence of light sterile neutrinos.

This thesis is structured as follows: Chapter 1 provides an overview of the key aspects of neutrino physics. The particular focus is put on the neutrino-mass determination with the so-called kinematic approach via single β-decay. Chapter 2 describes the working principle of the KATRIN experiment in detail. In order to perform a high-level data analysis, realistic models of the molecular tritium β-decay and the experimental response are indispensable. Both were implemented in the analysis framework Samak, which was largely developed in this and the author's previous work [1]. With accumulating statistics, the model required continued revision. In view of the increasing

---

[1] Natural units are used throughout this thesis, i.e. $c = 1$

precision, effects become relevant, that only have a tiny impact on the experimental spectrum, such as the energy and angular dependence of the inelastic scattering probabilities. Chapter 3 describes the analysis software and the analysis strategy. Moreover, a large selection of statistical methods for parameter inference, limit calculation and sanity checks were implemented and adapted for the use in KATRIN and subsequently applied to data and simulation. Furthermore, the influence of systematic uncertainties on the model spectrum, for example the uncertainty on the source potential distribution, is evaluated with extensive Monte Carlo simulations and incorporated in the chi-squared analysis with the covariance matrix approach. The individual systematic effects are addressed in detail in chapter 4. The following two chapters (5 and 6) introduce the reader to the first and second measurement campaigns of the KATRIN experiment. During this work, the data taking was supported by various near-time analyses to monitor the global system stability. The characteristic features of the respective measurement campaigns, such as the time evolution of the column density or the observed background rate over-dispersion, are summarized. The blinding protocol, crucial to guarantee a bias-free analysis, is presented in chapter 7. Chapters 8 and 9 are dedicated to the neutrino-mass analyses of the first and second measurement campaigns, respectively. The best-fit results are shown and upper limits on m_ν are derived. Additionally, numerous studies are carried out to test the robustness of the analysis. The combined analysis of both data sets is presented in chapter 10. The same data sets are further on analyzed with respect to light sterile neutrinos in chapter 11. Exclusion contours for different analysis cases are presented and compared to results from existing experiments. Furthermore, many complementary analyses, for example to investigate the correlation between active and sterile decay branch, are carried out. In chapter 12, the thesis concludes with a summary.

Chapter 1

Neutrino physics

This chapter gives an introduction to neutrino physics. It is structured as follows: Section 1.1 provides a brief overview of the postulation and the discovery of the neutrino. Thereafter, the groundbreaking discovery of neutrino oscillations and their theoretical description are addressed in section 1.2. In order for neutrino oscillations to occur, neutrinos must possess a mass. Possible approaches to determine the absolute neutrino-mass scale are presented in section 1.3. At last, the possible existence of additional *sterile* neutrinos and their experimental signatures are discussed in section 1.4.

1.1 Postulation and discovery of the neutrino

1.1.1 Postulation

In the beginning of the 20th century when radioactivity was first being explored and the nuclear structure was mostly unknown, James Chadwick made an observation that puzzled the physicists of his time. In 1914, he measured the energy spectrum of β-electrons, expecting a mono-energetic line based on the assumed two-body nature of β-decay. However, a continuous spectrum was observed instead [2]. To resolve the seemingly violation of energy conservation, Wolfgang Pauli postulated in 1930 the existence of a neutral spin $\frac{1}{2}$ particle, that would be produced alongside the electron and that would carry the missing part of the decay energy [3].

$$\mathrm{n} \rightarrow \mathrm{p} + \mathrm{e}^{-} + \bar{\nu}_{\mathrm{e}}. \tag{1.1}$$

Pauli named the particle "*neutron*" and restricted it to have at most 1 % of the mass of a proton. In 1934, Enrico Fermi derived the theoretical description of β-decay [4], which is still used by modern day experiments to predict the shape of β-spectra. Fermi changed the name of Pauli's hypothetical particle to "*neutrino*", as the comparably heavy neutron, as it is known today, had been already discovered two years earlier. By comparison with the available data, Fermi concluded that the neutrino must be either massless or lighter than an electron.

1.1.2 Discovery of the electron neutrino

As neutrinos interact only very rarely with other particles, it took 26 years since their postulation to confirm their existence experimentally. Carrying no charge, neutrinos only participate in the weak interaction, which has a characteristic[1] small cross section in the order of $\sigma \approx 10^{-43}\,\mathrm{cm}^2$. This circumstance has earned neutrinos the nickname "*ghost particles*". In principle, neutrinos also interact gravitationally due to their nonzero mass. However, in the context of laboratory-based experiments, this effect is negligible.

The first time neutrinos were detected in 1956 by Reines and Cowan at the Savannah River site in the United States [5]. They exposed large waters tanks to a high flux of electron antineutrinos from a nearby nuclear reactor.

---

[1] Considering neutrinos with $E = \mathcal{O}(\mathrm{MeV})$, e.g. from a nuclear reactor.

Occasionally, an electron antineutrino interacts with a proton from the water, producing a neutron and a positron during the process of inverse β-decay

$$\bar{\nu}_e + \mathrm{p} \rightarrow \mathrm{n} + \mathrm{e}^+. \tag{1.2}$$

The positron annihilates immediately with a surrounding electron, emitting two back-to-back gamma rays. The gamma rays were detected with a liquid scintillator, which was filled in the inter-space between the water tanks. To distinguish the neutrino-induced positrons from background events, the neutron had to be reconstructed as well. The neutron is moderated in the water and eventually captured on cadmium, which was dissolved in form of cadmium chloride in the water tanks. The neutron capture process is accompanied by the emission of several gamma rays. The following scintillation light is delayed with respect to the prompt annihilation signal by the neutron thermalization timescale of a few µs. The coincidence of prompt and delayed scintillation light pulses served as distinctive signature of an electron antineutrino interacting with the detector.

1.1.3 Discovery of muon and tau neutrinos

A second neutrino kind, the muon neutrino ν_μ, was discovered in 1962 by Ledermann, Schwartz and Steinberger at the Brookhaven Alternating Gradient Synchrotron (AGS) [6]. They investigated the pion decay reactions

$$\pi^- \rightarrow \mu^- + \bar{\nu}_\mu \qquad \text{and} \qquad \pi^+ \rightarrow \mu^- + \nu_\mu \tag{1.3}$$

with a spark chamber. As no electronic showers were observed, they concluded that the produced neutrinos must be intrinsically different to from the known electron flavor.

The third and last kind of neutrino in the standard model, the tau neutrino ν_τ, was discovered in 2000 by the DONUT experiment at Fermilab [7]. A high-energy proton beam was directed on a tungsten target inducing a particle shower. In some rare cases, subsequent decays lead to the production of τ leptons, which in turn decayed into ν_τ. A massive shielding was placed between the primary interaction point and an emulsion lead detector to remove all particles except the neutrinos from the beam. Propagating unhindered through the shielding, the tau neutrinos were finally measured through charged current interactions in the lead. The produced τ would only leave a short track in the detector, because of its short decay length of only 2 mm. The distinct signature was a track with a kink-like structure, which marks the τ decaying into other particles.

The picture of three generations of neutrinos was already established in 1989 by measurements of the Z^0 resonance by the ALEPH experiment at the Large Electron Positron (LEP) collider CERN [8]. Within the standard model, the Z^0 boson is expected to decay into all fermion species, that are lighter than $Z^0/2$, with comparable probability as long as the respective decay channel is energetically allowed. The decay into neutrinos cannot be observed directly. Thus, the associated partial decay width is invisible $\Gamma_{\mathrm{inv}} = N_\nu \Gamma_\nu$. However, it can be reconstructed through comparison of the visible partial decay width Γ_{vis}, corresponding to the Z^0 decay into charged leptons and quarks, to the total decay width $\Gamma_{\mathrm{Z}} = \Gamma_{\mathrm{inv}} + \Gamma_{\mathrm{vis}}$. The more generations of neutrino flavors exist, the larger Γ_{Z} is compared to Γ_{vis}. Latest result of several LEP experiments yield $N_\nu = 2.984 \pm 0.008$ [9], confirming exactly three kinds of light neutrinos, that participate in the weak interaction.

1.2 Neutrino oscillations

The discovery of neutrino oscillations around the turn of the millennium fundamentally changed the picture of particle physics. Neutrinos were observed to change their flavor while propagating from source to experiment. This mechanism is only possible if neutrinos possess a mass, which is not foreseen in the widely recognized standard model of particle physics.

The theoretical concept of neutrino oscillations is briefly revised in section 1.2.1. Thereafter, the solar neutrino problem, which triggered a huge experiment effort to search for neutrino oscillations in the mid-1960s, is addressed in section 1.2.2 alongside the solution found by the SNO experiment in 2001. Moreover, the discovery of atmospheric neutrino oscillation in 1998 by the Super-Kamiokande experiment is presented in section 1.2.2.1.

1.2.1 Theoretical description

The neutrino oscillations were first introduced by Pontecorvo in 1958 [10]. Initially, his theory proposed neutrino-antineutrino oscillations. Later, he reformulated it to neutrino-flavor oscillations in view of the solar neutrino problem [11]. In parallel, Maki, Nakagawa and Sakata developed a formalism that described the mixing between massive neutrinos in 1962 [12].

Integral part of the neutrino oscillation theory is the fact that the neutrino-flavor eigenstates do not coincide with the neutrino-mass eigenstates. However, $|\nu_e\rangle, |\nu_\mu\rangle$ and $|\nu_\tau\rangle$ can each be expressed as a linear combination of the mass states $|\nu_1\rangle, |\nu_2\rangle$ and $|\nu_3\rangle$:

$$\begin{pmatrix} |\nu_e\rangle \\ |\nu_\mu\rangle \\ |\nu_\tau\rangle \end{pmatrix} = \begin{pmatrix} U_{e1} & U_{e2} & U_{e3} \\ U_{\mu 1} & U_{\mu 2} & U_{\mu 3} \\ U_{\tau 1} & U_{\tau 2} & U_{\tau 3} \end{pmatrix} \begin{pmatrix} |\nu_1\rangle \\ |\nu_2\rangle \\ |\nu_3\rangle \end{pmatrix}. \tag{1.4}$$

The mixing between flavor and mass eigenstates is determined by the unitary transformation matrix U, which is named after its creators: Pontecorvo-Maki-Nakagawa-Sakata (PMNS) matrix. It is often stated in its factorized in the form

$$U = \begin{pmatrix} 1 & 0 & 0 \\ 0 & c_{23} & s_{23} \\ 0 & -s_{23} & c_{23} \end{pmatrix} \cdot \begin{pmatrix} c_{13} & 0 & s_{13}\, e^{-i\delta_\mathrm{D}} \\ 0 & 1 & 0 \\ -s_{13}\, e^{-i\delta_\mathrm{D}} & 0 & c_{13} \end{pmatrix} \begin{pmatrix} c_{12} & s_{12} & 0 \\ -s_{12} & c_{12} & 0 \\ 0 & 0 & 1 \end{pmatrix} \begin{pmatrix} e^{i\delta_\mathrm{M1}} & 0 & 0 \\ 0 & e^{i\delta_\mathrm{M2}} & 0 \\ 0 & 0 & 1 \end{pmatrix} \tag{1.5}$$

with $s_{ij} = \sin(\theta_{ij})$ and $c_{ij} = \cos(\theta_{ij})$. The PMNS matrix is characterized by three mixing angles θ and one complex Dirac phase δ_D, which can cause CP violation. In case neutrinos are Majorana particles, two additional Majorana phases δ_M appear, which are relevant for neutrinoless double β-decay.

As the mixing between first and third generation θ_{13} is found to be small, it is often instructive to use a simplified two-flavor oscillation model. Considering, for example, the oscillation between $|\nu_e\rangle$ and $|\nu_\mu\rangle$, equation (1.5) can be simplified to

$$\begin{pmatrix} |\nu_e\rangle \\ |\nu_\mu\rangle \end{pmatrix} = \begin{pmatrix} \cos\theta & \sin\theta \\ -\sin\theta & \cos\theta \end{pmatrix} \begin{pmatrix} |\nu_1\rangle \\ |\nu_2\rangle \end{pmatrix} \tag{1.6}$$

with the associated mixing angle θ. In weak interaction processes, neutrinos are always produced in flavor eigenstates. An electron neutrino, for example, produced at a reference time $t = t_0$ can be written as

$$|\nu(t = t_0)\rangle = \cos\theta\, |\nu_1\rangle + \sin\theta\, |\nu_2\rangle. \tag{1.7}$$

After the interaction, the mass eigenstates are the physical states that propagate through space with a definite energy E_i and momentum p_i. Thus, the neutrino evolves as

$$|\nu(t > t_0)\rangle = \cos\theta\, \mathrm{e}^{-iE_1 t}\, |\nu_1\rangle + \sin\theta\, \mathrm{e}^{-iE_2 t}\, |\nu_2\rangle. \tag{1.8}$$

Since the two mass eigenstates have different energy eigenvalues $E_1 \neq E_2$, the mass eigenstates soon propagate out of phase and the neutrino has no longer a defined flavor. However, if the neutrino is experimentally detected after some time t_1, it is projected onto a flavor eigenstate, which couples to the weak interaction. The survival probability is given by the modulus square:

$$P_\mathrm{surv}(t_1) = |\langle \nu(t_1)|\nu_e\rangle|^2 \tag{1.9}$$

$$\Rightarrow P_\mathrm{surv}(t_1) = 1 - \sin^2(2\theta)\sin^2\left(\frac{(E_2 - E_1)\, t_1}{4}\right). \tag{1.10}$$

Considering ultra relativistic neutrinos, their energies can be approximated as

$$E_i = \sqrt{p_i^2 + m_i^2} = p_i\sqrt{1 + \frac{m_i^2}{p_i^2}} \overset{\text{Taylor}}{\approx} p_i + \frac{m_i^2}{2p_i} \approx E + \frac{m_i^2}{2E} \tag{1.11}$$

and the survival probability can be rewritten as

$$\Rightarrow P_{\text{surv}}(t_1) = 1 - \sin^2(2\theta)\,\sin^2\left(\frac{\Delta m^2 L}{4E}\right) \tag{1.12}$$

with the traveled distance L and the neutrino mass splitting $\Delta m^2 = m_2^2 - m_1^2$ [1, 13]. The survival probability is depicted in figure 1.1 for the example of $\nu_e \rightarrow \nu_\mu$. It illustrates, that the amplitude of the neutrino oscillation is determined by the mixing angle while the oscillation frequency is given by the mass splitting Δm^2.

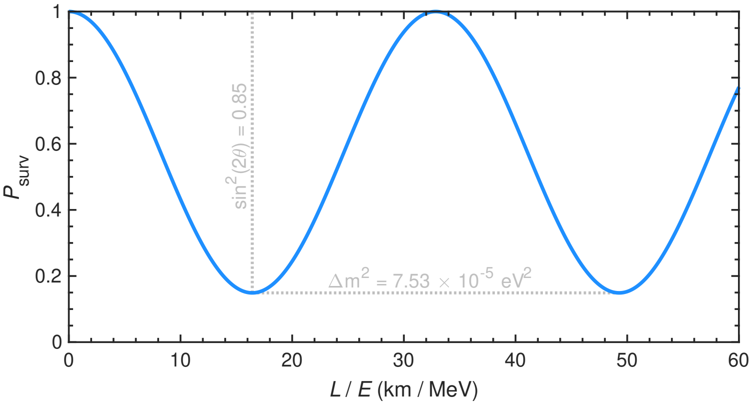

Figure 1.1: Two-flavor neutrino oscillations for $\nu_e \rightarrow \nu_\mu$. The survival probability as a function of L/E is calculated according to equation (1.12). The solar oscillation parameters are used: $\sin^2(\theta) = 0.307$ ($\sin^2(2\theta) = 0.851$) and $\Delta m^2 = (7.53 \pm 0.18) \times 10^{-5}\,\text{eV}^2$.

1.2.2 Solar neutrino problem

The sun emits vast amounts of electron neutrinos, creating an immense flux of 60 billion particles per cm^2 per second on earth [14]. The neutrinos are exclusively produced in electron flavor through nuclear fusion processes in the dominant pp-chain and the sub-dominant CNO cycle. Depending on the involved fusion isotopes, neutrino energies up 18 MeV can be reached.

For the first time solar neutrino neutrino were detected in 1970 by the Homestake experiment [15, 16]. Build underground in a gold mine in South Dakota under the leadership of Raymond Davis Jr., the experiment followed a radiochemical detection strategy with 600 t of perchloroethylene. The common dry-cleaning fluid is rich in the chlorine isotope ^{37}Cl, serving as target for neutrino capture

$$\nu_e + {}^{37}\text{Cl} \rightarrow {}^{37}\text{Ar} + e^- \tag{1.13}$$

with an energy threshold of 0.8 MeV. The Argon would subsequently decay via electron capture back into chlorine with a relatively short half-life time of only 35 days. Every few weeks, the ^{37}Ar isotopes were extracted and their quantify was determined with a proportional counter. The deduced neutrino flux could only account for a third of the prediction from the solar model.

When the result was confirmed by other experiments, such as GALLEX, SAGE and Kamiokande, the missing neutrino flux became famous as the solar neutrino problem. All of the aforementioned experiments were almost exclusively sensitive to the electron flavor, because solar neutrinos do not have enough energy to produce muon or tau leptons in charged current interactions. The solar neutrino problem could only be resolved in 2001 by the Sudbury Neutrino Observatory (SNO) [17], which was the first experiment that was sensitive to all neutrino flavors.

The SNO experiment, situated in an underground mine in Canada, detected solar neutrinos through their interaction with 1000 t of heavy water D_2O. The experiment was able to observe neutrinos through three different channels, namely elastic scattering off electrons (equation (1.14)) as well as charged current (equation (1.15)) and neutral current (equation (1.16)) interactions with deuterium. The last channel, in which the deuterium nucleus is dissociated, is equally likely for all neutrino flavors.

$$\begin{aligned} \nu_x + e^- &\rightarrow \nu_x + e^- && \text{CC for } \nu_e\text{, NC for all flavors} && (1.14)\\ \nu_e + d &\rightarrow p + p + e^- && \text{CC for } \nu_e && (1.15)\\ \nu_x + d &\rightarrow p + n + e^- && \text{NC for all flavors} && (1.16) \end{aligned}$$

Each channel produced a specific signal in form of Cherenkov light or Gamma rays, which were detected by a setup of 9600 photomultiplier tubes (PMTs). Finally, the total neutrino flux and the electron neutrino flux could be determined separately. While the electron neutrino flux was consistent with previous measurements, the total neutrino flux matched the expectation of the solar model. Arthur McDonald, the experiment's director, and his colleagues concluded that the electron neutrinos produced in the sun must change their flavor on their way to earth by the mechanism of neutrino oscillations.

Solar neutrino experiments are especially sensitive to the mixing between first and second generation. Latest results are [9]:

$$\Delta m^2_{12} = (7.53 \pm 0.18) \times 10^{-5}\,\mathrm{eV}^2, \qquad \sin^2(\theta_{12}) = 0.307 \pm 0.013. \tag{1.17}$$

1.2.2.1 Atmospheric neutrino oscillations

The Super-Kamiokande experiment is an underground neutrino observatory in the Kamioka mine in Japan. Studying electron and muon neutrinos created in the atmosphere, it achieved the first experimental confirmation of neutrino oscillations in 1998.

The earth atmosphere is constantly hit by cosmic rays, producing large amounts of secondary particles in form of hadronic showers. Subsequent decays of charged pions lead to the production of neutrinos and antineutrinos with a flavor composition of $\nu_\mu : \nu_e = 2 : 1$. The neutrino energies range from MeV up to PeV.

The Super-Kamiokande experiment comprises a 50 kt tank with ultra-pure water, which is surrounded by 11 146 PMTs. Neutrinos and antineutrinos can be detected by charged current interactions with water molecules

$$\nu_x + n \rightarrow p + \ell_x \qquad \text{and} \qquad \bar{\nu}_x + p \rightarrow n + \bar{\ell}_x. \tag{1.18}$$

The produced leptons ℓ_x emit Cherenkov light, which is used to reconstruct energy and direction of the incoming neutrinos. The direction provides information on the neutrino flight distance L, that is crucial to calculate the expected oscillation probability according to equation (1.12). Vertically upward going neutrinos travel much longer distances ($L \approx 13\,000\,\mathrm{km}$) than vertically downward going neutrinos ($L \approx 15\,\mathrm{km}$), because the former have to traverse the earth in order to reach the detector. Moreover, the lepton type and the associated neutrino flavor can be distinguished from the structure of the Cherenkov ring: Electrons produce fuzzy light rings, because they scatter off the ambient water molecule while they propagate. As muons interact only little, they create sharp light rings. Tau neutrinos could initially not be detected, due to the short half-life of the τ.

Events, that were assigned to ν_μ, exhibited a significant L/E dependence. Moreover, the ratio of ν_μ to ν_e events was much smaller than the expected. Both features could be explained by two-flavor neutrino oscillations $\nu_\mu \rightarrow \nu_\tau$. As tau neutrinos could not be reconstructed, the oscillation was observed in form of ν_μ disappearance. Latest results on the atmospheric mixing parameters are [9]:

$$\begin{aligned} \Delta m^2_{32} &= (2.453 \pm 0.033) \times 10^{-3}\,\mathrm{eV}^2, && \sin^2(\theta_{23}) = 0.546 \pm 0.021 && \text{for normal ordering,} && (1.19)\\ \Delta m^2_{32} &= (-2.536 \pm 0.034) \times 10^{-3}\,\mathrm{eV}^2, && \sin^2(\theta_{23}) = 0.539 \pm 0.022 && \text{for inverted ordering.} && (1.20) \end{aligned}$$

Events, reconstructed as ν_e, did not show a L/E dependence, i.e. no signature of neutrino oscillations. Due to the small mass splitting $\Delta m_{12} \approx 8 \times 10^{-5}$ and relatively high neutrino energies, the oscillation $\nu_e \rightarrow \nu_\mu$ occurs on length scales of $L \approx 10^5\,\mathrm{km}$, that are not accessible for atmospheric neutrino experiments. Thus, electron neutrinos reach the detector before they have oscillated. Even though the oscillation $\nu_e \rightarrow \nu_\tau$ occurs on accessible length scales with $\Delta m^2_{31} \approx \Delta m^2_{32}$, it could not be detected with Super-Kamiokande due to the small mixing angle $\sin^2(\theta_{13}) = (2.20 \pm 0.07) \times 10^{-2}$ [9].

1.3 Neutrino mass

Neutrino oscillations provide the possibility to infer the neutrino mass splittings Δm_{ij}^2 to a high precision. However, they are not sensitive to the absolute neutrino mass scale, e.g. the mass of the lightest mass eigenstate. Currently, three complementary approaches are being explored: Cosmology, neutrinoless double β-decay and the kinematic study of weak interaction processes such as single β-decay. Each method is addressed in the following.

1.3.1 Cosmology

The evolution of the universe from the Big Bang to its present state is described with the ΛCDM model. During the Big Bang, vast amounts of ultra-relativistic neutrinos and antineutrinos, so-called relic neutrinos, have been produced. Even though neutrinos are known to interact only very little, they have a large influence on structure formation processes in the evolution of the universe due to the extraordinary abundance. Having a large free-streaming length, relic neutrinos act as hot dark matter and wash out small scale structures. The observation of anisotropies in the cosmic microwave background in addition to large-scale structures (LSS) allows to infer the sum of the neutrino mass eigenstates

$$m_{\mathrm{tot}} = \sum_{i=1}^{3} m_i. \tag{1.21}$$

The current upper limits at 95 % confidence level (C.L.) lie between $m_{\mathrm{tot}} \leq 0.087\,\mathrm{eV}$ and $m_{\mathrm{tot}} \leq 0.54\,\mathrm{eV}$, depending on the considered data set and model parameters. The large variation stems from the model dependence of the cosmological approach. Some parameters, such as the Hubble constant and the number of neutrino species, are strongly correlated. Thus, different parameter combinations may mimic the same observation.

1.3.2 Neutrinoless double β-decay

Double β-decay, abbreviated as $2\nu\beta\beta$, is the process of two simultaneous β-decays in the same nucleus

$$2n \rightarrow 2p + 2e^- + 2\bar{\nu}_e. \tag{1.22}$$

For some isotopes single β-decay energetically forbidden. Some of these isotopes may decay via $2\nu\beta\beta$ instead. This is illustrated in figure 1.2 (left) at the example of the Germanium isotope ^{76}Ge. As the binding energy of ^{76}As is higher than the one of ^{76}Ge, the latter cannot undergo single β-decay. However, the double decay to ^{76}Se is kinematically allowed. Since its first experimental confirmation in 1987 [18], $2\nu\beta\beta$ has been observed for 12 different isotopes. Being a second order weak nuclear process, $2\nu\beta\beta$ is very unlikely, which is mirrored by the extremely large half-life times between 10^{18} and 10^{22} years [19].

Neutrinoless double β-decay, abbreviated as $0\nu\beta\beta$, is a hypothetical decay mode, in which no physical antineutrinos are emitted

$$2n \rightarrow 2p + 2e^-. \tag{1.23}$$

Instead, a virtual antineutrino produced in one of the β-decays is absorbed at the other vertex by a second neutron. As this process violates lepton number conversation by two units, it is not foreseen in the Standard model of particle physics. Neutrinoless double β-decay requires neutrinos to be so-called Majorana particles and to carry a mass. Majorana's theory states that there is no fundamental difference between neutrinos and antineutrinos, except from their chirality. Antineutrinos are produced in weak interaction processes as right-handed particles. However, since neutrinos possess a nonzero mass, they have a small left-handed component which scales with $m_{\beta\beta}/E$. Their absorption at the second vertex can only occur, if the right-handed antineutrino changes its handiness and becomes a left-handed neutrino. The larger the neutrino mass, the larger its left-handed component is and the more likely it is for $0\nu\beta\beta$ to occur. The mass that influences the half-life time is the coherent sum over all neutrino mass eigenstates, weighted by the respective entries of the PMNS matrix

$$m_{\beta\beta} = |\sum_{i=1}^{3} U_{ei}^2 m_i|. \tag{1.24}$$

By experimentally measuring the half-life time of $0\nu\beta\beta$-decaying isotopes, the absolute neutrino mass scale can be inferred. However, the translation between half-life time and $m_{\beta\beta}$ requires knowledge of the associated nuclear matrix element. To account for the theoretical uncertainty on the former, experiments usually provide a range of upper limits on $m_{\beta\beta}$ using different nuclear matrix elements. Moreover, due to the complex phases in the PMNS matrix, cancellations are possible in equation (1.24).

The experimental signature of $0\nu\beta\beta$, illustrated in figure 1.2 (right), is a sharp peak at the full decay energy. Its amplitude provides information on the half-life time of the decaying isotope. As of today, $0\nu\beta\beta$ has not been observed. The most stringent upper limits on the neutrino mass stem from the KamLAND-Zen experiment using ^{136}Xe with $m_{\beta\beta} < 61-165\,\text{meV}$ [20] and from the GERDA experiment using Ge with $m_{\beta\beta} < 79-180\,\text{meV}$ [21].

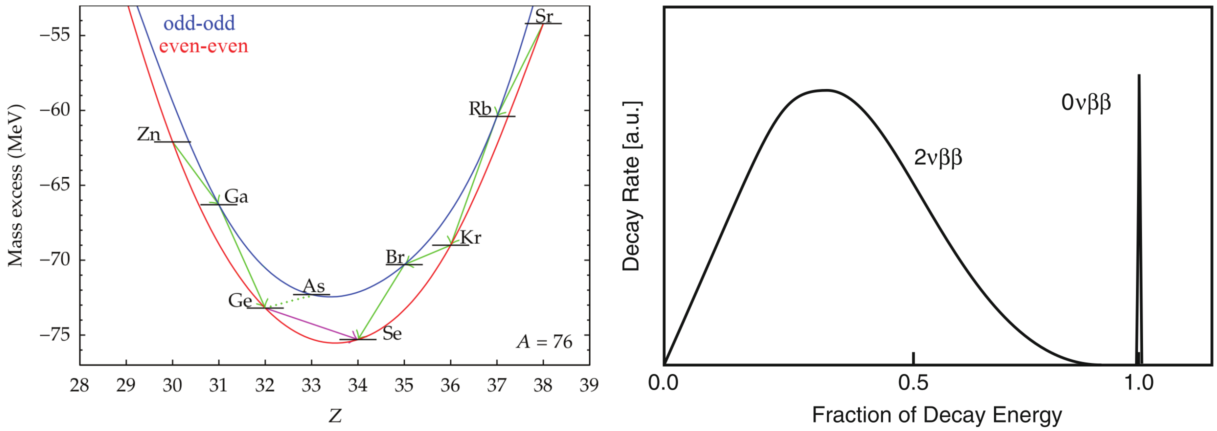

Figure 1.2: Left: Mass excess or equivalently binding energy for isotopes with $A = 76$. It is differentiated between isotopes with even numbers of protons and neutrons ("even-even") and isotopes with odd proton and neutron numbers ("odd-odd"). In general, odd-odd isotopes have larger binding energy than even-even isotopes with the same proton number Z. Energetically allowed single β-decay are highlighted as green arrows. As single β-decay is energetically forbidden for Germanium (dotted line), the isotope can only decay via double β-decay to Selenium (violet arrow). **Right:** Energy spectra of double β-decay ($2\nu\beta\beta$) and neutrinoless double β-decay ($0\nu\beta\beta$). While the standard double β-decay has a continuous electron energy spectrum, neutrinoless double β-decay manifests itself as a monoenergetic peak at the full decay energy. Taken from [13].

1.3.3 Single β-decay

High-precision measurements of single β-decay or electron capture are considered to be the most direct way to determine the absolute scale of the neutrino mass. As it requires no prior assumption on the nature of the neutrino (Dirac vs. Majorana), it is considered to be model-independent. In the following, the neutrino-mass determination using single β-decay is discussed in detail.

Nuclear β-decay is a radioactive decay, that is mediated by the weak interaction. A neutron decays into a proton under the emission of an electron and an electron antineutrino as stated in equation (1.1). The total energy Q, that is released in the decay, is given by the mass difference of the nucleus in the initial state ${}^{A}_{Z}\mathrm{X}$ and the nucleus in the final state ${}^{\;\;A}_{Z+1}\mathrm{X}'$ and the produced electron

$$Q = m({}^{A}_{Z}\mathrm{X}) - m({}^{\;\;A}_{Z+1}\mathrm{X}') - m_e. \tag{1.25}$$

The mass of the neutrino is assumed to be zero in the definition of the Q-value. The decay energy is distributed among the decay products. The daughter nucleus receives the recoil energy E_{rec}. If it is bound in a molecular structure, it can also obtain additional energy through vibrational and rotational excitation as well as through excitation of the shell electrons. This aspect is addressed in detail in section 2.2.1. The remaining energy, called endpoint E_0, is shared between the electron and the electron antineutrino

$$E_0 = Q - E_{\text{rec}} = E + E_\nu \tag{1.26}$$

with E being the kinetic electron energy and E_ν being the total neutrino energy. This equation underlines, that the energies of the leptons are related by energy conservation. Even if the electron antineutrino is created without any kinetic energy, the energy available to the electron will differ from E_0 by the rest mass of the neutrino.

The definition of the latter, however, requires further explanation. As $\bar{\nu}_e$ is created in the electron flavor eigenstate, it has no specific mass. Instead, using the formalism of quantum mechanics, $|\bar{\nu}_e\rangle$ can be described as a superposition of the three known neutrino mass eigenstates $|m_i\rangle$ weighted by the respective entries in the PMNS matrix U_{ei}

$$|\bar{\nu}_e\rangle = \sum_{i=1}^{3} U_{ei}\,|m_i\rangle\,. \tag{1.27}$$

Evaluation of the expectation value yields the probability $|U_{ei}|^2$, that the antineutrino carries a rest mass m_i. As the neutrino mass splittings Δm_{ij}^2 are known to be small compared to the sensitivity of any existing experiment [9], an effective electron antineutrino mass m_ν is defined in equation (1.28). Further on, m_ν is simply referred to as *neutrino mass*.

$$m_\nu = \sqrt{\sum_{i=1}^{3} |U_{ei}|^2\, m_i^2}. \tag{1.28}$$

The energy distribution $\frac{\mathrm{d}\Gamma}{\mathrm{d}E}$ of the β-decay electrons, visualized in figure 1.3, can be calculated by Fermi theory [22]

$$\begin{aligned}\frac{\mathrm{d}\Gamma}{\mathrm{d}E}(E, m_\nu^2) = {} & \frac{G_\mathrm{F}^2 \cdot \cos^2\theta_c}{2\pi^3} \cdot |\mathscr{M}_{\text{nucl.}}|^2 \cdot F(Z,E) \cdot (E + m_e) \cdot \sqrt{(E+m_e)^2 - m_e^2} \\ & \cdot (E_0 - E)\sqrt{(E_0-E)^2 - m_\nu^2} \cdot \Theta(E_0 - E - m_\nu).\end{aligned} \tag{1.29}$$

The formula contains several fundamental constants and kinematic parameters, namely:

G_F:	Fermi constant	E:	Electron kinetic energy
θ_c:	Cabibbo angle	m_e:	Electron mass
$\mathscr{M}_{\text{nucl.}}$:	Nuclear matrix element	E_0:	Endpoint energy (defined in equation (1.26))
$F(Z,E)$:	Fermi function of the daughter nucleus	m_ν:	Neutrino mass (defined in equation (1.28))
Z:	Atomic number	Θ:	Heaviside step function

The Heaviside step function ensures energy conservation, as it requires the total neutrino energy $E_\nu = E_0 - E \geq m_\nu$ to be larger than or equal to the neutrino mass. The nuclear matrix element determines the coupling strength between initial and final states of the system. In case of a super-allowed β-decaying isotope, such as tritium, $\mathscr{M}_{\text{nucl.}}$ is energy-independent in the endpoint region and thus has no influence on the shape of the spectrum. The Fermi function accounts for the Coulomb interaction between outgoing decay electron and the daughter nucleus[2]. As both $\mathscr{M}_{\text{nucl.}}$ and F are independent from the neutrino mass, the influence of m_ν^2 on the energy spectrum stems only from the phase space term $(E_0 - E)\sqrt{(E_0-E)^2 - m_\nu^2}$.

In principle, m_ν^2 could be determined by comparing the measured and the expected endpoint energy. However, as both cannot be determined with sufficient precision, the spectral shape in the vicinity of the endpoint has to be studied. The spectral distortion caused by m_ν^2 is illustrated in figure 1.3 (b) for several hypothetical m_ν^2 values. Relative to the rate, it is most prominent in the close vicinity of the endpoint. However, to fraction of β-electrons, that lie within the last 40 eV below E_0 is as small as 10^{-8}. At the time of writing, the KATRIN experiments provides the most stringent upper limit $m_\nu \leq 0.8\,\text{eV}^2$ at 90 % C.L. [23].

As the KATRIN experiment uses molecular tritium at nonzero temperature, the theoretical electron energy spectrum in equation (1.29) has to be revised. All KATRIN-specific modifications of the decay spectrum are addressed in section 2.2.1.

---

[2] In the case of tritium β-decay, $F(Z=2,E)$ has to be used.

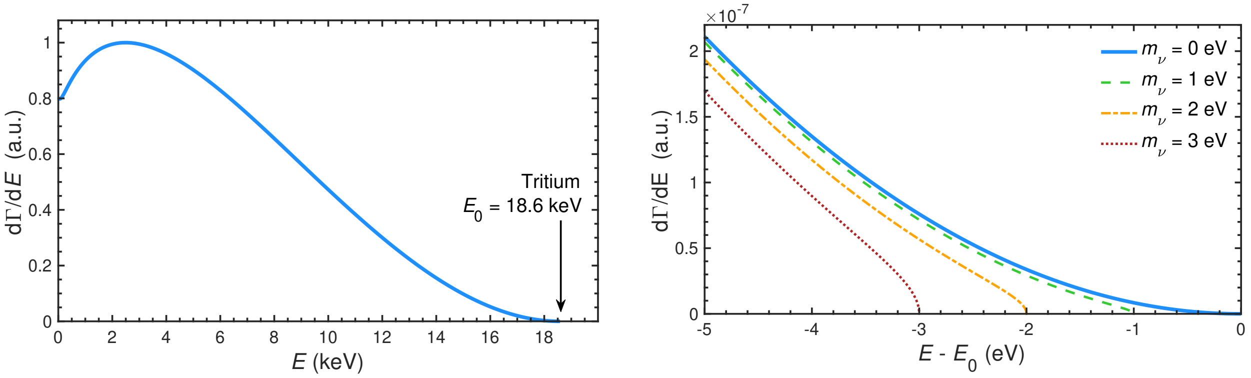

(a) Tritium β-spectrum

(b) Enlarged view of the endpoint region

Figure 1.3: Differential electron energy spectrum of the tritium isotope in arbitrary units (a.u.). They spectrum is calculated according to equation (1.29) with $Z = 2$. **(a):** The spectrum is shown in the complete energy range up to the tritium endpoint of $E_0 = 18.6\,\text{keV}$. **(b):** The imprint of the effective electron antineutrino mass m_ν (equation (1.28)) on the spectrum is shown for different hypothetical m_ν^2 values. The energy range is limited to the endpoint region, in which the relative spectral distortion is most prominent. The neutrino-mass imprint on the experimental spectrum, including a realistic background level, is discussed in appendix F.3.

1.4 Sterile neutrinos

The standard model of particle physics foresees three active neutrino generations; ν_e, ν_μ and ν_τ. Based on the measured width of the Z^0 resonance, it is indeed well established that there are only three light neutrinos, that interact via the weak interaction [8]. However, several minimal extensions of the standard model propose at least one additional neutrino species ν_s, so-called sterile neutrinos, which do not take part in the weak interaction [24]. In contrast to the known active flavors, the hypothetical neutrino species is associated with right-handed neutrinos. In this work the simplest case with only one additional sterile neutrino, so-called $3\nu+1$ framework, is considered.

The sterile neutrino flavor is accompanied by a fourth mass eigenstate m_4, which mixes to the active flavors

$$\begin{pmatrix} |\nu_e\rangle \\ |\nu_\mu\rangle \\ |\nu_\tau\rangle \\ |\nu_s\rangle \end{pmatrix} = \begin{pmatrix} U_{e1} & U_{e2} & U_{e3} & U_{e4} \\ U_{\mu 1} & U_{\mu 2} & U_{\mu 3} & U_{\mu 4} \\ U_{\tau 1} & U_{\tau 2} & U_{\tau 3} & U_{\tau 4} \\ U_{s1} & U_{s2} & U_{s3} & U_{s4} \end{pmatrix} \begin{pmatrix} |\nu_1\rangle \\ |\nu_2\rangle \\ |\nu_3\rangle \\ |\nu_4\rangle \end{pmatrix}. \tag{1.30}$$

with the extended 4×4 unitary PMNS matrix. As long as the mixings of the fourth mass eigenstates to the active flavors are relatively small, sterile neutrinos can be realized over a wide range of possible masses [25].

This work investigates the existence of sterile neutrinos at the eV mass scale, which are motivated by accumulating anomalies in short-baseline neutrino oscillation experiments. In the following, the experimental signatures of light sterile neutrinos are addressed in section 1.4.1. The experimental hints are summarized in section 1.4.2.

1.4.1 Signature of sterile neutrinos

Even though sterile neutrinos do not participate in the weak interaction, they still leave experimental footprints due to their mixing with the active flavors. In the following, different ways to search for sterile neutrinos are briefly presented. A comprehensive overview can be found for example in [26].

Neutrino oscillations As worked out in section 1.2.1, the neutrino oscillation period is given by the mass difference $(L/E)_{\text{osc}} \propto 1/\Delta m^2$. Neutrino oscillations involving eV-scale sterile neutrinos have much shorter wavelengths than the oscillations among the active flavors, since $m_4^2 \gg m_1^2, m_2^2, m_3^2$ [9]. For this reason, sterile neutrino oscillation experiments are located at a short distance from their neutrino source. Experiments studying low-energetic neutrinos, e.g. from a nuclear reactor, have typical baselines of a few ten meters. The typical baseline for experiments that investigate high-energetic neutrinos, e.g. from an accelerator, is a few hundred meters. As the oscillation between the active flavors has not yet developed at such short distances, the active-to-sterile oscillation can be well described with the two-flavor oscillation formula of equation (1.12).

If the experimentally accessible L/E ratio is much larger than the oscillation length $L/E \gg (L/E)_{\text{osc}}$, the oscillatory pattern cannot be resolved anymore by the detector. Instead, an overall suppression of the flux of the original neutrino flavor can be observed. In this case, only lower limits on Δm^2_{i4} can be set with $i \in [1,2,3]$.

Neutrino-less double β-decay If neutrinos are Majorana particles and $0\nu\beta\beta$ is triggered by light Majorana neutrino exchange, m_4 will contribute to the effective Majorana mass

$$\begin{aligned} m_{\beta\beta} &= |\sum_{i=1}^{4} U_{ei}^2\, m_i| \\ &= |(1-|U_{e4}|^2)\sum_{i=1}^{3} U_{ei}^2 m_i + |U_{e4}|^2 e^{i\gamma} m_4|. \end{aligned} \tag{1.31}$$

with a possible third Majorana phase $\gamma \in [-\pi, \pi]$. If the active-neutrino contribution to $m_{\beta\beta}$ was determined by other experiments, e.g. direct searches or cosmology, limits on $m_{\beta\beta}$ can be translated into constraints on sterile neutrinos in terms of m_4^2 and $|U_{e4}|^2$.

Single β-decay In single β-decay, antineutrinos are produced with electron flavor. Given the mixing between electron flavor and the fourth mass eigenstate is nonzero, the electron antineutrino comprises a small component of the fourth mass eigenstate. Thus, the β-decay spectrum in equation (1.29) has to be extended by an additional decay branch associated with m_4. In the $(3\nu+1)$-framework, the β-electron energy spectrum is the superposition of active and sterile branch

$$\frac{\mathrm{d}\Gamma}{\mathrm{d}E}(E, m_\nu^2, m_4^2, |U_{e4}|^2) = \underbrace{(1-|U_{e4}|^2)\cdot\frac{\mathrm{d}\Gamma}{\mathrm{d}E}(E, m_\nu^2)}_{\text{Active branch}} + \underbrace{|U_{e4}|^2\cdot\frac{\mathrm{d}\Gamma}{\mathrm{d}E}(E, m_4^2)}_{\text{Sterile branch}}. \tag{1.32}$$

In accordance with energy conservation, the sterile branch emerges only at electron energies $E \leq E_0 - m_4$, which results in a kink-like spectra distortion. The experimental signature is visualized in 1.4 at the example of a sterile neutrino with $m_4^2 = (20\,\text{eV})^2$ and $|U_{e4}|^2 = 0.2$. The mixing of the electron flavor to the fourth mass eigenstate $|U_{e4}|^2$, hereinafter abbreviated as active-to-sterile mixing, is largely exaggerated for illustration.

1.4.2 Sterile-neutrino anomalies

Since the 1990s several hints for the existence of sterile neutrinos emerged in short-baseline neutrino oscillation experiments. The so-called sterile-neutrino anomalies are discussed one by one in the following.

Reactor antineutrino anomaly The reactor antineutrino anomaly (RAA) describes the discrepancy between measured and predicted electron antineutrino flux from nuclear reactors at short baseline ($L < 100\,\text{m}$) [27].

Evidently, this measurement requires knowledge of the initial $\bar{\nu}_e$ spectrum, that is emitted by the nuclear reactor. Electron antineutrinos are produced in nuclear reactors by β-decaying fission products of the nuclear fuel, namely ^{235}U, ^{238}U, ^{239}Pu and ^{241}Pu. The total $\bar{\nu}_e$ flux, which is a superposition of thousands of β-decay branches, is predicted with a semi-empirical strategy: In a first step, the electron β-decay spectra are measured experimentally, by irradiating thin targets with Uranium and Plutonium and exposing them to a high neutron flux. In a second step, the measured electron spectra have to be converted into electron antineutrino spectra. Before 2011, the conversion was performed with an empirical model with 30 effective β-decays. In 2011 the conversion process was revised, including now all known β-decay branches of thousands of fission products in addition to virtual decay branches, which lead to an increase of the predicted $\bar{\nu}_e$ flux.

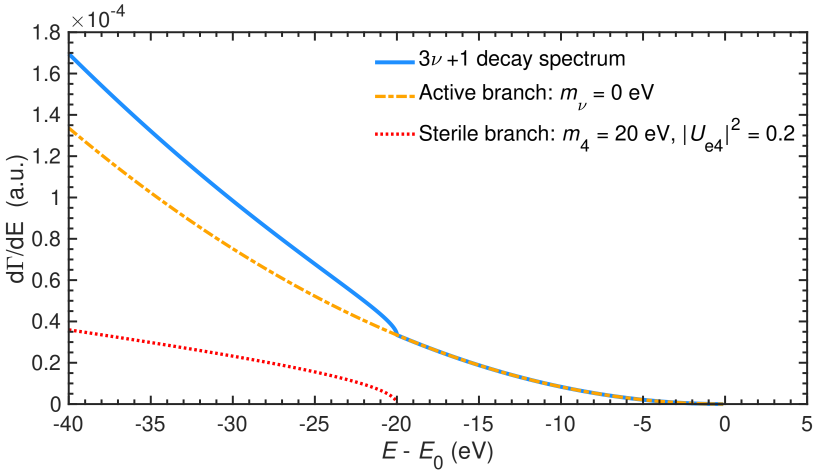

Figure 1.4: Sterile neutrinos in β-decay experiments. If eV-scale sterile neutrinos exist, the β-decay energy spectrum is a superposition of an active decay branch and a sterile decay branch (equation (1.32)). The signature of sterile neutrino is a kink-like spectral distortion.

Applied in the analysis of the reactor data, the flux re-evaluation lead to a 2.5σ deficit in $\bar{\nu}_e$ flux compared to the prediction, which is commonly referred to as the RAA [27]. The anomaly could be explained with neutrino oscillations involving a sterile neutrino $\bar{\nu}_e \to \nu_s$. As the flux deficit is energy-independent for $L \lesssim 15\,\mathrm{m}$, the sterile neutrino is required to have a mass of $\Delta m^2 \gtrsim 1\,\mathrm{eV}^2$. The RAA confidence region at 95 % C.L. is displayed in figure 11.8.

In 2021, the $\bar{\nu}_e$ flux prediction was again re-evaluated based on new measurements of the fission β-electron spectra of ^{235}U and ^{239}Pu at a research reactor at the Kurchatov Institute (KI) [28]. To eliminate systematic uncertainties on the absolute fission rate, the cumulative spectra of ^{235}U and ^{239}Pu were considered relative to each other. The ratio (^{235}U/^{239}Pu) was about 5 % lower compared to previous measurements at the Institute Laue-Langevin (ILL) [29], in which the absolute fission spectra were determined separately. The result may indicate, that the normalization of the ^{235}U spectrum at ILL has been overestimated. Correcting for this effect in the $\bar{\nu}_e$ flux prediction for ^{235}U, the authors of [28] can significantly reduce the discrepancy between observed and predicted total $\bar{\nu}_e$ flux (RAA). However, as the KI data provide only relative fluxes, the final conclusion on the RAA is still pending.

Gallium anomaly The Gallium anomaly (GA) is characterized by a rate deficit in calibration measurements from the solar neutrino experiments GALLEX [30, 31] and SAGE [32] in the 1990s and 2000s. The experiments were designed to measure electron neutrinos from the sun via neutrino capture on Gallium

$$\nu_e + {}^{71}\mathrm{Ga} \to {}^{71}\mathrm{Ge} + e^- . \tag{1.33}$$

After a certain measurement period, the produced Germanium was chemically extracted. Its abundance was determined via its subsequent decay through electron capture with a half-life of 11 days using a proportional counter.

The GA emerged in calibration measurements: To evaluate the detection efficiency of the system, different calibration sources with well known activity were inserted into the setup. While GALLEX used two ^{51}Cr sources, SAGE employed one ^{51}Cr source and one ^{37}Ar source. The calibration isotopes decay via electron capture, producing ν_e with discrete energies at several hundred keV. Both experiments observed less neutrino capture events from their calibration sources than expected. Combining both results, the deficit amounts to 15 % at 3σ significance [26]. Similar to the RAA, the rate deficit can be interpreted in terms of neutrino oscillations involving a sterile neutrino at the eV mass scale. The associated confidence region is shown in figure 11.8.

The Gallium anomaly was recently reaffirmed by the BEST collaboration using ^{51}Cr and a similar detection principle [33] . Different to its predecessors, BEST employed two nested ^{71}Ga targets in order to obtained information on the traveled distance of the hypothetical $\nu_e \rightarrow \nu_s$ oscillation. The inner spherical target volume had a diameter of 1.3 m and the outer cylindrical target volume had a diameter of 2.2 m. The calibration source was placed at the center of the setup. Their data confirmed the overall rate deficit of the GA. However, no significant difference between inner and outer target volume could be found. If the GA is interpreted in terms of sterile neutrinos, the oscillation must therefore occur at a length scale that is smaller or similar to the dimension of the experimental setup, which translates into $\Delta m^2 \gtrsim 1\,\mathrm{eV}^2$. Moreover, a relatively large mixing of $\sin^2(2\theta) \approx 0.4$ between electron flavor and new neutrino mass eigenstate is requires to explain the large rate deficit.

Neutrino-4 The Neutrino-4 collaboration claims to have found evidence for the existence of an eV-scale sterile neutrino based on measurements of very-short baseline neutrino oscillations at a nuclear reactor [34, 35]. However, as pointed out below, the significance of their finding is controversially debated in the sterile-neutrino community.

The Neutrino-4 experiment is located close to the SM-3 reactor in Dimitrovgrad in Russia and has started data taking in 2016. Electron antineutrinos emitted by the reactor are detected through inverse β-decay (see equation (1.2)) using a liquid scintillator, that is enriched with 0.1 % gadolinium. The $\bar{\nu}_e$ signature is the coincidence of a prompt positron signal and a delayed neutron capture signal. The detector is arranged in 50 segments and comprises a fiducial volume of $1.4\,\mathrm{m}^3$. As the setup is movable, the distance to the reactor core can be varied between $6-12\,\mathrm{m}$. The neutrino energy can be determined through the reconstructed energy of the prompt scintillation pulse. The experimental data is presented in form of the ratio between observed $\bar{\nu}_e$ events and distance-averaged $\bar{\nu}_e$ events as a function of L/E. Their latest chi-squared analysis assuming an oscillatory pattern yields $\Delta m^2 = 7.3\,\mathrm{eV}^2$ and $\sin^2(2\theta) = 0.36$ at a significance of 2.9σ [35]. The 2σ contour is displayed in figure 11.8.

The result was critically received by the sterile-neutrino community. The authors of [36] and [37] independently point out, that the energy resolution of the detector was seemingly not taken into account in the Neutrino-4 analysis. Moreover, the statistical significance of the sterile-neutrino signal is put into question. As pointed out by [36–38], neutrino-oscillation experiments are prone to false signal claims, if Wilk's theorem is applied unjustifiably. Using Monte-Carlo methods instead of Wilk's theorem, [36] finds a decreased significance of the Neutrino-4 result of only 2.2σ.

LSND and MiniBooNE anomalies The Liquid Scintillator Neutrino Detector (LSND) experiment observed in the 1990s an unexpected excess of $\bar{\nu}_e$ at short baseline from a pure $\bar{\nu}_\mu$ beam. The 3.8σ excess can be interpreted in terms of sterile neutrinos in the eV mass regime [39]. The experiment was followed up by the Mini Booster Neutrino Experiment (MiniBooNE) at Fermilab to test the LSND anomaly at different L/E ratios. However, a low-energy excess consistent with the LSND result was observed instead [40].

The LSND experiment took place at the Los Alamos Meson Physics Facility in the United States. A beam of 800 MeV protons was directed on a fixed target, producing large amounts of charged pions. While most π^- were captured in the target material, the π^+ were merely slowed down and decayed subsequently into relatively low-energy ν_μ, $\bar{\nu}_\nu$ and ν_e. Consequently, only very few $\bar{\nu}_e$ were produced. The LSND detector was located at 30 m distance from the beam dump. It comprised 67 t of liquid scintillator surrounded by 1220 PMTs. The electron antineutrinos were detected via inverse β-decay (see equation (1.2)), which produced the characteristic coincidence of prompt and delayed scintillation light.

The collaboration observed significantly more $\bar{\nu}_e$ events than expected (3.8σ) , which can be interpreted in terms of $\bar{\nu}_\mu \rightarrow \bar{\nu}_e$ oscillations. Due to the short baseline, the associated Δm^2 is at the eV scale, which implies an extension of the standard 3ν framework with an additional neutrino species. The LSND finding was challenged by the KARMEN experiment using a similar setup. Not observing a $\bar{\nu}_e$ excess, they could exclude large parts of the favored parameter space [41].

MiniBooNE was constructed at Fermilab to investigate the LSND anomaly. The experiment was conducted with larger neutrino energies up to 1250 MeV and at a larger baseline (541 m) than LSND, but with a similar L/E ratio. MiniBooNE was fed by a neutrino beam that was generated through collisions of 8 GeV protons with a fixed beryllium target. The charged mesons ($\pi^\pm$, $K^\pm$), produced in the collisions, decay in-flight in a 50 m long decay tunnel. Through the application of magnetic fields, only mesons with a specific electric charge could be selected.

This allowed for the operation in two different modes, namely $\nu_\mu \rightarrow \nu_e$ (search for ν_e appearance) and $\bar{\nu}_\mu \rightarrow \bar{\nu}_e$ (search for $\bar{\nu}_e$ appearance). The MiniBooNE detector comprised 800 t of mineral oil and 1280 PMTs. The electron (anti) neutrinos were detected through Cherenkov and scintillation light of charged particles, that are produced in ν interactions.

Both operation modes yielded a $\nu_e/\bar{\nu}_e$ excess at low energies with a combined significance of 4.7σ [40]. As for LSND, the result is compatible with two-flavor oscillations involving an eV-scale neutrino. Even though not located at the same L/E ratio, the MiniBooNE results are consistent with the LSND anomaly. The allowed parameter spaces of both experiments are shown in figure 1.5.

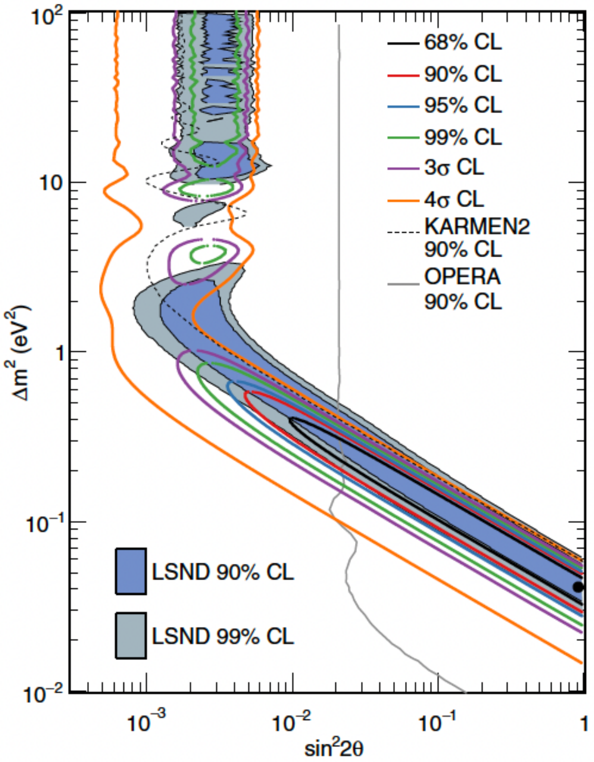

Figure 1.5: The LSND and MiniBooNE anomalies [40]. Both experiments observe an excess of $\bar{\nu}_e$ at a short baseline from a pure $\bar{\nu}_\mu$ beam, which can be interpreted as an $\bar{\nu}_\mu \rightarrow \bar{\nu}_e$ oscillation. MiniBooNE additionally finds a low-energy ν_e excess in the charge conjugated oscillation. The mass splitting Δm^2 required to explain the data is too large to be consistent with the standard 3ν picture. Thus, constraints on a fourth neutrino mass and its mixing are determined and depicted in this figure. The filled areas show the favored parameter space of the LSND anomaly at 90 % and 99 % C.L. [39]. The first six lines in the top left legend correspond to the MiniBooNE contours at different confidence levels. A part of the favored parameter space can be excluded by the KARMEN experiment [41], which did not observe an unexpected $\bar{\nu}_e$ excess in a setup similar to the LSND experiment.

Chapter 2

The KATRIN experiment

The Karlsruhe Tritium Neutrino (KATRIN) experiment [42] is designed to measure the effective electron antineutrino mass m_ν scale via the kinematics of single β-decay of molecular tritium.

2.1 Experimental setup

This section provides an overview of the setup of the KATRIN experiment. The focus is set on those components, which are substantial for the modeling of the experimental response function, described in section 2.2. A comprehensive description of all experimental constituents can be found in the references [42, 43].

The 70 m-long setup is illustrated in figure 2.1. The individual components are described in the following from rear to front end. Locations $\vec{r}$ within the setup are often described in terms of cylindrical coordinates with the z axis being aligned with the beam line[1]. The position in the (x, y)-plane is characterized by a radius r[2] and an azimuth angle $\phi = \angle(\vec{r}, \vec{e}_y)$[3]. Moreover, the polar angle $\theta = \angle(\vec{r}, \vec{B})$ is defined as the angle between the local magnetic field $\vec{B}$ and $\vec{r}$.

2.1.1 Rear section

The so-called rear section terminates the experimental setup at the rear end. It houses the rear wall (section 2.1.1.1), which ensures a well-defined and homogeneous source potential, and several calibration and monitoring devices. The most-relevant device is the electron gun (2.1.1.2), with which tritium activity and energy-loss function can be determined.

2.1.1.1 Rear wall

The rear wall is a stainless steel disk with a diameter of 14.6 cm, which seals the upstream end of the tritium source. All decay electrons, that do not reach the detector, are eventually guided back to the rear wall. Following the magnetic field lines, their trajectories end on the rear wall surface. Thereby, the low-energy decay electrons can be effectively removed from the system.

The rear wall surface potential defines the ground potential of the plasma inside the tritium source. The temporal and spatial homogeneity of the latter is of great importance, as it determines the starting potential of the β-electrons. In order to obtain temporal stability, the rear wall surface is coated with a gold layer. While being a good electrical conductor, gold is chemically stable, which translates into a stable work function.

---

[1] Pointing from the rear end ($z = 0$) to the front end.

[2] $r = 0$ corresponding to the beam line axis

[3] $\phi \in [0°, 360°]$ with $\phi = 0°$ pointing upward

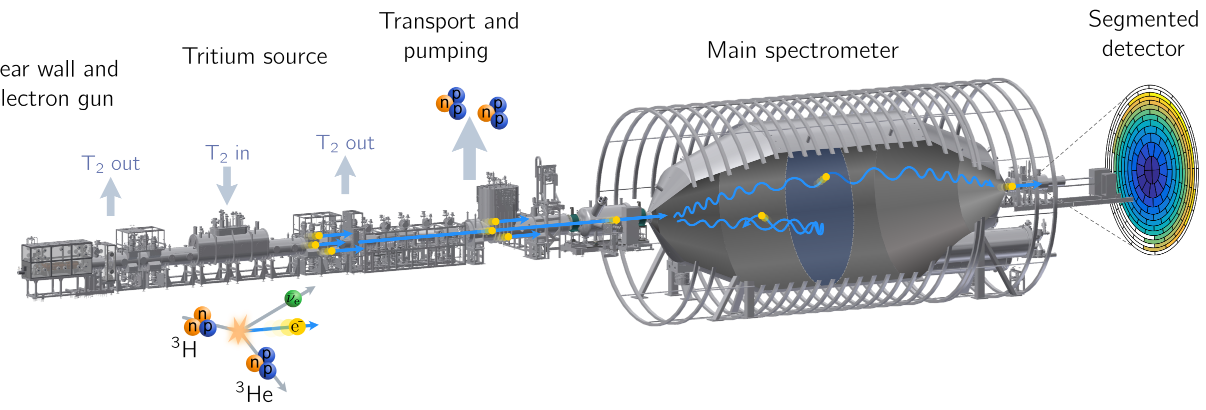

Figure 2.1: Experimental setup of the KATRIN experiment. From rear to front end it measures 70 m. The rear section houses the rear wall and several calibration and monitor devices. Molecular tritium is injected and decays in the windowless gaseous tritium source. From there the β-electrons are transported to the spectrometer section, with consists of two MAC-E filters. The pre-spectrometer reflects low energetic β-electrons, which cannot be used for the neutrino-mass determination. Through the application of large negative retarding potential to the main spectrometer, only electrons close to the tritium endpoint are transmitted. The electrons are finally counted by the focal plane detector at the front end. The figure is created by [44].

To compensate for work function differences between the gold rear wall surface and the stainless steel beam tube, a bias voltage U_{rw} is applied to the rear wall. Even though bias voltages of up to ±500 V are possible, the standard configuration during neutrino-mass measurements is in the order of $U_{rw} \approx \pm 0.1\,\mathrm{V}$. Simulations suggest than a spatially homogeneous rear wall potential minimizes longitudinal plasma potential inhomogenieties in the source [45]. Thus, the rear wall bias voltage is optimized before each measurement campaign [46].

Moreover, the rear wall surface can be used to monitor the source activity. As the gold layer has a high proton number, β-electrons that hit the gold surface will produce many X-rays through Bremsstrahlung. The X-rays can be further on registered with a silicon drift detector. Through its correlation with the X-ray intensity, the tritium activity can be determined. This method is called *Beta Induced X-ray Spectrometry* (BIXS) and is one of the methods used in KATRIN to monitor the source activity during tritium scans [47].

2.1.1.2 Photoelectric electron gun

The so-called photoelectric electron gun (e-gun) is situated upstream of the rear wall. It is a source of monoenergetic electrons, that can be used for various calibration purposes along the beam line.

UV light is guided through an optical fiber to a gold surface, where electrons are created by the photoelectric effect. The photoelectrons are then accelerated by electric fields up to kinetic energies of 21 keV. An upgrade to 35 keV is planned [48]. The produced electron beam has a small diameter ($d < 60\,\mu\mathrm{m}$ [49]) and its angular direction can be adjusted at will. A 5 mm hole at the center of the rear wall allows the electron beam to enter the tritium source.

Similar to β-electrons, the e-gun electrons scatter inelastically off tritium molecules when traversing the WGTS. The probability for n-fold scattering depends, as discussed in section 2.2.2, on the the product of gas density and the inelastic scattering cross section $\rho d\sigma$. Through measuring the count rate as a function of retarding energy with the focal plane detector (section 2.1.6), $\rho d\sigma$ can be experimentally determined at $\mathcal{O}(0.1\,\%)$ precision [50].

Moreover, the parametrization of the energy-loss function can be measured *in-situ* using e-gun electrons [48, 49]. The electron gun can also be used for other calibration purposes, such as the determination of the transmission properties of the main spectrometer.

2.1.2 Windowless gaseous tritium source

The windowless gaseous tritium source (WGTS) is a 10 m long stainless steel tube with an inner radius of $r_{\text{source}} = 45\,\text{mm}$. Molecular tritium gas is injected through capillaries into its center, from where it streams freely towards both ends. Due to the average bulk velocity of $13\,\text{m}\,\text{s}^{-1}$, only a small fraction of $\approx 10^{-9}$ of the tritium molecules undergoes β-decay before reaching the sides [51, 52]. The produced β-electrons are emitted isotropically. At the rear and front end of the WGTS, the tritium gas is pumped out by a set of turbomolecular pumping stations. Before it is re-injected into the WGTS, the tritium gas is refurbished to ensure a constant and high tritium purity $\varepsilon_{\text{T}} > 95\,\%$ (equation (2.1)). Thus, the tritium gas circulates in a closed loop system. The total tritium throughput amounts to 40 g per day at an inventory of 10 g [53].

The gas is a mixture of different tritium isotopologues, namely T_2, DT and HT. Stable isotopologues, such as D_2, HD and H_2, are only present in trace amounts. The atomic tritium purity is defined as

$$\varepsilon_{\text{T}} = c_{\text{T}_2} + \frac{1}{2}c_{\text{DT}} + \frac{1}{2}c_{\text{HT}} \tag{2.1}$$

with the relative molecular concentrations c_x. Apart from slightly different final-state distributions (section 2.2.1.1), the characteristics of the different isotopologues are very similar.

The source activity is governed by the product of ε_{T} and the gas column density ρd. The latter has a design value of $\rho d = 5 \times 10^{17}\,\text{molecules/cm}^2$, which results in an unprecedented high tritium activity of $10^{11}\,\text{Bq}$.

The WGTS and the tritium molecules therein are situated in a cryostat, which cools the source system to very low temperatures down to $T = 30\,\text{K}$. This is necessary to achieve the aforementioned high ρd at a feasible gas injection pressure $p_{\text{in}} = 3 \times 10^{-3}\,\text{mbar}$. Moreover, ultra-cold tritium gas has only little molecular motion, which minimizes the thermal Doppler broadening (section 2.2.1.2).

The tritium gas occurs in form of a weak cold magnetized plasma, which is induced by the high number of ions and low-energetic electrons in the source. The croygenic source temperature reduces unintended plasma effects, such as a deviation from spatial plasma potential homogeneity.

Furthermore, the central beam tube is surrounded by a system of superconducting solenoid magnets. The source magnetic field has a strength of $B_{\text{s}} = 2.5\,\text{T}$[4] and is orientated in bream direction. To collect as many electrons as possible, all β-electrons that are emitted with a polar emission angle $\theta < 90°$ (downstream direction) are magnetically guided toward the spectrometer section. The β-electrons emitted with $\theta > 90°$ (upstream direction) are guided toward the rear section.

2.1.3 Transport section

The purpose of the transport section is to adiabatically guide the decay electrons, that are emitted in downstream direction, from the source to the spectrometer section. At the same time, the tritium flow must be drastically reduced by 14 orders of magnitude from $1.8\,\text{mbar} \cdot \ell/\text{s}$ to $10^{-14}\,\text{mbar} \cdot \ell/\text{s}$, because the main spectrometer is required to be essentially tritium free. The effective elimination of tritium is realized by a sequence of differential and cryogenic pumping section.

The differential pumping section achieves a reduction of the tritium flow by seven orders of magnitude. It hosts a series of turbomolecular pumps, which are successively positioned along the beam line. To prevent a straight line of slight from the source to the CPS, the pumps are tilted by 20° against each other. Decay β-electrons pass the DPS unhindered by following the magnetic field lines of five super-conduction solenoid magnets up to 5.5 T [54]. Different to that, positively charged ions and neutral molecules are prevented from passing and are pumped out [55].

The remaining tritium flow is reduced by another seven orders of magnitude by the cryogenic pumping section. Embedded in a large cryostat, the CPS comprises seven beam tube elements from which the second and the fifths are inclined by 15°. These beam tube elements are cooled down to 3 K, which allows for the formation of an argon frost layer on the inner beam tube surface. Enhanced by the inclination of the beam tube elements, positive

---

[4] Design value: $B_{\text{s}} = 3.6\,\text{T}$ [42]

ions and molecules have a high change to hit the walls, on which they get stuck through cryosorption [56]. The argon frost layer has be regenerated regularly by purging it with helium. The decay β—electrons are magnetically guided to the spectrometer section by seven superconducting solenoid magnet, which produce magnetic fields up to 5.6 T.

2.1.4 Forward beam monitor

The forward beam monitor (FBM) is a silicon drift detector, whose task it is to continuously monitor the source activity. Being situated between the CPS and the pre-spectrometer, it is exposed to the full β-electron flux, that is emitted in downstream direction. Its exact position can adjusted with a manipulator. During normal operation, it is located on the eastern brim of the active flux tube. Thanks to the extraordinary high statistics up to 50 kcps, the source activity can be measured with a statistical precision of 0.1 % within a few seconds [57].

2.1.5 Spectrometer section

The spectrometer section evaluates the energies of the electrons using the established MAC-E filter principle [58, 59]. Employing a combination of magnetic adiabatic collimation (MAC) and electrostatic potential (E), a MAC-E filter acts on electrons as a high-pass energy filter. The spectrometer section in KATRIN comprises a tandem of two MAC-E filters, namely the pre- and main spectrometers. The following section addresses first the general working principle of the MAC-E filter technology (section 2.1.5.1). Thereafter, the two KATRIN-specific spectrometers are described (section 2.1.5.2).

2.1.5.1 MAC-E filter spectroscopy

A spectrometer of the MAC-E type is penetrated by a magnetic field, generated by solenoid magnets at its up- and downstream end. The resulting magnetic field lines are illustrated in figure 2.2 as black lines. The electrons, arriving at the spectrometer, have polar angles up to $\theta \leq 90$. Affected by the Lorentz force, they propagate in cyclotron motion along the magnetic field lines. The electron energy can be decomposed in a longitudinal $E_{\|}$ and a transversal $E_{\perp}$ component with respect to the magnetic field line

$$E = E_{\|} + E_{\perp} \tag{2.2}$$

A high voltage is applied to the spectrometer vessel, which elevates it onto a negative so-called retarding potential U as depicted in figure 2.2 by the blue arrows. The retarding potential acts as an electrostatic high-pass filter, reflecting all electrons with insufficient energy. As the electric field lines run parallel to the magnetic field lines, the high-pass filter is only sensitive to the longitudinal electron energy component. Thus, only electrons with $E_{\|} \geq qU$ are able to overcome the electrostatic barrier. However, the neutrino-mass determination requires knowledge of the total kinetic electron energy. Thus, the transversal energy component has to be significantly reduced. This is achieved by the magnetic adiabatic collimation principle. The magnetic field strength in the spectrometer $\vec{B}$ is reduced by four orders of magnitude from both spectrometer ends toward the analyzing plane, at which $\vec{B} = B_{\mathrm{a}}$ is minimal. As long as the reduction is sufficiently small, the electrons propagate adiabatically and the magnetic moment μ is conserved

$$\mu \approx \frac{p_{\perp}^2}{|\vec{B}|} \approx \mathrm{const} \tag{2.3}$$

with the electron momentum p. Consequently, the reduction of $|\vec{B}|$ leads to a transformation of $p_{\perp}$ into $p_{\|}$. The same applies to the kinetic electron energy, which can be calculated using the relativistic energy-momentum-relation

$$p^2 = E(\gamma + 1) \cdot m_e \text{ , with the relativistic Lorentz factor } \gamma = \frac{E}{m_e} + 1. \tag{2.4}$$

Due to the nonzero magnetic field in the analyzing $B_{\mathrm{a}} > 0\,\mathrm{T}$, the transveral component cannot be eliminated completely and the MAC-E filter remains insensitive to a small residual energy ΔE. This residuals energy determines the energy resolution of the MAC-E filter

$$\frac{\Delta E}{E} = \frac{B_{\mathrm{a}}}{B_{\max}} \frac{\gamma + 1}{2}. \tag{2.5}$$

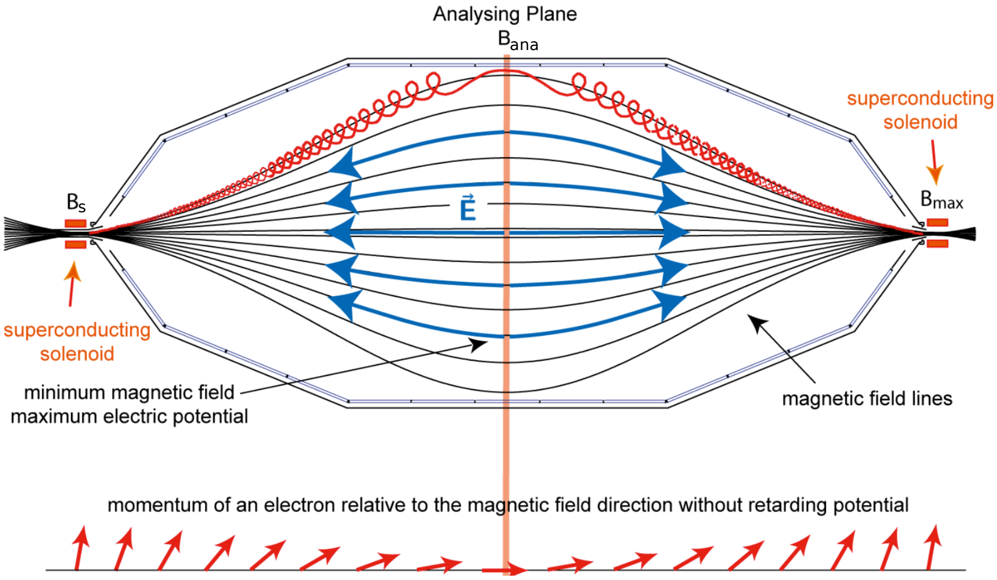

Figure 2.2: Working principle of a MAC-E filter. Two solenoid magnets at the rear and front end form a magnetic field, whose field lines are illustrated as black lines. Electrons move in cyclotron motion (red example trajectory) around the magnetic field lines. The electric field in the spectrometer, visualized as blue arrows, forms a negative electrostatic barrier, which reflects electrons below a threshold energy. The electric and magnetic fields are configured as such that the maximal potential, the so-called retarding potential qU, and the minimal magnetic field strength B_{ana} are both located in the analyzing plane. The transversal electron energy component is converted into longitudinal energy through the reduction of the magnetic field by four orders of magnitude. The figure is adapted from [60].

The magnitude of ΔE is given by the ratio of minimal B_a and maximal B_{max} magnetic field in the spectrometer. The more the magnetic field is reduced in the analyzing plane, the better the energy resolution is. The magnetic fields can also be configured to select certain electrons. In case the magnetic field of the pinch magnet at the downstream side of the spectrometer B_{max} is larger than the source magnet field, only electrons with polar emission angles $\theta \leq \theta_{max}$ are transmitted.

$$\theta_{max} = \text{arsin}\sqrt{\frac{B_s}{B_{max}}}. \tag{2.6}$$

The magnetic field and thus also the transversal energy component increases again downstream of the analyzing plane. The directions of electrons with larger initial polar angles than θ_{max} flip and the associated electrons are magnetically reflected back toward the rear section. The rejection of large polar angles is advantageous, because these electrons will have traveled longer distance in the WGTS and have thus a large probability for multiple scattering.

2.1.5.2 Pre- and main spectrometer

Being located downstream of the CPS, the pre-spectrometer is the first spectrometer that is encountered by electrons. With a length of 3.4 m and a diameter of 1.7 m, it is significantly smaller and has a worse energy resolution than the large main spectrometer. Its task is to filter out the low energetic β-electrons, that are not relevant for the neutrino-mass analysis. Due to the steep rate decrease of the β-spectrum at high energies, only a tiny fraction of β-electrons carry analyzable information on the neutrino mass (see figure 1.3). The last 40 eV below E_0, for example, comprise only a relative share of 10^{-8} electrons. It is desirable to stop the large number of uninteresting β-electrons from entering the main spectrometer, in which they could cause additional background through scattering on residual gas. By setting the pre-spectrometer voltage to −10 kV, the β-electron flow can be reduced by 85 %. The drawback, however, is the formation of a penning trap between the pre- and main spectrometer, which causes a time-depended background (see section 2.2.4). For this reason, the pre-spectrometer was switched off in later measurement campaigns.

The main spectrometer is located downstream of the pre-spectrometer. The standard magnetic field configuration is $B_s = 2.5\,\text{T}$, $B_a = 6.3 \times 10^{-4}\,\text{T}$ and $B_{\text{max}} = 4.2\,\text{T}$[5], which results in an energy resolution of $\Delta E = 2.8\,\text{eV}$. As the magnetic field strength reduction along the beam line must occur slowly in order to guarantee adiabatic motion, the main spectrometer is required to have a certain length. Designed to reach an even lower energy resolution of 0.93 eV, the main spectrometer is 23.8 m long. The large diameter ($d = 9.8\,\text{m}$) of the spectrometer in the analyzing plane is necessary due to the conservation of the magnetic flux.

The main spectrometer is operated at an ultra-high vacuum of 10^{-11} mbar to minimize the scattering probability with residuals gas. Moreover, the spectrometer is equipped with an inner electrode system comprising 24 000 wires on the inner of the spectrometer walls. Being set to a $\mathcal{O}(100\,\text{V})$ more negative potential than the spectrometer vessel, their task it to hinder muon induced background electrons from the spectrometer wall to reach the active flux tube.

2.1.6 Focal plane detector

Electrons that overcome the retarding potential of the main spectrometer are magnetically guided by the pinch and the detector magnet to the focal plane detector (FPD). The task of the FPD is to count the electron rate as a function of retarding potential, which is varied step-wise. As all electrons above a certain energy threshold are transmitted, the FPD measures the *integral* electron energy spectrum.

The FPD is a silicon *p-i-n* diode array, that is segmented into 148 pixels of equal area. As displayed in figure 3.1, the pixels are arranged in twelve concentric rings, comprising twelve pixels each. Additionally, four pixels in the center form the so-called *bullseye*. Each pixel records its own integral tritium spectrum.

The main advantage of the pixel segmentation is its sensitivity to the arrival position of the incident particle in the detector plane. As the electric and magnetic fields inside the KATRIN setup are well known, a volume of possible particle tracks can be reconstructed for each FPD pixel. Due the circular geometry of the FPD, it is useful to characterize the position in terms of radius and azimuth angle. Of particular interest is the localization of the electron position in the tritium source and in the analyzing plane. The outer-most pixels, for example, collect only β-electrons that were emitted at large radii in the WGTS and that traversed the analysis plane at the outer brim of the flux tube. A pixel-wise analysis of the recorded spectra allows for the investigation of systematic effects, such as spatial variations of the retarding potential in the analyzing plane as well as radial and azimuthal inhomogeneities of the electric source potential. Moreover, the pixel segmentation helps identifying possible sources for background electrons. Pixels with undesired behavior, such as an elevated background rate or a high noise level, can be identified and excluded from subsequent analyses.

Being coupled to the main spectrometer, the detector chamber must be operated at an ultra-high vacuum of $< 10^{-9}$ mbar. Moreover, it is cooled with liquid nitrogen to reduce leakage current and noise.

The FPD pixels have a typical detection efficiency of $\epsilon_{\text{FPD}} \approx 95\,\%$. Their average energy resolution is 1.52 keV (FWHM) for 18.6 keV photoelectrons [61]. The energy resolution of the FPD is not relevant for the energy resolution of KATRIN, because the integral spectrum is measured as a function of the retarding energy, which is determined by the high-precision main spectrometer. Nevertheless, the energy resolution of the FPD can still be used to exclude backgrounds at very different energies compared to the tritium endpoint, such as electrons arising from cosmic rays or environmental radiation. The detector region of interest (ROI) defines the energy window, within which data is selected for the subsequent high-level analysis. The electrons from the main spectrometer are accelerated toward the FPD with a post acceleration of up to 12 kV. To cover the boosted β-electron energies, the ROI is shifted likewise. This is done as the intrinsic detector background is lower at higher energies.

---

[5] The design magnetic field configuration is ($B_s = 3.6\,\text{T}$, $B_a = 3 \times 10^{-4}\,\text{T}$, $B_{\text{max}} = 6\,\text{T}$, which leads to an energy resolution of 0.93 eV [42].

2.2 Model of the experimental spectrum

To infer physics parameters of interest $\mathbf{\Theta}$ (see section 3.3.1), such as m_ν^2, the measured integral spectrum $\mathbf{N}^{\mathrm{exp}}(\mathbf{qU})$ has to be described with an appropriate model $\mathbf{N}^{\mathrm{model}}(\mathbf{qU}, \mathbf{\Theta})$. The model of the signal comprises two fundamental components, namely the theoretical prediction of the differential tritium β-spectrum $\frac{\mathrm{d}\Gamma}{\mathrm{d}E}(E, \mathbf{\Theta})$ and the experimental response function $R(E, qU)$. The signal strength is determined by the normalization factor A. Moreover, background component B is added. The expected electron rate can be calculated as

$$\dot{N}^{\mathrm{model}}(qU, \mathbf{\Theta}) = A \cdot \int_{qU}^{\infty} \frac{\mathrm{d}\Gamma}{\mathrm{d}E}(E, \mathbf{\Theta}) \cdot R(E, qU)\, \mathrm{d}E + B. \tag{2.7}$$

The rates are then converted into counts through multiplication with the associated measurement time t

$$N^{\mathrm{model}}(qU) = \dot{N}^{\mathrm{model}}(qU) \cdot t(qU). \tag{2.8}$$

In the following section, the individual terms in equation (2.7) are addressed one after the other. First, the theoretical β-spectrum from equation (1.29) has to be revised, as KATRIN uses molecular tritium at non-zero temperature. Section 2.2.1 addresses key features of molecular tritium, the final-state distribution, the thermal Doppler effect and small theoretical corrections. Second, a comprehensive description of the experimental response function is given in section 2.2.2. The latter includes inelastic scattering in the source and the transmission properties of the MAC-E filter. Sections 2.2.3 and 2.2.4 address the signal normalization and the background model, respectively. At last, the measurement time distribution, which specifies the high-voltage set points qU and associated measurement times $t(qU)$, is presented in section 2.2.5.

2.2.1 Differential energy spectrum for molecular tritium β-decay

Like its predecessors Mainz [62] and Troitsk [63], the KATRIN experiment studies the β-decay of tritium to determine the neutrino mass

$$^3_1\mathrm{He} \longrightarrow {}^3_2\mathrm{He}^+ + e^- + \bar{\nu}_e. \tag{2.9}$$

Tritium possesses two key features, which render it a suitable isotope to research

1. Tritium decay is a super-allowed β-decay, which leads to a short half-life of $T_{1/2} = 12.3\,\mathrm{years}$. This is advantageous, because high count rates can be achieved at rather low source densities. Moreover, the nuclear matrix element of a super-allowed β-decay is energy-independent and easily calculable.

2. Tritium possesses the second lowest endpoint of all β-decaying isotopes $E_0 = 18.6\,\mathrm{keV}$. The total count rate is smaller compared to isotopes with higher E_0: $\Gamma \propto E_0^4$ for low E_0. However, the relative fraction of β-electrons in the interesting region close the endpoint is larger compared to isotopes with higher E_0: $\propto E_0^{-3}$. Additionally, a lower endpoint is technically easier to handle, because it requires less negative high voltages for the MAC-E filters (see section 2.1.5).

Due to technical reasons, KATRIN employs tritium in molecular form (mostly T_2). As a consequence, the daughter molecule can be electronically excited. The arising consequences to the differential β-spectrum are discussed in section 2.2.1.1. Moreover, the tritium source is operated at nonzero temperature. The thermal motion influences the differential energy spectrum in form of the Doppler effect, presented in section 2.2.1.2.

2.2.1.1 Final-state distribution

As described in section 1.3.3, the kinematics of the β-decay products are related through energy and momentum conservation. As the energy of the daughter molecule cannot be measured in KATRIN, it has to be derived theoretically from quantum mechanics. The spectrum of possible molecular excitation energies and associated transition probabilities can be calculated by solving the Schrödinger equation for all initial of final states. The calculation is described in the references [64, 65]. Here, only a qualitative description of the final-states is given.

The final-state distribution is displayed in figure 2.3 for the three tritium isotopologues in the WGTS, namely T_2, DT and HT. In its electronic ground state, the daughter molecule receives energy in form of rotational and vibrational excitation. The ground state corresponds to the low energy peak in figure 2.3. It is centered around the average recoil energy $E_{\text{rec.}} = 1.69\,\text{eV}$ and has a cumulative population probability of 57.4 % (considering T_2).

Moreover, the shell electrons of the daughter molecule can be electronically excited to higher electronically bound states or they can be even ionized. The so-called excited states and the electronic continuum corresponds to the higher energies $\geq 19\,\text{eV}$ in figure 2.3. The final-state distribution is one of the most important external inputs in the model calculation. Each final state f reduces the energy available to the β-electron by the associated excitation energy E_f. Taking all possible final states into account, the phase space is a superposition of reduced-energy phase spaces weighted by the respective excitation probabilities P_f. The standard formula from Fermi theory (equation (1.29)) has to be modified as follows:

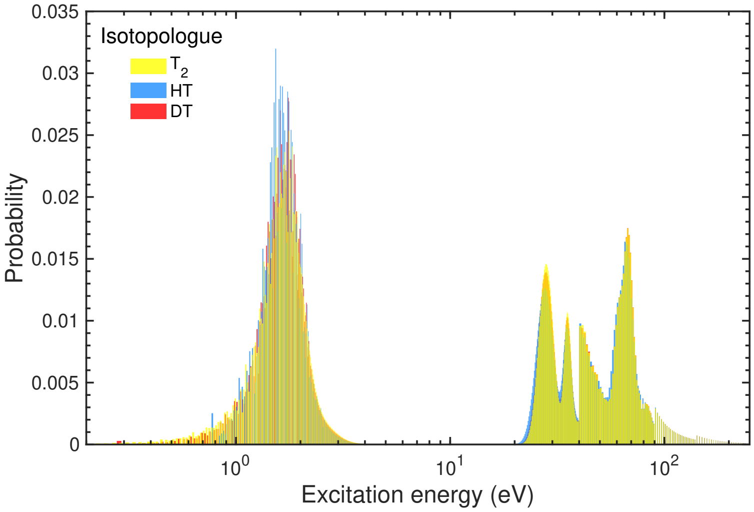

Figure 2.3: Final-state distribution of tritium isotopologues present in the WGTS. As they have different molecular structures, their final-state distributions are different. The ground state peak of T_2 is centered at its average recoil energy $E_{\text{rec.}} = 1.69\,\text{eV}$. The respective ground state peaks of DT and HT are slightly shifted compared to the T_2 distribution, to account for their slightly different electronic binding and recoil energies compared to T_2.

$$\begin{aligned}\frac{\mathrm{d}\Gamma}{\mathrm{d}E}(E,m_\nu^2) = &\frac{G_\mathrm{F}^2\cdot\cos^2\theta_c}{2\pi^3}\cdot|\mathcal{M}_{\text{nuc.}}|^2\cdot F(Z,E)\cdot(E+m_e)\cdot\sqrt{(E+m_e)^2-m_e^2} \\ &\cdot\sum_f P_f\cdot(E_0-E-E_f)\sqrt{(E_0-E-E_f)^2-m_\nu^2}\cdot\Theta(E_0-E-E_f-m_\nu).\end{aligned} \tag{2.10}$$

In the boundary case with no final-state excitation (e.g. free neutron decay) $E_f = 0$, equation (2.10) converges to equation (1.29).

Due to their different molecular structures, the present tritium isotopologues are characterized with slightly different FSD. Thus, the differential spectrum has to be computed for each isotopologue separately $\left(\frac{\mathrm{d}\Gamma}{\mathrm{d}E}\right)_x$. The full spectrum is given by the sum of the isotpologue-wise spectra weighted by their relative molecular abundances

$$\frac{\mathrm{d}\Gamma}{\mathrm{d}E}(E,m_\nu^2) = c_{\mathrm{T}_2}\left(\frac{\mathrm{d}\Gamma}{\mathrm{d}E}\right)_{\mathrm{T}_2} + \frac{1}{2}c_{\mathrm{DT}}\left(\frac{\mathrm{d}\Gamma}{\mathrm{d}E}\right)_{\mathrm{DT}} + \frac{1}{2}c_{\mathrm{HT}}\left(\frac{\mathrm{d}\Gamma}{\mathrm{d}E}\right)_{\mathrm{HT}}. \tag{2.11}$$

2.2.1.2 Doppler effect

The gas inside the WGTS is subject to thermal motion, because the source is kept at nonzero temperature ($T_{\text{source}} = 30\,\text{K}$). As a consequence, the differential energy spectrum (equation (2.10)) is influenced by the Doppler Effect.

The latter can be mathematically incorporated in the model by convolving the differential spectrum with a Gaussian function. The Gaussian standard deviation σ_G, interpreted as an energy broadening, is mostly driven by the source temperature. It calculate as

$$\sigma_\mathrm{G} = \sqrt{\frac{2E_\mathrm{cms} k_\mathrm{B} T_\mathrm{source} m_\mathrm{e}}{M}} \tag{2.12}$$

with the electron center of mass energy E_cms, the Boltzmann constant k_B and the mass M of the tritium isotopologue. In the following, only the thermal Doppler Effect is considered. The Doppler Effect due to a non-zero bulk velocity is expected to negligible [51].

Since the differential spectrum is binned, an analytical convolution is not possible. Therefore, the convolution is implemented using the FSD: Each discrete final state is replaced by a Gaussian function. The expectation value of the Gaussian corresponds to the excitation energy of the final state and the integral of the Gaussian is the excitation energy. The standard deviation of the Gaussian is the broadening due to the Doppler Effect σ_G. At last, the modified FSD is calculated through summation of all broadening final states.

The influence of the Doppler Effect on the neutrino mass squared is estimated to be $\Delta m_\nu^2 = 0.02\,\mathrm{eV}^2$, if the effect is neglected in the analysis.

2.2.1.3 Theoretical corrections

The differential energy spectrum of the super-allowed tritium β-decay is very well described by the Fermi theory section 1.3.3. However, small known deviations arise at the particle, nuclear, atomic levels. In addition to the conventional relativistic Fermi function the following effects can be added to equations (1.29) and (2.10):

- Radiative corrections due to real and virtual photons
- Exchange between the β-electron and the orbital electron
- Influence of the finite nuclear extension on the solution of the Dirac equation
- Recoil effects due to the finite nuclear mass including those from V-A interference and weak magnetism
- Impact of the recoiling Coulomb field
- Convolution of the electron and neutrino wave functions with the nucleonic wave function through the finite nuclear volume
- Screening by the coulomb field of the orbital electrons of the daughter atom[6].

A full discussion and mathematical description of these effects can be found in [51, 66].

2.2.2 Experimental response function

The experimental response function $R(E, qU)$, illustrated in figure 2.4, gives the probability that an electron overcomes the retarding energy and reaches the focal plane detector

$$R(E, qU) = \int_0^{E-qU} \sum_i T_i(E - \varepsilon_\mathrm{scat.} - \varepsilon_\mathrm{sync.}, qU) \cdot P_\mathrm{i} \cdot f_i(\varepsilon_\mathrm{scat.})\,\mathrm{d}\varepsilon_\mathrm{scat.}. \tag{2.13}$$

The so-called integrated transmission function T, described in section 2.2.2.1, summarizes the electromagnetic working principle of the main spectrometer as a MAC-E filter. Furthermore, all considerable electron energy-losses ε along the beam line have to be taken into account. The dominant energy-loss stems from inelastic scattering with tritium molecules in the WGTS $\varepsilon_\mathrm{scat.}$, which is addressed in section 2.2.2.2. The latter is characterized by the scattering probabilities P_i for i scatterings and the associated energy-loss functions f_i. Elastic scattering, found to be negligible, is briefly mentioned in section 2.2.2.3. Moreover, energy-loss through the emission of synchrotron radiation $\varepsilon_\mathrm{sync.}$ is addressed in section 2.2.2.4.

---

[6] This is effect is not implemented in Samak.

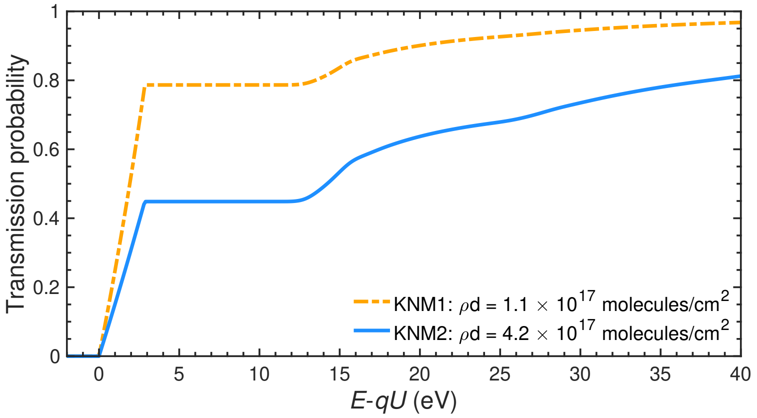

Figure 2.4: Experimental response function $R(E, qU)$ for $qU = 18\,542\,\text{eV}$. Electrons with energies below the retarding energy of the main spectrometer are not transmitted. The slope for $0 \leq E - qU \leq \Delta E$ is given by the energy resolution of the MAC-E filter (section 2.2.2.1). The transmission probability for electrons with large surplus energies $E - qU > \Delta E$ is determined by their energy loss through inelastic scattering (section 2.2.2.2) and the emission of synchrotron radiation (section 2.2.2.4). The transmission plateau at $\Delta E < E - qU \lesssim 12\,\text{eV}$, for example, comprises only electrons that traversed the WGTS without inelastic scattering. Its transmission probability is therefore given by the zero-scattering probability P_0 (section 2.2.2.2). The response function for the first two measurement campaigns (KNM1 and KNM2) are depicted as an example. The height of the zero-scattering plateau is smaller in KNM2 compared to KNM1, as its mean column density was significantly larger.

2.2.2.1 Spectrometer transmission

The transmission function $\mathcal{T}$ states the probability that an electron entering the spectrometer with the kinetic energy E is transmitted. Being analytically computable, its formula is derived for example in [51]. As described in section 2.1.5, electrons are only transmitted in a MAC-E filter, if their longitudinal energy component is larger than the retarding energy in the analyzing plane. The transmission condition can be expressed in terms of the total kinetic energy and initial polar angle θ_s

$$\begin{aligned} E_{\parallel}^{\text{ana}} &> qU \\ \Rightarrow E - E_{\perp}^{\text{ana}} &> qU && |\text{ equations (2.3) and (2.4)} \\ \Rightarrow E - E_{\perp}^{\text{s}} \cdot \frac{B_\text{ana}}{B_\text{s}} \cdot \frac{\gamma+1}{2} &> qU && |E_{\perp}^{\text{s}} = E \cdot \sin^2\theta_\text{s} \\ \Rightarrow E(1 - \sin^2\theta_\text{s} \cdot \frac{B_\text{ana}}{B_\text{s}} \cdot \frac{\gamma+1}{2}) &> qU \end{aligned} \tag{2.14}$$

In its most general form, the transmission function can thus be written as

$$\mathcal{T}(E, \theta_\text{s}, qU) = \begin{cases} 1 & \text{for } E(1 - \sin^2\theta_\text{s} \cdot \frac{B_\text{ana}}{B_\text{s}} \cdot \frac{\gamma+1}{2}) > qU \\ 0 & \text{otherwise} \end{cases} \tag{2.15}$$

As θ_s cannot be distinguished in KATRIN and the measured spectrum contains electrons with different $\theta_s \in [0, \theta_\text{max}]$, it is sensible to calculate an average transmission function.

Isotropic transmission function: Assuming an isotropic angular distribution, the average transmission function is calculated as

$$T(E,qU) = \int_0^{\theta_{\max}} \mathcal{T}(E,\theta_\mathrm{s},qU) \cdot \sin\theta_\mathrm{s}\, d\theta_\mathrm{s} \tag{2.16}$$

$$\Rightarrow T(E,qU) = \begin{cases} 0 & \text{for } E < qU \\ \frac{1-\sqrt{1-\frac{E-qU}{\Delta E}\frac{B_\mathrm{s}}{B_\mathrm{a}}}}{1-\sqrt{1-\frac{\Delta E}{E}\frac{B_\mathrm{s}}{B_\mathrm{a}}}} & \text{for } qU < E < qU + \Delta E \\ 1 & \text{for } qU + \Delta E < E \end{cases} \tag{2.17}$$

with maximal initial polar angle $\theta_{\max}$ from equation (2.6) and the energy resolution ΔE from equation (2.5). The transmission function is normalized to 1. The acceptance angle $\theta_{\max} < \pi$ is included later on as a normalization factor of the integral spectrum.

Non-isotropic transmission function: Even though the β-electrons are emitted isotropically in the β-decay, the angular distribution is in reality no longer uniform for a fixed electron energy E once the β-electrons exit the source. As described in section 2.2.2.2, many β-electron scatter inelastically off tritium molecules. Electrons with a large θ_s travel longer distances in the source and thus have a larger probability to scatter at least once compared to electrons with small θ_s. Consequently, the angular distribution of the unscattered electrons has a preference for small emission angles, whereas the angular distributions of electrons that scattered several times have an accumulation of large emission angles as displayed in figure 2.6. To account for the actual angular distribution, $\mathcal{T}(E,\theta_\mathrm{s},qU)$ has to be weighted with the respective scattering probabilities $P_i(\theta_\mathrm{s})$[7]. The integrated transmission for the i-th scattering is calculated as

$$T_i(E,qU) = \int_0^{\theta_{\max}} \mathcal{T}(E,\theta_\mathrm{s},qU) \cdot \sin\theta_\mathrm{s} P_i(\theta_\mathrm{s})\, d\theta_\mathrm{s}. \tag{2.18}$$

The difference between the isotropic transmission function (equation (2.16)) and the more realistic nonisotropic transmission function is visualized in figure 2.5 (left) for unscattered electrons ($i = 0$).

2.2.2.2 Inelastic scattering

As briefly mention in the section 2.2.2.1, the most considerable electron energy-loss occurs via inelastic scattering off tritium molecules. Inelastic scattering is only relevant inside the WGTS, as it is the beam line element with by far the largest pressure. The energy loss through inelastic scattering is characterized by two components. Firstly, the inelastic scattering probabilities describe the probability for i-fold scattering. Secondly, the energy-loss function states the probability that an electron looses a certain energy while scattering.

Inelastic scattering probabilities

As the scattering probability is low for single tritium molecules, the number of scatterings i during propagation follows a Poisson distribution. The probability for i-fold scattering is given by [67]

$$P_i(z_\mathrm{s},\theta_\mathrm{s},E) = \frac{(\lambda(z_\mathrm{s},\theta_\mathrm{s}) \cdot \sigma_\mathrm{inel}(E))^i}{i!} e^{-\lambda(z_\mathrm{s},\theta_\mathrm{s})\cdot\sigma_\mathrm{inel}\cdot(E)} \tag{2.19}$$

with the energy-dependent inelastic scattering cross section $\sigma_\mathrm{inel.}$. For electron energies of $E = 18\,574\,\mathrm{eV}$, the cross section amounts to $\sigma_\mathrm{inel.} = 3.64 \times 10^{-18}\,\mathrm{cm}^{-2}$. Its energy dependence is discussed in appendix A.1.

Moreover, the scattering probabilities depend on the effective column density $\lambda(z_s,\theta_s)$, that the electron traverses

---

[7] Addressed in detail in the following section, the scattering probabilities also depend on more parameters than only θ_s. For the sake of readability, these dependence are not explicitly stated here.

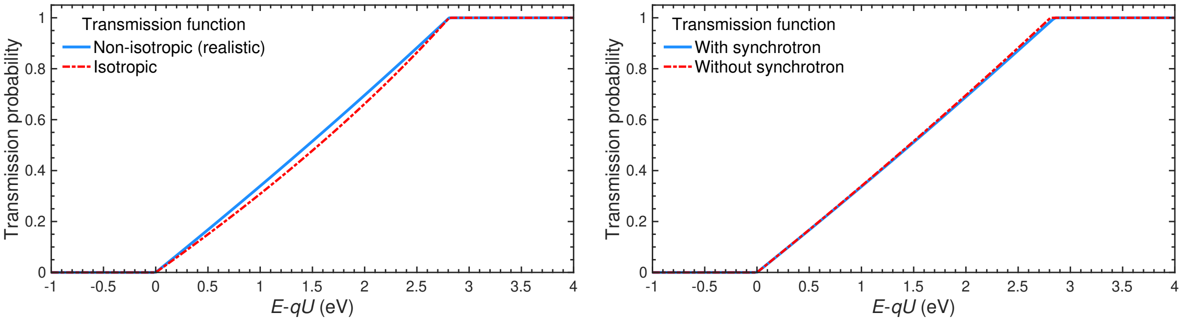

Figure 2.5: Integrated transmission functions, using the KNM2 configuration (chapter 6) for illustration. All integrated transmission functions are normalized to have a maximal transmission probability of 1 for electrons with large surplus energies. **Left:** Comparison of transmission functions with isotropic and non-isotropic angular distribution. The red curve is calculated according to equation (2.16), assuming that θ_s is isotropically distributed before entering the main spectrometer. The blue curve is calculated according to equation (2.18), assuming a realistic non-isotropic angular distribution for unscattered electrons ($i = 0$). **Right:** Electrons loose energy through synchrotron radiation in the source and transport section. The effect can be accounted for through modification of the spectrometer transmission function (section 2.2.2.4).

on its trajectory in the WGTS,

$$\lambda(z_s, \theta_s) = \frac{1}{\cos\theta_s} \cdot \int_{z_s}^{d} \rho(z')dz' \tag{2.20}$$

with the length of the WGTS d, the electron starting position z_s and the electron emission angle θ_s. The total column density is defined as $\lambda(z_s = 0, \theta = 0) = \rho d$.

The scattering probabilities as a function of θ_s, averaged over all starting positions, are displayed in figure 2.6. They enter the calculation of the non-isotropic transmission function in equation (2.18). The average scattering

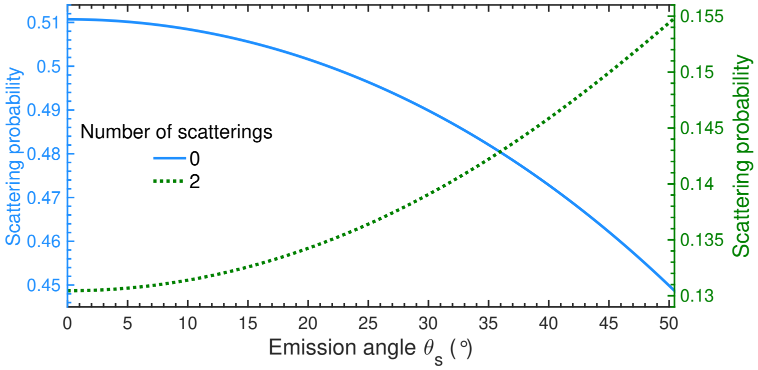

Figure 2.6: Angular dependent scattering probabilities. As electrons travel longer distances in the WGTS when being emitted at large polar angles, they are likely to undergo more inelastic scatterings than electrons with small θ_s. As a consequence, the distribution of polar emission angles is not uniform for a fixed election energy, once the β-electrons exit the source. Electrons that leave the source unscattered (blue curve) often have small θ_s, whereas electrons that scatter twice (green curve) are more likely to have large θ_s. The z_s dependency is eliminated through numerical integration over the whole source beam tube.

probabilities for all starting positions $z_s \in [0, L]$ and accepted emission angles $\theta_s \in [0, \theta_{\max}]$ can be obtained by through numerical integration over z_s and θ_s. Assuming an isotropic angular distribution, the average probabilities are given by

$$P_i(E) = \frac{1}{1-\cos(\theta_{\max})}\frac{1}{\rho d}\int_0^L dz_s \int_0^{\theta_{\max}} d\theta_s \left[\rho(z_s)\cdot \sin\theta_s \cdot P_i(z_s,\theta_s,E)\right]. \tag{2.21}$$

The average probabilities for zero to seven scatterings are stated in table 2.1, using the configuration of the second KATRIN measurement campaign (see chapter 6) as an example. **Energy-loss function**

i	0	1	2	3	4	5	6	7
P_i (%) (KNM1)	78.67	18.01	2.91	0.37	0.04	0.003	3×10^{-4}	2×10^{-5}
P_i (%) (KNM2)	44.87	29.61	15.48	6.63	2.40	0.75	0.21	0.05

Table 2.1: Average inelastic scattering probabilities according to equation (2.21) using the experimental conditions of the first (KNM1) and second (KNM2) measurement campaigns as examples (table C.3 and $E = 18\,574\,\mathrm{eV}$). As $\rho d\sigma$ was significantly lower in KNM1 compared to KNM2, the associated probability for zero scattering is much larger.

The energy-loss function $f_1(\varepsilon_{\mathrm{scat.}})$ describes the probability for an electron to loose the energy $\varepsilon_{\mathrm{scat.}}$ during one inelastic scattering process. The electron energy loss arises from a combination of rotational, vibrational and electronic excitation of the tritium molecule up to the ionization threshold at 15.486 eV [68]. Several attempts to derive an energy-loss function model from literature values exist, such was [69]. However, the different literature-based calculations exhibit large discrepancies among each other and are therefore not suitable for a high-precision experiment like KATRIN. Alternatively, the energy-loss function can be inferred from a measurement in a KATRIN-like setup using a semi-empirical model. This was done for the first time at the Troitsk ν-mass experiment [67, 70]. As the systematic uncertainties of these measurements exceed the design uncertainty budget of KATRIN [42], new measurements using the experimental setup of KATRIN were performed, reaching an unprecedented precision [68].

In KATRIN, the energy-loss function was measured by counting the transmitted electrons from the monoenergetic photoelectric electron gun (section 2.1.1.2) with the FPD. The electron gun generates electrons with a pulsed laser, which can be operated in two modes: A fast mode with a repetition rate of 100 kHz, generating a quasi-continuous electron beam, and a slow mode with a repetition rate of 20 kHz, resulting in a pulsed electron beam. The slow mode offers the possibility to calculate time-of-flight for individual electrons, which can be used to obtain a differential energy spectrum. The regular integral measurement is performed in the fast operation mode. The analysis infers the energy-loss function with a semi-empirical parametrization consisting of three Gaussian functions [68]

$$f_1(\varepsilon_{\mathrm{scat.}}) = \begin{cases} \sum_j = \sum^3 a_j \exp\left(-\frac{(\varepsilon_{\mathrm{scat.}}-\mu_j)^2)^2}{2\sigma_j^2}\right) & \text{for } \varepsilon_{\mathrm{scat.}} \leq \varepsilon_c \\ \frac{f_1(\varepsilon_{\mathrm{scat.}})}{f_{\mathrm{BED}}(\varepsilon_c)} & \text{for } \varepsilon_{\mathrm{scat.}} > \varepsilon_c \end{cases} \tag{2.22}$$

with the parameters The probability density functions for multiple scatterings $f_i(\varepsilon)$ is obtained by convolving

a_j : Gaussian amplitudes, μ_j : Gaussian mean energy, σ_j : Gaussian standard deviation,
ε_c ionization threshold energy, f_{BED} ionization continuum [71].

equation (2.22) $(i-1)$-times with itself

$$\begin{aligned} f_2(\varepsilon_{\mathrm{scat.}}) &= f_1(\varepsilon_{\mathrm{scat.}}) \circledast f_1(\varepsilon_{\mathrm{scat.}}) \\ f_i(\varepsilon_{\mathrm{scat.}}) &= f_1(\varepsilon_{\mathrm{scat.}}) \underbrace{\circledast f_1(\varepsilon_{\mathrm{scat.}}) \circledast \ldots \circledast f_1(\varepsilon_{\mathrm{scat.}})}_{i-1}. \end{aligned} \tag{2.23}$$

A combined fit to a set of differential and integral spectra yields the best-fit energy-loss function parameters and associated fit uncertainties. The results from two different energy-loss analyses are used in this work, as summarized in appendix A.2. The energy-loss function from [72] is displayed in figure 2.7 for the first three scatterings. A full description of the energy-loss function measurement and the analysis can be found in [48, 49, 68].

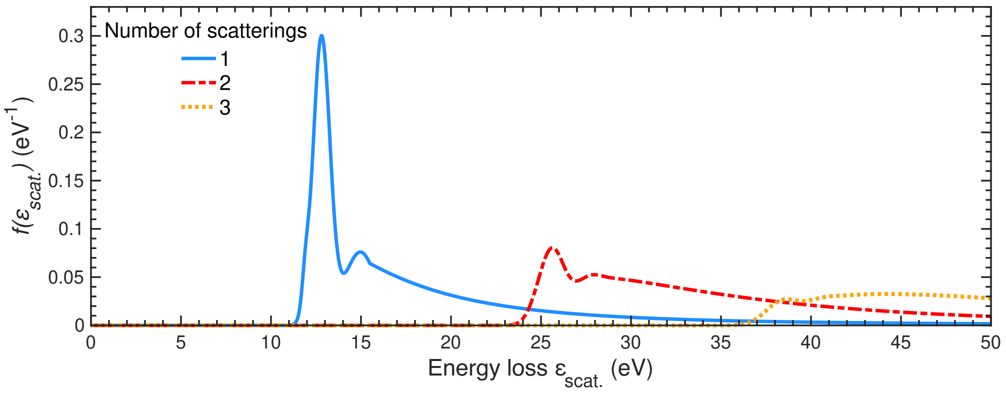

Figure 2.7: Energy-loss function for the first three inelastic scatterings. The energy-loss function was determined *in-situ* with the KATRIN experiment using the semi-empirical model in equation (2.22), described in detail in [68]. The best fit parameter and uncertainties are stated in appendix A.2 and [72]. The uncertainties are too small to be visible.

2.2.2.3 Elastic scattering

In addition to inelastic scattering, electrons also scatter elastically off tritium molecules in the WGTS. However, the associated cross section is one order of magnitude smaller than the inelastic one and the median energy-loss is negligible $\bar{\varepsilon}_{\text{elastic}} = 4\,\text{meV}$ [51]. Thus, the effect is not included in the experimental response function used in this work.

2.2.2.4 Synchrotron radiation

The electrons loose energy due to the emission of synchrotron radiation while propagating through the magnetic fields of the source and transport sections. The synchrotron energy loss $\varepsilon_{\text{sync.}}$ of an electron traveling through a uniform magnetic field B for a time t is given by [73]

$$\varepsilon_{\text{sync.}}(E) = \frac{\mu_0}{3\pi m_e^3} \cdot B^2 \cdot E_\perp \cdot \gamma \cdot t. \tag{2.24}$$

with the vacuum permeability μ_0. For a fixed magnetic field configuration, $\varepsilon_{\text{sync.}}$ is mostly driven by the transversal energy component and the propagation time. Both can be expressed in terms of the initial polar angle θ_{s} (see section 2.2.2.1) and the electron starting position z_{s}. Large θ_{s} correspond to a large relative $E_\perp$ and result therefore into a high synchrotron energy-loss. Moreover, electrons with low z_s travel longer distance in the source and emit more synchrotron radiation.

The precise calculation of $\varepsilon_{\text{sync.}}$, taking into account the complex magnetic field geometry in KATRIN, requires a comprehensive Monte Carlo simulation. The simulation framework KASSIOPEIA [73, 74] allows to calculate $\varepsilon_{\text{sync.}}(\theta_{\text{s}}, z_{\text{s}})$ for any magnetic field configuration. As this simulation is rather time consuming, an effective analytical synchrotron-loss model is developed and validated with the Monte Carlo simulation. The synchrotron energy loss can be well approximated by [73]

$$\varepsilon_{\text{sync.}}(E, B, \theta) = \frac{\mu_0}{3\pi m_e^3} \cdot B^2 \cdot E \cdot \sin^2\theta \cdot \gamma \cdot \frac{\ell}{v_{\text{e}} \cdot \cos\theta}. \tag{2.25}$$

with the traveled length ℓ and the electron velocity v_e. The total synchrotron energy loss in the source and transport section then calculates as

$$\varepsilon_{\text{sync.}}(E, \theta_{\text{s}}) = \varepsilon_{\text{sync.}}(E, B_{\text{s}}, \theta_{\text{s}}) + \varepsilon_{\text{sync.}}(E, B_{\text{t}}, \theta_{\text{t}}) \tag{2.26}$$

with the magnetic field B_{t} and the modified polar angle in the transport section

$$\theta_{\text{t}} = \theta_{\text{s}} \cdot \sqrt{B_{\text{t}}/B_{\text{s}}}. \tag{2.27}$$

Considering the standard magnetic field settings[8], the energy loss through synchrotron radiation can be up to 43 meV for the maximal accepted polar angle $\theta_{\mathrm{max}} = 50.4°$. To incorporate the synchrotron radiation in the experimental response, the transmission function in equation (2.18) has to be modified accordingly:

$$\mathcal{T}(E, qU, \theta_{\mathrm{s}}) \rightarrow \mathcal{T}(E - \varepsilon_{\mathrm{sync.}}(E, \theta_{\mathrm{s}}), qU, \theta_{\mathrm{s}}). \tag{2.28}$$

The average transmission function can be obtained through integration over all accepted initial polar angles $\theta_{\mathrm{s}} \in [0, \theta_{\mathrm{max}}]$. The influence on the integrated transmission function is depicted in figure 2.5 (right).

2.2.3 Signal normalization

The signal strength of the modeled integral spectrum in equation (2.7) is given by the factor A. This factor comprises two components, namely the effective source activity A_{source} and the signal strength correction factor $N_{\mathrm{sig.}}$:

$$A = A_{\mathrm{source}}(1 + N_{\mathrm{sig.}}). \tag{2.29}$$

A_{source} describes the source activity, as it is seen be the FPD. It is calculated from the operational parameters before the spectral fit as

$$A_{\mathrm{source}} = \underbrace{\varepsilon_{\mathrm{T}} \cdot 2\rho d \cdot \pi r^2_{\mathrm{source}} \cdot \lambda_{\mathrm{Tritium}}}_{\text{I) Total number of tritium decays per second}} \cdot \underbrace{\frac{1}{2}(1 - \cos\theta_{\mathrm{max}})}_{\text{II) Accepted solid angle}} \cdot \underbrace{\epsilon_{\mathrm{FPD}} \cdot \frac{N_p}{148}}_{\text{III) FPD efficiency and coverage}} \tag{2.30}$$

with the tritium decay constant $\lambda_{\mathrm{Tritium}} = 1.78 \times 10^{-9}\,\mathrm{s}^{-1}$. The first term gives the total tritium decay rate in the WGTS. The second term takes into account that β-electrons, regardless of their energy, can be only transmitted to the FPD if they are emitted in downstream direction and if $\theta_{\mathrm{s}} \leq \theta_{\mathrm{max}}$. The third term considers the FPD detection efficiency and coverage. The latter is given by the amount of the active detector pixels N_p.

The calculation of A_{source} is not accurate enough, mainly due to uncertainties of the FPD efficiency and the size of the flux tube. To account for unknown normalization effects, $N_{\mathrm{sig.}}$ is introduced as a nuisance parameter in the fit. Its contribution to the total normalization A is usually on the percent level.

2.2.4 Background model

The background model B consists of three components:

$$B(qU, t) = \underbrace{B_{\mathrm{base}}}_{\text{I) Steady-state background}} + \underbrace{\frac{1}{2} \cdot s_{\mathrm{time}} \cdot t(qU)}_{\text{II) Scan-step-time-dependent background}} + \underbrace{s_{\mathrm{qU}} \cdot (qU - 18\,574\,\mathrm{eV})}_{\text{III) Retarding-potential-dependent background}} . \tag{2.31}$$

Steady-state background: B_{base} makes up the largest fraction of the background. Different processes have identified that contribute to the steady-state background [75]. The largest contribution stems likely from so-called Rydberg atoms, that are produced through radioactive decays in the spectrometer walls. Being highly excited but neutral, Rydberg atoms can pass the inner electrode system and enter the active flux tube volume. Here, they are ionized by black body radiation. If emitted downstream of the analyzing plane, the generated low-energetic electrons are accelerated toward the FPD, where they are indistinguishable from β-electrons [69]. Another process that causes steady-state background is the α-decay of short-lived radon isotopes in the main spectrometer pumps. Multiple high-energetic electrons are produced subsequent to the α-decay through shake-off, internal conversion and relaxation processes. If these electrons enter the main spectrometer, they have a high chance to become trapped due to their large transversal energy component. Through scattering with residual gas, a primary electron with $E = \mathcal{O}(\mathrm{keV})$ creates $E = \mathcal{O}(100)$ secondary electrons. Similar to electrons from Rydberg atoms, the low energetic secondary electrons are accelerated toward the FPD if produced in downstream direction. The third steady-state background contributions stems from intrinsic detector background. The steady-state background is included as a nuisance parameter in the standard analysis. It was observed during data taking, that the steady-state background rate varies more than expected from a Poisson distribution. The over-dispersion is incorporated as a systematic uncertainty (section 4.10.1).

---

[8] $B_{\mathrm{s}} = 2.52\,\mathrm{T}$, $B_{\mathrm{t}} = 3.6\,\mathrm{T}$ and $B_{\mathrm{max}} = 4.24\,\mathrm{T}$.

Scan-step-time dependent background: The scan-step-time dependent background contribution originates from low energetic electrons that accumulate in the inter-spectrometer penning trap. Due to the combination of different retarding potentials in the two-spectrometer setup and the strong magnetic fields, a penning trap formed between the pre- and main spectrometer. If an electron passes through this region and looses energy due to scattering on residual gas molecules or by cyclotron radiation, it becomes trapped. Accumulating electrons in the penning trap can lead to a discharge, which results in additional background in the main spectrometer. The background rate increases with a slope s_{time} as a function of time. To mitigate this effect, an electron catcher was activated to remove trapped electrons after every scan step [76]. Thus, the background rate is reset to its original value after every scan step. The accumulated background rate for a given scan step is therefore determined by the associated scan-step measurement time $t(qU)$. Practically, the scan-step-time dependent background is inferred from background measurements above the tritium endpoint. Its uncertainty is propagated as a systematic uncertainty (section 4.10.2).

Retarding-potential-dependent background: A retarding-potential-dependent background contribution has to-date never been observed in KATRIN. However, due to the low background rate $\mathcal{O}(100\,\mathrm{mcps})$, it cannot be excluded with satisfying confidence. The hypothetical retarding-potential dependence is modeled with a linear function with a slope s_{qU}. In the standard analysis, it is included as a systematic uncertainty (section 4.10.3).

2.2.5 Measurement time distribution

As described in section 2.1.6, the FPD counts the number of transmitted electrons for different high-voltage set points. The measurement at a fixed qU value is called a *scan step*. Consecutive measurements of $\mathcal{O}(40)$ scan-steps yield the integral tritium β-spectrum, which also referred to as a (tritium) *scan*. The set of qU-values and the time spent at each set point $t(qU)$ is defined by the measurement time distribution (MTD). The MTDs of the first two measurement campaigns are depicted in figures 5.1 and 6.1, respectively. A typical scan lasts 2 h. In principle, the measurement time could be arbitrarily distributed among the scan steps. In practice, the MTD is optimized with respect to the neutrino-mass sensitivity. Most time is spent at retarding energies $qU - E_0 \approx -10\,\mathrm{eV}$, for which the neutrino-mass imprint in the integral spectrum is most prominent. Less measurement time is spent at lower retarding energies, as the rate of the integral spectrum steeply increases for decreasing retarding energies. Thus, sufficient statistics can be collected even with little measurement time $t(qU) = \mathcal{O}(30\,\mathrm{s})$. Moreover, set points above the tritium endpoint are included to measure the background. More details on the MTD optimization can be found in [1, 77].

Chapter 3

Analysis strategy

3.1 Analysis software

The analysis software used in this work is called "Simulation and Analysis with MATLAB® for KATRIN", hereinafter abbreviated as Samak. It was largely developed in [1] and over the course of this thesis. It is designed to perform high-level analyses of tritium β-spectra measured by the KATRIN experiment. Its key features are the following:

1. Interface with KATRIN data files:
   Samak is able to read the scan-wise KATRIN data files, which contain the measured spectra and the all operational parameters. The retrieved parameters can be displayed and analyzed for stability.

2. Model of tritium β spectrum:
   The modeling of the theoretical tritium β-spectrum, the experimental response function and the integral spectrum is implemented according to section 2.2. In case data is analyzed, all necessary model input parameters can be directly read from the data file(s). In case a simulation is carried out, the model parameters are retrieved from a configuration file, that can adjusted be at will.

3. Systematic uncertainties:
   Systematic uncertainties are incorporated through covariance matrices. A dedicated class in Samak is able to calculate covariance matrices for all relevant systematic effects in KATRIN (chapter 4). The magnitude of each systematic uncertainty and the sample size can be freely specified. Diagnostic tools are able to examine the covariance matrices for convergence and positive definiteness. Moreover, automatized graphical displays are available. Furthermore, several systematic effects can also be included in form of a pull-term in the χ^2-analysis.

4. Data combination strategies:
   Different analysis strategies in terms of scan and pixel combination can be used in Samak. They are discussed in more detail in section 3.2.

5. Analysis:
   Samak is designed to analyze both tritium data and Monte-Carlo (MC) simulations. The parameter inference and construction of confidence regions is based on the method of least squares. The employed statistical methods are described in more detail in section 3.3. The main focus of the analysis is put on the neutrino mass. However, also physics beyond the neutrino mass, such as sterile neutrinos and the cosmic neutrino background, can be investigated with Samak.

3.2 Data combination

A measurement campaign typically comprises $\mathcal{O}(100)$ tritium scans. Each scan contains 148 tritium spectra, one for each FPD pixel. The total number of recorded tritium spectra thus amounts to $\mathcal{O}(10^4)$. As each of them has a relatively low statistics, they have to be combined in order to reach a considerable m^2_ν sensitivity. Individual scans and pixels, exhibiting irregular behavior, for example high-voltage fluctuations or high noise levels, are excluded from the combination. Sections 3.2.1 and 3.2.2 address the scan and the pixel combination strategies used in the KATRIN analysis.

In the following, the selected scans are labeled by an index $s = 1, ..., N_s$ and the selected pixels are labeled by an index $p = 1, ..., N_\text{p}$. If no vector notation is used, the scan steps are referred to with an index i.

3.2.1 Scan combination

The MTD is approximately the same for all scans within a measurement campaign. All scans contain the same number of scan steps and the approximately the same measurement time per scan step $t_{i,s}$. The selected scans are combined by scan-step-wise addition of all scans

$$N^{\text{exp}}(\langle qU_i \rangle) = \sum_s^{N_s} N_s^{\text{exp}}(qU_i) \tag{3.1}$$

As the retarding energies are not exactly identical from scan-to-scan, they are approximated by the time-weighted average

$$\langle qU_i \rangle = \frac{\sum_s^{N_s} qU_{i,s} \cdot t_{i,s}}{\sum_s^{N_s} t_{i,s}}. \tag{3.2}$$

To keep the equations simple, the subscript p has been dropped. $\mathbf{N}^{\text{exp}}(\langle \mathbf{qU} \rangle)$ is later-on referred to as *stacked* spectrum.

Prerequisite for the applicability of the scan stacking technique is an excellent high-voltage reproducibility at the $\mathcal{O}(10\,\text{mV})$ level for all scan-steps. Moreover, all other operational parameter, such as column density and isotopologue concentrations, have to be stable from scan-to-scan. Before applying the stacking technique, all relevant parameters of the considered data set are examined if they meet the stacking requirements. The first two measurement campaigns pass the quality criteria and the stacking technique is applied (see sections 8.2.1 and 9.2.1). The model, that describes the stacked spectrum, is addressed in section 3.2.3.

3.2.2 Pixel combination

Each FPD pixel covers a different part the flux tube, as described in section 2.1.6. The outer-most pixels see only β-electrons that were emitted at the outer-most part of the WGTS; the central pixels see only β-electron from the central part of the WGTS, etc. Any azimuthal and radial variations of the electric and magnetic fields in the source and in the analyzing plane, therefore translate into pixel-wise differences of the tritium β-spectra. In case these inhomogeneities are sufficiently small, the pixel-wise spectra can be combined analogous to equation (3.1): The pixel-wise counts are summed up and the associated retarding energies are averaged. Like for the scan combination, the applicability of the selected pixel combination is validated for each measurement campaign (sections 8.2.2 and 9.2.2).

Different pixel-combination options are available in Samak:

- *Uniform*: In the simplest case, all selected pixels are combined into a single, so-called uniform, spectrum.
- *Multi-Ring:* The pixels can be grouped according to their radial position into 13 rings.
- *Multi-slice:* The pixels can be grouped according to their azimuth angle into 24 slices.

The different pixel combination options are illustrated in figure 3.1. In principle, also any other arbitrary arrangement is possible in Samak. The level of granularity, that means the number groups, can be chosen at will. Sometimes it can be beneficial to arrange the pixels in larger groups to improve the statistics within each group. For this purpose, two or more groups are combined. All pixel combinations, that are used throughout this work, are displayed in appendix B.

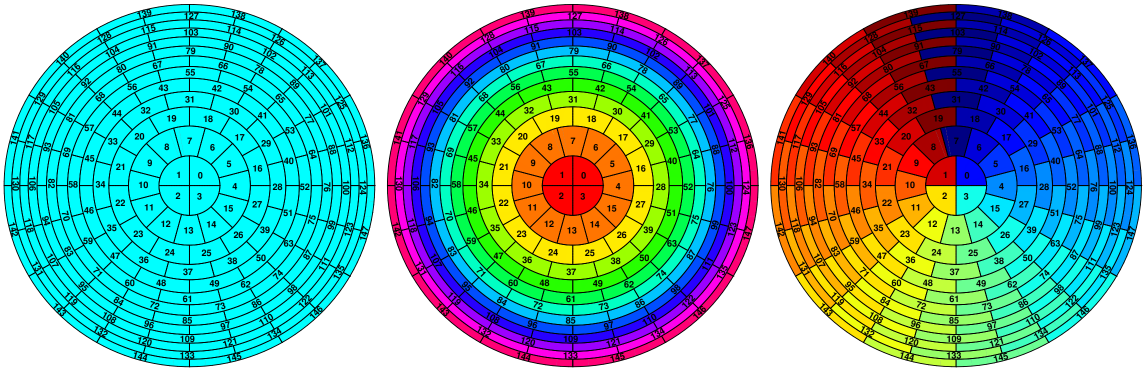

(a) Uniform (b) Radial position: multi-ring (c) Azimuth angle: multi-slice

Figure 3.1: Overview of the basic FPD pixel combinations. More options are stated in appendix B. **(a)** The pixel-wise spectra are summed up to a single effective spectrum. This pixel combination is called *Uniform*. **(b)** The spectra with the same radial position are combined, which result in 13 effective spectra. This pixel combination is called *multi-ring*. **(c)** The spectra with the same azimuth angle are stacked, which gives 24 effective spectra. This pixel combination is called *multi-slice*.

3.2.3 Model of combined spectrum

As described in the two previous sections, many tritium spectra are combined, that were measured at slightly different experimental conditions. The combined spectrum is described by an effective model, that is configured with the time-weighted-average input parameters. The column density used in the effective model, for example, is calculated from the scan- and pixel-wise parameter values

$$\langle \rho d \rangle = \frac{\sum_s^{N_s} \sum_p^{N_p} \rho d_{s,p} \cdot t_s}{\sum_s^{N_s} \sum_p^{N_p} t_s}. \tag{3.3}$$

with the total measurement time per scan

$$t_s = \sum_i t_{i,s}. \tag{3.4}$$

The same is true for all input parameters, that enter the model calculation in section 2.2.

In case the FPD is not considered uniform, each group of combined pixels is analyzed by an individual model with the group-specific average input parameters. In the standard analysis, the physics parameter of interest $\boldsymbol{\Theta}$ are considered to be common to all groups, whereas the nuisance parameters $\boldsymbol{\eta}$ (section 3.3.1) can take individual values for each group. As a consequence, the use of a finer FPD granularity leads to a larger number free fit parameters.

3.3 Statistical methods

This section summarizes the statistical methods that are used in this work: Section 3.3.1 described the parameter inference and uncertainty estimation with the method of least-squares. Furthermore, a review of different confidence belt construction techniques is given in Section 3.3.2 at the example of the neutrino mass. At last, section 3.3.3 addresses the propagation of systematic uncertainties.

3.3.1 Parameter inference

The model of the integral spectrum $\mathbf{N}^{\text{model}}(\boldsymbol{\Theta}, \boldsymbol{\eta})$ depends on one or more physics parameters of interest $\boldsymbol{\Theta}$, whose values are unknown prior to the measurement. In the neutrino-mass analyses, only 1 parameter is of immediate interest, namely $\Theta = m_\nu^2$. Different to that, the sterile-neutrino analyses investigate 2 physics parameters

$\boldsymbol{\Theta} = [m_4^2, |U_{e4}|^2]$. Additionally, the model also depends on the several nuisance parameters $\boldsymbol{\eta}$, which are not of immediate interest, but have to be accounted for in the spectral fit. Both $\boldsymbol{\Theta}$ and $\boldsymbol{\eta}$ are free fit parameter, which results in $N_{\text{par}} = N_{\Theta} + N_{\eta}$ free fit parameters. The baseline settings are summarized in table 3.1

Moreover, the model depends on *systematic* nuisance parameters ζ, such as $\rho d\sigma$ or the tritium isotopologue concentrations. These parameters are fixed according to the best knowledge of the operational parameters and therefore not varied in the spectral fit. Systematic uncertainties $\Delta\zeta$ are incorporated in the analysis, for example, in form of a covariance matrix V. Their treatment is discussed in more detail in section 3.3.3.

	Neutrino-mass analysis	Sterile-neutrino analysis
Physics parameters of interest $\boldsymbol{\Theta}$	m_ν^2	$m_4^2, \lvert U_{e4}\rvert^2$
Nuisance parameters $\boldsymbol{\eta}$	$E_0^{\text{fit}}, N_{\text{sig}}, B_{\text{base}}$	$(m_\nu^2), E_0^{\text{fit}}, N_{\text{sig}}, B_{\text{base}}$
Systematic nuisance parameters ζ	Fixed in fit; incorporated in covariance matrix	
Number of free fit parameters N_{par}	4	(6) 5

Table 3.1: Baseline settings for the uniform analysis of an integral spectrum with respect to the neutrino-mass or the sterile neutrinos. The spectral model $\mathbf{N}^{\text{model}}$ depends on three kinds of parameters. The physics parameters of interest $\boldsymbol{\Theta}$ and the nuisance parameters $\boldsymbol{\eta}$ are free parameter, whose values are inferred in the fit. The treatment of m_ν^2 in the sterile neutrino search, is addressed in more detail in chapter 11. The systematic nuisance parameters ζ are fixed in the fit according to the experimentalist's best knowledge. The associated systematic uncertainties are propagated through covariance matrices, as discussed in section 3.3.3. If not explicitly stated otherwise, these fit parameter configuration are considered in the respective analyses.

Least-squares fit: The objective of the spectral fit is to find the best-fit values $[\hat{\boldsymbol{\Theta}}, \hat{\boldsymbol{\eta}}]$, that maximize the agreement between data $\mathbf{N}^{\text{exp}}$ and model $\mathbf{N}^{\text{model}}(\boldsymbol{\Theta}, \boldsymbol{\eta})$.

The data points at each scan step follow a Poisson distribution, since the electrons arrive at a constant rate and independently from each other. Thanks to KATRIN's high source activity and the combination of many scans and pixels, the number of observed electrons is high ($> 10^3$) for all scan-steps. In the large sample limit, the Poisson likelihood can be well approximated by a Gaussian likelihood with the chi-squared function

$$-2\ln\mathscr{L}(\boldsymbol{\Theta}, \boldsymbol{\eta}) = \chi^2(\boldsymbol{\Theta}, \boldsymbol{\eta}) = \left(\mathbf{N}^{\text{exp}} - \mathbf{N}^{\text{model}}(\boldsymbol{\Theta}, \boldsymbol{\eta})\right)^{\intercal} \mathbf{V}^{-1} \left(\mathbf{N}^{\text{exp}} - \mathbf{N}^{\text{model}}(\boldsymbol{\Theta}, \boldsymbol{\eta})\right). \tag{3.5}$$

In the well-established method of least squares, the spectral fit searches for $[\boldsymbol{\Theta}, \boldsymbol{\eta}] = [\hat{\boldsymbol{\Theta}}, \hat{\boldsymbol{\eta}}]$, that minimizes the chi-squared function

$$\chi^2_{\text{min}} = \chi^2(\hat{\boldsymbol{\Theta}}, \hat{\boldsymbol{\eta}}). \tag{3.6}$$

Fit parameter uncertainties: Classically, the uncertainties on the fit parameters are calculated by constructing confidence belts. Different confidence belt construction techniques are discussed in section 3.3.2 at the example of m_ν^2. However, it was pointed out by Wilks [78], that in case the (profile) likelihood function follows a Gaussian distribution, the fit uncertainties can be conveniently obtained from the shape of the chi-squared function. Often, only subset of fit parameters $\boldsymbol{\Theta}_k \in \boldsymbol{\Theta}$ is considered at once with $N_k < N_{\text{par}}$ being the number of considered parameters. In this case, the profile chi-squared function $\chi^2(\boldsymbol{\Theta}_k)$ is used. The latter is calculated by minimizing the chi-squared function for fixed values of $\boldsymbol{\Theta}_k$ with respect to all other fit parameters. The fit uncertainties $\Delta\hat{\boldsymbol{\Theta}}_k$ at a confidence level (C.L.) α are given by the distance to $\hat{\boldsymbol{\Theta}}_k$, for which the profile chi-squared function increases by the critical chi-square $\Delta\chi^2_{\text{crit.}}(\alpha)$ compared to its minimum

$$\chi^2(\hat{\boldsymbol{\Theta}}_k \pm \Delta\hat{\boldsymbol{\Theta}}_k) - \chi^2_{\text{min}} = \Delta\chi^2_{\text{crit.}}(\alpha). \tag{3.7}$$

Following Wilks's theorem [78], $\Delta\chi^2_{\text{crit.}}(\alpha)$ can be calculated for the α of choice as

$$\int_0^{\Delta\chi^2_{\text{crit.}}(\alpha)} f_{N_k}(x)\mathrm{d}x = \alpha \tag{3.8}$$

with $f_{N_k}(x)$ being the chi-squared distribution for N_k degrees of freedom (dof). The uncertainty estimation for $\boldsymbol{\eta}$ is carried out analogously. For 1 fit parameter of interest, for example in the neutrino-mass analysis, $\Delta\chi^2_{\text{crit.}} = 1$ corresponds to a fit uncertainty at 68.3 % C.L..

Goodness of fit: The chi-squared formalism provides a measure for the goodness of fit: χ^2_{min} follows a chi-squared distribution with $N_{\text{dof}} = N_i - N_{\text{par}}$ dof. The p-value as a measure of the goodness of fit can then be calculated with

$$p = \int\limits_{\chi^2_{\text{min}}}^{\infty} f_{N_{\text{dof}}}(x)\mathrm{d}x. \tag{3.9}$$

A p-value below 5 % merits further investigation. Possible reasons for a low p-value are an inaccurate model and under-estimated or neglected systematic uncertainties.

3.3.2 Confidence belts

Next to inferring the m^2_ν central value and fit uncertainty from the data, the objective of the neutrino-mass analyses is to obtain a m^2_ν confidence region, that is based on a so-called confidence belt. In the frequentist interpretation, a confidence interval has the following meaning: If m^2_ν was measured infinite times, in the fraction α of the experiments the true (unknown) value of m^2_ν would lie inside the confidence interval $[m^2_{\nu,1}, m^2_{\nu,2}]$

$$P(m^2_\nu \in [m^2_{\nu,1}, m^2_{\nu,2}]) = \alpha. \tag{3.10}$$

The frequentist confidence interval is calculated by constructing a confidence belt. A confidence belts consists of many so-called acceptance regions $[x_1(m^2_\nu), x_2(m^2_\nu)]$, that are calculated for all potentially true m^2_ν values. The acceptance region is defined as

$$P(x \in [x_1, x_2] | m^2_\nu) = \alpha. \tag{3.11}$$

with $P(x|m^2_\nu)$ being the p.d.f. for a fixed m^2_ν value. Different confidence belt construction techniques are displayed in figure 3.4. The acceptance interval for a hypothetical "true" m^2_ν-value can be drawn as a horizontal line in x direction at $m^2_\nu = m^2_{\nu,\text{ true}}$. The confidence interval for a measured value $\hat{x}$ is given by the intersection of a vertical line in m^2_ν direction at $x = \hat{x}$ and the acceptance regions. If all acceptance regions fulfill equation (3.11), also the confidence interval (equation (3.10)) has the correct coverage α.

The classical way to calculate $P(x|m^2_\nu)$ is with a simulated Monte Carlo (MC) spectra. Many statistically randomized data sets are calculated, assuming a neutrino mass squared of m^2_ν. A fit with free neutrino mass squared is performed on each of these sample spectra. The distribution of the fit result samples $P(x|m^2_\nu)$. This method has two disadvantages: Firstly, to be sensitive to the tails of the distribution $P(x|m^2_\nu)$, very large sample numbers (> 5000) are needed. Secondly, this method gets quickly computational expensive with increasing sample size. Therefore, an alternative approach is followed in this work using a so-called Asimov spectrum, which is not statistically randomized. For each m^2_ν of interest, an Asimov spectrum is calculated. The associated profile chi-squared functions $\chi^2(x, m^2_\nu)$ are calculated, by fitting the Asimov spectra multiple times assuming a different, but fixed neutrino masses x. All other fit parameters are free in the fit. The profile chi-squared function can be converted into the probability density function $P(x|m^2_\nu)$ with:

$$P(x|m^2_\nu) \propto \exp\left(-\frac{1}{2}\chi^2(x, m^2_\nu)\right) \tag{3.12}$$

To ensure the probability interpretations, equation 3.12 is normalized to 1. An example probability density function is illustrated in figure 3.2 for $m^2_\nu = 0.2\,\text{eV}^2$. The acceptance region is a function of m^2_ν, and has therefore to be calculated for every m^2_ν of interest. To determine the acceptance region *uniquely*, an auxiliary criterion next to equation (3.11) is needed.

In principle, one has complete freedom to choose the auxiliary criterion, as long as the choice is not based on

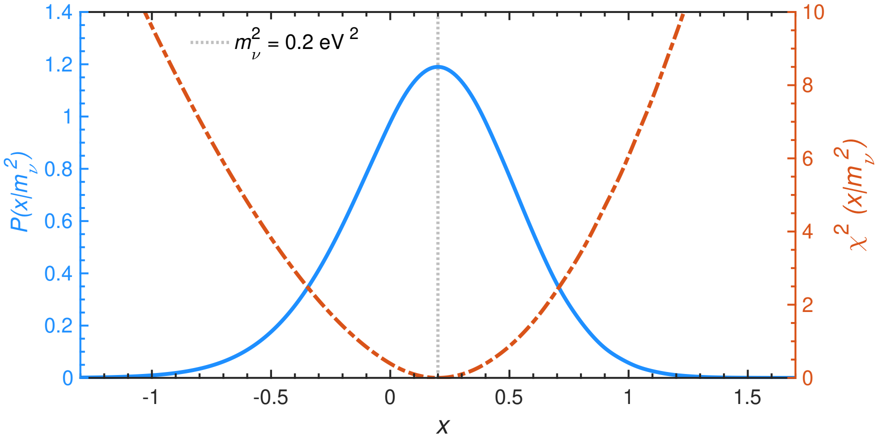

Figure 3.2: The profile chi-squared function $\chi^2(x|m_\nu^2)$ is obtained by analyzing a simulated Asimov spectrum. This simulated spectrum has asymptotic statistics, as it is not statistically randomized. The probability density function $P(x|m_\nu^2)$ can be obtained from $\chi^2(x|m_\nu^2)$ using equation (3.12).

the analyzed data set. In the following, different strategies are discussed. First, the classical confidence belts by Neyman [79] and the arising problems close to physical boundaries are briefly are discussed. Furthermore, the confidence belt construction techniques used in this work according to Feldman and Cousins (FC) and Lokhov and Tkachov (LT) are presented.

Neyman confidence belt: A common choice for an auxiliary criterion is either equation 3.13, which leads to an upper limit, or equation 3.14, which corresponds to a central confidence interval.

$$P(x < x_1|m_\nu^2) = \alpha \tag{3.13}$$

$$P(x < x_1|m_\nu^2) = P(x > x_2|m_\nu^2) = (1-\alpha)/2. \tag{3.14}$$

When constructing a confidence interval for the neutrino mass squared, a quantify known to be positive, the criteria above has problematic consequences. When the measured neutrino mass squared is significantly larger than zero, it is desired to quote a two sided confidence interval. However, when the measured neutrino mass is not significantly larger than zero, the lower bound will reach into the unphysical negative mass regime, as can be seen in figure 3.4 (red dash-dotted line) for $x = \hat{x} \leq 0.5\,\mathrm{eV}^2$. In that case the experimentalist would like to quote an upper limit on the neutrino mass instead. Even though one has complete freedom in choosing the type of confidence interval, this choice cannot be made based on the measured value. It has be demonstrated in [80], that this "flip-flopping" leads to a confidence interval without correct coverage, that means eq. 3.11 is not full filled for all possible m_ν^2.
Besides that, two complications arise in case the measured neutrino mass is a significant underfluctuation with respect to the expected value: Firstly, when opting for an upper limit, one finds an empty confidence interval. This is illustrated by the green dashed line in figure 3.4 for $x = \hat{x} \leq 0.4\,\mathrm{eV}^2$. Secondly, when choosing a central confidence interval, the lower and the upper boundary are in the unphysical negative regime.

Feldman-Cousins confidence belt: Feldman and Cousins were aware of the problem described above and presented a new criterion, which uniquely determines the acceptance region [80]. The advantage of this criterion is that the obtained confidence interval is never empty and always positive, as illustrated in figure 3.4 (blue line). Moreover, the correct coverage is maintained, when going from a one sided confidence interval to a two sided confidence interval.

For this criterion, FC define the likelihood ratio $R(x, m_\nu^2)$[1]

$$R(x, \Theta) = \frac{P(x|m_\nu^2)}{P(x|\hat{m}_\nu^2)}. \tag{3.15}$$

It was pointed out be [81], that the likelihood ratio be can equivalently expressed in terms of chi-squared difference

$$-2\ln R(x, m_\nu^2) \equiv \Delta\chi^2_{\mathrm{FC}}(x, m_\nu^2) = \chi^2(x, m_\nu^2) - \chi^2_{\mathrm{best}} \tag{3.16}$$

with

$$\chi^2_{\mathrm{best}} = \begin{cases} \chi^2(x, m_\nu^2 = x) = 0 & \text{for } x \geq 0 \\ \chi^2(x, m_\nu^2 = 0) & \text{for } x < 0 \end{cases} \tag{3.17}$$

Like $P(x|m_\nu^2)$, $\Delta\chi^2_{\mathrm{FC}}$ is evaluated using a simulated spectrum without statistical fluctuations (Asimov). The first term is the regular profile chi-squared, illustrated for example in figure 3.2 for $m_\nu^2 = 0.2\,\mathrm{eV}^2$. For the second term ($\chi^2_{\mathrm{best}}$) one differentiates between two cases:

1. In case $x \geq 0$, then $\chi^2_{\mathrm{best}} = 0$. A simulated Asimov spectrum with the MC truth $m_\nu^2 = x$ is fit with the identical model spectrum.

2. In case $x < 0$, the chi-squared is evaluated using a simulated Asimov spectrum with the MC truth $m_\nu^2 = 0\,\mathrm{eV}^2$ and a model spectrum with $m_\nu^2 = x$. This implements a boundary at $m_\nu^2 = 0\,\mathrm{eV}^2$.

The difference between $\chi^2(x, m_\nu^2)$ and $\Delta\chi^2_{\mathrm{FC}}(x, m_\nu^2)$ is illustrated in figure 3.3 for $m_\nu^2 = 0.2\,\mathrm{eV}^2$. The acceptance region is uniquely determined by ordering the $P(x|m_\nu^2)$ in equation (3.11) according to $\Delta\chi^2_{\mathrm{FC}}(x, \mu)$ with the auxiliary criterion

$$\Delta\chi^2_{\mathrm{FC}}(x_1, m_\nu^2) = \Delta\chi^2_{\mathrm{FC}}(x_2, m_\nu^2). \tag{3.18}$$

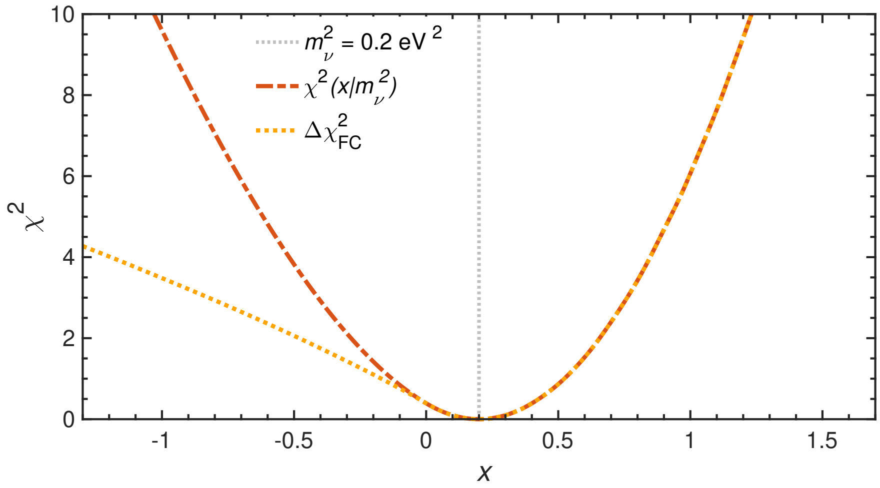

Figure 3.3: Feldman and Cousins define $\Delta\chi^2_{\mathrm{FC}}$ in equation (3.16), which specifies the ordering of $P(x|m_\nu^2)$. To obtain only one possible solution for the acceptance region (equation (3.11)), the auxiliary criterion in equation (3.18) is used.

---

[1] Note that even though numerical identical, $P(x|m_\nu^2)$ is here interpreted as a likelihood instead of a probability density, because its calculation is based on a fixed measured value x.

Lokhov and Tkachov (LT): The Lokhov-Tkachov confidence belt [82] is calculated with the same framework as described above. Similar to FC, the physical boundary of the neutrino mass at zero is taken into account in the construction of these confidence intervals. The difference to FC is, that LT do not use the likelihood ratio ordering to achieve this.

They define that the estimator of the neutrino mass x has to be always positive. When the lower limit of the acceptance region x_1 happens to be in the negative mass regime for a particular *true* m^2_ν, x_1 is set to $-\infty$ and the probability distribution function in integrated from $-\infty$ to x_2. Consequently, when experimentally measuring a negative mass, the corresponding upper limit coincides with the sensitivity. Therefore, this method is also called method of sensitivity limit. The LT confidence belt is illustrated in figure 3.4 (orange dotted line).

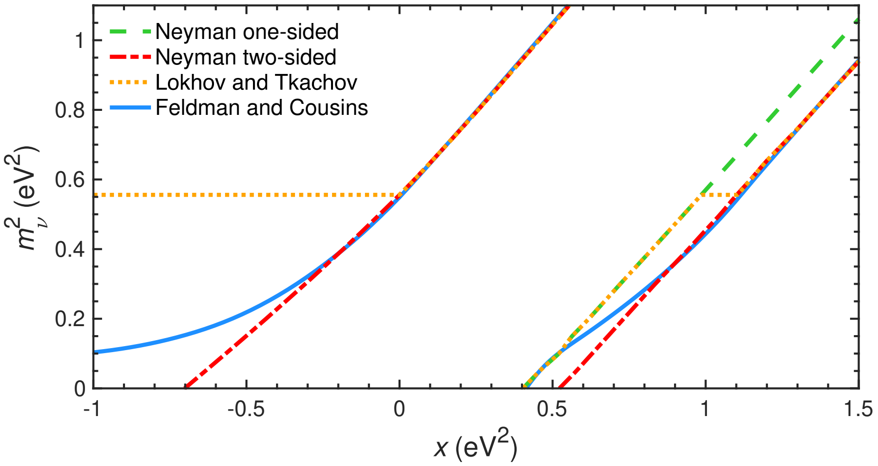

Figure 3.4: Illustration of different confidence-belt-construction techniques. A confidence belt is a conjunction of many acceptance regions $[x_1(m^2_\nu), x_2(m^2_\nu)]$ (horizontal direction), that are calculated for many different values of m^2_ν. The acceptance region construction is based on the coverage criterion in equation (3.11) and one additional auxiliary criterion. The latter can be chosen arbitrarily as long as the choice is not influenced by the experimental outcome of x. The one- and two-sided Neyman confidence belts use equations (3.13) and (3.14), respectively [79]. The Lokhov and Tkaschov confidence belt use equation (3.13) for $x_1 < 0$ and equation (3.14) otherwise [82]. Feldman and Cousins employ the so-called likelihood ratio (or equivalent the chi-squared difference) ordering in equation (3.16). The confidence interval $[m^2_{\nu,1}(x), m^2_{\nu,2}(x)]$ for a measured value x is given by the intersection with the acceptance regions in vertical direction. The confidence belts shown here are based on the KNM2 data set for illustration.

3.3.3 Systematic uncertainty propagation

Systematic nuisance parameters ζ are model input parameters, whose values and uncertainties $\hat{\zeta} \pm \Delta\hat{\zeta}$ are estimated by external measurements prior to the spectral analysis. The underlying physical processes of the systematic effects in KATRIN are addressed in chapter 4. To guarantee a bias-free parameter inference, systematic uncertainties have to be accounted for in the chi-squared function. Two complementary uncertainty propagation strategies are used in this work: the covariance matrix approach and the use of pull terms.

3.3.3.1 Covariance matrix approach

Systematic uncertainties can be incorporated in the chi-squared function by a covariance matrix (see equation (3.5)), which is the baseline strategy in this work. The covariance matrix approach is already extensively described in [1, 65], thus only a brief summary is provided here.

The systematic nuisance parameters ζ are randomized according to their associated probability density functions, generating $\mathcal{O}(10^4)$ sample values $\{\zeta_{\text{sample}}\}$. Correlations among $\boldsymbol{\zeta}$ are taken into account. If not specified otherwise, the p.d.f.s are assumed to be Gaussian with $\boldsymbol{\mu} = \hat{\boldsymbol{\zeta}}$ and $\boldsymbol{\sigma} = \Delta\hat{\boldsymbol{\zeta}}$. Subsequently, each random sample ζ_{sample} serves as input for one simulation of an integral spectrum $N^{\text{model}}_{\text{sample}}$, which results in $\mathcal{O}(10^4)$ different sample spectra $\{N^{\text{model}}_{\text{sample}}\}$.

The signal normalization $N_{\text{sig.}}$, being a free fit parameter, absorbs all uncertainties on the overall signal strength. Therefore, systematic uncertainties that translate solely into an overall fluctuation of $\{N^{\text{model}}_{\text{sample}}\}$ must be eliminated. This is archived by normalizing the statistics of each sample spectrum to the average statistics of all sample spectra, effectively transforming $\{N^{\text{model}}_{\text{sample}}\}$ into shape-only sample spectra. The shape-only covariance matrix $\mathbf{V}$ is determined from $\{N^{\text{model}}_{\text{sample}}\}$ using the sample covariance matrix as an estimator. Its entries encode the shape-only uncertainties on the model points and their scan-step dependent correlations. In this work, covariance matrices are displayed as fractional covariance matrices $\mathbf{V}_{\text{frac}}$, which show the relative influence of a systematic effect on the model spectrum

$$\mathbf{V}_{\text{frac}} = \frac{\mathbf{V}}{(\mathbf{N}^{\text{model}})^{\intercal}\mathbf{N}^{\text{model}}}. \tag{3.19}$$

If a set of systematic effects are uncorrelated, the associated covariance matrices can be calculated independently from one another. Besides systematic uncertainties, a covariance matrices with the statistical (Poisson) uncertainties on its diagonal is determined. The sum of all covariance matrices gives the total covariance matrix, as it is used in the fit.

3.3.3.2 Pull-term approach

A complementary uncertainty propagation technique is the pull-term approach. Being statistically equivalent to covariance matrices, this method is used as a cross check in this work. The chi-squared function in equation (3.5) is extended with so-called pull-terms

$$\chi^2(\boldsymbol{\Theta}, \boldsymbol{\eta}, \zeta) = \chi^2(\boldsymbol{\Theta}, \boldsymbol{\eta}) + \chi^2_{\text{pull}}(\zeta) \tag{3.20}$$

with

$$\chi^2_{\text{pull}}(\zeta) = \frac{(\zeta - \hat{\zeta})^2}{(\Delta\hat{\zeta})^2}. \tag{3.21}$$

In this approach, $\boldsymbol{\zeta}$ is not fixed in the fit but a variable fit parameter. However, it is constrained by the pull term according to the best knowledge $\boldsymbol{\zeta} = \hat{\boldsymbol{\zeta}} \pm \Delta\hat{\boldsymbol{\zeta}}$.

Chapter 4

Systematic effects in KATRIN

This chapter is devoted to systematic effects, that were observed in the first two measurement campaigns of the KATRIN experiment. Loosely arranged from source to detector section, each systematic effect is discussed in a separate section.

4.1 Theoretical corrections

As described in section 2.2.1.3, small known corrections on the particle, nuclear, atomic levels can be applied to the standard Fermi function. As the integration of these theoretical corrections in the spectral model can be computationally expensive, they are often neglected in case their influence on the neutrino mass is small compared to the sensitivity. In case of exclusion, the missing theoretical corrections are incorporated as a systematic uncertainty in form of a covariance matrix M^{TC}. The latter is calculated by comparing the integral spectrum with theoretical correction (R^{TC}) to the default one (R^{NC})

$$M_{\mathrm{ij}}^{\mathrm{TC}} = (R_{\mathrm{i}}^{\mathrm{TC}} - R_{\mathrm{i}}^{\mathrm{NC}})(R_{\mathrm{j}}^{\mathrm{TC}} - R_{\mathrm{j}}^{\mathrm{NC}}). \tag{4.1}$$

Figure 4.1 illustrates the relative difference between corrected and uncorrected integral spectrum for six of the above mentioned effects as a function of retarding energy. The largest correction stems from radiative effects, inducing a relative spectral change up to -8×10^{-3}. Recoil effects due to the finite nuclear mass (V-A interference

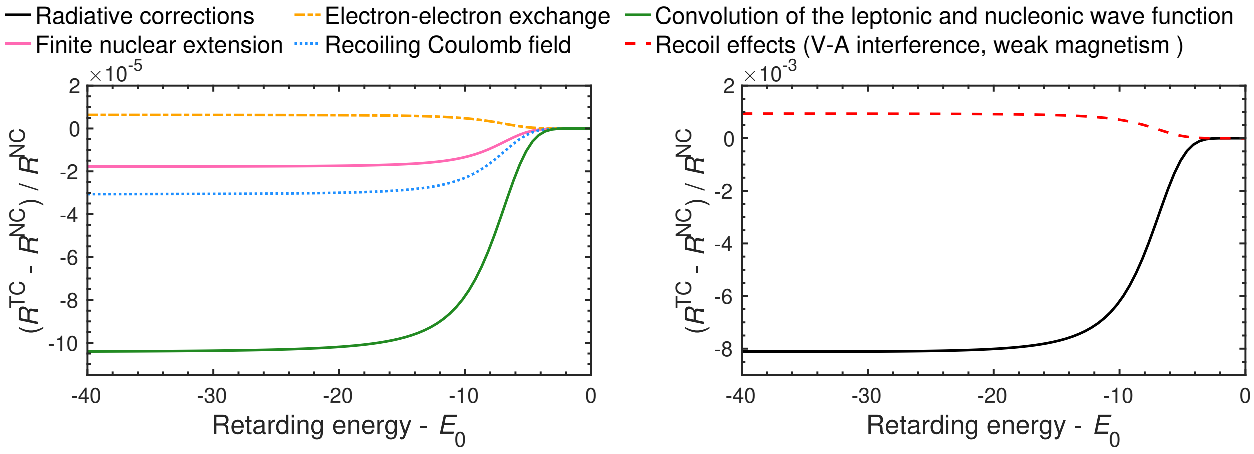

Figure 4.1: Theoretical correction (section 2.2.1.3) to the standard Fermi-function (section 1.3.3) originate from the particle, nuclear and atomic level. The relative rate difference between integral spectrum with (TC) and without (NC) theoretical correction is compared. The radiative correction yield the largest spectral change.

and weak magnetism) change the spectrum up to 1×10^{-3}. All other corrections are one order of magntiude or more smaller than that the second largest correction.
What concerns the analysis of the first two measurement campaigns, only the radiative corrections are included in the model.

4.2 Final-state distribution

As described in section section 2.2.1.1, the FSD describe translational, rotational and electronic excitation states of the daughter nucleus. Due to energy conservation, the FSD directly affects the electron energy spectrum. Therefore, precise knowledge of the final-state distribution is essential for KATRIN. As the molecular excitation cannot be measured in KATRIN, the FSD have to be calculated *ab initio*. The importance of an adequate description and uncertainty estimation of the FSD has been impressively demonstrated by past neutrino mass experiments in the 1980s. Studying the kinematics of tritium β-decay in the endpoint region similar to KATRIN, experiments at Lawrence Livermore National Laboratory (LLNL) and Los Alamos National Laboratory (LANL) reported on negative m_ν^2 fit results [83, 84]. Originating from a rate excess near the endpoint, the anomalies were significant at the 2σ (LANL) and 6σ (LLNL) level. Both analyses used the FSD calculation from Fackler *et al.* [85]. When their tritium data was reevaluated with a modern FSD calculation from Saenz *et al.* [64], the significance of both results was diminished and the extracted m_ν^2 values were consistent with zero [86]. Even though being a striking experimental confirmation of the theoretical calculation by Saenz *et al.*, this illustrates the necessity of a reliable FSD error estimation, especially considering the large statistical power of the KATRIN.

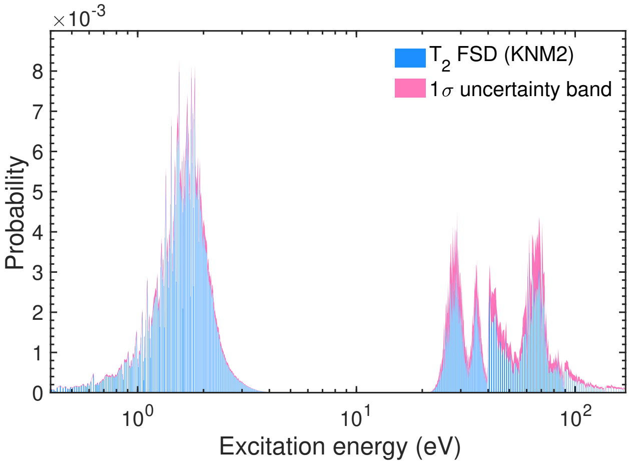

Figure 4.2: Illustration of the systematic uncertainty on the final-state distribution. The blue bars depict the (binned) FSD used in KNM2 for the T_2 isotopologue. The FSD uncertainty propagation for HT and DT is carried out analogously. To propagate the systematic uncertainty on normalization and variance, an ensemble of randomized FSD is generated following the prescription above. The pink band gives the uncorrelated 1σ variation within each FSD bin. This illustration uses $\Delta N_{\mathrm{GS}} = 1\,\%$, $\Delta p_{\mathrm{GS}} = 4\,\%$ and $\Delta p_{\mathrm{ES}} = 18\,\%$.

As theorists don't provide any error estimation on the FSD, a heuristics treatment is developed to cover any unknown FSD inaccuracies [1]. For this, the differences between the FSD calculations from Fackler *et al.* and Saenz *et al.* serve as conservative indication for the magnitude of the systematic error. The description of the ground states, comprising all translational and vibrational excitations with energies below 5 eV, are very similar from one computation to another. Calculations for higher excited states and for the electronic continuum exhibit larger differences. The FSD uncertainty is divided into two aspects:

Firstly, a normalization uncertainty ΔN_{GS} on the cumulative ground-state probability N_{GS} is formulated. The latter is randomized according to a Gaussian distribution with $\sigma = \Delta N_{\mathrm{GS}}$. The ground-states of the FSD are re-weighted accordingly. Following the specification in the KATRIN Design Report [42], a relative uncertainty of 1 % is assumed as default value

$$\Delta N_{\text{GS}} = 0.01 \cdot N_{\text{GS}}. \tag{4.2}$$

The cumulative excited-state probability N_{ES} is adjusted accordingly for each sample s, following conservation of probability[1]

$$N^s_{\text{ES}} = N_{\text{ES}} + N_{\text{ES}} - N^s_{\text{GS}}. \tag{4.3}$$

Secondly, an uncertainty on the variance of the FSD is designed. To account for the different level of accuracy between ground and excited states, it is distinguished between ground-state variance uncertainty $\Delta\sigma^2_{\text{GS}}$ and variance uncertainty for the entire energy range $\Delta\sigma^2_{\text{ES}}$. The variance uncertainties are implemented in form of bin-to-bin uncorrelated probability variations Δp_{GS} and Δp_{ES}, that are tuned to match the desired $\Delta\sigma^2$. The details of this procedure can be found in [1]. After the suggestion of [87] and specification in the KATRIN Design Report [42], a $\Delta\sigma^2_{\text{GS}} = 1\,\%$ and $\Delta\sigma^2_{\text{GS}} = 2-3\,\%$ are used as default values.

The FSD uncertainties are finally propagated to the integral spectrum in form of a covariance matrix. The latter is calculated in the usual manner, based on the randomized FSD samples. Figure 4.2 illustrates the ensemble of randomized FSD for the T_2 isotopologue. The decay of other tritium isotopologues in the WGTS, namely HT and DT, is characterized by slightly different FSD (section 4.5). Their uncertainty propagation is carried out analogously to the T_2 FSD.

4.3 Source potential

As described in section 2.1.2, the molecular tritium in the source occurs in a state of a cold and strongly magnetized plasma. The electric potential of the plasma defines the starting potential of the β-electrons. Therefore, any potential homogeneities propagate directly into the tritium spectrum and need to be accounted for in the model. Unknown spatial or time-wise plasma potential variations can lead to a bias in the neutrino mass.

Within the WGTS, free electrons and ions are magnetically confined in radial direction. Thus, the plasma potential is mostly influenced by the bias voltage of the rear wall U_{RW}, rather than the (grounded) beam tube. Nevertheless, intrinsic work function differences between the gold-plated rear wall and the stainless-steel beamtube surface can give rise to spatial plasma potential inhomogenieties. It is expected from simulations that the spatial inhomogeneities vanish with the optimal U_{RW} configuration [45], which is determined in advance of each measurement campaign.

Moreover, the plasma potential can be characterized experimentally using krypton as a calibration source with a well-defined energy spectrum [88, 89]. The main goal of the krypton measurements is the determination of the longitudinal potential distribution and short-term fluctuations. Both radial and long-term plasma potential variations can also be inferred directly from tritium data, whereas a remaining inhomogeneities would be only perceivable as a neutrino-mass bias.

In the following sections, the determination of longitudinal (section 4.3.1), radial (section 4.3.2) and time-wise (section 4.3.3) plasma potential variations and their uncertainties treatments are discussed.

4.3.1 Longitudinal homogeneity

The longitudinal plasma potential can be modeled with two parameters: an energy broadening σ_0^2 and an energy-loss shift Δ_{10}. In the following, their physical meaning is briefly illustrated. A comprehensive discussion of the phenomenological plasma model is given in [88].

If the plasma potential has a longitudinal z-dependency, each FPD pixel sees a superposition of spectra with different electron starting potentials. The effective spectrum can be described with the average plasma potential and an increased experimental energy resolution $\Delta E' = \sqrt{\Delta E^2 + \sigma_0^2}$. Technically, the energy broadening is incorporated in the model by convolving the FSD and a Gaussian with the variance σ_0^2. This procedure is illustrated in figure 4.3 (left) for an arbitrary energy broadening $\sigma_0^2 = 0.2\,\text{eV}^2$. The second plasma parameter, Δ_{10}, takes anti-symmetric

---

[1] The cumulative probability of the entire FSD calculations at hand differ from unity by $\ll 1\,\%$.

spatial plasma potential variations into account: Electrons that are emitted at the rear-end of the WGTS (low z), traverse a longer path in the source than electrons emitted at the front-end (high z). Encountering more tritium molecules, low z electrons have a larger probability to scatter at least once than high z electrons. If the plasma potential is, for example, more positive for low z than for high z, electrons that scatter at least once have on average a lower starting energy than electrons that don't scatter. This effect is is modeled as an energy-loss offset between zero and one scatterings as illustrated in figure 4.3 (right) for an arbitrary energy-loss shift $\Delta_{10} = 0.5\,\mathrm{eV}$. Both longitudinal plasma parameters, can be assessed in krypton measurements. In the WGTS, gaseous $^{83\mathrm{m}}$Kr is

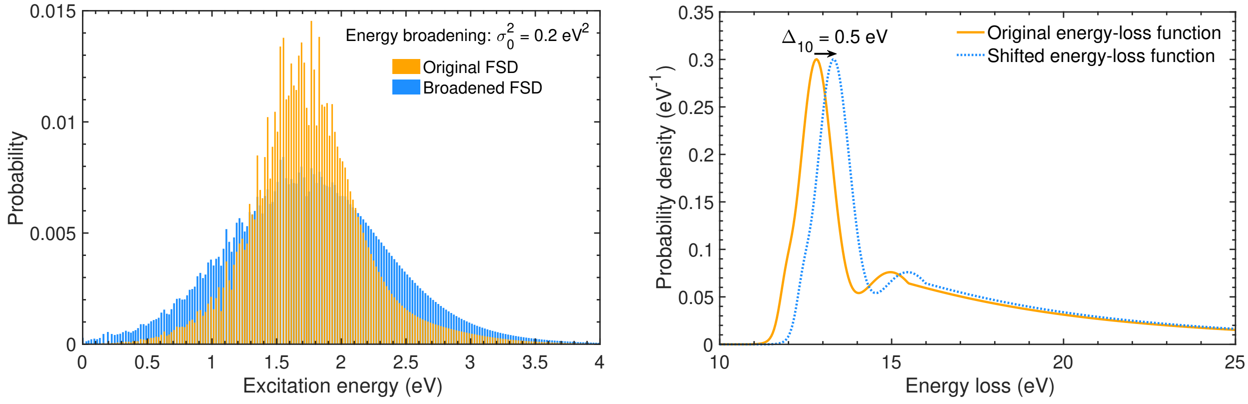

Figure 4.3: Illustration of longitudinal plasma parameters. **Left:** The energy broadening σ_0^2 is incorporated in the model by convolving the Final-state distribution with a Gaussian with $\sigma_2 = \sigma_0^2$. By means of illustration, the broadening effect is demonstrated here on the ground state only. **Right:** Anti-symmetric plasma potential variations are taken into account by the energy-loss shift parameter Δ_{10}. The latter describes an energy offset between zero and one-fold scattering.

produced in an excited state via electron capture of ^{83}Rb. The krypton excitation energy is split over an intermediate state into two excitation energies of 32.2 keV and 9.4 keV. Deexcitation occurs either by γ-emission or internal conversion, where only the latter contributes to the krypton spectrum. The kinetic energy of the electron is the difference between the excitation energy and the binding energy of the electron. Since the emitted electrons can originate from various atomic shells, several spectral lines are expected per transmission energy. Only the 32.2 keV transition can be used for calibration purposes, as its energy is above the tritium endpoint. The spectral lines have a small natural line width $\mathcal{O}(1\,\mathrm{eV})$, rendering them an attractive calibration source. By comparing the experimental spectrum to a reference spectrum, that is recorded in the absence of plasma, σ_0^2 and Δ_{10} can be determined.

The correlated uncertainties σ_0^2 and Δ_{10} from the krypton data analysis are propagated to the integral spectrum in the usual manner. Pairs of σ_0^2 and Δ_{10} are randomly drawn from a multivariate Gaussian distribution, each pair serving as input for one spectrum calculation. The longitudinal plasma covariance matrix is then estimated from the ensemble of sample spectra.

4.3.2 Radial homogeneity

A radial inhomogeneity of the plasma potential can be resolved with the pixel segmentation of the FPD. Each FPD pixel detects only electrons from a specific flux tube volume, that is associated with a specific radial starting position within the WGTS. The pixel-wise distribution of fitted endpoints mirrors the radial plasma potential variation. As the electrons are negatively charged, a more positive plasma potential results in a lower endpoint.

As long as each pixel, or group of pixels with similar electron starting potential, is described with an individual endpoint in the spectral analysis, no neutrino-mass bias is induced. Consequently, by making use of the FPD segmentation with multipixel or multiring fit (see chapter 3), unknown radial plasma potential variations can be accounted for.

However, simulations suggest that a radially homogeneous plasma potential minimizes longitudinal inhomogeneities [45]. On top of that, a multipixel analysis is substantially more complex and computationally expensive than a uniform analysis, mostly due to the increasing number fit parameters. Because of that, the rear-wall bias voltage is optimized with respect to radial plasma homogeneity in advance of each measurement campaign.

4.3.3 Long-term stability

A changing plasma potential over time leads to a time-dependent electron starting potential. To good approximation, this is equivalent to a time-dependent effective tritium endpoint. A spectrum, that is recorded over a period of changing plasma potential, is consequently a superposition of spectra with different endpoints. Similar to a longitudinal plasma inhomogeneity, the plasma variation σ_t^2 can be modeled as an energy-broadening of the same magnitude. The latter is implemented in the model through a broadening of the FSD in the same way as σ_0^2, illustrated in figure 4.1 (left).

The time-wise plasma potential variations σ_t^2 can be inferred from tritium data in several ways. The option pursued in this work is the rate analysis of a high-statistics monitor scan-step, that is recorded at $qU - E_0 < -300\,\mathrm{eV}$ (KNM2). After being corrected for scan-wise activity and retarding potential fluctuations, this scan-step is sensitive to plasma potential time evolution. The analysis of the rate monitor point in KNM2 can be found in section section 6.6.2. Another option is the analysis of the time evolution of the fitted endpoint. For the spectral fits, only scan-steps are used that were discarded for the neutrino-mass analysis to avoid double usage of data.

The long-term plasma potential variation is combined with the longitudinal homogeneity (section 4.3.1) by summation in quadrature $\sigma_{\mathrm{plasma}}^2 = \sigma_0^2 + \sigma_t^2$.

4.4 Source activity

The source activity A_{source} is determined by the amount of tritium in the source. The higher both column density and tritium purity are, the more β-decays occur and the higher is the source activity

$$A_{\mathrm{source}} \propto \rho d \cdot \epsilon_{\mathrm{T}}. \tag{4.4}$$

The latter, among other fixed quantities such as the acceptance angle[2], determines the signal strength of the experimental tritium spectrum. Consequently, any uncertainty on A_{source} propagates into an uncertainty on the observed signal rate. When discussing the uncertainty propagation, two aspects have to be examined: The uncertainty on the absolute value of A_{source} (section 4.4.1) and the stability of the source activity within a scan (section 4.4.2).

4.4.1 Uncertainty on absolute value

If A_{source} is constant over the time-scale of a tritium scan, all scan-steps underlie the same signal strength. In this case, the uncertainty on the absolute value of A_{source} translates into an uncertainty on the overall signal normalization for the entire spectrum. Since the latter is included as a free fit parameter in all spectral analyses, this aspect does not require additional uncertainty propagation.

4.4.2 Scan fluctuations

If A_{source} varies within a scan, the scan-steps observe different signal amplitudes. The spectral model, however, only accounts for one average signal normalization for the entire spectrum. This could potentially cause a small spectral distortion and a neutrino-mass bias. As the scan-wise activity variations are small for both measurement campaigns, the former is not included in the spectral model but accounted for as a systematic uncertainty. The treatment of the activity variations within a scan is performed as follows.

In the stacked scan analysis with n_s scans and n_k scan-steps, each scan-step k of scan s is associated with a

---

[2] The full discussion on the expected signal strength is given in section 2.2.3.

measured source activity A^{sk}_{source}. As a first step, the mean activity of each scan is normalized to the global mean source activity to mitigate scan-wise normalization differences

$$\hat{A}^{sk}_{\text{source}} = A^{sk}_{\text{source}} \frac{\frac{1}{n_s n_k}\sum_s \sum_k A^{sk}_{\text{source}}}{\frac{1}{n_k}\sum_k A^{sk}_{\text{source}}} = A^{sk}_{\text{source}} \frac{\langle\langle A_{\text{source}}\rangle\rangle}{\langle A^{s}_{\text{source}}\rangle}. \tag{4.5}$$

The relative systematic activity uncertainty for a stacked scan-step is the error of the mean

$$\sigma^{k}_{\text{sys}} = \frac{\sqrt{\frac{1}{n_s}\sum_s (\hat{A}^{sk}_{\text{source}} - \langle \hat{A}^{k}_{\text{source}}\rangle)^2}}{\sqrt{n_s}} \cdot \frac{1}{\langle \hat{A}^{k}_{\text{source}}\rangle}. \tag{4.6}$$

Scan-step-wise correlations are taken into account, by calculating the fractional covariance matrix for all scan-steps:

$$M^{\text{activity}}_{\text{frac.}} = \text{cov}(\hat{A}^{sk}_{\text{source}})\frac{1}{n_s}\frac{1}{\langle \hat{A}^{k}_{\text{source}}\rangle^2}. \tag{4.7}$$

As the signal normalization of the integral spectrum is directly proportional to the source activity, $M^{\text{activity}}_{\text{frac.}}$ can be used as the fractional covariance matrix for the integral spectrum prediction.

4.5 Molecular gas composition

The gas injected into the WGTS comprises mainly three different tritium isotopologues: T_2, HT and DT. The β-decay of each isotopologue is described with a slightly different final-state distribution, as illustrated in figure 2.3. Systematic uncertainties on the relative molecular abundances propagate into the spectral shape. The observable integral spectrum is a superposition of three slightly different integral spectra, one for each isotopologue respectively. Figure 4.4 shows the relative difference of integral spectra, that contain only one molecular species. The integral spectrum of T_2 is used as a reference. To mitigate normalization effects, the activity is assumed to be identical for all three cases.

The gas composition is continuously monitored by a Laser Raman spectroscopy system in the TLK infrastructure. The uncertainty of this measurement is mostly driven by the trueness of the LARA calibration [90].

As other molecules are only present in trace amounts, the relative molecular concentrations of the tritium isotopologues are strongly correlated with each other. The correlations are estimated from LARA data for all sub-scans within all golden scans for each measurement campaign respectively. The resulting concentration correlation matrix in conjunction with the trueness values from [90] yield the concentration covariance matrix. The impact on the integral spectrum is estimated with an ensemble test. $\mathcal{O}(10^3)$ concentration triplets are randomly drawn from the Gaussian multivariate distribution with the concentration covariance matrix. Each concentration triplet serves as input for an integral spectrum calculation. Using a spectral model with average concentration values, each sample spectrum is then analyzed with respect to the neutrino mass. The standard deviation of the m^2_ν fit-value distribution equals the 1σ contribution to the systematic sensitivity budget.
It turns out that the impact on the neutrino mass is very small compared to the KNM1 and KNM2 sensitivities (sections 8.6 and 9.7). Therefore, this systematic uncertainty is neglected in the spectral analyses presented in this thesis.

4.6 Number of scatterings

Electrons in the source loose energy by scattering inelastically off ambient tritium molecules (see section 2.2.2.2). The probability for s-fold scattering and the expected number of scatterings

$$N_{\text{scat.}} = \rho d \cdot \sigma_{\text{inel.}}. \tag{4.8}$$

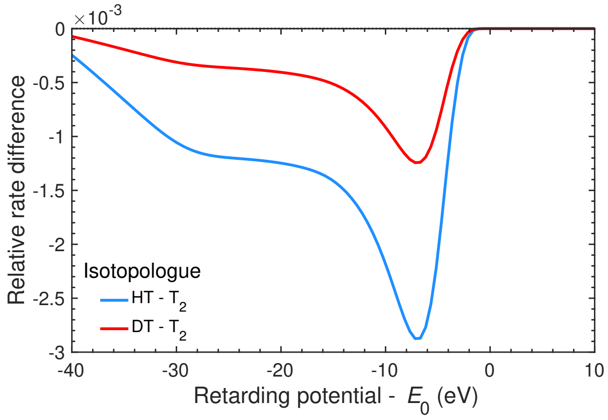

Figure 4.4: Integral spectra for different tritium isotopologues. The tritium isotopologues present in the WGTS are described with slightly different FPD. Here, the relative difference of an integral spectrum, that contains only HT or DT, to a T_2-only integral spectrum is shown. The activity is assumed to be constant for all spectra to mitigate normalization effects.

are determined by the column density in conjunction with the inelastic scattering cross section $\sigma_{\text{inel.}}$. As ρd and $\sigma_{\text{inel.}}$ always appear as a product in the response function calculation, their uncertainties are treated simultaneously. $N_{\text{scat.}}$ can be determined using a mono-energetic electron source, which is installed at the rear end of the WGTS. When passing through the WGTS, the electrons loose a certain amount of energy with a given probability through inelastic scattering off the tritium gas. By analyzing the integral electron source spectrum, $N_{\text{scat.}}$ can be inferred to great accuracy. The only drawback from this method is that it cannot be applied to monitor $N_{\text{scat.}}$ while data taking, as its measurement interferes with the tritium scans. Other monitor parameters, that scale with ρd and can be measured continuously, are consulted to interpolate $\rho d \cdot \sigma_{\text{inel.}}$ to all times. Several parameters are available such as the gas throughput in the injection capillaries or the FBM rate [91].

4.7 Energy-loss function

At each inelastic scattering in the source, an electron looses a variable amount of energy. As explained in section 2.2.2.2, the energy-loss function determines the probability to loose a certain amount of energy per inelastic scattering. As the theoretical description of this process isn't accurate enough, dedicated measurements inside the KATRIN apparatus are performed [68].

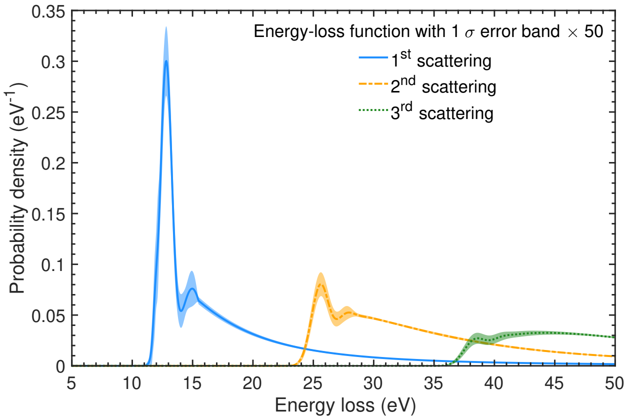

Figure 4.5: Energy-loss function (section 2.2.2.2) for the first the scatterings with 1σ error band. By way of illustration, the error band is scaled with a factor 50.

The data is fit with a semi-empirical parametrization, comprising nine physics parameters of interest. The fit uncertainties on these nine parameters and the associated correlation matrix are used to generate an ensemble of randomized energy-loss functions. By way of illustration, figure 4.5 shows the mean energy-loss function for the first three scatterings with associated error bands scaled by a factor of 50, which are estimated from an ensemble of 1000 samples. Each sample energy-loss function then serves as input for an integral spectrum calculation. As a last step, the spectral covariance matrix is computed from the ensemble of integral spectra.

4.8 Magnetic fields

The magnetic fields inside the KATRIN apparatus are key ingredients for the response function calculation. Source and pinch magnetic field determine the maximal detected polar angle, which influences the mean scattering probabilities as well as the mean energy loss through synchrotron radiation. In conjunction with the former two magnetic fields, the magnetic field in the analyzing plane determines the transmission properties and energy resolution of the MAC-E filter in the main spectrometer.

Moreover, the θ_{max} affects the number of tritium electrons seen by the FPD. This relation applies equally to all retarding energies, thus rendering it a pure normalization effect which doesn't require additional uncertainty treatment.

Both source and pinch magnetic fields are generated by solenoid magnets, whose field strengths can be configured by the applied electric current. The systematic uncertainty on both fields is assessed by comparing reference measurements to a corresponding magnetic field simulation. The relative difference between the measurement and the simulation is used as systematic uncertainty for all magnetic field configurations, i.e. applied electric currents.

The magnetic field in the analyzing plane can be measured with a condensed krypton source placed in the active flux tube volume. Such an *in-situ* measurement of B_{ana} took only place after the second measurement campaign and was thus not available for the analyses in this work. In any case, such a calibration measurement cannot be accomplished during neutrino-mass campaigns. Therefore, an extensive magnetic field model within the simulation software *Kassiopeia* is consulted. The simulation is complemented by high-precision Bartington magnetometers, that are arranged on the outside of the main spectrometer near the analyzing plane. The deviation between measured and simulated magnetic field *outside* the active flux tube is used as an estimate for the systematic uncertainty on the simulated value *inside* the flux tube, i.e. B_{ana}.

Even though uncorrelated, the systematic uncertainties on all magnetic fields are treated simultaneously as they all require thousands of re-calculations of the response function. For the propagation to the integral spectrum, an ensemble of randomized magnetic field values is drawn from a Gaussian distribution. The resulting ensemble of integral spectra is then used to estimate the spectral covariance matrix.

4.9 Retarding potential

The high-voltage, that defines the retarding potential of the main spectrometer, is continuously monitored by a high-voltage divider with a precision at the part-per-million level [92]. Thanks to this extraordinary high precision, the systematic uncertainty on the absolute high-voltage scale is negligible for the neutrino mass analysis [42].

To enable run combination through stacking, each retarding potential set point has to be reproduced from scan-to-scan as good as possible. To first order, scan-wise variations of retarding potential values translate into an decrease in energy resolution by $\sigma(qU)$. If unaccounted in the analysis, this leads to a neutrino-mass bias of $\Delta m_\nu^2 \approx -2\sigma^2$. In the first two measurements campaigns the retarding potential could be reproduced within a few meV. The influence on the neutrino mass was therefore negligible.

4.10 Background

The background model consists of three components: A dominant steady-state background rate and two smaller components: one retarding potential dependent, one scan-step-duration dependent. The underlying physical processes of each background component are described in section 2.2.4. All three contributions come with their own systematic uncertainty, that are addressed in the following sections, respectively.

4.10.1 Steady-state background: Non-Poisson over-dispersion

The steady-state background rate B_{base} is included as a nuisance parameter in the spectral analysis. Thus, a systematic uncertainty on the absolute scale of this background component doesn't require further treatment.

However, as described in section 2.2.4, a significant fraction of the steady-state background doesn't follow the expected Poisson distribution. To extract the actual distribution, the rates of all scan-steps above the tritium endpoint are analyzed for each measurement campaign respectively. The background rate over-dispersion is quantified in terms of a *Non-Poisson factor*

$$f^2_{\text{Non-Poisson}} = \frac{\sigma^2_{\text{Gauss}}}{\sigma^2_{\text{Poisson}}} \tag{4.9}$$

with the observed variance σ^2_{Gauss}, extracted from a Gaussian fit, and the expected Poisson variance $\sigma^2_{\text{Poisson}}$. The spectral covariance matrix is calculated as

$$M_{\text{Non-Poisson}} = \sqrt{B_{\text{base}}\vec{t}}\,(f^2_{\text{Non-Poisson}} \cdot \mathbb{1})\sqrt{B_{\text{base}}\vec{t}'} \tag{4.10}$$

with the scan-step duration $\vec{t}$ and the identity matrix $\mathbb{1}$. As the Non-Poisson background component is uncorrelated from scan-step to scan-step, $M_{\text{Non-Poisson}}$ comprises only non-zero entries on its diagonal. Thus, $M_{\text{Non-Poisson}}$ effectively increases the statistical uncertainty on the steady-state background.

4.10.2 Scan-step-time-dependent background rate

The scan-step-duration-dependent background originates from electrons that are stored in a penning trap between the pre- and main spectrometer [76]. As discussed in section 2.2.4, this effect increases the background rate linearly over the duration of a scan-step. Central value and uncertainty on s_{time} are obtained from the analysis of tritium data: The time evolution of the rate within a scan-step is analyzed in bins of 1 s. All scan-steps are fit simultaneously with a linear model, containing a common s_{time} and individual rate offsets for all scan-steps.

The systematic uncertainty $\sigma(s_{\text{time}})$ from the linear fit is accounted for with a covariance matrix in the spectral analysis. The covariance matrix is calculated in the usual manner: An ensemble of background spectra is calculated, drawing random values of s_{time} from a Gaussian distribution with $\sigma = \sigma(s_{\text{time}})$ and $\mu = s_{\text{time}}$. As an independent cross check, s_{time} can alternatively be included as a nuisance parameter in the spectral analysis. In this case, Δs_{time} is incorporated in a Gaussian pull term in the χ^2 function

$$\chi^2_{\text{pull}} = \left(\frac{\mu - s_{\text{time}}}{\sigma(s_{\text{time}})}\right)^2. \tag{4.11}$$

4.10.3 Retarding-potential-dependent background rate

To-date, no significant retarding-potential-dependent background rate near the tritium endpoint has been found. However, an unaccounted s_{qU} (equation (2.31)) could bias the neutrino mass. Constraints $\sigma(s_{\text{qU}})$ can come from dedicated background measurements or directly from tritium scans. The options are discussed in the following.

4.10.3.1 External constraints from background campaigns

Dedicated background measurements with decoupled WGTS can potentially provide the strongest constraints on s_{qU}. These measurements are conducted with closed valves to the source section, effectively removing all β-electrons. With only background electrons left, s_{qU} can be measured over a large retarding potential interval extending up to several keV below the endpoint [93].

However, the background rate in KATRIN changed significantly over the past years [75]. This can be attributed partly to changes in the experimental setup, such as improved vacuum conditions, and partly to unknown reasons.

Therefore, it's crucial to only consult external $\sigma(s_{\mathrm{qU}})$ from measurements with similar background conditions as in the respective neutrino-mass campaign.

External constraints can be propagated to the integral spectrum through a covariance matrix. An ensemble of background spectra is generated, using randomly drawn values for s_{qU} as input. The external constraint on s_{qU} is used as standard deviation for the underlying Gaussian probability density function.

4.10.3.2 Retarding-potential dependence as nuisance parameter

The retarding-potential dependency of the background rate can also be directly inferred within the spectral analysis. The analysis model is extended by s_{qU} (see section 2.2.4) as an additional nuisance parameter. Within a tritium scan, the background is mostly determined from scan-steps above E_0. For lower (less negative) retarding potentials, signal-to-background ratio quickly start to rise above unity, which limits the available retarding potential range which is sensitive to s_{qU}. Moreover, the measurement time in the background region is restricted to $\approx 20\,\%$ of the total measurement time. As a consequence, constraints from tritium data are relatively poor compared to external constrains from dedicated background measurements. The weaker the constraints on s_{qU}, the larger is the contribution to the m_ν^2-systematic uncertainty budget. If available, external constraints can be included as a Gaussian pull term in the χ^2 function

$$\chi^2_{\mathrm{pull}} = \left(\frac{s_{\mathrm{qU}}}{\sigma(s_{\mathrm{qU}})} \right)^2 . \tag{4.12}$$

4.10.3.3 Constraints from simulated tritium data

As described in the preceding paragraph, the sensitivity on s_{qU} is relatively poor if it's inferred within the neutrino-mass analysis. On top of the limited background statistics within tritium data, the neutrino mass and endpoint are correlated with s_{qU} (see section 9.9) additionally limiting the s_{qU} sensitivity. If no significant retarding-potential dependency is observed in the data, the scan-steps above the endpoint can also be analyzed separately focusing solely on s_{qU}.

Instead of analyzing the actual background data, 10^4 background spectra are simulated in order to avoid using the same data twice. The MC spectra are randomly fluctuated around the average (steady-state) background rate according to their associated uncertainties. The Non-Poisson background component is taken into account. A linear function, anchored at the scan-step closest to the endpoint, is then fit to each randomized background spectrum. As a next step, the 10^4 hypothetical s_{qU} values are used to calculate retarding-potential-dependent background spectra, extrapolated to the entire analysis interval. The latter serve as input samples for a covariance matrix.

This method also allows to include external slope constraints by using it as a cut-off threshold. Every sample fit with $s_{\mathrm{qU}} > \sigma(s_{\mathrm{qU}})$ is discarded from the set. Consequently, the covariance matrix is calculated using only a subset of all samples.

4.11 Detector efficiency

The number of detected signal electrons scale linearly with the detector efficiency ϵ_{FPD}. As the signal normalization is a nuisance parameter in the spectral analysis, an uncertainty on the absolute efficiency value is absorbed in the fit. However, a series of effects (intrinsic pixel differences, ROI, pile-up, back-scattering) lead to different efficiencies for each pixel and qU. The recorded spectra are corrected for these effects.

The relative uncertainty on the efficiency correction $\Delta\epsilon_{\mathrm{FPD}}$ is incorporated in a covariance matrix M_{FPD}. $\Delta\epsilon_{\mathrm{FPD}}$ is assumed to be energy independent and uncorrelated for all scan-steps. Therefore, the fractional efficiency covariance matrix has only diagonal elements:

$$M^{\mathrm{FPD}}_{\mathrm{frac.}} = \Delta\epsilon^2_{\mathrm{FPD}} \cdot \mathbb{1}. \tag{4.13}$$

Chapter 5

First measurement campaign

This chapter introduces the reader to the first science run of the KATRIN experiment, short KNM1. KNM1 took place in spring 2019 from April 10 to May 13. For the first time the source was operated at high tritium activity (2.45×10^{10} Bq), which makes KNM1 the first campaign with considerable neutrino-mass sensitivity.

The data taking procedure and the associated measurement time distribution is described in section 5.1. Section 5.2 presents the golden scan and pixel selection based on data-quality cuts.

Prerequisite for a stacked-scan uniform analysis is an excellent stability of the relevant slow control parameters. Sections 5.4 - 5.9 evaluate the stability of column density, molecular gas composition, electric and magnetic potentials and detector efficiency. An overview of all relevant parameter is given in appendix C. The background conditions are discussed in section 5.10.

5.1 Measurement time distribution

The integral β-spectrum was measured in 39 scan steps in an energy range of $[E_0 - 93\,\text{eV}, E_0 + 47\,\text{eV}]$[1]. The time spent at each scan step is defined by the measurement-time distribution depicted in figure 5.1. With 274 recorded scans, each lasting approximately 2 hours, data with a total net measurement time of 541.7 hours was collected.

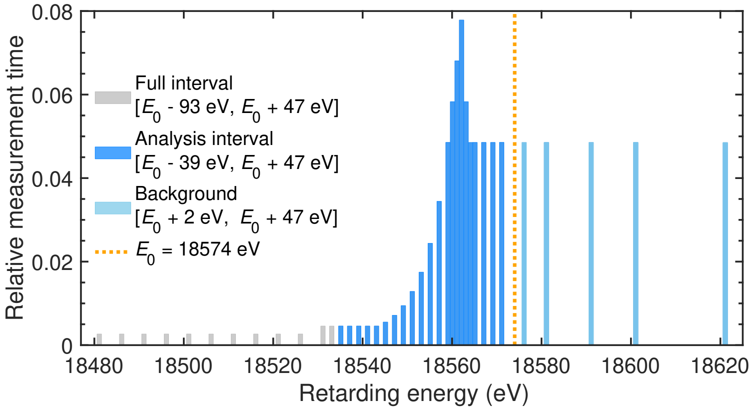

Figure 5.1: Measurement-time distribution (MTD) for KNM1. The full measurement interval consists of 39 scan steps (grey), from which 27 are selected for the analysis (dark and light blue). Within the analysis interval, 26 % of the measurement time is spent at retarding energies above the endpoint to determine the background rate. The most time is spent in the region, which is most sensitive to the neutrino-mass signal.

The following analyses restrict the energy range to 27 scan steps within $[E_0 - 39\,\text{eV}, E_0 + 47\,\text{eV}]$, if not stated

---

[1] $E_0 = 18\,574\,\text{eV}$ is used as reference value

otherwise. The analysis interval is illustrated in figure 5.1 in light and dark blue coloring. This narrower interval is chosen as such that it is dominated by statistical uncertainties. Within the analysis interval, the measurement time amounts to 521.7 net hours.

Most of the time is spent in the region around 14 eV below E_0, in which the neutrino-mass signal is most prominent[2]. The five scan steps with retarding energies above the endpoint are devoted to determine the background rate. They make up 26 % of the measurement time within the analysis interval.

Subsequent to each scan, the rate was measured deep into the tritium spectrum at $qU = E_0 - 203\,\text{eV}$ for 297 s. Utilizing the high statistics of $\approx 5.6 \times 10^3$ cps[3], this additional scan step was used to monitor the rate stability.

5.2 Data selection

During KNM1, more data was recorded than eventually used for the spectral analyses. The selection of *good* data is based on strict quality-cuts, which address mostly the completeness of the meta data and the stability of the relevant slow-control parameters. In the following, the scan and pixel selections are presented.

5.2.1 Golden pixels

Based on strict quality cuts, 117 out of 148 FPD pixels were selected for the final analysis. Consequently, 31 pixels (21 %) were excluded. The pixel selection is illustrated in figure 5.2. The full list is given in appendix D.3.

Six pixels (97, 98, 110 - 122) revealed an enhanced intrinsic noise level. Four other pixels (99, 100, 112, 123) were shadowed by the FBM that slightly reached into the flux tube. Lastly, 21 pixels (124 - 130, 134 - 147) were excluded due to a misalignment between the flux tube and the FPD.

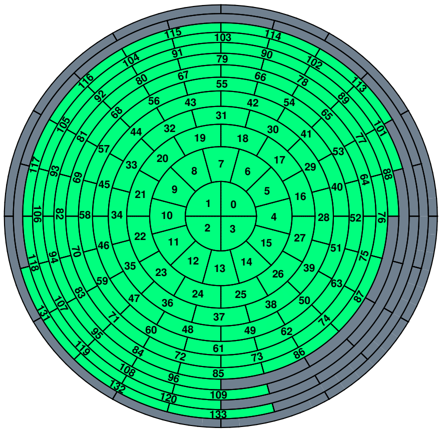

Figure 5.2: Golden pixel selection for KNM1. 117 out of 148 FPD pixels are selected for the analysis.

5.2.2 Golden scans

For the spectral analyses, 274 out of 373 tritium scans were selected. The golden scan list is defined in appendix D.1.

All 87 scans, that were recorded at a suboptimal optimal rear-wall bias voltage $R_{\text{RW}} \in [175\,\text{mV}, 300\,\text{mV}]$ are not included in the final analysis. Moreover 12 scans are excluded due to missing meta data, early terminated data taking or unstable source parameters.

---

[2] Given the KNM1 configuration, the neutrino-mass signal peaks at $qU - E_0 = -10\,\text{eV}$, assuming $m_\nu^2 = 0.1\,\text{eV}^2$.

[3] Median count rate over the course of KNM1.

5.3 Molecular gas composition

KNM1 was the first measurement campaign with a high tritium purity $\varepsilon_T = 97.56\,\%$. The molecular gas was mostly composed of T_2 ($c_{T_2} = 95.25\,\%$) with smaller admixtures of HT ($c_{HT} = 3.54\,\%$) and DT ($c_{DT} = 1.08\,\%$). The stable isotopologues (D_2, HD, H_2) were only present in trace amounts.

The tritium purity as well as the molecular composition of the tritium gas vary between the batches provided by the Tritium Laboratory Karlsruhe. Details on the reprocessing and purification procedure can be found in [94]. Figure 5.3 shows the time evolution of ε_T and the concentrations of the active isotopologues. The noticeable jumps coincide with the injection of a new batch in the KATRIN source system.
The tritium purity varied from scan to scan up to 1.4 percentage points. The molecular concentration of T_2 exhibits peak-to-peak fluctuations of 2.7 percentage points.

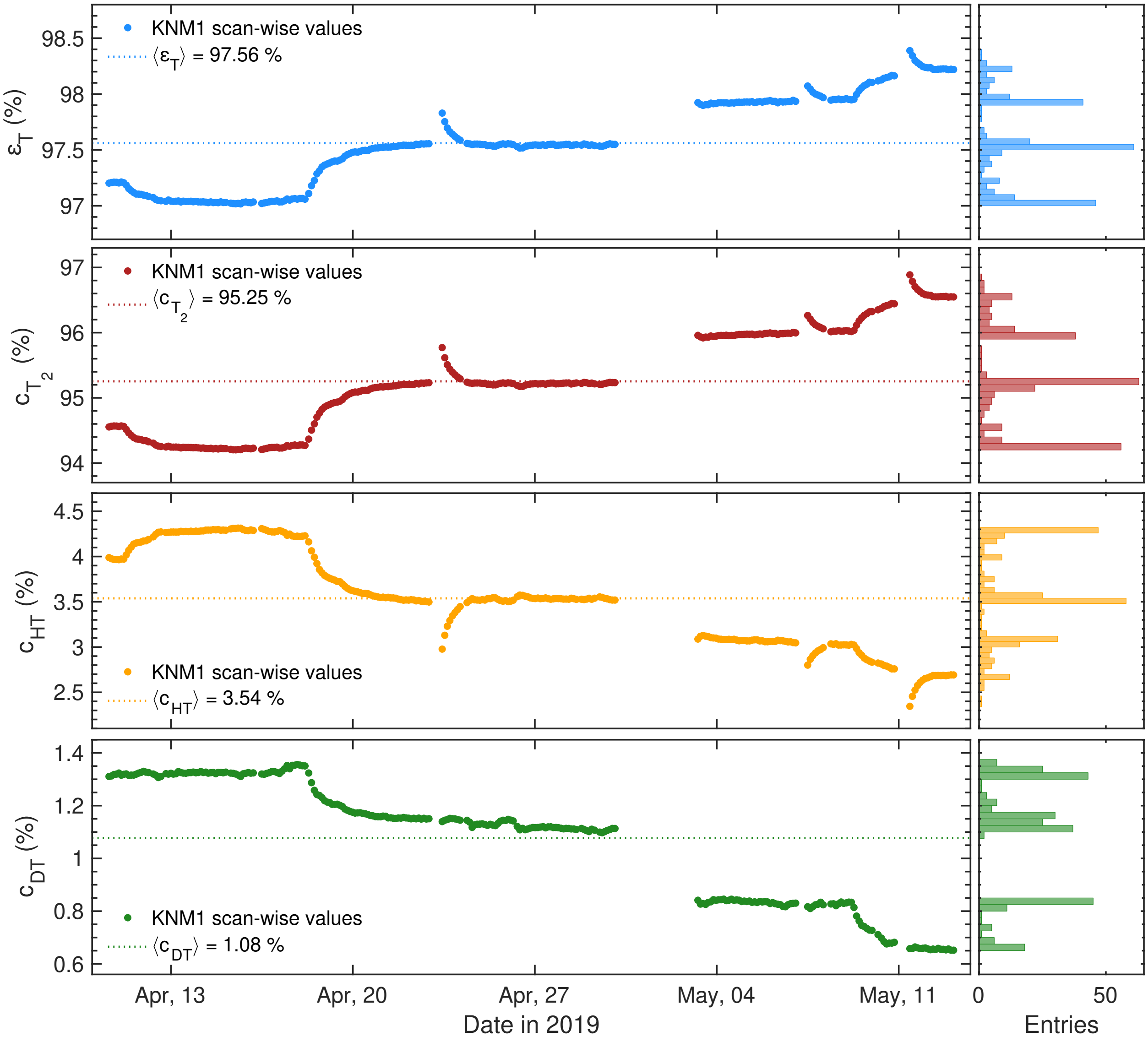

Figure 5.3: Scan-wise atomic tritium purity (top) and molecular concentrations of tritiated hydrogen isotopologues (bottom three) in the source during KNM1. The visible kinks originate from the injection of a fresh tritium batch into the source.

5.4 Column density

KNM1 was the first time that the source system and the injection capillaries were exposed to large amounts of tritium. Radio-chemical reactions between the tritium molecules and the stain-less steel surfaces lead to the production of CO and tritiated hydrocarbons [95]. The carbon compounds thereupon condensed on the cold surfaces, impeding the tritium flow through the capillaries. As a result, the column density drifted over time at constant tritium injection pressure and the nominal value could not be established.

To improve the stability during this burn-in period, the column density was lowered to $\rho d = 1.11 \times 10^{17}$ molecules/cm^2, which corresponds to 22 % of its nominal value. The scan-wise column density is shown in figure 5.4. As can be seen, the tritium injection pressure was increased several times over the course of KNM1, to minimize scan-wise column density variations. Both measures archived a scan-wise stability of $\sigma(\rho d) = 0.8\,\%$. The implication of the column density drift on the stacked-scan analysis is found be to negligible (see section 8.2.1). The uncertainty on the absolute value of $\rho d \sigma_{\text{inel.}}$ is 0.85 %, which is propagated as a systematic uncertainty in the analysis.

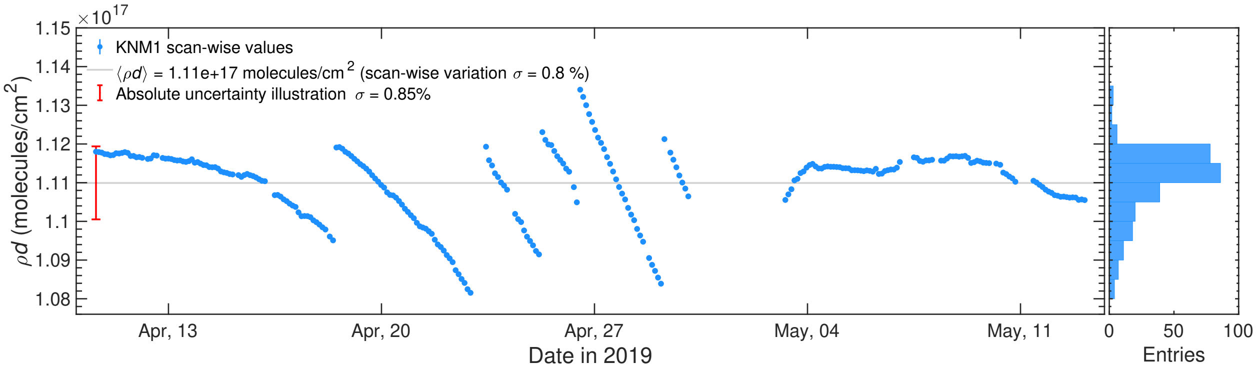

Figure 5.4: Scan-wise mean column density as a function of time in KNM1. The visible drift was caused by radio-chemical reactions between tritium molecules and the stain-less steel surfaces in the source system. A relative stability of 0.8 % could be archived by increasing the tritium injection pressure several times. The uncertainty on the absolute column density is 0.85 %.

5.5 Source activity stability within a scan

Due to time-wise changes in the column density and tritium purity, the source activity was not perfectly constant in KNM1. While the scan-wise stability of ρd and ε_T was discussed in the previous sections 5.3 and 5.4, this section addresses the average activity stability within a scan. As described in section 4.4.2, an activity variation within a scan can lead to a shape distortion of the integral spectrum. To compensate this effect, activity variations within a scan are accounted for in the systematics budget. Figure 5.5 show the relative source activity variation of all golden scans and scan-steps. Scan-wise differences are eliminated by normalizing the scan-wise activities to the global mean activity in KNM1, following equation equation (4.5). On average, $\hat{A}_{\text{source}}$ was stable at the $\langle \sigma^k_{\text{sys}} \cdot \sqrt{274} \rangle =$ 0.9% level within a scan. As the spectra of all golden scans are combined into a single effective spectrum by stacking, some scan-wise variation will average out. The relevant number for the uncertainty propagation is therefore the error of the mean (equation (4.6)), which is on average $\langle \sigma^k_{\text{sys}} \rangle = 0.006\,\%$. Correlations among the scan-steps are neglected in the KNM1 analysis.

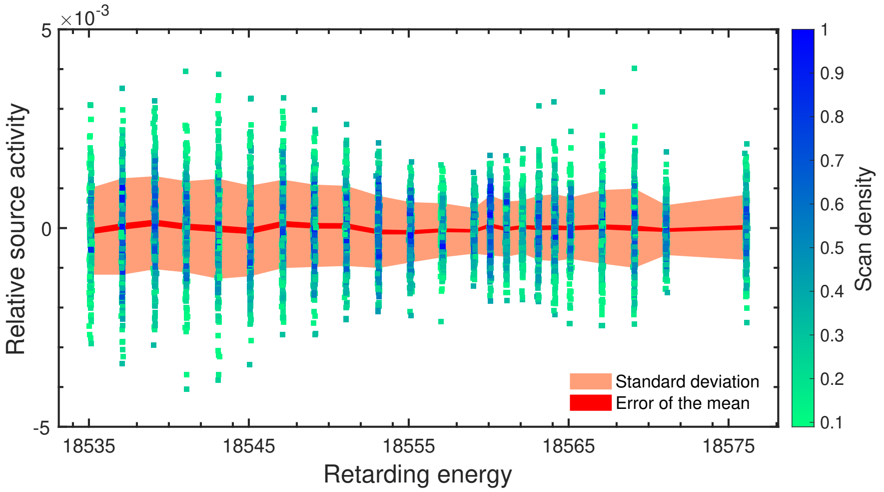

Figure 5.5: Source activity variation for all scan-steps in KNM1. To compensate overall normalization effect, the scan-wise activities are normalized to the global mean activity, according to equation (4.5). On average, the activity varied within a scan-step by 0.9 % for 274 golden scans.

5.6 Source potential

As described in section 4.3, the operation at optimal rear wall bias voltage is essential to establish a homogeneous electric source potential. Over the course of KNM1, the rear wall bias voltage was changed several times $U_{\mathrm{rw}} \in [-183\,\mathrm{mV}, -149\,\mathrm{mV}, 175\,\mathrm{mV}, 300\,\mathrm{mV}]$ to find the most stable run condition. The near-time evaluation of the tritium endpoint in the full interval as well as the analysis of the plasma-induced electric current on the rear wall revealed an optimal bias voltage around $U_{\mathrm{rw}} \approx -150\,\mathrm{mV}$. Within this configuration, no significant radial endpoint dependence was found. To have similar and stable source potentials for all scans, only scans with $U_{\mathrm{rw}} = -183\,\mathrm{mV}$ (19 scans) and $U_{\mathrm{rw}} = -149\,\mathrm{mV}$ (255 scans) are selected for the golden scan list. No further long-term plasma potential drifts were found (opposed to KNM2).

Subsequent to the neutrino-mass measurement, krypton measurements were performed to evaluate the longitudinal plasma potential homogeneity [88]. Ideally, the source should be operated under the same conditions as in the respective measurement campaign. Due to technical reasons, krypton measurements had to be performed at a higher source temperature (100 K) to avoid freeze-out on the stainless-steel surfaces. As the increased temperature is known to strongly suppress the electron-ion recombination rate, plasma effects are expected to be more prominent in krypton mode compared the tritium-only mode [65, 96]. Moreover, the column density was increased to 30 % of its nominal value. In addition to these different source conditions, which need to be accounted for by plasma simulations, several systematic uncertainties played an important role. Firstly, the reference line width of the L_3-line could not be determined to the desired accuracy. Moreover, Δ_{10} could not be assessed directly from the krypton measurement, because of systematic uncertainties on the energy-loss function for krypton electrons with energies around 32.2 keV. As the electron gun, used in the first two measurement campaigns, was only able to reach energies up to 21 keV [68], the energy dependence of the energy-loss function could not be investigated experimentally for the entire energy range.

Due to these reasons, the energy broadening $\sigma_0 < 75\,\mathrm{mV}$ and energy-loss shift $\Delta_{10} < |-66\,\mathrm{mV}|$ extracted from the krypton measurement are considered as conservative upper limits for the neutrino-mass analysis [97]. Due to the immaturity of the plasma model, the large systematic uncertainties in the krypton measurements and the small influence on the neutrino mass, the longitudinal plasma uncertainties were not included in the systematic uncertainty treatment of KNM1.

5.7 Retarding potentials

The KATRIN experiments employs a setup of two MAC-E filter: the pre- and main spectrometer (section 2.1). Their retarding potentials are discussed in the following.

5.7.1 Pre-spectrometer

The pre-spectrometer was set to a retarding potential of $-10\,\mathrm{kV}$ to stop low-energy electrons with $E_{\mathbf{kin.}} \leq 10\,\mathrm{keV}$ from reaching the main spectrometer.

As described in section 2.2.4, the combination of two MAC-E filters leads to a formation of a penning trap between the spectrometers. Electron catchers are installed to remove the trapped electrons after every scan-step. However, it was discovered only after the second measurement campaign, that the penning trap still causes an increase of background rate within each scan step (sections 4.10.2 and 5.10.5).

5.7.2 Main spectrometer

The voltage applied to the main spectrometer was continuously monitored with a high-voltage divider with ppm precision. Figure 5.6 shows the high-voltage variation within each scan-step for all golden scans. On average, the high-voltage set points could be reproduced within $\sigma = 34\,\mathrm{mV}$. The variation of the retarding potential within a scan step was on average 15 mV, which is found to be negligible.

The radial homogeneity of the retarding potential is displayed in figure 5.7 (a). The field map is obtained with a Kassiopeia simulation as it cannot be directly measured during tritium scans. Among the active pixels, qU varied within $\sigma = 33\,\mathrm{mV}$.

Moreover, inner electrode system of the main spectrometer was configured to always have a 200 V more negative potential than the retarding potential in order to hinder charged particles from the spectrometer surface to reach the active flux tube volume.

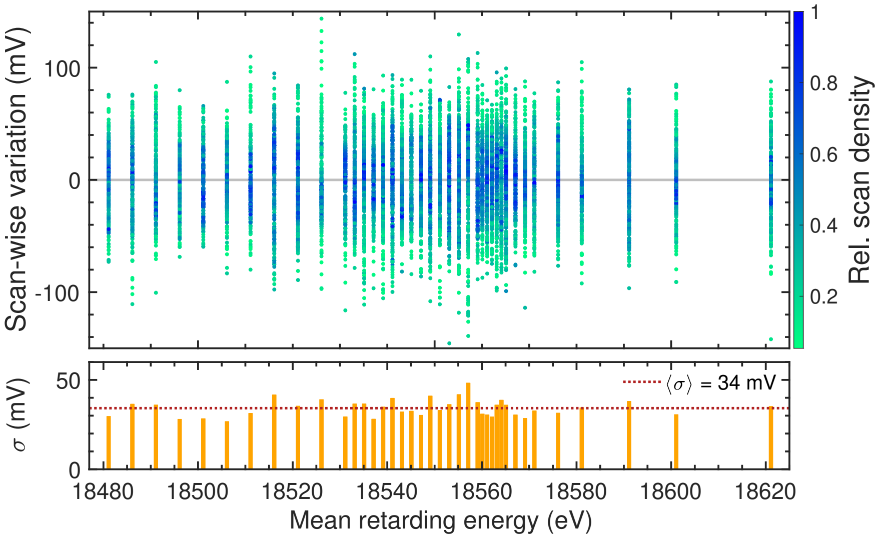

Figure 5.6: High-voltage reproducibility in KNM1. To perform the analysis on the stacked spectrum, the retarding potential values of each scan-step have to be reproduced from scan to scan as precisely as possible. The top plot shows the actual measured retarding potential values of all golden scans. The bottom plots states the scan-wise standard deviation for each scan step. During KNM1, the mean retarding potential variation per scan-step were $\sigma = 34\,\mathrm{mV}$.

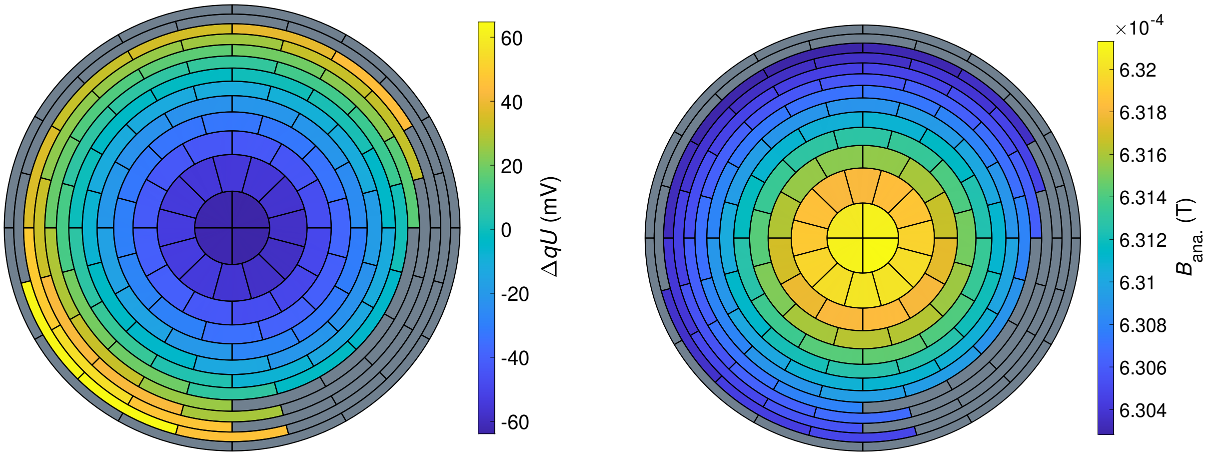

(a) Retarding potential offsets (b) Magnetic fields in the analyzing plane

Figure 5.7: Potentials in the analyzing plane as they are seen by the FPD. Pixels that are not included in further analyses are colored in grey. The pixel-wise retarding potentials (a) vary within $\sigma = 33\,\text{mV}$ from pixel to pixel. The magnetic field strengths in the analyzing plane (b) exhibit variations within $\sigma = 5.3 \times 10^{-6}\,\text{T}$.

5.8 Magnetic fields

As described in section 4.8, the magnetic field strength inside the active flux tube volume cannot be monitored continuously throughout the measurement campaign. Instead the magnetometer grid around the main spectrometer vessel collects input data for a precise magnetic field model [98]. The magnetic field configuration was the following: $B_{\text{source}} = 2.52\,\text{T}$, $B_{\text{ana.}} = 6.31 \times 10^{-4}\,\text{T}$ and $B_{\text{max.}} = 4.23\,\text{T}$. All magnetic fields are assumed to be constant over time [98].

The radial distribution of the magnetic field in the analyzing plane is shown in figure 5.7 (b). Among all active pixels, the $B_{\text{ana.}}$ varied within $\sigma = 5.3 \times 10^{-6}\,\text{T}$.

5.9 Detector efficiency

The mean FPD efficiency is estimated to be $\epsilon_{\text{FPD}} \approx 0.95$. The data is corrected for small efficiency differences between pixels and retarding energies, that originate from intrinsic pixel differences, ROI, pile-up and backscattering. All individual corrections are $<< 0.1\,\%$ [99]. The FPD region-of-interest (ROI) is fixed to $14\,\text{keV} \leq E < 32\,\text{keV}$, regardless of the main spectrometer retarding potential qU. While the intrinsic FPD background contribution is independent of qU, the contribution of other background sources and the tritium signal are not. As a consequence the ROI coverage as well as the signal-to-background ratio changes with qU. To compensate these effects, a relatively wide ROI was chosen.

5.10 Background

Five scan steps in the MTD (section 5.1) are located above the tritium endpoint $qU > 18\,574\,\text{eV}$. They are used to monitor the background rate. The average count rate of these scan steps considering all active pixels and golden scans is 292 mcps. In the following sections 5.10.1 to 5.10.3, different aspects of the steady-state background rate are discussed: Radial distribution (section 5.10.1) and Non-Poission over-dispersion (section 5.10.2) are derived from the five scan steps above E_0. Moreover, a discussion on signal-to-background ratio based on simulation results are presented in section 5.10.3. Other backgrounds, such as the scan-step-time dependent background and retarding-potential-dependent background, are discussed in section 5.10.5 and section 5.10.5, respectively.

5.10.1 Steady-state background: Radial distribution

Due to the generation mechanism of Rydberg electrons, one of the dominant background sources, the steady-state background rate is not expected to be uniform over the FPD [100]. As can be seen in figure 5.8, the background rate increases for increasing radial pixel position.

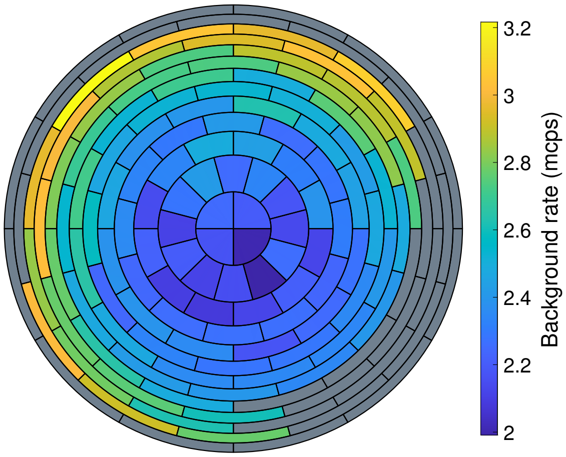

Figure 5.8: Background rate distribution over all active FPD pixels in KNM1. Excluded pixels are colored in grey. The background rate is estimated as mean count rate considering the five scan steps above E_0 of all golden scans. Pixels at large radii measure a higher background rate than pixels located in the center of the detector. This radial pattern is expected, because a large fraction of background electrons stems from α-decay on the inner surfaces of the main spectrometer [100]. The cumulative background rate over all active pixel amounts to 291.4 mcps.

5.10.2 Steady-state background: Non-Poisson over-dispersion

As described in section 2.2.4, the steady-state background counts fluctuate more than expected from a Poisson distribution. This over-dispersion is quantified as a Non-Poisson factor in equation (4.9), which is the ratio between observed and statistically expected standard deviation.

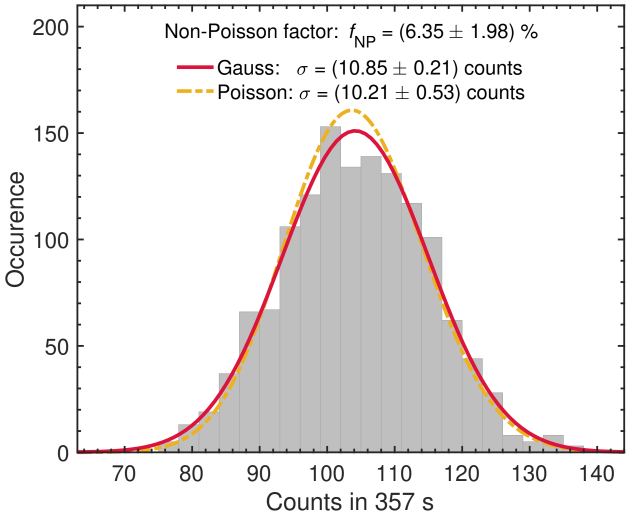

Figure 5.9: Background count distribution in KNM1 considering five scan steps above E_0 and all golden scans and pixels.

Figure 5.9 shows the background count histogram, obtained from the five scan steps above E_0 within all golden scans and pixels. The scan-steps are corrected for slightly different measurement times. The distribution is fit twice: Once with a Gaussian model and once with a Poisson model. The Non-Poisson background contribution is $f_{\text{Non-Poisson}} = (6.25 \pm 1.98)\,\%$[4]. The uncertainty is estimated via the boot-strapping technique.

5.10.3 Steady-state background: Signal-to-background ratio

All tritium induced electrons are regarded as signal, whereas all other electrons are considered background. The signal-to-background $R_{\text{sig.}}/R_{\text{bkg.}}$ ratio varies strongly as a function of retarding energy. While the steady-state background rate is expected to be constant, the number of expected signal electrons grows steeply with decreasing qU. As a consequence, the signal-to-background ratio peaks at the scan step with lowest retarding energy $R_{\text{sig.}}/R_{\text{bkg.}} = 68.6$ (analysis interval), whereas it practically vanishes for scan steps close and above the endpoint. The equilibrium between signal and background electrons is observed at $qU - E_0 \approx -12\,\text{eV}$.

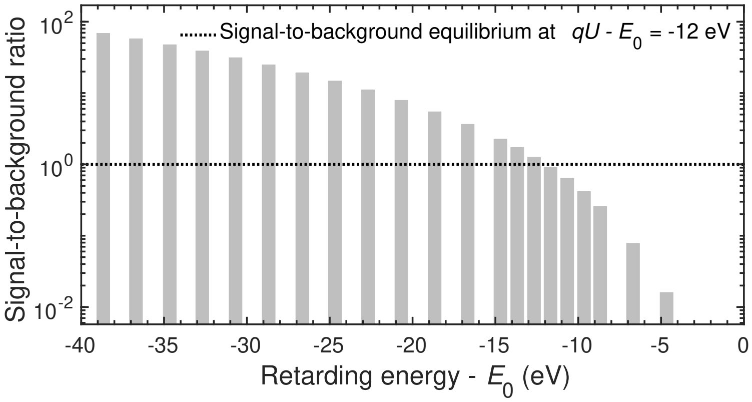

Figure 5.10: Signal-to-background ratio in KNM1. The ratio is increasing with decreasing retarding energy, due to the combination of constant background rate and increasing β-spectrum rate. Given the observed background level of 292 mcps and a source activity of 2.45×10^{10} Bq, the equilibrium between signal and background counts is found around $qU - E_0 = 12\,\text{eV}$. The ratio is calculated with the KNM1 Twin simulation, described in section 8.1.

5.10.4 Retarding-potential-dependent background

The hypothetical retarding-potential-dependency of the background rate is investigated by fitting a linear function to the scan steps above the tritium endpoint. The fit, visualized in figure 5.11, finds a positive slope $s_{\text{qU}} = (47 \pm 51)\,\text{mcps/keV}$ at low significance ($< 1\sigma$).

As the sensitivity on the background slope is relatively poor, an external constraint from a dedicated background measurement is consulted. Completed in 2018, the background measurement during the First Tritium campaign (FT) is the latest reference prior to KNM1. The measurement range extended down to 1.6 keV below the endpoint so that the slope could be determined with much higher precision than in KNM1. The observed slope is consistent with zero $s_{\text{qU}} = (4 \pm 5)\,\text{mcps/keV}$ [75]. However, for yet unknown reasons the steady-background rate per active pixel was approximately 7 % higher than in KNM1. As this might point towards changed background sources with a potentially different qU-dependence, it is debatable whether the FT constraint can be transferred to the KNM1 analysis. Moreover, only a small fraction of the large measurement interval in FT is relevant for the neutrino-mass analysis at hand. For the mentioned reasons, a conservative upper limit of $\sigma(s_{\text{qU}}) = 15\,\text{mcps/keV}$ is used in KNM1, which corresponds to the threefold uncertainty of FT.

---

[4] Background specialists in KATRIN found $f_{\text{Non-Poisson}} = 6.4\,\%$ in a similar analysis. For consistency among fitting teams, their value is used for the spectral analysis.

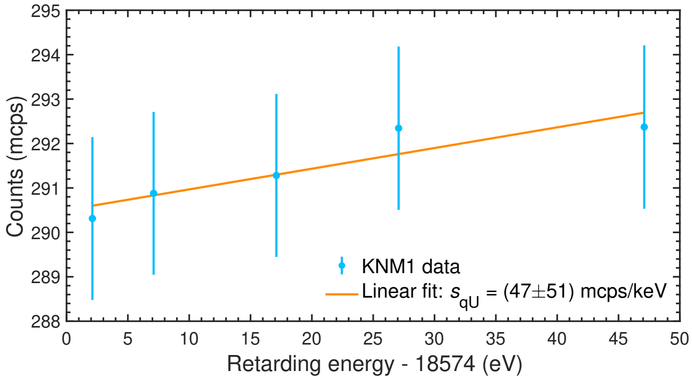

Figure 5.11: Retarding-potential-dependent background in KNM1. A linear fit to all scan steps above the tritium endpoint is performed. On top of statistical uncertainties also the non-Poisson over-dispersion is taken into account. The fitted slope is not significant ($< 1\sigma$).

The hypothetical qU-dependence is accounted for in the systematic uncertainty budget following the strategy in section 4.10.3.3. Randomized background simulations are fit using a linear regression as displayed in figure 5.12 (left). All slopes that are smaller than the FT constraint $s_{qU} \leq 15\,\text{mcps/keV}$ (figure 5.12 (right)) are then propagated into a background covariance matrix for the full analysis interval.

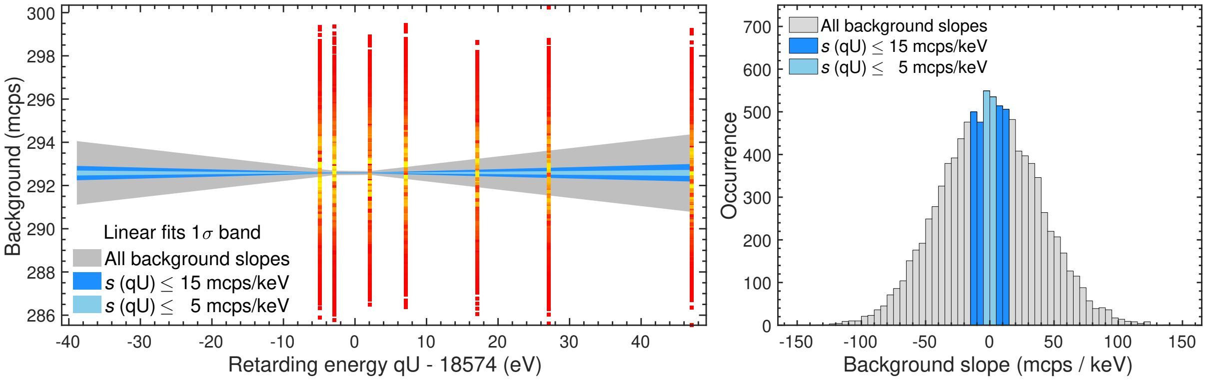

Figure 5.12: The possible retarding-potential dependency of the background rate is incorporated in the systematic uncertainty budget following the method of section 4.10.3.3. **Left**: Randomized background spectra are generated using the average steady-state background rate and the associated uncertainties. In addition to the 5 scan steps above the endpoint, also two scan steps with low signal-to-background ratio are included in the simulation. All 1×10^4 MC samples are displayed as small squares. The coloring indicates the sample density from red (low density) to yellow (high density). Each sample is fit using a linear regression. **Right:** The fitted slope values are then propagated into a covariance matrix. Using the slope constraint from FT, only $s_{qU} \leq 15\,\text{mcps/keV}$ are considered.

5.10.5 Scan-step-time dependent background

The scan-step-time-dependent background is neglected in the KNM1 analysis. This systematic effect was only discovered during KNM2, for which it is significant. For KNM1, the effect is compatible with zero. In the reanalysis, performed after the original publication, a time-wise background rate increase of $s_{\text{time}} = (2.2 \pm 4.3)\,\mu\text{cps/s}$ is taken into account.

Chapter 6

Second measurement campaign

This chapter introduces KATRIN's second science run, hereinafter abbreviated as KNM2. It took place in fall 2019 from September 27 to November 14[1]. Its key feature is the improved sensitivity compared to KNM1, reaching for the first time into the sub-eV regime. As the measurement phase was no longer limited to the burn-in configuration of KNM1, the column density could be substantially increased. As a result, an unprecedented tritium activity of 9.46×10^{10} Bq could be reached. Moreover, improved vacuum conditions lead to a background reduction from 292 mcps in KNM1 to 220 mcps in KNM2.

The measurement time distribution and data selection are presented in sections 6.1 and 6.2, respectively. Sections 6.3 to 6.5 and 6.7 to 6.9 and sections 6.6.1 to 6.6.3 examine the stability of the relevant experimental parameters. An overview of all relevant parameter is given in appendix C. Additionally, characteristic features and systematic uncertainties are discussed. The background is characterized in section 6.10.

6.1 Measurement time distribution

The measurement time distribution of KNM2 is displayed in figure 6.1. It consists of 38 scan-steps in an energy range of $[E_0 - 90\,\text{eV}, E_0 + 135\,\text{eV}]$[2]. With 361 tritium scans, each lasting approximately 2 hours, a total net. measurement time of 713.8 hours was collected. The analysis presented in this work is based on 28 scan steps

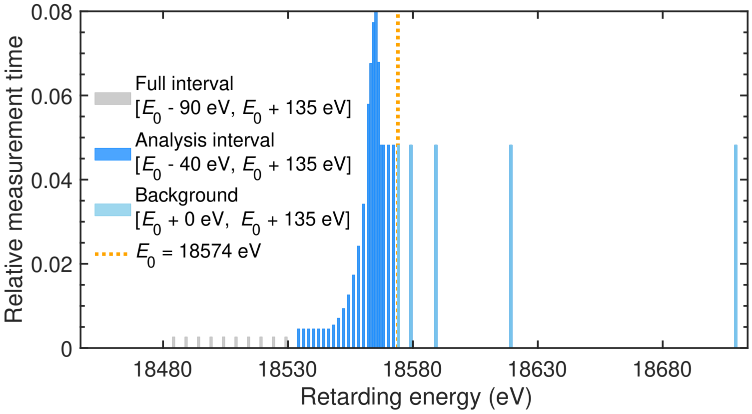

Figure 6.1: Measurement-time distribution (MTD) for KNM2. The full measurement interval consists of 38 scan steps (grey), from which 28 are selected for the analysis (dark and light blue). Within the analysis interval, 26 % of the measurement time is spent at retarding energies above the endpoint to determine the background rate. The most time is spent in the region, which is most sensitive to the neutrino-mass signal.

---

[1] Defined by date of first and last golden scan.

[2] $E_0 = 18\,574\,\text{eV}$ is used as reference value.

in the interval $[E_0 - 40\,\text{eV}, E_0 + 135\,\text{eV}]$, highlighted in blue colors in figure 6.1. The analysis range is selected so that the neutrino mass analysis is dominated by statistical uncertainties. The analysis interval comprises 694.3 net. hours.

Similar to KNM1, five data points are located above the tritium endpoint to determine the background rate. As the uncertainty on its retarding-potential-dependency turned out to be one of the largest systematic uncertainties in KNM1, the background range was extended up to 135 eV above E_0 in KNM2. The time spend in this region makes up 26 % of the time in the analysis interval. The analysis focusing solely on the background scan-steps is presented in section 6.10.

In addition to the 38 scan steps, that are displayed in figure 6.1, a scan-step at $qU = E_0 - 300\,\text{eV}$ was recorded to monitor the rate stability. Compared to KNM1, the HV set point of the rate monitor point reaches further into the tritium spectrum to take advantage of the high statistics $\approx 6.7 \times 10^4$ cps[3]. The analysis of the rate monitor point is presented in section 6.6.2.

6.2 Data selection

More data was recorded during KNM2 than eventually analyzed for the neutrino-mass. The selection of *good* data is based on strict quality-cuts, mostly focusing on the stability of the relevant slow-control parameters or completeness of the meta data. In the following, the scan and pixel selections are presented.

6.2.1 Golden pixels

Based on strict quality cuts, 117 out of 148 FPD pixels were selected for the final analysis. Consequently, 31 pixels (21 %) were excluded. The golden pixel numbers is given in E.3 and displayed in figure 6.2. The pixel selection is similar, but not identical to KNM1.

Six pixels (97, 98, 110 - 122) are excluded because of an enhanced intrinsic noise level. Different to KNM1, only one pixel (100) was shadowed by the FBM rather than two. This could be archived by an optimized FBM monitoring position. Moreover, 24 pixels (112, 113, 123 - 130, 134 - 147) are excluded due to the misalignment between the flux tube and the FPD.

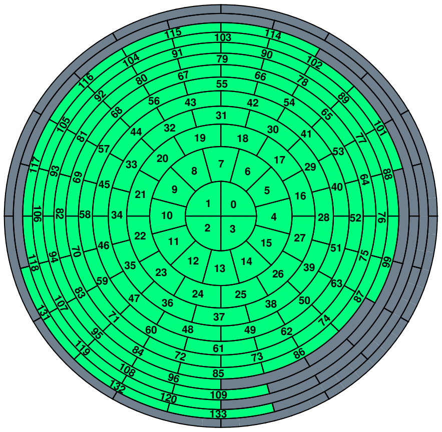

Figure 6.2: Golden pixel selection for KNM2. 117 out of 148 FPD pixels are selected for the analysis.

---

[3] Median over KNM2

6.2.2 Golden scans

For the spectral analyses, 361 tritium scans with stable run conditions were selected. The golden scan list is defined in appendix E.1. 36 scans were rejected. The most common reason for rejection was a malfunction of the LARA software, which lead to missing information on the isotopologue concentrations for the affected scans. Moreover, several scans were rejected due to short-term failures of the inner-electrode system.

6.3 Molecular gas composition

KNM2 was conducted with high purity molecular tritium gas $\varepsilon_\mathrm{T} = 98.63\,\%$. The gas is an admixture of T_2 ($c_{T_2} = 97.34\,\%$), HT ($c_{HT} = 2.28\,\%$) and DT ($c_{DT} = 0.31\,\%$). The relative contribution of T_2 is higher by 2 percentage points compared to KNM1. The time-wise evolution, displayed in figure 6.3, exhibits similar features as in KNM1. The kink-like structures indicate the injection of a fresh tritium batch into the WGTS.

The maximal variation from scan-to-scan were as small as 0.7 and 1.4 percentage points for ε_T and c_{T_2}, respectively.

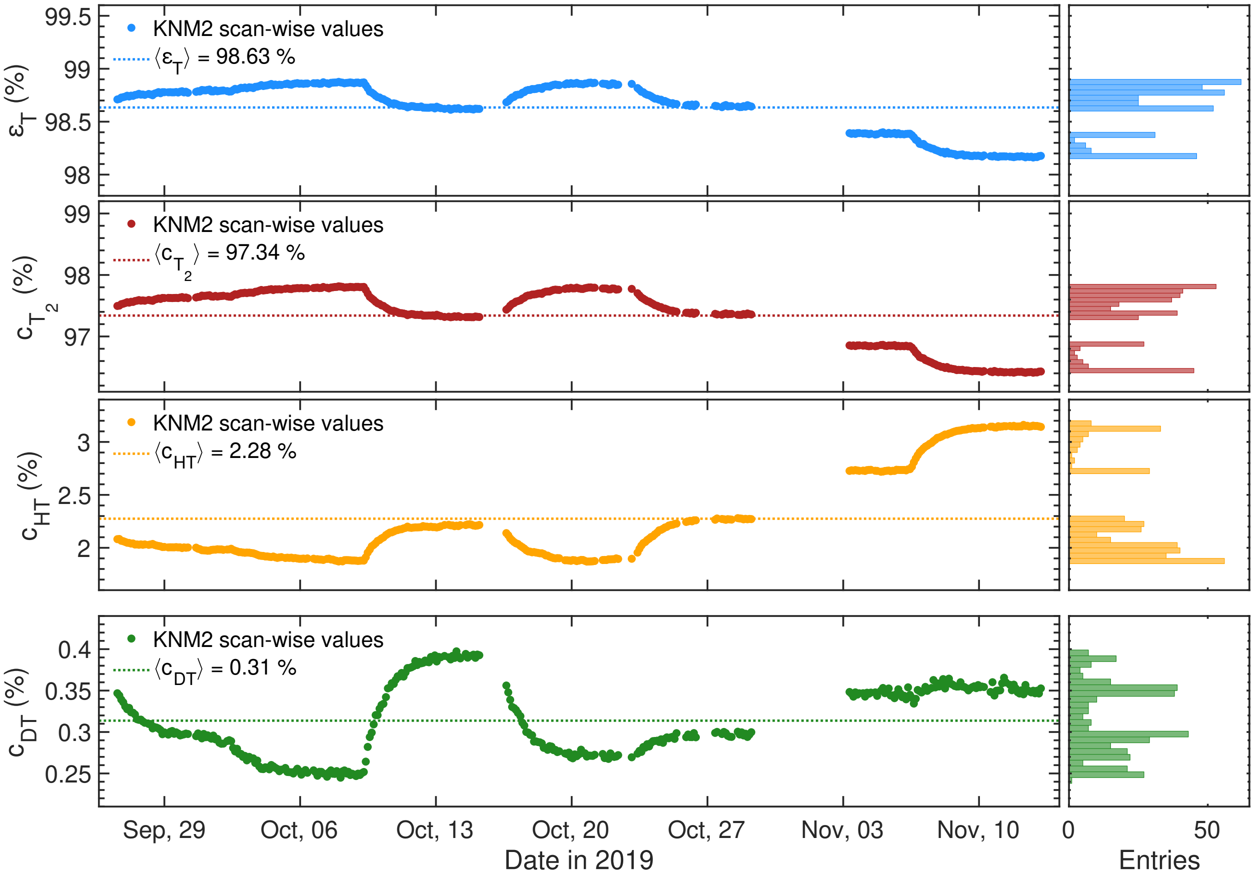

Figure 6.3: Scan-wise atomic tritium purity (top) and molecular concentrations of tritiated hydrogen isotopologues (bottom three) in the source during KNM2. The visible kinks originate from the injection of a fresh tritium batch into the source.

6.4 Column density

After completion of the burn-in phase (see section 5.4), the WGTS was no longer restricted to operate at reduced source activity. Instead, the column density could be set to $\langle \rho d \rangle = 4.23 \times 10^{17}$ molecules/cm^2, which corresponds to 84.5 % of its design value. The increase by 62.4 percentage points compared to KNM1 translates into an increase of signal electron rate by a factor of 1.9 within the analysis interval.

The column density is displayed in figure 6.4 as a function of live time. Variations from scan-to-scan were as small as $\sigma(\rho d) = 0.1\,\%$, demonstrating an excellent stability. A few individual scans exhibited slightly larger ρd drift with maximal peak-to-peak fluctuations of 0.5 %. However, the average drift within a scan was small (0.06 %).

The relevant uncertainty on ρd for the neutrino-mass analysis is the one on the absolute value $\Delta \rho d = 0.25\,\%$. The latter is illustrated as red error bar.

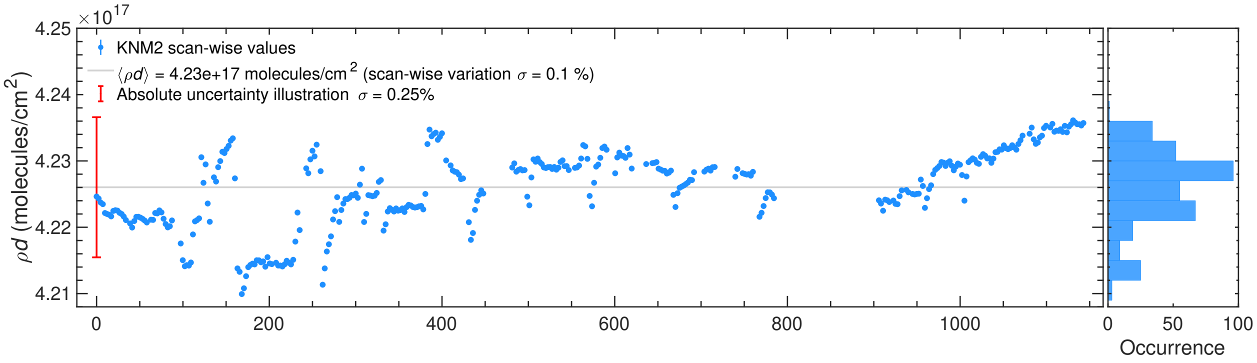

Figure 6.4: Scan-wise mean column density as a function of time in KNM2. The uncertainty on the absolute column density of 0.25 % is illustrated in red.

6.5 Source activity stability within a scan

In order to model the tritium spectra with an energy-independent signal normalization, the source activity has to be stable within each scan. The uncertainty propagation of activity fluctuations within scans is described in section 4.4.2.

The activity variations $\hat{A}^{sk}_{\mathrm{source}}$, relative to their scan-wise means, are displayed in figure 6.5 (left) for all golden scans. The standard deviation and error of the mean (equation (4.6)) are calculated for each scan-step. On average, the relative source activity exhibited an excellent stability with $\langle \sigma^k_{\mathrm{sys}} \cdot \sqrt{361} \rangle = 0.04\,\%$ and $\langle \sigma^k_{\mathrm{sys}} \rangle = 0.002\,\%$. Compared to KNM1, the stability improved by a factor of > 2.

In addition to σ^k_{sys}, also the correlations among the scan-steps are taken into account in the KNM2 analysis following equation (4.7). The correlation matrix cov($\hat{A}^{sk}_{\mathrm{source}}$) is displayed in figure 6.5 (right). On top of the fully correlated diagonal entries, some moderate correlations and anti-correlations are can be seen on the off-diagonal. The full spectral covariance matrix, considering 4 pseudo-rings is displayed in appendix E.7.

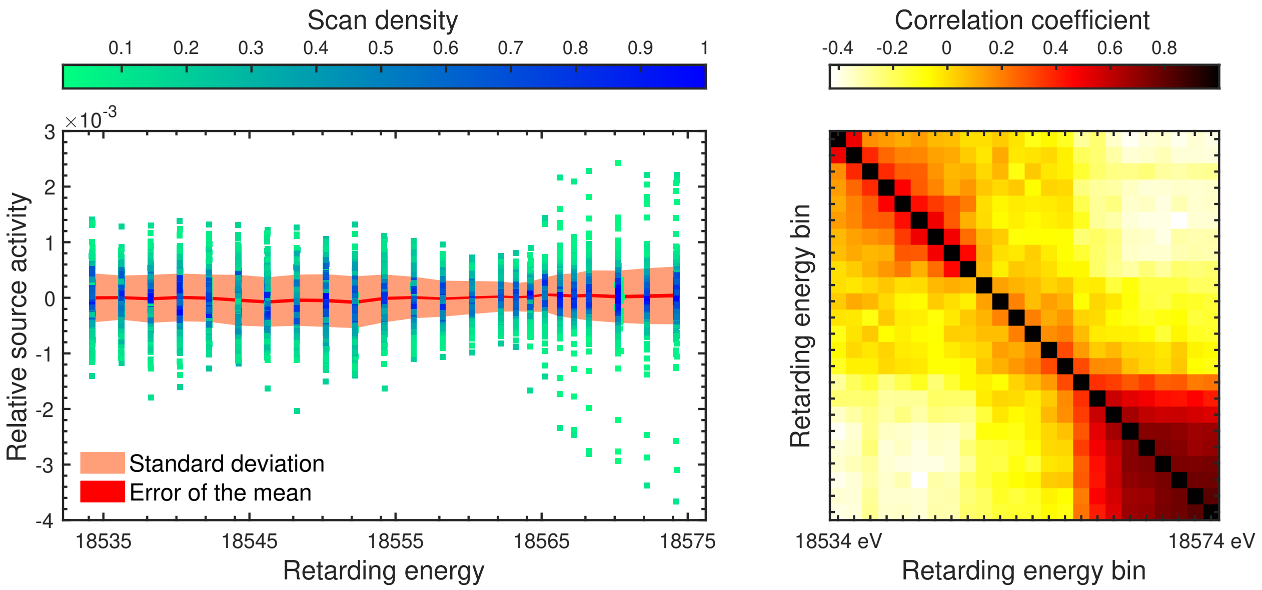

Figure 6.5: Left: Source activity variation for all scan-steps in KNM2. To compensate overall normalization effect, the scan-wise activities are normalized to the global mean activity, according to equation (4.5). On average, the activity varied within a scan-step by 0.04 % for 361 golden scans, which corresponds to an error of the mean $\langle \sigma^k_{\mathrm{sys}} \rangle = 0.002\,\%$. **Right:** Tritium activity correlation matrix. In addition to the scan-step-wise variations, the correlations among the retarding energy bins are taken into account.

6.6 Source potential

6.6.1 Longitudinal homogeneity

The constraints on longitudinal plasma potential homogeneity, including short-term fluctuations and anti-symmetric spatial variations, are inferred from the krypton campaign, that took place subsequent to KNM2 [88]. Introduced in section 4.3.1, the longitudinal plasma is described by two parameters: an energy broadening σ_0^2 and an energy-loss shift Δ_{10}.

The krypton campaign in KNM1 (see section 5.6) suffered from several non-understood systematic effects. Thus, its longitudinal plasma potential constraints were not used in the KNM1 analysis. While still being subject to large systematic uncertainties, the KNM2 krypton campaign yielded consistent results. The detailed analysis of the krypton data is presented in [88, 89]. The relevant input parameter for the neutrino-mass analysis are:

$$\sigma_0^2 = (0.0124 \pm 0.0161)\,\mathrm{eV}^2 \tag{6.1}$$

$$\Delta_{10} = (0.00 \pm 0.61)\,\mathrm{eV}. \tag{6.2}$$

The energy-loss shift is not directly accessible in the krypton data, because the energy-loss function is not known at 30 keV. Therefore, a conservative upper limit based on the measured energy broadening is derived instead [88].

The large systematic uncertainty arising from the different source temperature was addressed in the KNM3 krypton campaign. The temperature in the KNM3 krypton configuration was decreased from 100 K (KNM1,KNM2) to 80 K in order to better match the tritium-only source conditions. To avoid freeze-out, the co-circulating krypton has to be operated at a higher temperature than in the standard neutrino-mass configuration (30 K). It was worked out that 80 K are sufficient to fulfill this condition.

Moreover, in later krypton campaigns a novel krypton-operation mode made the operation at high column densities up to $\rho d = 75\,\%$ of its nominal value possible, which was previously prevented by accumulating impurities in the gas mixture.

6.6.2 Long-term potential variations

The long-term source potential stability can be quantitatively assessed through complementary channels such as the tritium endpoint and rate monitor point. This latter is considered in this work and its analysis is presented in the following section.

As discussed in section 4.3.3, the long-term plasma potential variations can be accounted for in the model and uncertainty treatment by an effective energy broadening σ_t. Consequently, the goal of the analysis of the rate-monitor scan step at $qU - E_0 = -300\,\text{eV}$ is the inference of σ_t.

In preparation for the analysis, the rate R_{300} at $qU - E_0 = -300\,\text{eV}$ is corrected for activity and retarding potential variations. Thereafter, source potential shifts arising from different rear-wall potential settings are inferred. Additionally, small potential drifts within each rear-wall period were observed and translated into an period-wise energy broadening. At the end, the potential shifts and drifts are converted into the global energy broadening σ_t, which is the relevant input for the neutrino-mass analysis.

6.6.2.1 Rate correction

The rate R_{300} at $qU - E_0 = -300\,\text{eV}$ for each golden scan is displayed in the top panel of figure 6.6 (grey points). Due to fluctuations of the source activity and the retarding potential, the rates vary more then expected from statistical uncertainties. However, both are known effects and can be accounted for. The corrected rate is displayed as colored points. Its now only subject to statistical fluctuations and variations caused by the source potential. The rate correction is performed as follows:

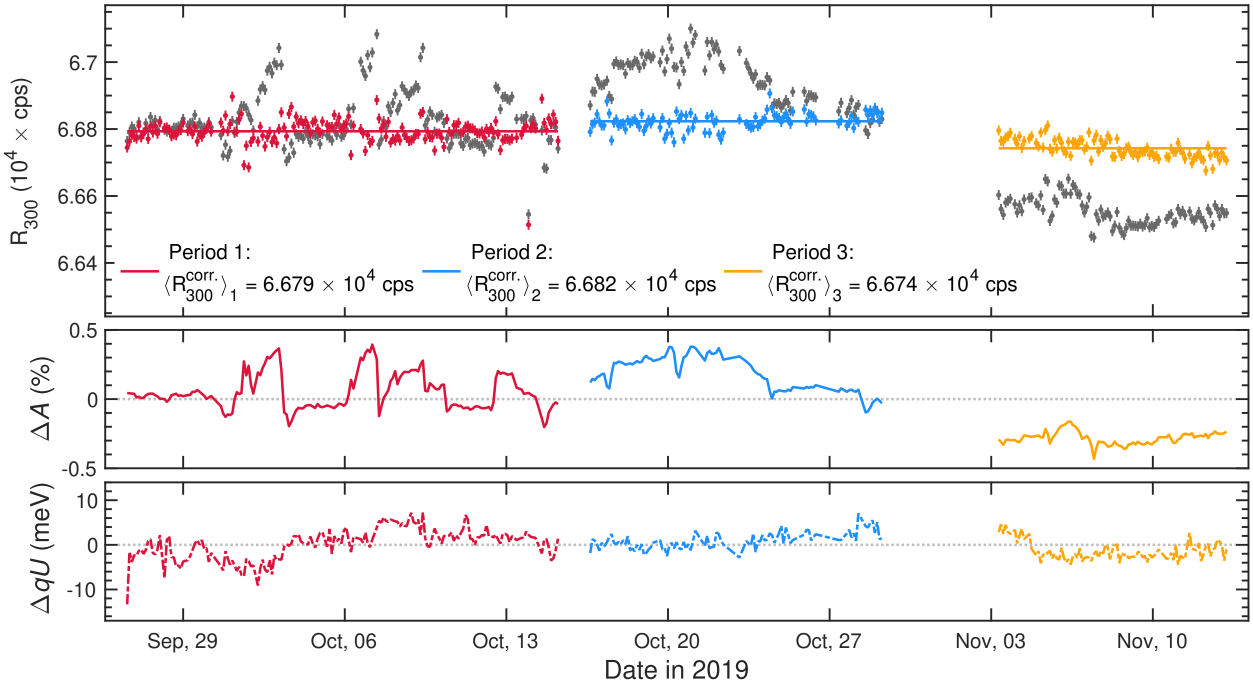

Figure 6.6: Time evolution of the rate monitor point in KNM2. The scan step at $qU - E_0 = -300\,\text{eV}$ is displayed for each golden scan in grey. The rate is further on corrected for known source activity and retarding potential fluctuations (colored points).

1. **Activity correction:** The difference of the scan-wise activity with respect to the mean activity is shown in the middle panel of figure 6.6. By comparing the top and middle panel, it is evident that the uncorrected rate follows the pattern of the activity evolution closely. Indeed, their correlation coefficient is very high $\rho = 0.97$. The activity corrections factor f_A eliminates rate fluctuations caused by the changing source

activity. The scan-wise values are normalized to the mean activity of KNM2

$$f_\mathrm{A} = \frac{\langle A_\mathrm{source} \rangle}{A_\mathrm{source}}. \tag{6.3}$$

2. **Retarding-potential correction:** The scan-wise retarding potentials are displayed with respect to the mean retarding potential in the bottom panel of figure 6.6. The calculation of the ΔqU correction requires input from a simulation to translate the observed potential variation into an expected rate variation. A simulated tritium spectrum $R_{300}^\mathrm{sim.}$ is initialized with KNM2-like settings. Then it is evaluated at several retarding energies around $qU - 18574 = (-300 \pm 1)\,\mathrm{eV}$, as illustrated in appendix E.4. In this small energy window, the rate-to-qU relation is approximated by a linear function with a slope of

   $$\alpha = -0.74\,\mathrm{cps/mV} \quad \text{with} \quad \langle R_{300}^\mathrm{sim.} \rangle = 6.59 \times 10^4\,\mathrm{cps}. \tag{6.4}$$

   The observed qU variations can now be converted into rate variations

   $$f_{qU} = \Delta qU \left(\alpha \cdot \frac{\langle R_{300} \rangle}{\langle R_{300}^\mathrm{sim.} \rangle} \right). \tag{6.5}$$

The rate is finally corrected taking into account both effects:

$$R_{300}^\mathrm{corr.} = (R_{300} \cdot f_\mathrm{A}) + f_{qU}. \tag{6.6}$$

6.6.2.2 Rear-wall periods and energy shifts

During KNM2, the rear-wall-bias voltage was adjusted twice, effectively dividing the data set into three periods with different electron starting potentials. As the latter doesn't linearly scale with U_RW, potential shifts between the rear-wall periods have to be experimentally determined. The period-wise scan lists are defined in appendix E.2.

The relative shifts between the rear-wall periods p are calculated by comparing their average rate $\langle R_{300}^\mathrm{corr.} \rangle_p$ to the overall KNM2 average $\langle R_{300}^\mathrm{corr.} \rangle$

$$\Delta \langle R_{300} \rangle_p = \langle R_{300}^\mathrm{corr.} \rangle - \langle R_{300}^\mathrm{corr.} \rangle_p \tag{6.7}$$

Central values and uncertainties are stated in table 6.1 for each period. The rate uncertainties stem from the error of the mean of $\langle R_s^\mathrm{corr.} \rangle_p$. As the choice of reference rate is arbitrary, no additional uncertainty on $\langle R_s^\mathrm{corr.} \rangle$ is taken into account. The rate difference is then converted into an meV-equivalent, using the rate-to-qU relation from equation (6.4)

$$\Delta U_{\mathrm{eq.,p}} = \Delta \langle R_{300} \rangle_p \left(\frac{1}{\alpha} \cdot \frac{\langle R_{300}^\mathrm{sim.} \rangle}{\langle R_{300} \rangle} \right). \tag{6.8}$$

Relative to each other, the obtained potential shifts are $\mathcal{O}(\pm 100\,\mathrm{mV})$.

Rear-wall period	U_RW (mV)	Number of scans	Source potential shift $\Delta\langle R_{300}\rangle_p$ (cps)	$\Delta U_\mathrm{eq.}$ (mV)	Energy broadening $\sigma_\mathrm{t,p}$ (cps)	$\sigma_\mathrm{t,p}$ (mV)
1	−49.6	171	5.0 ± 2.9	-6.7 ± 3.8	26.6 ± 2.7	35.8 ± 3.7
2	−7.7	97	35.0 ± 2.5	-46.9 ± 3.4	19.8 ± 2.7	26.5 ± 3.7
3	193.0	93	-45.7 ± 2.8	$+61.3 \pm 3.7$	22.4 ± 2.1	30.0 ± 2.9

Table 6.1: Difference of period-wise mean rate to KNM2 mean rate. The scan lists for the rear-wall periods are given in appendix E.2.

6.6.2.3 Period-wise energy broadening

The potential drifts within each period are described by energy broadenings $\sigma^2_{\mathrm{t,p}}$. The latter are obtained by fitting a Gaussian and a Poissonian distribution to the period-wise counts. The fits are displayed in figure 6.7. The difference of variances is attributed to a plasma potential

$$\sigma^2_{\mathrm{t,p}} = \sigma^2_{\mathrm{Gauss}} - \sigma^2_{\mathrm{Poisson}}. \tag{6.9}$$

The broadenings $\sigma^2_{\mathrm{t,p}}$ in terms of rate are then converted to an mV equivalent, which can be used as input for the neutrino mass analysis. Results are shown in tab. 6.1. The uncertainties are obtained via the bootstrapping technique.

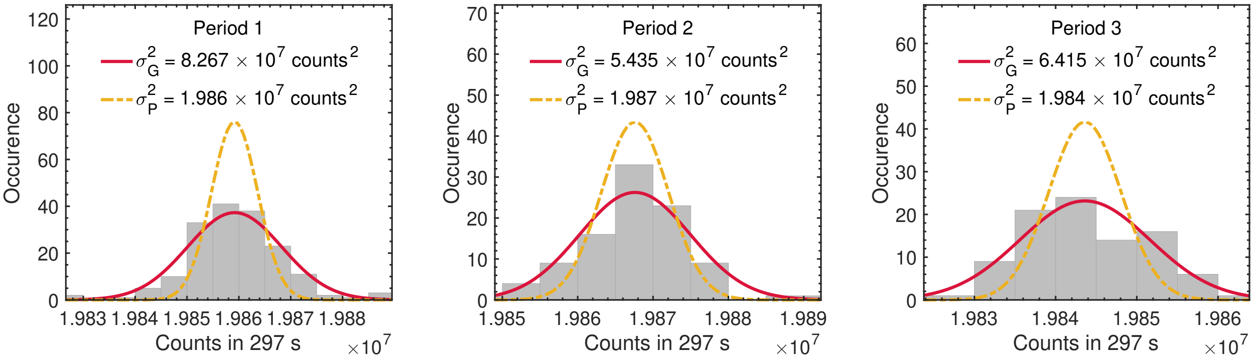

Figure 6.7: Histograms of counts at $qU - 18574 = (-300 \pm 1)\,\mathrm{eV}$ for each rear-wall period. The counts are corrected for activity and retarding potential variations. A Gaussian and Poisson function is fit to each sub-set. The difference in variances is interpreted as a period-wise plasma potential broadening.

6.6.2.4 Global energy broadening

The period-wise shifts and broadenings can be effectively described as a global broadening of the stacked tritium spectrum

$$\sigma_t = (51 \pm 2)\,\mathrm{meV}. \tag{6.10}$$

This value is derived from a MC simulation using the period-wise $\Delta U_{\mathrm{eq.,p.}}$ and $\sigma_{\mathrm{t,p}}$ obtained in the previous sections as input.

A global plasma potential probability density function is constructed by superimposing 3 Gaussian functions, one for each period. The position of each Gaussian corresponds to $\Delta U_{\mathrm{eq.,p.}}$ and the Gaussian width to the associated period-wise broadening $\sigma_{\mathrm{eq.,p.}}$. Each Gaussian is normalized to the period-wise measurement time in relative to the total measurement time. The effective source potential model is displayed in figure 6.8.

The effective global broadening is estimated by sampling from the source potential distribution: $\mathcal{O}(10^4)$ source potentials are randomly drawn from the effective source potential model. The (normalized) histogram is displayed in figure 6.8. The uncertainty on σ_t is estimated by drawing $\mathcal{O}(10^4)$ values for the $\Delta U_{\mathrm{eq.,p.}}$ and $\sigma_{\mathrm{eq.,p.}}$ from their respective distributions. Each random pair of shifts and broadenings is translated into a global broadening with the method described above. The standard deviation of the resulting global broadening distribution is taken as uncertainty $\sigma(\sigma_t)$.

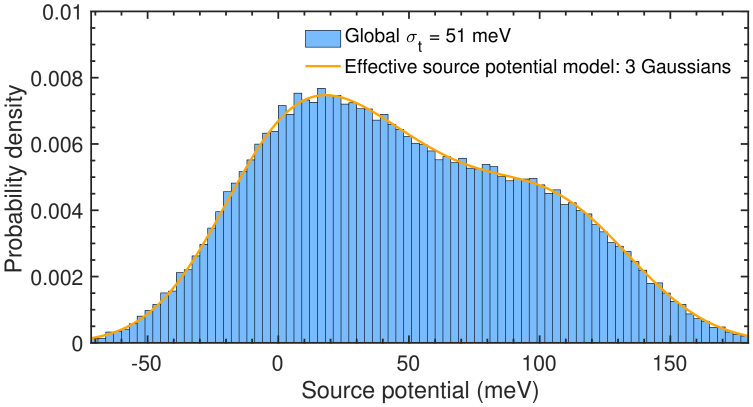

Figure 6.8: Global broadening

6.6.2.5 Pseudo-ring-wise global energy broadening

The rate monitor analysis, presented in the previous sections 6.6.2.1 to 6.6.2.4, is performed on the combined-pixel data (uniform). To investigate whether the source potential time evolution is different for different for FPD radii, the R_{300}-analysis is repeated on the pixel-segmented data. To ensure sufficient statistics, the pixel-wise rates from the active pixels are stacked into four pseudo-rings. The associated pixels numbers are stated in appendix B.

The resulting global broadenings are summarized in table 6.2. No significant differences in σ_t among the pseudo-rings are observed. The period-wise energy shifts (compare section 6.6.2.2) vary between the pseudo-rings by $\mathcal{O}(100\,\mathrm{mV})$.

	Uniform	Pseudo-ring 1	Pseudo-ring 2	Pseudo-ring 3	Pseudo-ring 4
σ_t (mV)	51 ± 2	52 ± 3	51 ± 2	49 ± 3	43 ± 4

Table 6.2: Effective global broadening due to long-term plasma drifts and different rear-wall potentials in KNM2. The uniform result is used in the neutrino-mass analysis and its uncertainty propagation. To search for radial structures, the rate-monitor analysis is additionally performed for each pseudo-ring. Within uncertainties, the results are consistent with each other.

6.6.3 Radial homogeneity

In addition to longitudinal and temporal variations, the source potential could also have a radial dependence. The latter could appear in combination with longitudinal and temporal inhomogeneities or it could occur in form of a constant potential offsets as a function of radius. The three possibilities are addressed in the following. None of them exhibits a considerable radial dependence.

6.6.3.1 Radial and longitudinal

The KNM2 krypton campaign revealed small radial features in the L_3-line position and the energy broadening [89]. However, to date it is unclear if the radial dependence is a physical effect from the longitudinal source potential distribution or if it stems from systematic uncertainties on the background model.

6.6.3.2 Radial and temporal

The rate-monitor analysis performed on the pixel-wise R_{300} data (section 6.6.2.5) shows no significant radial σ_t.

6.6.3.3 Radial only

The pseudo-ring-wise potential shifts, obtained from the rate-monitor analysis (section 6.6.2.5), exhibit radial differences of $\leq 40\,\mathrm{mV}$. Due to their small magnitude, their influence on the neutrino mass is expected to be negligible $\Delta m_\nu^2 \approx -0.002\,\mathrm{eV}^2$.

6.6.4 Effective source potential model

Longitudinal and long-term source potential variations are characterized by the energy broadenings σ_0^2 and σ_t^2, respectively. In the model, they are combined as one effective energy broadening

$$\sigma_{\mathrm{plasma}}^2 = \sigma_0^2 + \sigma_t^2 = (0.015 \pm 0.016)\,\mathrm{eV}^2. \tag{6.11}$$

The description of the longitudinal source potential requires additional the energy-loss shift parameter Δ_{10} (equation (6.2)), which is only included as a systematic uncertainty in KNM2. The associated covariance matrix is displayed in appendix E.7. No considerable radial dependence of the source potential was observed in KNM2 and therefore by default not included in the model. However, radial-dependent potential offsets can be (optionally) included as free fit parameter in the spectral analysis.

6.7 Retarding potentials

The following section addresses the retarding potentials of the pre- and main spectrometer.

6.7.1 Pre-spectrometer

The retarding potential of the pre-spectrometer was constant during KNM2. It was set to $-10\,\mathrm{kV}$.

As described in mode detail in section 5.7.1, a penning trap formed between the pre- and main spectrometer due to the combination of different retarding potentials and strong magnetic fields. Like in KNM1, a penning wiper removes the stored electrons after every scan step, to avoid discharges that would cause additional background for the main spectrometer. However, it was discovered after KNM2, that the penning trap nevertheless causes a scan-step-time-dependent background rate (section 4.10.2). For KNM2, the effect was significant (see section 6.10.5) and thus included in the model.

6.7.2 Main spectrometer

The retarding potential of the main spectrometer was varied in 39 HV set points (including the rate monitor point) according to the measurement time distribution (figure 6.1). Its temporal reproducibility is presented in figure 6.9. The top panels shows the scan-wise qU variation, relative to the average potential the of respective scan-step. The lower panel displays the standard deviation $\sigma(qU)$ of each scan-step. On average, the high-voltage could be reproduced with $\langle\sigma(qU)\rangle = 10\,\mathrm{mV}$, which surpasses the design goal by a factor of 5 [42].

The scan step at $\langle qU\rangle = 18\,570\,\mathrm{V}$ exhibits a worse reproducibility than the other scan steps ($\sigma(qU) = 55\,\mathrm{mV}$). The issue was already discovered during data taking and stems from problems with the data acquisition software (ORCA). The time evolution of the retarding potentials of this particular scan step is displayed in appendix E.5. After the problem was solved on October 2, the scan-wise variations could be reduced to $\sigma(qU) = 2\,\mathrm{mV}$. The radial distribution of the retarding potential in the analyzing is displayed in figure 6.10 (a). As the field map cannot be measured during tritium scans, it is calculated with a Kassiopeia simulation. Among the active pixels, qU varied within $\sigma = 33\,\mathrm{meV}$, which is comparable to KNM1.

Furthermore, inner electrode system of the main spectrometer was set to 200 V below the retarding potential.

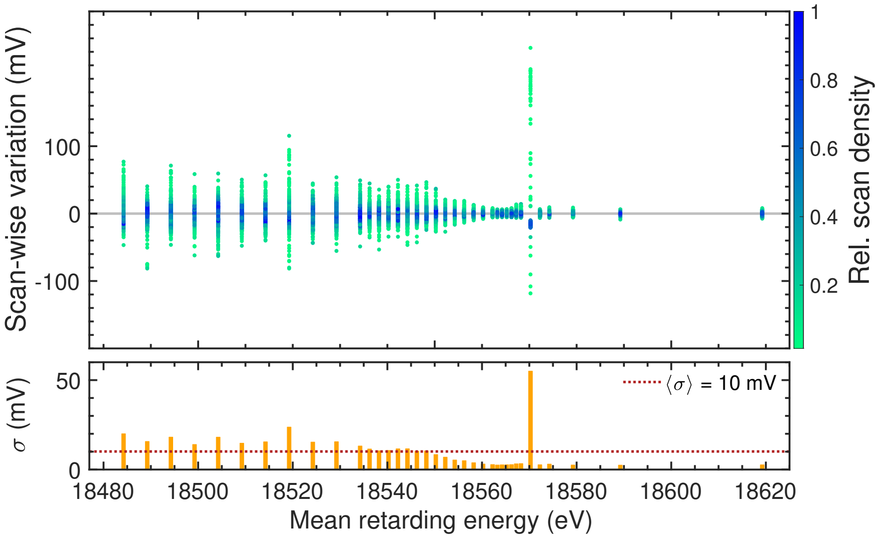

Figure 6.9: High-voltage reproducibility in KNM2. To perform the analysis on the stacked spectrum, the retarding potential values of each scan-step have to be reproduced from scan to scan as precisely as possible. The top panel displays the retarding potential values of all golden scans, relative to the respective scan-step average. The bottom panel shows the scan-wise standard deviation for each scan step. During KNM2, the mean retarding potential variation per scan-step were $\sigma = 10\,\text{meV}$.

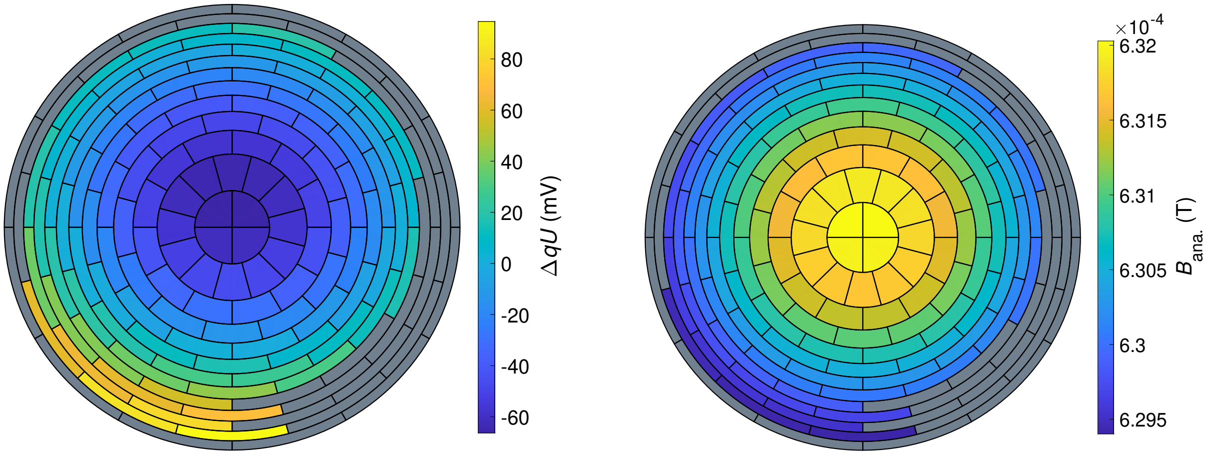

(a) Retarding potential offsets

(b) Magnetic fields in the analyzing plane

Figure 6.10: Electric and magnetic potential in the analyzing plane as they are seen by the FPD in KNM2. Pixels that are excluded from the golden pixel list are colored in grey. The retarding potentials (a) exhibit small fluctuations within $\sigma = 33\,\text{mV}$. The pixel-wise magnetic field strengths (b) vary within $\sigma = 7.0 \times 10^{-7}\,\text{T}$

6.8 Magnetic fields

The magnetic field configuration in KNM2 is very similar to KNM1:

$$B_{\text{source}} = 2.52\,\text{T} \qquad \pm 1.7\,\% \tag{6.12}$$

$$B_{\text{ana.}} = 6.31 \times 10^{-4}\,\text{T} \qquad \pm 1.0\,\% \tag{6.13}$$

$$B_{\text{max.}} = 4.23\,\text{T} \qquad \pm 0.1\,\%. \tag{6.14}$$

The stated uncertainties are of systematic nature and stem from the difference between measured and simulated field strength outside the active flux tube (see section 4.8). The systematic uncertainties are propagated to the integral spectrum with a covariance matrix in the usual manner. The covariance matrix is displayed in appendix E.7. The magnetic fields are assumed to be constant over time [98].

The radial distribution of B_{ana} is shown in figure 6.10 (b). Among all active pixels, the magnetic field strength exhibits an excellent stability $\sigma = 7 \times 10^{-7}\,\mathrm{T}$.

6.9 Detector efficiency

The same FPD wafer as in KNM1 was used. Therefore efficiency ($\epsilon_{\mathrm{FPD}} \approx 0.95$) and correction factors are identical to section 5.9. Moreover, the same detector ROI of $14\,\mathrm{keV} \leq E < 32\,\mathrm{keV}$ was used.

6.10 Background

In the spectral analysis, the background rate is mostly inferred from the five scan-steps recorded at retarding energies $qU > E_0$ (figure 6.1). This section takes a closer look at these data points.

The cumulative background rate, gathered from the golden pixels, amounts to 221.6 mcps. As outlined in section 2.2.4, the background is modeled by three components. The characteristics of the steady-state background component, which accounts for the largest share, is discussed in sections 6.10.1 to 6.10.3. Sections sections 6.10.4 and 6.10.5 are devoted to the retarding-potential and the scan-step-time dependency of the background rate, respectively.

6.10.1 Steady-state background: Radial distribution

The pixel-wise background rate is displayed in figure 6.11. It is estimated as the mean rate of the five background scan-steps for each pixel. Similar to KNM1, the rate increases as a function of FPD radius. The reason can be found in the Rydberg atoms, which are created on the main spectrometer surface.

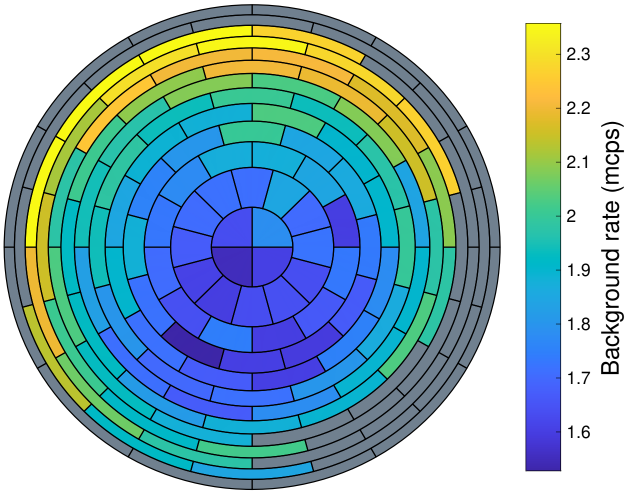

Figure 6.11: Pixel-wise background rate distribution in KNM2. Due to the generation of Rydberg atoms on the spectrometer walls, the background rate increases for increasing radial pixel position on the FPD. The stacked background rate over all golden pixel is 221.6 mcps.

6.10.2 Steady-state background: Non-Poisson over-dispersion

Similar to KNM1, an over-fluctuation of the steady-state background rate compared to the Poisson expectation is observed in KNM2. The over-dispersion is quantified in terms of a Non-Poisson factor $f_{\text{Non-Poisson}}$ (equation (4.9)).

Additionally, the background rate increased by (0.38 ± 0.04) mcps/day over the course of KNM2 (see analysis in section 9.4.2). As the temporal increase would artificially enhance the Non-Poisson over-dispersion, the effect has to be eliminated in the $f_{\text{Non-Poisson}}$ calculation[4]. The background count correction is illustrated in figure E.3.

The corrected background count distribution, normalized to 357 s, is shown in figure 6.12. A Gaussian and a Poisson distribution is fit to the data. Comparison of the variances yields $f_{\text{Non-Poisson}} = (11.14 \pm 1.93)\,\%$[5]. The uncertainty is estimated via the boot-strapping method.

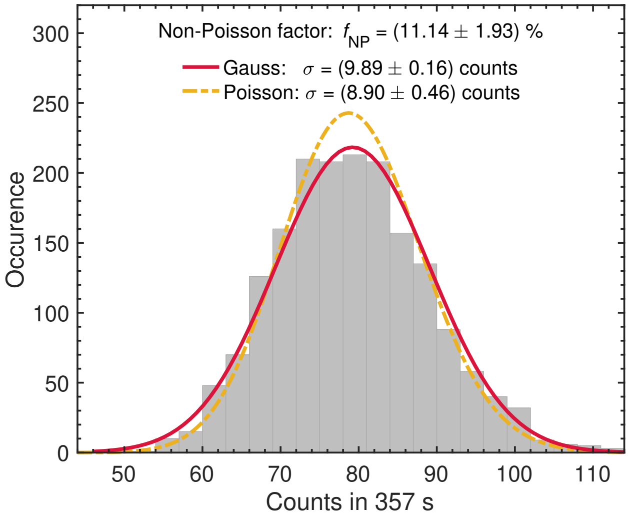

Figure 6.12: Background count distribution in KNM2 considering five scan steps above E_0 and all golden scans and pixels. The counts are corrected for the observed temporal background rate increase of (0.38 ± 0.04) mcps/day. The ratio of Gaussian and Poisson σ yields the Non-Poisson over-dispersion $f_{\text{Non-Poisson}} = (11.14 \pm 1.93)\,\%$.

6.10.3 Steady-state background: Signal-to-background ratio

A large signal-to-background ratio $R_{\text{sig.}}/R_{\text{bkg.}}$ is essential to improve the statistical sensitivity on the neutrino-mass. Through the increase in source activity and decrease in background rate, $R_{\text{sig.}}/R_{\text{bkg.}}$ could be enhanced in KNM2 compared to KNM1.

As discussed in section 5.10.3, the signal-to-background ratio decreases as a function of retarding energy. The relation is shown in figure 6.13 for the KNM2 statistics. At the lowest retarding energy in the analysis interval, $R_{\text{sig.}}/R_{\text{bkg.}} = 230$ is maximal. The equilibrium between signal and background rate is observed at $qU - E_0 \approx -9$ eV.

---

[4] The background rate is only corrected for the $f_{\text{Non-Poisson}}$ analysis and not for the neutrino-mass analysis.

[5] Background specialists in KATRIN found $f_{\text{Non-Poisson}} = 11.2\,\%$ in a similar analysis. For consistency among fitting teams, their value is used for the spectral analysis.

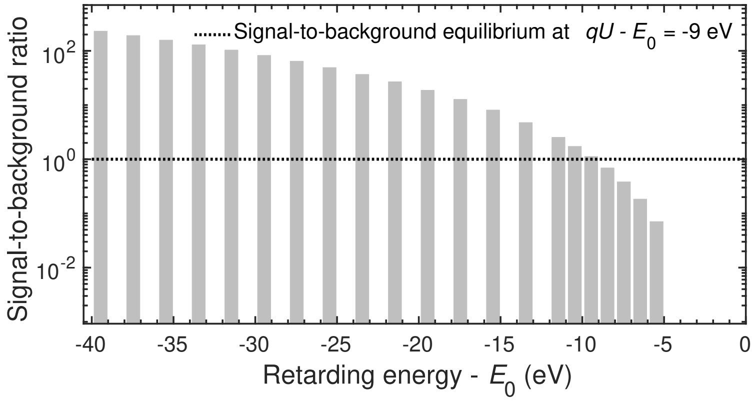

Figure 6.13: Signal-to-background ratio in KNM2. The ratio is increasing with decreasing retarding energy. The reason for this is the combination of predominant constant background rate and steeply increasing β-spectrum. The equilibrium between signal and background counts is found around $qU - E_0 = 9\,\text{eV}$.

6.10.4 Retarding-potential-dependent background

The scan-steps above the tritium endpoint are analyzed for a retarding potential dependence. The data is fit with a linear regression, displayed in figure 6.14, considering statistical uncertainties as well as the Non-Poisson over-dispersion. The obtained slope of $s_{\mathrm{qU}} = (18 \pm 13)\,\mathrm{mcps/keV}$ has a positive sign, but only a low significance of 1.3σ. A more detailed analysis on the KNM2 retarding-potential-dependent background, including the full experimental model and correlation to the neutrino-mass, follows in section section 9.9. As the background slope is not significant, it is set to zero in the baseline analysis. However, the uncertainty on the retarding-potential dependence is accounted for in the systematic uncertainty budget. Just like KNM1, the latest high-sensitivity reference is the background measurement within the FT campaign. As discussed in section 5.10.4, the applicability of the FT background-slope constraint is questionable, because of a different background level and a largely extended analysis interval. However, due to lacking alternatives, the FT constraint $\sigma(s_{\mathrm{qU}}) = 4.74\,\mathrm{mcps/keV}$ is used. Different to KNM1, the onefold instead of the threefold uncertainty is considered to be less conservative.

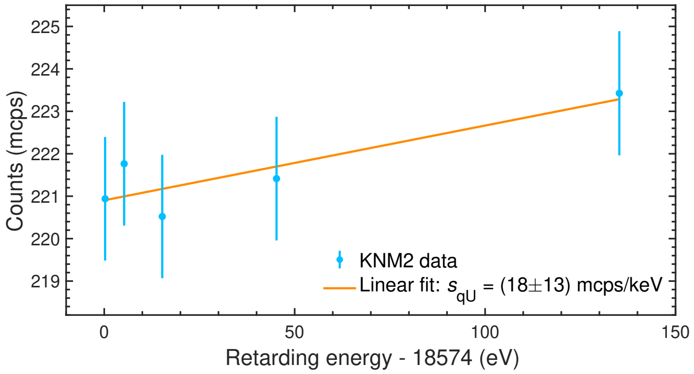

Figure 6.14: Linear fit to all scan steps above the tritium endpoint. The background data are stacked over all golden pixels and scans. The Non-Poisson over-dispersion is taken into account in addition to statistical uncertainties. Due to large uncertainties, the slope has only low significance (1.3σ).

Following the strategy in section 4.10.3.1, 10^4 random s_{qU} values are drawn from a Gaussian distribution with $\mu = 0\,\mathrm{mcps/keV}$ and $\sigma = 4.74\,\mathrm{mcps/keV}$. In case a Multi-ring analysis is performed, the constraint is scaled to the statistical uncertainty of each ring r, respectively:

$$s_{\mathrm{qU}}^{r} = s_{\mathrm{qU}} \cdot \sqrt{\frac{B_{\mathrm{base}}^{r}}{B_{\mathrm{base}}^{\mathrm{uniform}}}}. \tag{6.15}$$

The qU-dependence is considered to be uncorrelated from ring-to-ring. The s_{qU} samples are then propagated to the integral background spectrum and finally summarized in a spectral covariance matrix, displayed in appendix E.7.

6.10.5 Scan-step-time dependent background

The scan-step-time dependency of the background rate is determined using tritium data with finer time binning. The analysis yields [23]

$$s_{\mathrm{time}} = (3 \pm 3)\,\mu\mathrm{cps/s} \tag{6.16}$$

Its uncertainty is propagated to the integral spectrum through a covariance matrix in the usual manner (see section 4.10.2). The KNM2 multiring covariance matrix is display in displayed in appendix E.7.

Chapter 7

Blinding procedure

The following chapter is dedicated to the blinding protocol that is enforced in the neutrino-mass and sterile-neutrino analyses in KATRIN. The full analysis chain is developed and tested on an ensemble of simulated tritium scans, called *Monte Carlo twins*. Being a fundamental part of the blinding process, their calculation is introduced in section 7.1 first. Thereafter, the model blinding through the Final-state distribution is presented in section 7.2.

7.1 Monte Carlo twins

A MC twin scan is a simulated integral tritium spectrum that mimics a specific experimental tritium scan. For each scan within a data set, a matching MC twin is calculated. As this simulated data set is used, *inter alia*, to spot small systematic features or potential bugs in the analysis code and to benchmark the different analysis softwares, the MC twins are not statistically randomized. All slow-control parameters associated to an experimental tritium scan are used as model input for the corresponding MC twin. The relevant parameters are: isotopologue concentrations, number of scatterings ($\rho d \sigma_{\text{inel.}}$), source temperature, magnetic fields, retarding potentials, measurement time distribution and absolute measurement time.

On top of identical slow-control parameters, the same energy-loss function and the same level of model detail (Synchrotron loss, Non-isotropic transmission, etc.) as in the subsequent data analysis are used. Consequently, both MC twin and experimental scan are modeled with the same response function. The Final-state distribution, used for the MC twin calculation, depends on the step in the blinding protocol (section 7.2).

As the twins are also used to estimate the sensitivity of the considered data set, it is crucial that they contain the same statistics as the experimental data. Therefore, the scan-wise fit results[1] of $N_{\text{sig.}}$ and B_{base} are chosen to match the observation. While $N_{\text{sig.}}$ is identical for pixels, the simulated background rate reproduces the average radial pattern. Moreover, neutrino mass ($m_\nu^2 = 0\,\text{eV}^2$) and endpoint (data-set dependent) are the same for all MC twin spectra within a specific data set. Depending on the data set set, also further experimental features, such as plasma potential variations, are modeled in the MC twins. For me more details see section 9.1. Figure 7.1 illustrates one arbitrary experimental tritium scan and the matching MC twin scan.

7.2 Blinding protocol

A strict blinding protocol was established to prevent human-induced bias. In the case of KATRIN, this means that the analysts are hindered to infer the central value of m_ν^2, until the full analysis chain is developed. The latter includes data selection, analysis cuts, spectral model configuration and systematic uncertainties estimation. Any (subconscious) model tuning that would bias m_ν^2, for example to more positive values, is effectively eliminated.

Model blinding, alternatively to data blinding, is enforced through a modification of the FSD. As described in section 4.2, the FSD are a crucial ingredient of the differential spectrum. In particular the variance of the electronic

---

[1] Uniform fits to each experimental scan with $m_\nu^2 = 0\,\text{eV}$ in the standard analysis interval considering only statistical uncertainties.

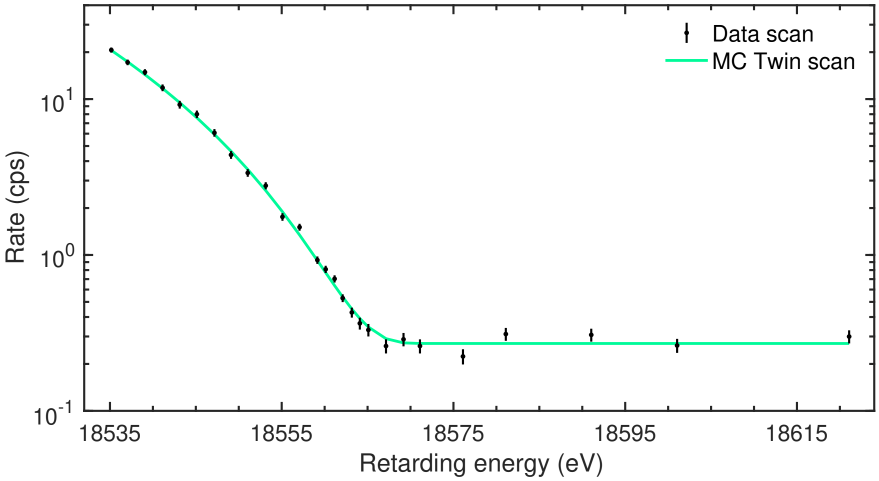

Figure 7.1: Tritium scan and corresponding MC twin. The latter is simulated using the scan-specific slow control parameters as model input. Simulated background and signal normalization are chosen the match the experimental data. For illustration purposes, an arbitrary scan within the KNM1 golden scan list was chosen (KATRIN internal scan number 51 833).

ground-state probability distribution σ^2_{GS} strongly influences the m^2_ν fit result. By modifying the true σ^2_{GS} by $\Delta\sigma^2_{\mathrm{GS}}$, a neutrino-mass-squared bias of $\Delta m^2_\nu \approx 2\Delta\sigma^2_{\mathrm{GS}}$ is induced. As the quantity $\Delta\sigma^2_{\mathrm{GS}}$ can be positive or negative, also m^2_ν can be biased in both directions. In practice, the FSD ground-state probability distribution is replaced by a Gaussian with $\sigma^2_{\mathrm{Gauss}} = \sigma^2_{\mathrm{GS}} + \Delta\sigma^2_{\mathrm{GS}}$. The value of $\sigma^2_{\mathrm{Gauss}}$ is randomly drawn from a uniform distribution, in order to obtain an uniform distributed neutrino-mass-squared bias. To avoid accidental unblinding, the modified FSD is provided by an external software, written by a person outside the spectral-analysis team. The random value of $\sigma^2_{\mathrm{Gauss}}$ is not communicated to the analysts.

Interpreting the range of $|2\Delta\sigma^2_{\mathrm{GS}}|$ as an additional systematic uncertainty of the blind analysis, the blind neutrino-mass sensitivity is worse than the actual one. Lower and upper bounds for $\sigma^2_{\mathrm{Gauss}}$ are chosen in a way that the blind sensitivity coincides with the reference sensitivity from previous experiments [62, 63]. However, as $\sigma^2_{\mathrm{Gauss}}$ is restricted to positive values, the lower bound on $\Delta\sigma^2_{\mathrm{GS}}$ cannot meet this condition if the difference between actual sensitivity and reference sensitivity is too large. If that is the case, σ^2_{GS} is used as lower bound for $\Delta\sigma^2_{\mathrm{GS}}$. As the mean energy of the ground-state excitation and the cumulative probability remain unchanged, neither the fit endpoint nor the signal normalization are affected by this blinding procedure.

The blinding protocol advances in three stages: In the first stage, the analysis is performed with a blinded model on MC twins (section 7.1), that were calculated using the blinded FSD. The goal of this stage is to compare the blind sensitivities among all independent fitting teams. Moreover, a detailed fitter comparison evaluates the consistency of spectral model and systematic uncertainty propagation. Additionally, this first stage allows for scan-wise analyses with fixed $m^2_\nu = 0\,\mathrm{eV}^2$ and blinded model, to monitor the experimental stability in near-time. After completion of the first blinding stage, all systematic uncertainties, the limit-setting strategy and all model inputs are frozen.

In the second blinding stage, the analysis is performed on the complete data set with free m^2_ν, still employing the blinded model. Biased central value of m^2_ν and uncertainties are compared among the fitting teams. If the results are consistent and show no unexpected behavior, such as significant radial or retarding potential dependencies of m^2_ν, the protocol proceeds to the third stage: Unblinding.

In the third and last stage, the neutrino mass campaign is unblinded. That means the data is analyzed with respect to m^2_ν using the original FSD. Moreover, the MC twins are recalculated using the original FSD to assess the unblinded sensitivity. Apart from the FSD, no further changes in the model are allowed.

Chapter 8

Neutrino-mass analysis of KNM1

This chapter is dedicated to the neutrino-mass analysis of the KNM1 data set.

8.1 Monte Carlo twins

Following the blinding protocol presented in chapter 7, the analysis chain is developed on MC twins. The KNM1 twins are calculated according to section 7.1 with a constant endpoint of $E_0 = 18\,573.73\,\mathrm{eV}$ for all scans. No further experimental features other than the measured scan-wise slow control parameters had to be taken into account in the KNM1 twin calculation.

8.2 Data combination

As described in chapter 5 the KNM1 data consists of 274 golden scans with 117 golden pixels each, which results in 32 058 low-statistics tritium spectra. This section is dedicated to the scan (section 8.2.1) and pixel combination (section 8.2.2) technique and their validation.

8.2.1 Scan combination

The scan-wise tritium spectra of all golden scans are stacked to one effective spectrum. This scan combination technique is described in detail in section 3.2.1. As each tritium scan has slightly different slow-control parameter (chapter 5), each experimental scan could be in principle described with one response function. In practice, the stacked spectrum is described with one average model using the average slow-control parameter. Figure 8.2 (left) shows the stacked scan response function as well as 1σ band of the scan-wise response functions. The differences are $\ll 1\,\%$.

The influence on m_ν^2 is evaluated by fitting the stacked MC Twin spectrum with the average model. The fit yields a bias of $m_\nu^2 = -4.5 \times 10^{-3}\,\mathrm{eV}^2$, which is negligible compared to the KNM1 sensitivity. Consequently, the scan combination by stacking is justified.

To identify the source of the small nonzero m_ν^2, new MC Twin-like spectra are generated. For selected simulation inputs the average slow-control values are used, whereas the remaining parameters resemble the scan-wise values. The m_ν^2 fit results are shown in figure 8.2 (right). The labels on the x-axis indicate the parameters whose values are simulated equally for all scans. If all slow-control parameters are identical for all simulated scans, the m_ν^2 bias vanishes. The scan-wise retarding potential variations (see figure 5.6), have the largest influence of m_ν^2. For future measurement campaigns, $\sigma(qU)$ could be accounted for in the average model as an energy broadening, similar to the spatial plasma variations (see section 4.3.1).

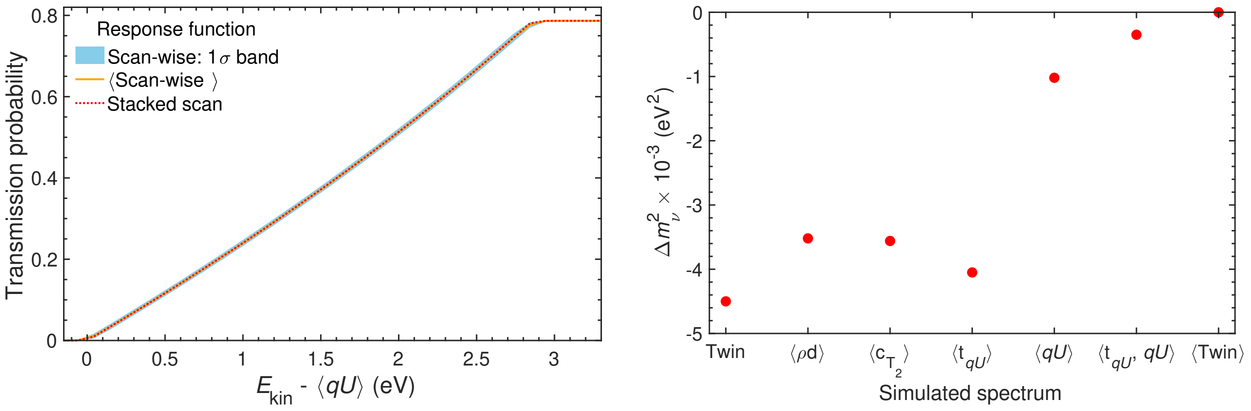

(b) KNM1

Figure 8.1: Left: Scan-wise response functions in KNM1 compared to the average response function, that is modeled with the scan-average slow-control parameters, such as ρd and qU. The energy range is limited to the transmission edge, where the differences are most prominent. **Right:** Different MC Twin-like spectra are fit using the stacked scan model. Fitting the stacked MC Twin spectrum, which mimics the experimental data, the neutrino-mass is biased by $m_\nu^2 = -4.5 \times 10^{-3}\,\mathrm{eV}^2$. As this bias is negligible compared to the KNM1 sensitivity, the scan stacking technique is applicable in KNM1. The other entries show the m_ν^2 fit result of stacked Twin-like spectra. In the simulation of these spectra, one or several scan-wise slow control parameters were replaced by their average values. The variation of the retarding potentials qU from scan to scan has the largest impact on the neutrino mass among all slow control parameters considered.

8.2.2 Pixel combination

The pixel-wise tritium spectra of all golden pixels are stacked to one effective spectrum. This uniform combination strategy is described in detail in section 3.2.2. As the magnetic and electric fields are in practice not perfectly homogeneous in the analyzing plane (figure 5.7), each pixel could be theoretically characterized with an individual response function. In the uniform model, however, the effective spectrum is described with one average response function that is calculated with the mean field strength values.

The validity of the uniform analysis for the KNM1 statistics is evaluated using the MC twins. Within the MC twins generation, the magnetic and electric fields in the analyzing plane are considered as uniform. That means that every MC Twin scan is calculated with an pixel-average response function. To evaluate the impact on the neutrino-mass, the uniform simulated spectrum is repeatedly fit with a model using the pixel-wise field strength values.

Figure 8.2 (left) demonstrates that the variation of the pixel-wise response function are very small. Moreover, the mean pixel-wise response function overlaps almost perfectly with the average response function. The m_ν^2 fit results are shown in figure 8.2 (right). The fit results vary within $\sigma(m_\nu^2) = 2 \times 10^{-3}\,\mathrm{eV}^2$, which is small compared to the KNM1 sensitivity.

The FPD segmentation can also be used to spot unknown radial plasma potential variations in the source. Given that no hint for a radial dependent source potential was found (sections 5.6 and 8.7) and the negligible variation of the pixel-wise response function, the uniform analysis is considered as suitable for KNM1.

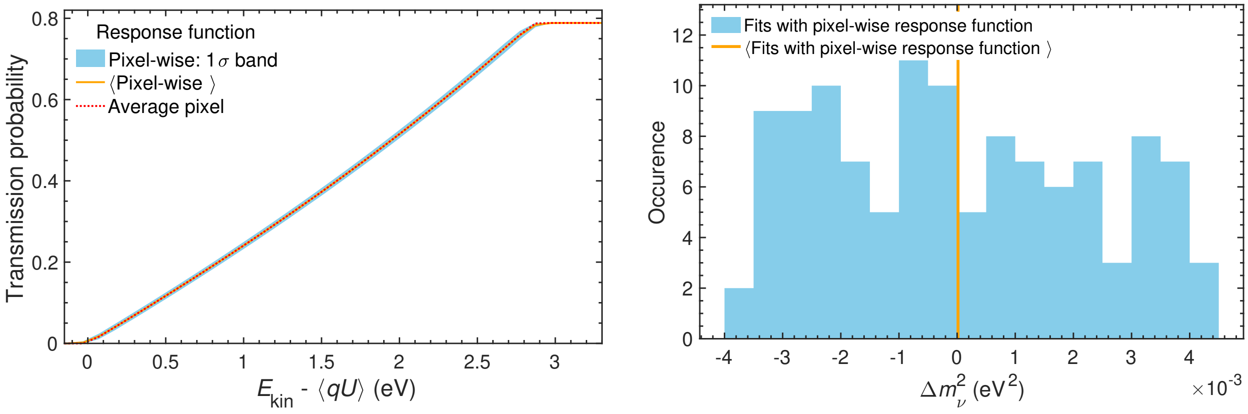

Figure 8.2: Left: Pixel-wise response function in KNM1 compared to the average response function, that is modeled with the pixel-average magnetic and electric field values . The energy range is limited to the transmission edge, where the differences are most prominent. **Right:** The pixel-average MC Twin spectrum is fit using the pixel-wise response function. The m^2_ν fit values vary within $\sigma(m^2_\nu) = 2 \times 10^{-3}\,\text{eV}^2$.

8.3 Spectral model configuration

The model of the integral spectrum is presented in detail in section 2.2. To simplify and speed up the model calculation, some details in the experimental description can be approximated and neglected if the impact on the neutrino mass is small compared to the expected sensitivity. For KNM1, the upper threshold for an effect to be neglected is set to $\Delta m^2_\nu < 0.02\,\text{eV}^2$, which roughly corresponds to the size of the Doppler Effect (included). Moreover, the Final-state distribution and the parametrization of the energy-loss function are essential inputs of the model calculation. They rely on theoretical calculation of the molecular transition probabilities (FSD) or on a dedicated *in-situ* measurement (Energy-loss function). Both are subject to change over time, as calculation and experiment evolve and become more accurate. Additionally, the understanding of the experimenters is constantly increasing over time. Therefore, some systematic effect might re-evaluated at a later time. In KNM1 the scan-step-time-dependent background rate was only discovered after the publication in [96, 101]. The model settings used in KNM1 are summarized in appendix C.

8.4 Scan-wise analysis: Nuisance parameter stability

As described in section 5.1 and section 5.2.2, 274 tritium scans were selected for the KNM1 neutrino-mass analysis with a duration of 2 h each. To evaluate the global system stability of the measurement campaign, the individual tritium scans are analyzed successively. The FPD pixels are combined following section 8.2.2.

As the neutrino-mass sensitivity within a single scan is relatively poor, $\sigma(m^2_\nu) \approx 7\,\text{eV}^2$, the fit uses fixed $m^2_\nu = 0\,\text{eV}^2$. Only the standard nuisance parameter $\boldsymbol{\eta} = (E_0^{\text{fit}}, B_{\text{base}}, N_{\text{sig.}})$ are are allowed to vary in the fits. The single scans are *by far* dominated by statistical uncertainties, thus most systematic uncertainties are neglected. Only the largest systematic effect is included: the Non-Poisson background rate over-dispersion. The latter can also be interpreted as an enhanced statistical uncertainty of the steady-state background rate and is statistically uncorrelated from scan to scan.

The stability of each free nuisance parameters η as a function of tritium scans s is evaluated in terms of chi-squared

$$\chi^2 = \sum_{s=1}^{N_{\text{scan}}} \left(\frac{\eta_s - \langle \eta \rangle}{\sigma(\eta_s)} \right)^2 \tag{8.1}$$

with $N_{\text{scan}} = 274$ and the weighted average $\langle \eta \rangle$. If η is indeed stable over time, χ^2 is expected to follow a chi-squared distribution with $N_{\text{scan}} - 1 = 273$ degrees of freedom. The corresponding p-value is labeled as $p_{\text{const.}}$.

Moreover, to test whether η fluctuates randomly around its mean, the Wald-Wolfowitz runs test is performed [102]. In contrast to the chi-squared test in equation (8.1), which evaluates average the distance between η and $\langle\eta\rangle$, the runs test examines the order of occurrence. A run is a sequence of at least two adjacent values of η, that are either above or below $\langle\eta\rangle$. This test evaluates if the number of runs is lower or higher than expected from a statistically independent sample. The significance is quantified in terms of a p-value p_{runs}.

In the following, the time evolution of the three standard nuisance parameters is analyzed: E_0^{fit}, B_{base} ,N_{sig}. Moreover, the scan-wise p-values are shown.

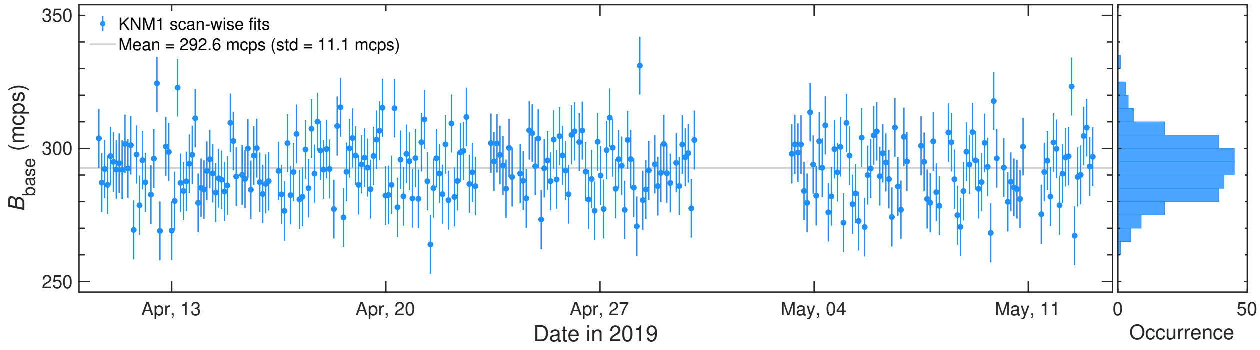

(a) Time evolution of the effective fit endpoint in KNM1

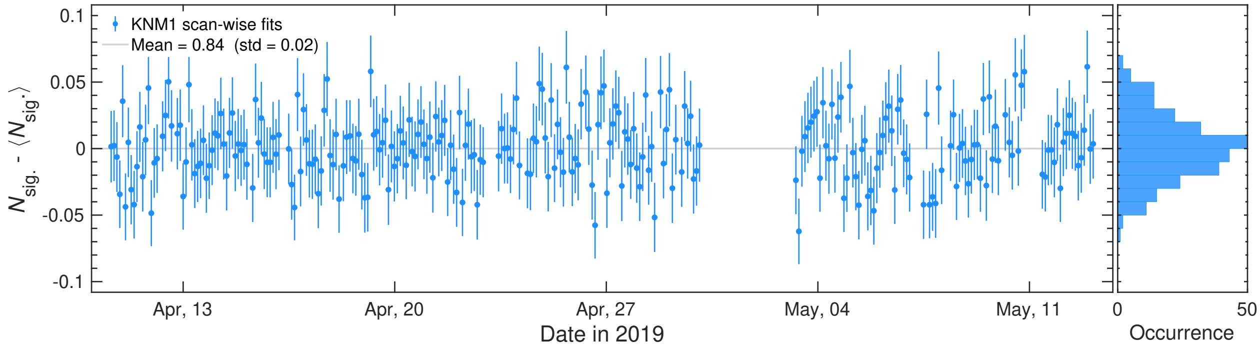

(b) Time evolution of the steady-state backgroundrate in KNM1

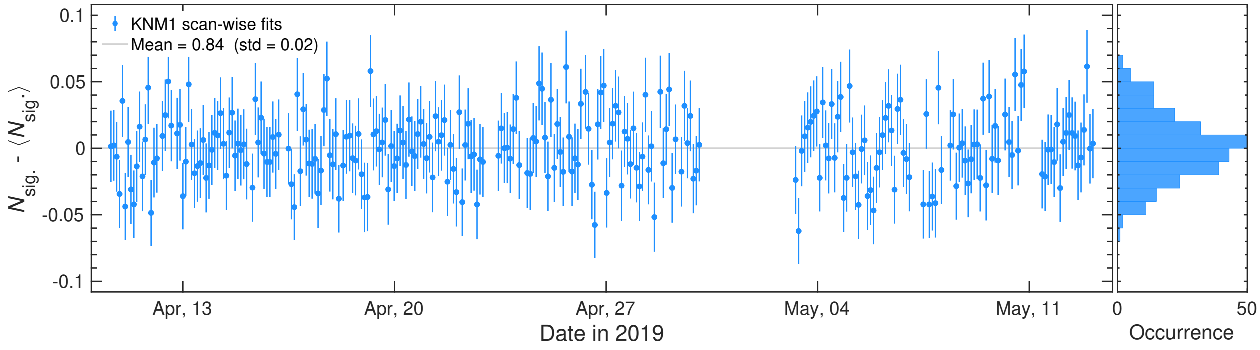

(c) Time evolution of the signal normalization fractor in KNM1

Figure 8.3: KNM1 time evolution of the nuisance parameters: (a) fit endpoint, (b) steady-state background rate and (c) signal normalization. Every tritium scan within the golden scan list (section 5.2.2) is fit separately. The standard analysis energy range (section 5.1) is used. As the statistics of a single scan are very limited, only uncertainties from statistics and the Non-Poisson background rate over-dispersion are considered. Moreover m_ν^2 is fixed to $0\,\text{eV}^2$.

8.4.1 Effective tritium endpoint

A change in the absolute scale of the electron starting potential in the WGTS over time would propagate to an unstable fit endpoint. Figure 8.3 (a) depicts the scan-wise E_0^{fit} fit results. The latter vary within $\sigma(E_0^{\mathrm{fit}}) = 0.25\,\mathrm{eV}$ around the weighted mean $\langle E_0^{\mathrm{fit}} \rangle = 18\,573.78\,\mathrm{eV}$.

Summation over the scan-wise residuals yields $\chi^2 = 236.7$ (273 dof), which corresponds to an excellent $p_{\mathrm{const.}} = 0.94$. Moreover, no obvious structure is visible. This is supported by the runs test with $p_{\mathrm{runs}} = 0.52$, attesting no significant deviation from random occurrence.

8.4.2 Steady-state background rate

The fit values of the steady-state background rate over the course of KNM1 are shown in figure 8.3 (b). The mean background rate is $\langle B_{\mathrm{base}} \rangle = 292.6\,\mathrm{mcps}$ with fluctuations of $\sigma(B_{\mathrm{base}}) = 11.1\,\mathrm{mcps}$. The good $\chi^2 = 279.9$ (273 dof) and $p_{\mathrm{const.}} = 0.37$ demonstrate, that within uncertainties B_{base} is constant over time. As discussed in section 5.10.2, the steady-state background counts fluctuate more than expected from a Poisson distribution. The 6.4 % over-dispersion is accounted for in the single-scan fits as an additional (systematic) uncertainty. If the over-dispersion was neglected in the single-scan analysis, $p_{\mathrm{const.}} = 7 \times 10^{-4}$ would be drastically reduced. The runs test doesn't reveal any unexpected behavior, $p_{\mathrm{runs}} = 0.76$.

8.4.3 Signal normalization

The scan-wise signal normalization factors are shown in figure 8.3 (c). The fit values fluctuate within $\sigma(N_{\mathrm{sig.}}) = 0.02$ around the average value $\langle N_{\mathrm{sig.}} \rangle = 0.84$. The signal normalization factor corrects the expected signal strength to the actually observed one, as discussed in section 2.2.3. Thus, unnoticed variations in the source activity would translate into unstable $N_{\mathrm{sig.}}$ fit values. However, the chi-squared test attests with $\chi^2 = 234.3$ (273 dof) and $p_{\mathrm{const.}} = 0.96$, that the signal normalization is indeed constant within uncertainties. Moreover, the runs test doesn't find a significant ($p_{\mathrm{runs}} = 0.43$) deviation from random occurrence.

8.4.4 Goodness-of-fit

The scan-wise goodness-of-fits are shown in figure 8.4. If the model describes the data well and the single-scan uncertainties are correctly estimated, the distribution of p-values should follow a uniform distribution. As can be seen in the right panel of figure 8.4, the observed distribution follows only very approximately a uniform one. Indeed, the Kolmogorow-Smirnow-Test rejects the uniform hypothesis. Large p-values occur more often than small ones, which means that the scan-wise fits are on average *too good*. The runs test finds $p_{\mathrm{runs}} = 0.83$, thus no deviation from random occurrence.

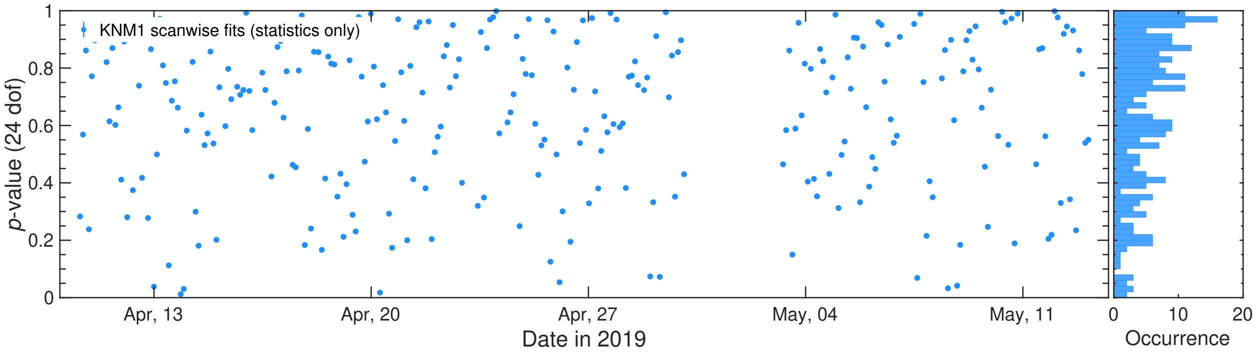

Figure 8.4: Goodness-of-fit time evolution in KNM1. Every tritium scan within the golden scan list (section 5.2.2) is fit separately. The standard analysis energy range (section 5.1) is used. As the statistics of a single scan are very limited, only uncertainties from statistics and the Non-Poisson background rate over-dispersion are considered. Moreover m_ν is fixed to zero.

8.5 Baseline neutrino-mass analysis

This section presents the baseline neutrino-mass-fit of the KNM1 measurement campaign in the standard analysis interval including statistical and systematic uncertainties. Best-fit parameters (section 8.5.1), chi-squared profile (section 8.5.2), fit parameter correlations (section 8.5.4) and improved upper limit section 8.5.3 are discussed.

8.5.1 Best-fit result

Data and best-fit model within the analysis range are shown in figure 8.5 a). The statistical error bars of the data points are scaled by a factor of 50 to make them visible. The fit model describes the data very well, which is mirrored with the excellent $p = 0.53$ ($\chi^2_{\text{min}} = 21.7$ at 23 dof).

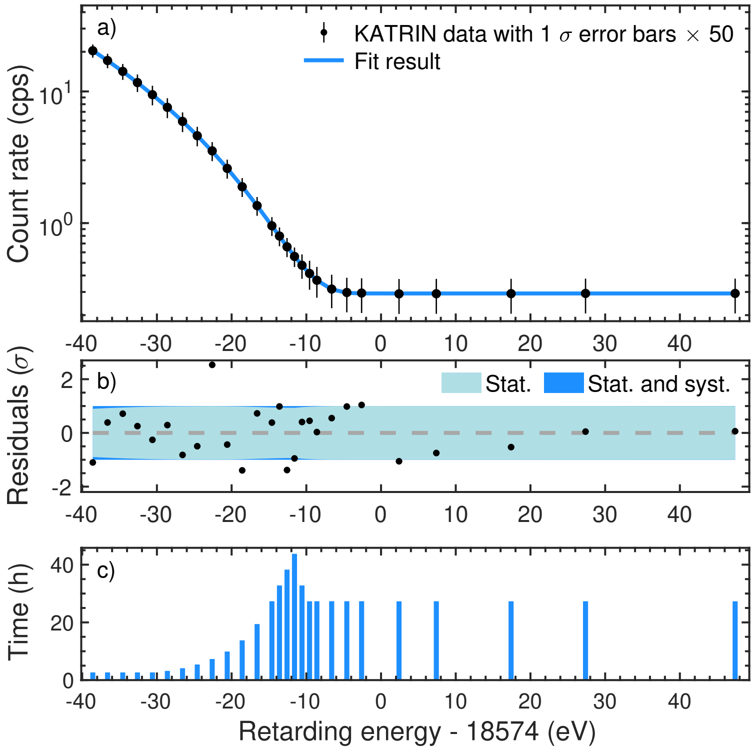

Figure 8.5: Uniform fit to KNM1 data. **a)** Overlay of data and best-fit model. The uncertainties are enhanced by a factor of 50 for better visibility. **b)** Normalized residuals between data and best-fit model. **b)** Measurement-time distribution.

The residuals, displayed in figure 8.5 b), are normalized with the square-root of the diagonal entries of the covariance matrix that is used in the fit. Off-diagonal entries, which incorporate scan-step dependent correlations, are not included in this visual representation. The blue area is the $1\,\sigma$ uncertainty band. The region highlighted in a lighter blue corresponds to the statistical contribution to the total uncertainty budget. The normalized residuals vary within $< 2.6\sigma$. Moreover, no significant pattern is visible, which is supported by the runs test $p_{\text{runs}} = 0.53$.

The best-fit parameter values and 1σ uncertainties are:

$$m_\nu^2 = (-0.96^{+0.88}_{-1.05})\,\text{eV}^2 \tag{8.2}$$

$$E_0^{\text{fit}} = (18573.73 \pm 0.06)\,\text{eV} \tag{8.3}$$

$$B_{\text{base}} = (292.3 \pm 0.7)\,\text{mcps} \tag{8.4}$$

$$N_{\text{sig.}} = 0.837 \pm 0.003. \tag{8.5}$$

The best-fit value of the neutrino mass-squared lies 1σ into the negative regime. Even though a negative mass is nonphysical, the phase space in equation (2.10) allows for negative m_ν^2-values. As the analysis follows the Frequentist philosophy, no prior knowledge on m_ν^2 is incorporated in the parameter inference and the phase space isn't modified artificially to forbid negative values. Thus, the same phase space is used for negative and positive m_ν^2. It was validated on the MC twins that this approach ensures a bias-free the neutrino mass inference.

8.5.2 Profile chi-squared

The fit is performed with the Minuit software using the Minos minimization algorithm [103], which provides the asymmetric fit uncertainties at 68.3 % C.L. in equation (8.2). As a sanity check to validate the convergence of the fit, the profile chi-squared function is manually calculated around its minimum: A model with fixed m_ν^2 is fit to the spectrum. The fit is repeated for different m_ν^2 values. The resulting profile chi-squared is displayed in figure 8.6. The dash-dotted orange curve is based on only statistical uncertainties, whereas the solid blue curve taken all uncertainties into account. Central values and fit uncertainties are in good agreement with the result provided by Minos.

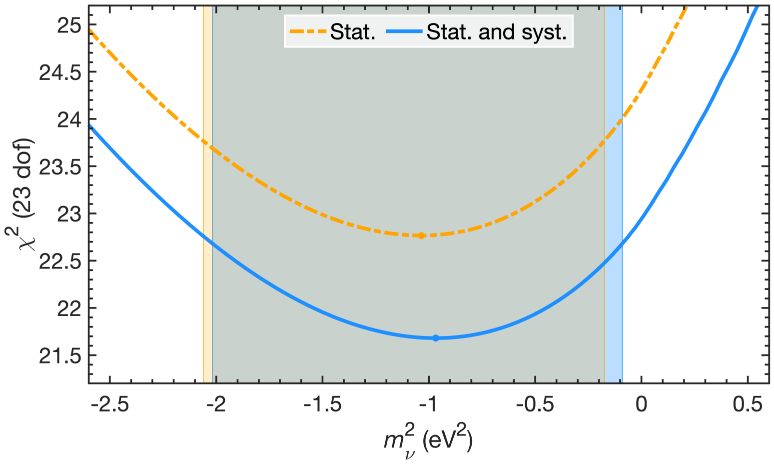

Figure 8.6: As a sanity check, the KNM1 chi-squared profile is calculated manually around its minimum. The orange dash-dotted line corresponds to the analysis with only statistical uncertainties, whereas the solid blue line is based on the full uncertainty budget. The corresponding 1σ confidence regions are illustrated as the colored areas.

8.5.3 Confidence belt and upper limit

It was decided before the unblinding that a confidence belt at 90 % C.L. will be constructed. Depending on the inferred best-fit value, a two-sided confidence region or an upper limit will be quoted as the main result. The m_ν^2 best-fit result combined with its expected likelihoods can be converted into a confidence belt and corresponding confidence region using statistical means. Two different limit-setting strategies, technically introduced in section 3.3.2, are realized for KNM1: The method of Lokhov-Tkachov [82] and the well-known method of Feldman-Cousins [80].

The confidence belts are presented in figure 8.7. The main difference between the two limit-setting strategies is the handling of negative neutrino masses. While Feldman-Cousins use the likelihood-ratio ordering principle, Lokhov-Tkachov opt for referring to the sensitivity at the null hypothesis $m_\nu^2 = 0\,\mathrm{eV}^2$. Both strategies ensure the correct coverage for all possible m_ν^2 measurements. However, the Feldman-Cousins method generally results in more aggressive upper limits, if the measured neutrino mass value is negative.

For KNM1, the upper limits at 90 % C.L. are

$$m_\nu \leq 1.1\,\mathrm{eV} \quad (\mathrm{Lokhov-Tkachov}) \tag{8.6}$$

$$m_\nu \leq 0.8\,\mathrm{eV} \quad (\mathrm{Feldman-Cousins}). \tag{8.7}$$

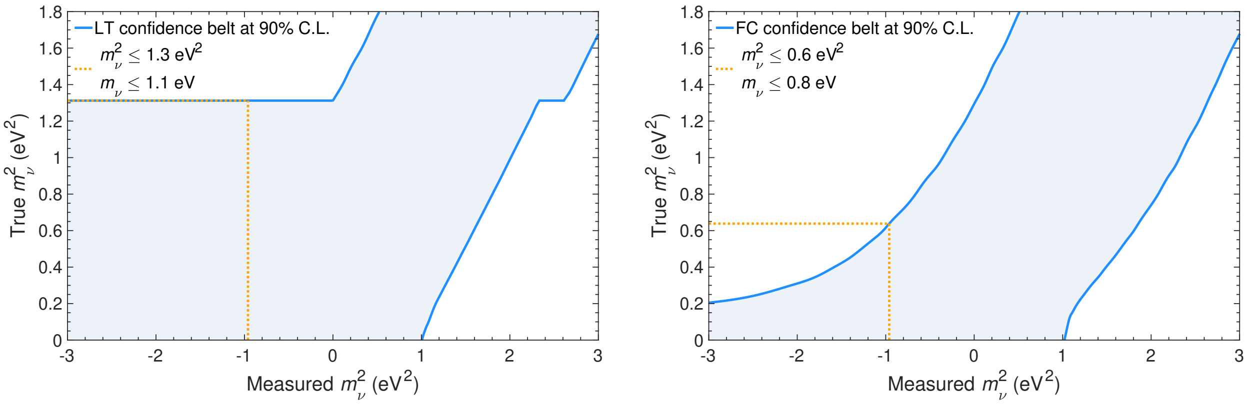

Figure 8.7: As the first measurement campaign is not sensitive enough to determine the neutrino mass at high confidence, an upper limit is quoted instead. Two limit-setting strategies are explored: The method of Lokhov-Tkachov (LT) [82] (**left**) yields $m_\nu \leq 1.1\,\mathrm{eV}$ (90 % C.L.), which coincides with the KNM1 sensitivity. The method of Feldman-Cousins (FC) [80] (**right**) results in $m_\nu \leq 0.8\,\mathrm{eV}$ (90 % C.L.).

8.5.4 Fit parameter correlations

The correlations among the fit parameters are estimated by fitting 2000 randomized spectra. The latter are generated through randomization of the MC twins following the uncertainties of the fit covariance matrix. The m^2_ν best-fit value from the data analysis (section 8.5.1) is used as input for the MC Twin simulation. Each sample spectrum is then fit using statistical and systematic uncertainties. The fit results are displayed in figure 8.8. The histograms on the diagonal panels show the distribution of each fit parameter. The off-diagonal scatter plots set the fit parameter in relation to one another. Here, the coloring indicates the density from low (dark blue) to high (yellow). The Pearson correlation coefficients ρ, measuring the degree of linear correlation, is stated in the top left corner for each fit parameter pair. The classification of the size of ρ is based on the guideline offered by [104].

A very high positive correlation ($\rho = 0.93$) is observed between the neutrino mass and the fit endpoint. An increasing endpoint shifts to first order the entire energy spectrum towards larger energies. The neutrino mass has (almost) the opposite effect: An increasing neutrino mass causes a spectral shape distortion towards smaller energies. Therefore, a (too) large E_0^{fit} can be compensated to some extent by a (too) large m^2_ν and vice versa.

Moreover, the endpoint has a high negative correlation with the signal normalization ($\rho = -0.89$). For fixed retarding potentials, an increasing endpoint effectively corresponds to a measurement of the tritium spectrum *deeper* in the spectrum. Due to the steep rise of the tritium spectrum towards lower energies, the count rate at fixed qU is expected to increase. The signal normalization has a similar influence on the spectrum: The larger the signal normalization, the larger is the count rate. The observed correlation between E_0^{fit} and $N_{\mathrm{sig.}}$ is negative, because a (too) large fit endpoint can be partially compensated by a (too) small signal normalization or vice versa.

The correlation between m^2_ν and $N_{\mathrm{sig.}}$ is moderately negative ($\rho = -0.69$). This can be explained by the strong positive correlation between m^2_ν and E_0^{fit}. The correlations between the remaining parameter pairings are low.

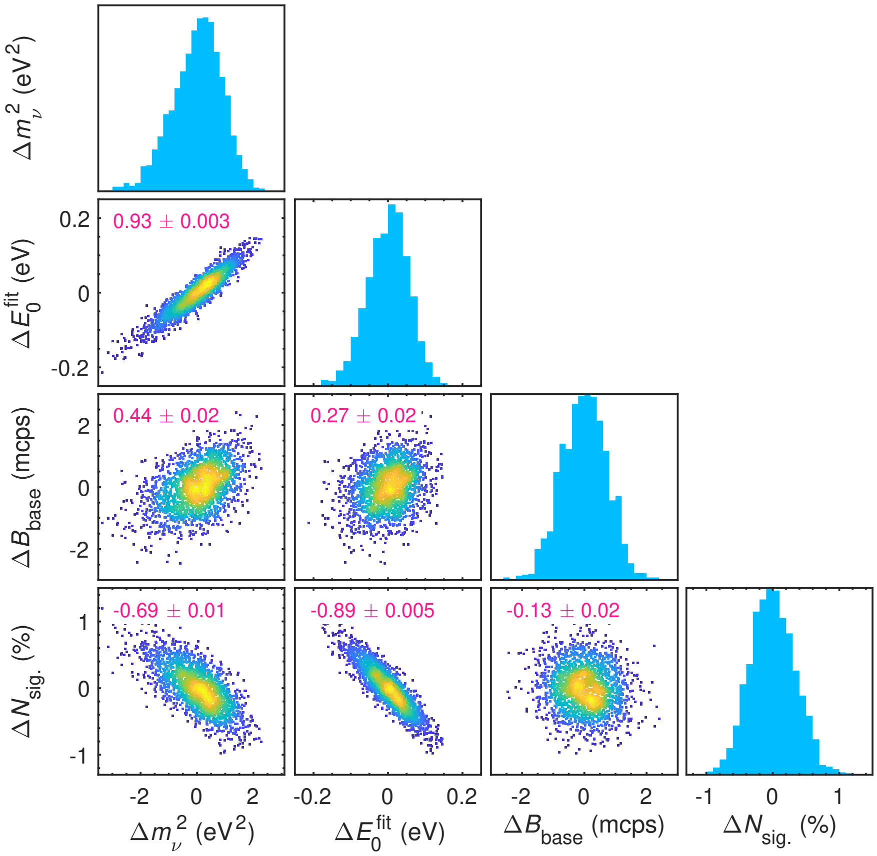

Figure 8.8: The fit parameter correlations are investigated by fitting 2000 randomized MC Twin spectra. Statistical and systematic uncertainties are used both in the randomization and in the fit. The histograms on the diagonal display the fit-value distribution of each parameter on its own. The scatter plots on the off-diagonal panels show the correlation among the respective parameters. The color code indicates the density ranging from low (dark blue) to high density (yellow). The values in the top left corners are the corresponding Pearson correlation coefficients. The uncertainties are calculated via the bootstrapping technique.

8.6 Systematic uncertainty breakdown

The systematic uncertainties are incorporated in covariance matrices. As discussed in chapter 4, each effect is described by an individual covariance matrix. The KNM1 covariance matrices are displayed in appendix D.5. The fit covariance matrix, including all effects, is the sum of all matrices. To evaluate the individual influences on the m_ν^2 uncertainty, the data is fit twice: Once considering only statistical uncertainties and once using the covariance matrix of interest on top of that. The systematic-only contribution for effect i can be then calculated as

$$\sigma_{\mathrm{syst}}^{i} = \sqrt{\sigma_{\mathrm{tot,i}}^{2} - \sigma_{\mathrm{stat}}^{2}} \tag{8.8}$$

with $\sigma_{\mathrm{total,i}}$ being the uncertainties provided by fit with covariance matrix i at 68.3 % C.L. and σ_{stat} being the statistics-only uncertainty. Even though the minimization algorithm Minos [103] provides asymmetric m_ν^2 uncertainties, only the average value is displayed in this context. The breakdown of all uncertainties on m_ν^2 is visualized in figure 8.9 on the data spectrum. The expected contribution to the sensitivity, obtained from analyzing the MC twins, is written on the very right in grey as reference. Due to the non-zero best-fit result, slight differences between data and simulation are expected.

Including statistical and all systematic uncertainties, the total uncertainty on m_ν^2 amounts to $\sigma_{\mathrm{tot}}(m_\nu^2) = 0.97\,\mathrm{eV}^2$. The statistical uncertainty is the dominant contribution with $\sigma_{\mathrm{stat}}(m_\nu^2) = 0.93\,\mathrm{eV}^2$, making up 93 % of the total variance. The remaining uncertainty is attributed to systematic effects, which sum up to only $\sigma_{\rm syst}(m_\nu^2) = 0.26\,\mathrm{eV}^2$. The largest systematic contribution stems from the Non-Poisson background rate over-dispersion with $\sigma_{\rm syst}^{\rm NP}(m_\nu^2) = 0.22\,\mathrm{eV}^2$, introduced in section 5.10.2. Second and third largest effects are tritium activity fluctuations during a scan (see section 4.4.2) and the retarding-potential-dependent background rate (see section 4.10.3).

The latter employs the background slope constraint from FT $s_{\rm qU} \leq 15\,\mathrm{mcps/keV}$ (see section 5.10.4). If no external constraint is applied in the covariance matrix, the systematic uncertainty increases to $\sigma(m_\nu^2) = 0.27\,\mathrm{eV}^2$ (sensitivity $\sigma(m_\nu^2) = 0.31\,\mathrm{eV}^2$).

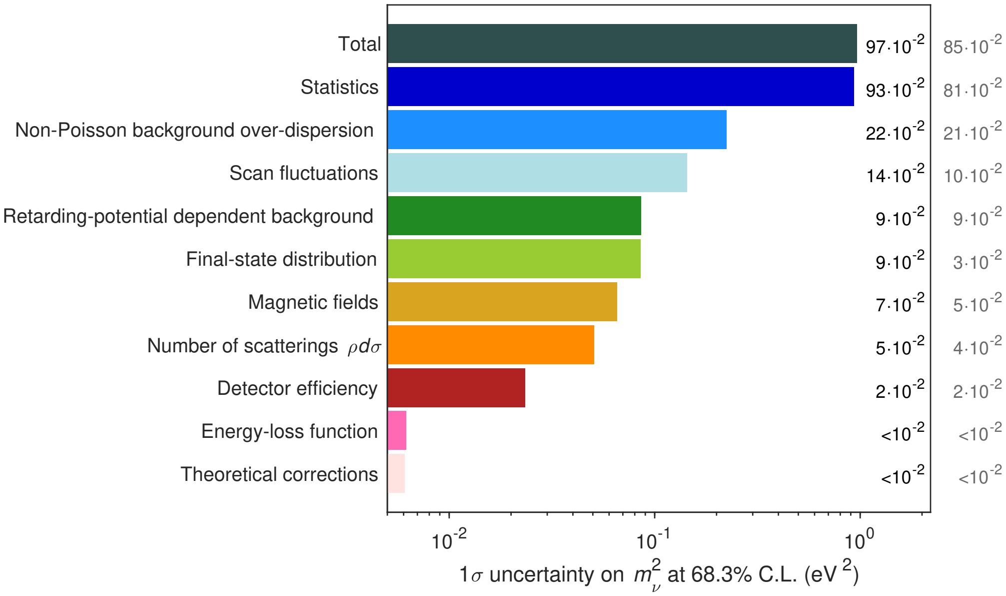

Figure 8.9: KNM1 uncertainty breakdown. The top two bars indicate the total and the statistical uncertainty. Additionally, the influence of each systematic effect on m_ν^2 is evaluated individually. The remaining bars and the black values beside them visualize the contribution of each effect in the *data* analysis. The right-most grey values indicate the expected sensitivity. The analysis is strongly dominated by the statistical uncertainty. The largest systematic effect stems from the Non-Poisson background rate over-dispersion.

8.7 Radial fit parameter dependencies

In the baseline analysis the pixels are stacked into one effective spectrum. This is possible due to the excellent stability of the magnetic and electric fields in the source and the analyzing plane, as discussed in section 8.2.2. To search for unknown radial inhomogeneities, e.g. due to a hypothetical mismodelling of the plasma potential in the WGTS, the FPD rings are analyzed independently from each other. An unaccounted radial dependency of the plasma potential would manifest itself in a radial dependent fit endpoint. As discussed in section 4.3, simulations suggest that a radial plasma potential dependency often entails a longitudinal plasma inhomogeneity. As the latter causes a bias in the neutrino mass, the radial patterns of m_ν^2 and $E_0^{\rm fit}$ are the focus of the ring-wise analysis.

To collect sufficient statistics, the actual FPD rings are grouped into four pseudo-rings according to appendix B. The statistics of each pseudo-ring, considering only the active pixels in KNM1 is summarized in table D.1. The pseudo-ring-wise fit results of the four fit parameters are displayed in figure 8.10. Neutrino mass and endpoint, being strongly (positive) correlated, exhibit a similar pattern. Both fit parameters indicate a downward trend as a function of pseudo-ring. In contrast to that, the background and signal normalization increase with increasing radius.

To quantify these radial tendencies more precisely, a linear function with free slope and offset is fit to each parameter evolution. Central values and 1σ uncertainties are stated in the corresponding legends of figure 8.10. The linear slope for m_ν^2 is significant[1] at 1.61σ. The endpoint slope has a similar significance of 1.71σ. As both slopes are not very significant, for instance not above 95 % C.L., the radial patterns don't cause a serious concern for the (uniform) neutrino-mass analysis. However, more detailed plasma investigations within dedicated Krypton campaigns are foreseen in the future.

The steady-state background exhibits a significant (39σ) radial dependency. The radial background rate increase is anticipated, because a large fraction of B_{base} arises from impurities in the main spectrometer walls (see also section 5.10.1). However, the poor linear fit quality ($p = 9.7 \times 10^{-11}$) suggests that the background-pseudo-ring-relation cannot be described well with a linear model.

The positive slope of $N_{\text{sig.}}$ is moderately significant at 1.48σ. Unknown radial differences in the pixel detection efficiency or in the flux tube volume calculation could cause a radial dependent signal normalization. As long as these effects are independent of the retarding energy, they don't jeopardize the neutrino-mass analysis.

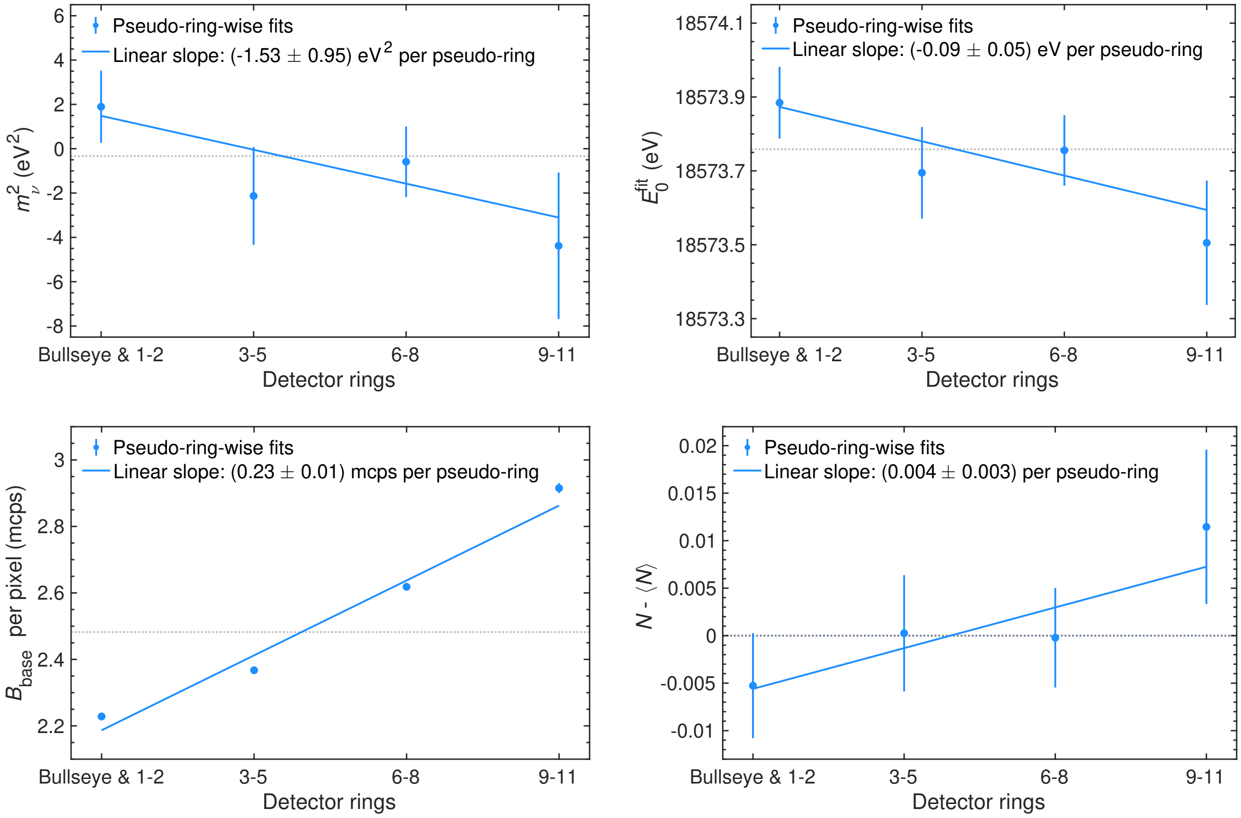

Figure 8.10: Ring-wise analysis of KNM1 data. The latter is grouped into 4 pseudo-rings (table D.1). To search for possible radial patterns, each pseudo-ring is fit independently, inferring m_ν^2, E_0^{fit}, $B_{\text{base}}$and$N_{\text{sig.}}$ respectively. Statistical as well as Non-Poisson uncertainties are taken into account. On top of that, a linear model is fit to each radial parameter evolution. **Top left:** Neutrino mass squared. The linear slope has negative sign and is significant at $1.61\,\sigma$ with a good fit quality $p = 0.48$. **Top right:** Endpoint. The negative slope significant at $1.71\,\sigma$. Linear fit has a good $p = 0.53$. **Bottom left:** Background. The positive slope, anticipated from the physics model of the background, is significant is at $39\,\sigma$. However, the poor $p = 9.7 \times 10^{-11}$ attests that the background rate doesn't increase linearly with pseudo-ring. **Bottom right:** Relative signal normalization. The positive slope is moderately significant at $1.48\,\sigma$. The linear fit has a good fit quality $p = 0.7$.

---

[1] For simplicity, the significance is obtained from scaling the 1σ uncertainty provided from the fit.

8.8 Extended fit interval

The standard analysis interval is restricted to 27 scan steps, ranging from −39 eV below to 47 eV above the fit endpoint. The full measurement interval, however, comprises 39 scan steps and retarding energies down to −93 eV below E_0 (section 5.1).

An extension of the fit interval generally leads to reduced statistical uncertainties, as more data points are included. The drawback are increasing (known) systematic uncertainties one the hand and the risk of unknown energy-dependent systematic effects on the other hand.

In this section, the decision to use the −39 eV range as standard analysis interval is evaluated. Firstly, the fit-range-dependent sensitivity is presented in section 8.8.1. Secondly, the retarding-potential dependence of the fit result is discussed in section 8.8.2.

8.8.1 Fit-interval-dependent neutrino-mass sensitivity

The m_ν^2 sensitivity as a function of fit interval is estimated twice: once using only statistical uncertainties and once taking the complete uncertainty budget into account. The systematic-only sensitivity is calculated according to equation (8.8). Here, the sensitivity is studied rather than actual fit uncertainties of the data analysis, because the best-fit value influences the fit uncertainty. The results are displayed in figure 8.11.

As expected, the statistical m_ν^2 uncertainty decreases monotonously with increasing fit range (decreasing lower fit boundary). Opposed to that, the contribution of systematic uncertainties increases. When the entire measurement interval is analyzed, statistical and systematic uncertainties are in equilibrium.

From the perspective of the m_ν^2 sensitivity alone, a larger analysis interval than the selected −39 eV range would have been profitable in KNM1. However, a more conservative analysis interval was chosen, due to the lack of extensive systematic uncertainty investigations and and ongoing calculations of the excited states of the FSD.

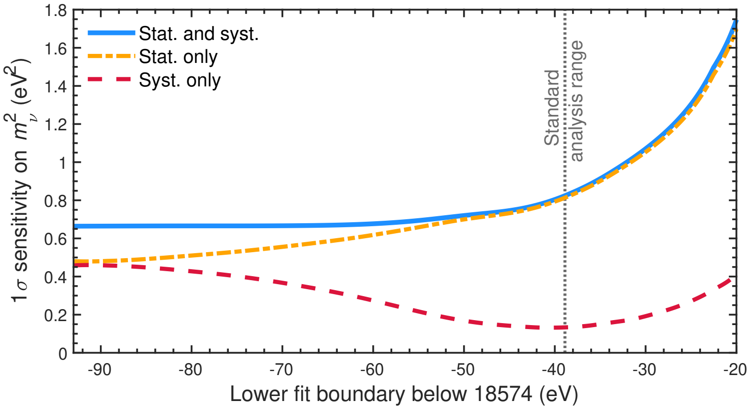

Figure 8.11: Neutrino-mass sensitivity at 68.27 % C.L. for different fit intervals. The sensitivity is calculated using the MC twins.

8.8.2 Retarding-potential fit parameter dependencies

In order to search for energy-dependent systematic effects, fits within different fit intervals are performed. Each fit considers both statistical as well as systematic uncertainties. The upper boundary, $qU = E_0 + 47\,\text{eV}$, is the same for all fit intervals. The lower boundary is increased scan-step-wise from $qU - E_0 = -93\,\text{eV}$ to $qU - E_0 = -19\,\text{eV}$, which results in 23 different fit intervals.

The best-fit parameters as a function of lower fit boundary are displayed in figure 8.12 and figure F.1. The standard analysis interval is highlighted in orange. The reference line is anchored at the corresponding best-fit value. The left-most point corresponds to the largest fit interval (39 scan steps), whereas the right-most point is associated to the smallest fit interval considered (17 scan steps).

Due to the decreasing statistics, the uncertainties on m_ν^2, E_0^{fit} and $N_{\mathrm{sig.}}$ increase from left to right. In contrast to that, the uncertainties on B_{base} are almost independent of the lower fit boundaries, because the background-sensitive scan-steps above the endpoint are included in all considered fit intervals. Even smaller intervals were not analyzed, due to the vanishing sensitivity to m_ν^2.

The fit-interval-dependent fit results are strongly correlated, because they are based in part on the same data. Therefore, it is not straightforward to interpret the observed patterns. Due to the correlation, the fit results are expected to vary less than their fit uncertainties from one analysis interval to another. Additionally, the correlations are not equally strong for all HV set point and fit parameter, because not all scan-steps contribute the same amount to the respective parameter sensitivity.

To estimate the expected variation while taking the correlation into account, a MC simulation on randomized twins is performed. One-thousand sample spectra are generated by randomly drawing from a multivariate distribution given by the fit covariance matrix. Each sample spectrum is then analyzed in the 23 fit intervals defined above. The 23 fit results of each sample are compared to the respective fit value in the standard analysis range. The standard deviation over all samples for each fit interval yields the expected variation. This is visualized in figure 8.12 as the grey uncertainty band.

No significant deviation from the standard analysis range is found and consequently no hint for an unaccounted energy-dependent systematic effect. Hence, an extension to larger analysis ranges could be considered in future neutrino-mass campaigns.

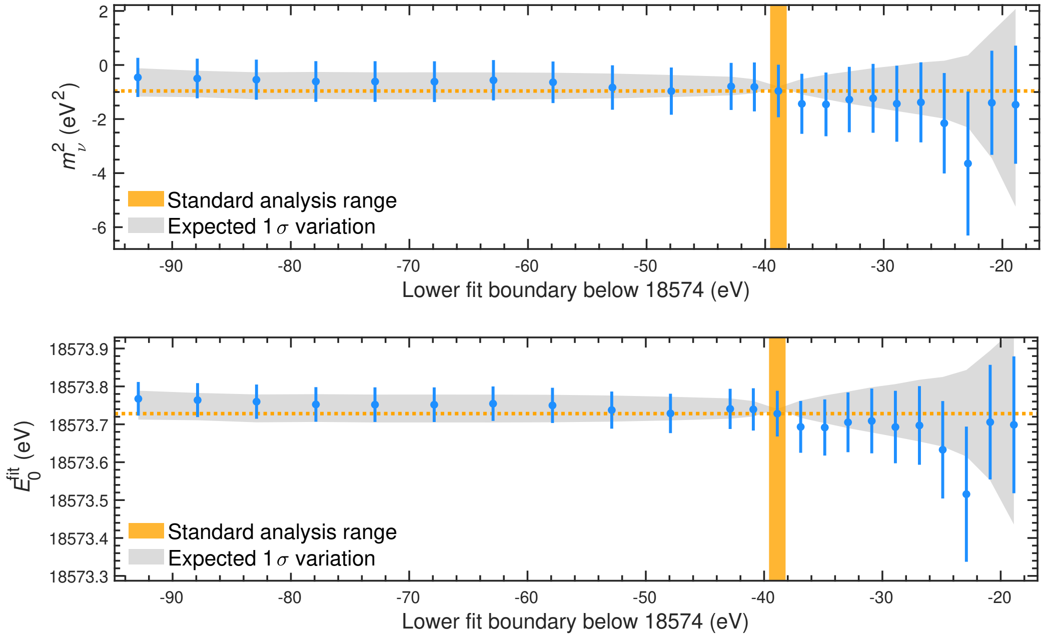

Figure 8.12: Best-fit results of the 4 standard fit parameters as a function of lower fit boundary. Both statistical and systematic uncertainties are taken into account. The upper fit boundary is fixed to $qU = E_0 + 47\,\mathrm{eV}$ and is the same for all fit intervals. The standard analysis range is highlighted in orange. To interpret the correlated fit results, the same study is performed on 1000 randomized MC twins. The expected variation from the fit in the standard analysis interval is displayed as grey uncertainty band. No significant deviation and therefore no hint for an unaccounted energy-dependent systematic effect is found. The retarding-potential dependencies of B_{base}, $N_{\mathrm{sig.}}$ and p can be found in appendix F.1.

8.9 Alternative scan selection

In the standard analysis all 274 golden scans are stacked into one effective spectrum. This is possible due to the excellent time-stability of all operational parameter and the good HV-set-point reproducibility, as discussed in section 8.2.1. To search for systematic effects, that only influence certain scans, a variety of alternative scan lists are analyzed. The latter are subselections from the golden scan list and are based on some common attribute. The alternative scan list *Up scans* comprises for example only scans that were recorded with time-wise increasing (absolute) retarding potentials. All scan lists are defined in detail in appendix D.2.

Every alternative scan selection is analyzed in the standard analysis interval taking statistical and Non-Poisson uncertainties into account. The m_ν^2 best-fit values, 1σ uncertainties and p—values are summarized in figure 8.13. The golden pixel selection is highlighted in green. The fit results are correlated among each other, as they share partly the same underlying data. This complicates the evaluation of the parameter stability. The larger the fraction of common data, the less the fit values are expected to differ between each other. In particular, they are expected to vary less than their fit uncertainties.

To obtain an indication which magnitude of m_ν^2 variations is acceptable, 2000 random scan lists are stacked and analyzed. Each random scan selection contains 137 (half) out of 274 golden scans. The 1σ variation of the resulting m_ν^2 best-fit distribution is displayed as a grey band in figure 8.13. The latter only serves as an orientation, because not all alternative scan selections contain the same number of scans.

All alternative scan lists infer m_ν^2-values within 3σ of the random scan selection. Moreover, 8 out of 12 considered scan selections (66.7 %) even lie within the 1σ uncertainty band. The largest deviation is obtained using the "$U_{\mathrm{RW}} = -183\,\mathrm{meV}$" scan selection, which contains only 19 scans with this particular rear-wall bias voltage. Due to the low statistics, the discrepancy is not significant. The p—values of all scan selections are well above the critical 5 %.

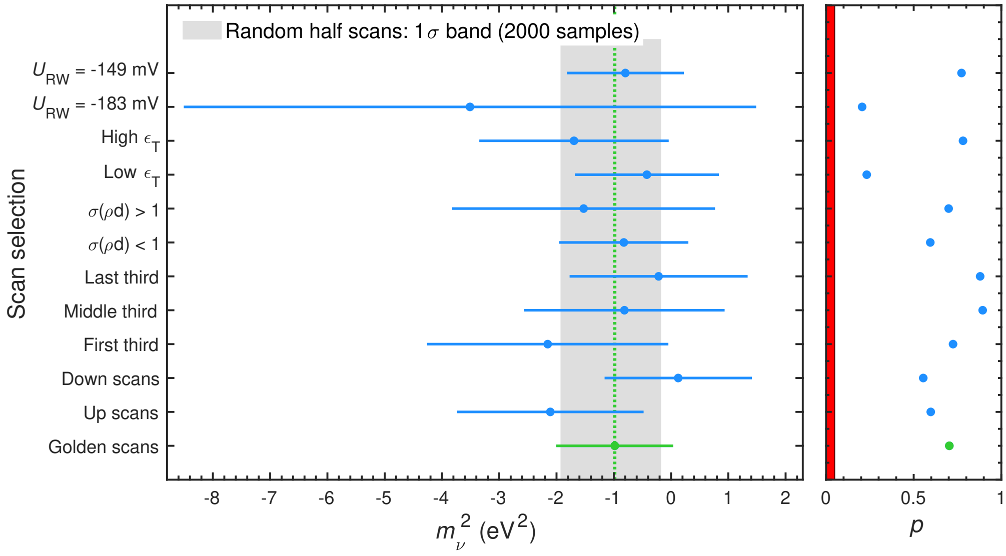

Figure 8.13: Alternative scan selections within the golden scan selection are analyzed for the standard 4 fit parameters. Statistical and Non-Poisson uncertainties are considered. The m_ν^2 fit values with uncertainties (left panel) as well as the fit qualities (right panel) are displayed. The golden scan list is highlighted in green. All fits find a good p-value well above the critical 5 %, indicated in red. The expected degree of m_ν^2 variation is calculated by analyzing 2000 stacked spectra, drawing randomly half of the scans from the golden scan selection. No significant outliers are found. The scan numbers for each alternative scan selection are stated in appendix D.2.

8.10 Alternative pixel selection

To search for systematic effects, that only influence certain areas of the detector, different pixel subselections within the golden pixel list (appendix D.3) are analyzed. In section 8.10.1, alternative pixel lists that contains approximately half of the golden pixels each are analyzed. Section 8.10.2 investigates pixel subselections with different azimuth angles.

8.10.1 Alternative half pixel lists

For each selection, the FPD is divided into two parts of roughly equal statistics. As some FPD areas comprise more inactive pixels than others, the number of pixels is not always the same. The associated pixel lists are given in appendix B. Every alternative pixel selection is analyzed individually for the standard 4 fit parameters taking statistical and Non-Poisson uncertainties into account. The m_ν^2 best-fit values, 1σ uncertainties and $p-$values are displayed in figure 8.14.

The pixel selections come in 3 pairs: "Inner/Outer", "North/South", "East/West". The pixel lists within each pair are the counterparts of each other and are therefore statistically uncorrelated. The significance s of the deviations of fit results i from fit result j can be evaluated as

$$s_{ij} = \frac{|m^2_{\nu,i} - m^2_{\nu,j}|}{\sqrt{\sigma_i^2(m_\nu^2) + \sigma_j^2(m_\nu^2)}}. \tag{8.9}$$

The fit results within a pair deviate by $s = 0.9\sigma$ (Inner/Outer), $s = 1.1\sigma$ (North/South) and $s = 2.0\sigma$ (East/West). A more detailed study on the east-west asymmetry is presented in the following section 8.10.2.

To compare the fits among the pairs or to the golden pixel selection, their correlation has to be taken into account as they are based on partly the same data. Similar to section 8.9, 2000 random pixel lists are analyzed, each comprising half of the active pixels. The grey band in figure 8.14 corresponds to 1σ of the resulting m_ν^2 distribution. All pixel selections lie within 3σ of the uncertainty band. However, the m_ν^2 values based on the eastern and the western pixels exhibit a deviation of $2.5\,\sigma$ compared to the expectation of the random pixel selections.

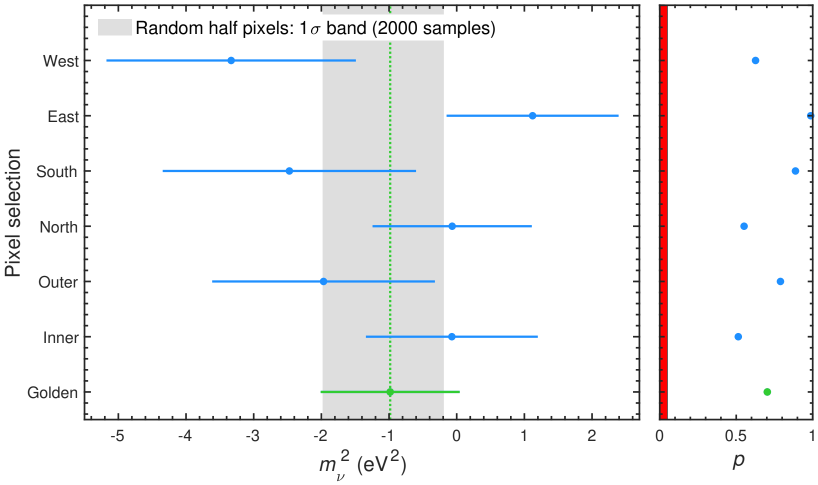

Figure 8.14: Alternative pixel lists within the golden pixel selection are analyzed for the standard 4 fit parameters. Statistical and Non-Poisson uncertainties are taken into account. The m_ν^2 fit values with uncertainties (left panel) as well as the fit qualities (right panel) are displayed. All fits find a good p-value well above the critical 5 %. The alternative selections can be grouped into three pairs, whose pixel numbers are counterparts of each other. The m_ν^2 fit values of eastern and western pixels deviate by 2.0σ from each other. The remaining pairs show no significant deviation. To compare all pairs among each other, 2000 random pixel selection are analyzed, each comprising half of the active pixels.

8.10.2 Azimuthal position

In the previous section, an east-west asymmetry in m_ν^2 of elevated significance was found. To investigate the azimuthal dependence with a higher angular resolution, the pixels are grouped according to their azimuth angle θ_{FPD} on the FPD. The finest subdivision comprises 24 slices, depicted in figure 3.1 (c), whose pixels all have the same average azimuth angle. As the statistics within each slice is rather low, the slices are further on grouped into 8 pseudo-slices, illustrated in figure B.1 (e). Each pseudo-slice comprises three neighboring slices. The associated pixel numbers are summarized in appendix B.

Each pseudo-slice is fit considering statistical uncertainties and the Non-Poisson over-dispersion. The neutrino-mass-fit result is shown in figure 8.15 as a function of $\langle\theta_{\mathrm{FPD}}\rangle$. The best-fit results of E_0^{fit}, B_{base} and $N_{\mathrm{sig.}}$ are given in appendix F.2. The respective fits of the pseudo-slices with the three smallest mean azimuth angles $\langle\theta_{\mathrm{FPD}}\rangle \in \{0°, 45° \text{ and } 90°\}$ yield positive m_ν^2-values, whereas all other pseudo-slices find negative m_ν^2. The significance of the m_ν^2 deviation between these two groups is 2.3σ. The m_ν^2-asymmetry between eastern and western halves (section 8.10.1) is thus driven by the north-west region of the detector (small azimuth angle).

However, the m_ν^2 distribution is also compatible with a constant ($p = 0.28$). As no physical effect is known that could cause an azimuth-dependence in m_ν^2, the observed asymmetry is likely to be a statistical fluctuation.

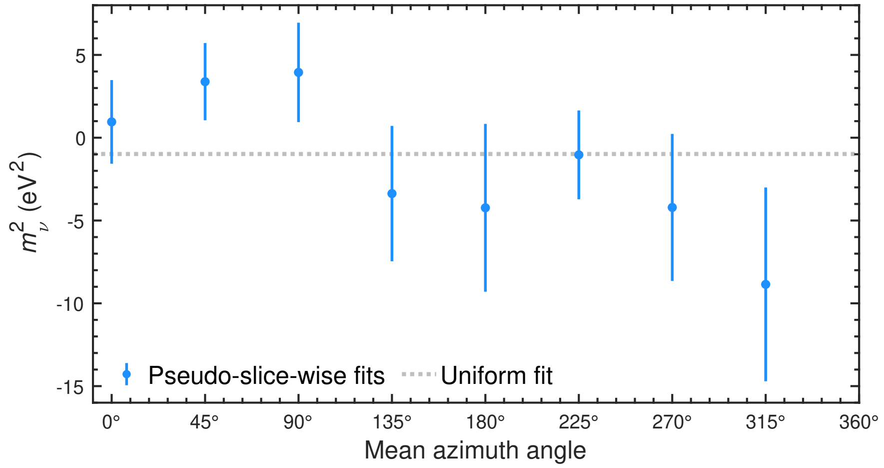

Figure 8.15: Neutrino-mass-squared as a function of azimuthal FPD position. The azimuth angle of 0° is assign to north. The angle is measured clockwise.

8.11 Statistical tests with CATS

The data set is further on subjected to statistical tests to search for unusual behavior using the diagnostics toolkit CATS [105]. The latter is based on a local linearization of the chi-squared function. Systematic uncertainties are taken into account with a covariance matrix.

8.11.1 Cook's distance

The Cook's distance D evaluates the degree of influence of each data point on the fit result. One the one hand, its calculation is based on the normalized residuals r_i, displayed in the middle panel of figure 8.5. Normalized residuals are useful to spot outliers in the data set. On the other hand, the leverage l_i of each data point is considered

$$\ell_i = \frac{\partial R_\beta^{\mathrm{model}}(m_\nu^2, E_0^{\mathrm{fit}}, B_{\mathrm{base}}, N_{\mathrm{sig.}}, qU_i)}{\partial R_\beta^{\mathrm{data}}(qU_i)}. \tag{8.10}$$

The leverage describes the potential of a data point to influence the best-fit model. In other words, ℓ_i reflects the sensitivity of a scan-step i on the free model parameters. A leverage of $\ell = 0$ corresponds to no influence, whereas $\ell = 1$ indicates that one degree of freedom is effectively spend to infer that particular scan step.

The Cook's distance is then calculated as follows

$$D_i = \frac{|r_i|^2}{n_{\text{par}}} \cdot \frac{\ell_i}{(1 - \ell_i)} \tag{8.11}$$

with $n_{\text{par}} = 4$ being the number of free fit parameters. A large residual combined with a high leverage results in a large Cook's distance. Data points with $D \geq 1$ may distort the accuracy of the fit result and thus merit further investigations [105].

Figure 8.16 displays the standardized residuals as a function of their leverage for each scan-step. The regions with $D \geq 0.5$ and $D \geq 1$ are highlighted in blue and red color respectively. As already discussed in section 8.5.1, r varies within less than 3σ. Thus, no outlier is observed. The scan step measured at the lowest retarding energy ($qU - 18\,574\,\text{eV} = -39\,\text{eV}$) has a slightly elevated leverage $l = 0.36$. Being the data point with the highest statistics, this scan-step drives the determination of the signal normalization and has there therefore a large leverage.

No data point with large cook's distance in the critical region $D > 1$ is observed.

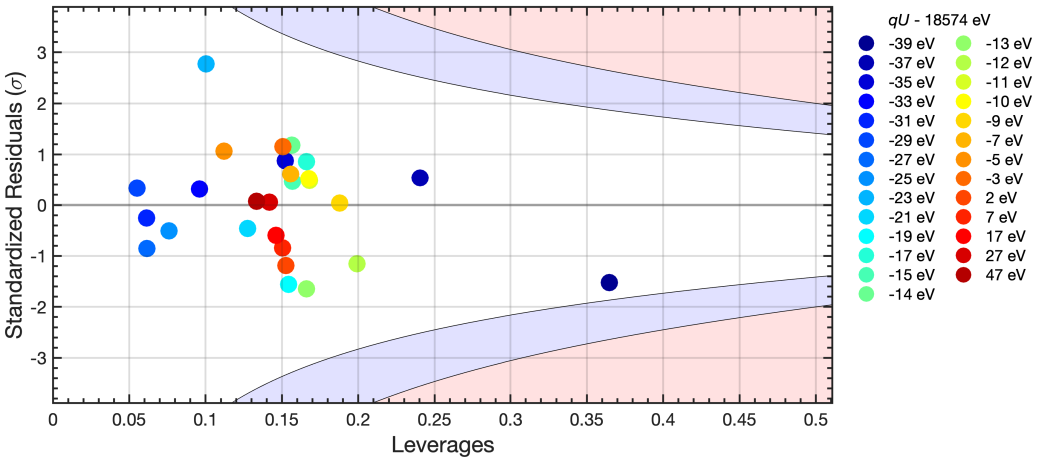

Figure 8.16: The influence of each scan-step on the fit result is evaluated. Standardized residuals r of all data point are displayed as a function of leverages ℓ. A data point with both large r and high ℓ has a large Cook's distance D. If D is larger than 1, the data point can potentially jeopardize the accuracy of the fit result. However, no influential data point is observed.

8.11.2 Fits with excluded data points

This section performs an alternative method to search for influential data points. One data point at a time is excluded from the analysis, effectively removing information from the chi-squared function. The change of the fit result with respect to the fit with all data points indicates the influence of the removed data point. A strongly changing fit result indicates a large influence of the associated data point and vice versa.

The m_ν^2 fit values as a function of removed scan step is presented in figure 8.17. The fit results are strongly correlated among each other, therefore the fit uncertainties are not displayed. For reference, $\sigma(m_\nu^2) = 0.97\,\text{eV}^2$ for the standard analysis range. No distinct pattern is visible, which is supported by a runs test $p_{\text{runs}} = 0.26$. As the fits are based partly on the same data, m_ν^2 is expected to vary less than its uncertainty. However, only qualitative statements can be made, because the MC expectation was not calculated due to high computing time.

Scan steps with little neutrino mass sensitivity, e.g. scan steps far above the endpoint, have as expected only little impact an the fit parameter. The region most sensitive to m_ν^2 is located around $qU - 18\,574\,\mathrm{eV} \approx -10\,\mathrm{eV}$ (see appendix F.3). As many data points are distributed at these retarding energies (figure 8.5 c)), the removal of a single point influences the fit result only slightly. A moderate change $\mathcal{O}(0.5\mathrm{eV}^2)$ is observed upon the removal of individual data point at $qU - 18\,574\,\mathrm{eV} = \{-19\,\mathrm{eV}, -23\,\mathrm{eV}, -39\,\mathrm{eV}\}$, respectively.

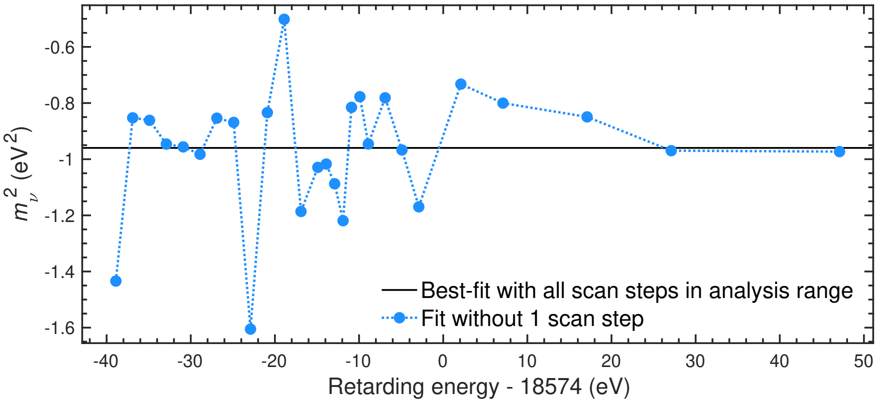

Figure 8.17: The influence of each scan step on the fit result is determined by successively excluding scan steps from the analysis. Here, the m_ν^2 fit result as a function of removed data points is shown. In the region, which is most sensitive to m_ν^2 ($qU - 18\,574\,\mathrm{eV} \approx -12\,\mathrm{eV}$), large changes are expected. The fit uncertainties are not included in the figure, because the fit results are strongly correlated.

8.12 Reanalysis with updated model configuration

After the original publication in [96, 101], a reanalysis with slightly updated model configuration was performed. Both original and updated settings are summarized in table C.2. Both FSD and energy-loss function are replaced by a slightly more refined version, that was also used for the KNM2 analysis. Additionally, the non-isotropic transmission is included in the reanalysis, because its impact on m_ν^2 is larger than previously expected. Moreover, the existence of the scan-step-time-dependent background was only discovered during the second measurement campaign. For KNM1 the time-wise background rate increase has a slope of $s_{\mathrm{time}} = (2.2 \pm 4.3)\,\mu\mathrm{cps/s}$. All other configuration and systematic uncertainties are identical to section 8.5.

The result of the reanalysis is displayed in figure 8.18. Including all updates and systematic uncertainties, the reanalysis yields $m_\nu^2 = (-1.14 \pm 1.00)\,\mathrm{eV}^2$, which is $0.17\,\mathrm{eV}^2$ more negative than the original result. This best-fit value would thus not change the LT-limit reported in section 8.5.3. The goodness of fit of the reanalysis $\chi^2_{\mathrm{min}} = 21.2\,(23\,\mathrm{dof}\, p = 0.57)$ improves slightly with respect to the original publication by $\Delta\chi^2_{\mathrm{min}} = 0.5$.

To estimate the influence of the individual model updates, the latter are switched on one-by-one. The new final-state distribution and energy-loss function cause only minor changes in m_ν^2 by $\mathcal{O}(10^{-3}\,\mathrm{eV}^2)$. The inclusion of the non-isotropic scattering probabilities in the transmission function has with $\Delta m_\nu^2 = -8 \times 10^{-2}\,\mathrm{eV}^2$ the largest influence on the neutrino mass. Only slightly smaller (in absolute) follows the scan-step-time-dependent background rate with $\Delta m_\nu^2 = -6 \times 10^{-2}\,\mathrm{eV}^2$.

Compared to the sensitivity of $\sigma(m_\nu^2) \approx 1\,\mathrm{eV}^2$, the updated model configuration does not change the outcome of the neutrino mass-analysis significantly.

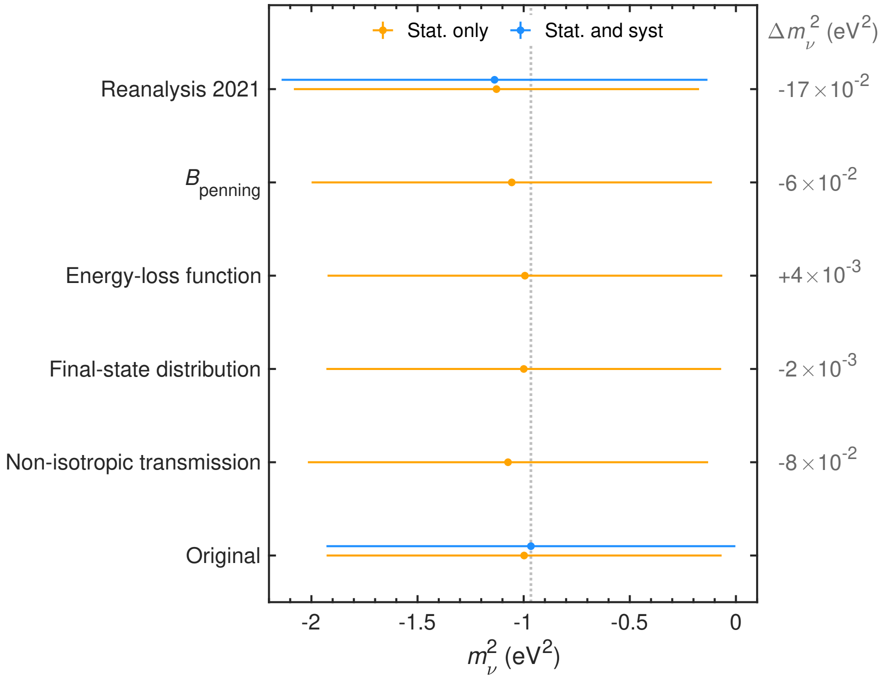

Figure 8.18: The standard neutrino-mass analysis is repeated with an updated model configuration. The new settings are stated in table C.2. The reanalysis finds $m_\nu^2 = (-1.14 \pm 1.00)\,\mathrm{eV}^2$, which is more negative than the original result by $0.17\,\mathrm{eV}^2$. This shift is mostly driven by the implementation of the non-isotropic transmission function and the scan-step-time-dependent background rate. Overall, the reanalysis is consistent with the original publication considering the KNM1 neutrino mass sensitivity of $\sigma(m_\nu^2) \approx 1\,\mathrm{eV}^2$.

Chapter 9

Neutrino-mass analysis of KNM2

This chapter is dedicated to the neutrino-mass analysis of the KNM2 data set. Many methods are similar to the KNM1 neutrino-mass analysis. In theses cases the corresponding KNM1 sections are referenced to avoid lengthy repetitions.

9.1 Monte Carlo Twins

The analysis chain is validated first on MC twins following the blinding protocol described in chapter 7. The KNM2 MC twins are calculated according to section 7.1 with a constant endpoint of $E_0 = 18\,573.70\,\mathrm{eV}$ for all scans. Moreover, the effective source potential broadening (section 6.6.4) and the scan-step-time dependency of the background rate (section 6.10.5) are included.

9.2 Data combination

The KNM2 data set comprises 361 golden scans with 117 golden pixels each, which results in 43 327 golden tritium spectra. Thanks to the excellent stability of the relevant experimental parameters (see chapter 6), these low-statistics spectra can be combined to a great extend.

Different combination strategies are introduced in general in section 3.2. In the following, the selected scan (section 9.2.1) and pixel (section 9.2.2) combination techniques for the KNM2 analysis are discussed. The focus is put on their respective validation in terms of neutrino-mass bias.

9.2.1 Scan combination

All golden scans are combined through stacking. This is possible due to the excellent scan-wise stability of the experimental parameters. The most critical parameter in this context is the high-voltage reproducibility, as discussed in section 4.9. The observed $\langle \sigma(qU) \rangle = 10\,\mathrm{meV}$ (section 6.7) is expected to induce a neutrino-mass bias of $\Delta m_\nu^2 \approx 2 \times 10^{-4}\,\mathrm{eV}^2$, which is negligible compared to the neutrino-mass sensitivity. As the high-voltage reproducibility is slightly different for each set point, the neutrino-mass bias is also calculated by a fit to the stacked MC twin spectrum. The fit result coincides with the expectation. Consequently, stacking is a suitable run combination technique for KNM2.

9.2.2 Pixel combination

Due to pixel-wise variations of qU (section 6.7) and B_ana (section 6.8), the stacking of different pixels can lead to a neutrino-mass bias. The latter is estimated through a simulation: An integral spectrum is calculated for each golden pixel using the associated qU and B_ana values. The spectra are then stacked and fit using the average model. If all golden pixels are stacked, the (uniform) fit finds $\Delta m_\nu^2 = 3 \times 10^{-3}\,\mathrm{eV}^2$, which is negligible given the

KNM2 sensitivity. Consequently, the uniform fit is justified in terms of electric and magnetic field homogeneity in the analyzing plane. The same applies to multi-ring fits, because the number of combined pixels is smaller than in the uniform case.

Apart from analyzing plane inhomogeneities, the FPD segmentation can also be used to search for radial variations of the source potential. As discussed in section 6.6.3, neither rate monitor point nor krypton data analysis found a considerable radial source-potential dependency. Nevertheless, the main neutrino-mass analysis of the tritium scans performs a multi-ring fit with four pseudo-rings and ring-wise potential offsets to be conservative.

9.3 Spectral model configuration

The specral model configuration that is used in the KNM2 analysis is summarized in appendix C.

9.4 Scan-wise analysis: Nuisance parameter stability

To evaluate the temporal system stability, all 361 golden scans are analyzed individually. As the neutrino-mass-squared sensitivity in a single scan is relatively low $\sigma(m_\nu^2) \approx 6.5\,\mathrm{eV}^2$ (68.3 % C.L.), m_ν^2 is fixed to zero. Moreover, the single-scan fits include only statistical uncertainties and the enhanced statistical background rate uncertainty from the Non-Poisson over-dispersion. The standard analysis range is used (section 6.1).

The uniform fit results of effective endpoint (section 9.4.1), steady-state background rate (section 9.4.2) and signal normalization (section 9.4.3) are presented in the following. Analogous to KNM1 (section 8.4), their compatibility with no time dependence is evaluated in terms of a p-value according to equation (8.1) with $N_{\mathrm{scan}} = 361$ and 360 dof. Moreover, the Wald-Wolfowitz runs test with p_{runs} is performed to search for non-random patterns (see also section 8.4). At the end, the scan-wise goodness-of-fit is evaluated in section 9.4.4.

9.4.1 Effective tritium endpoint

The fit endpoint, displayed in figure 9.1, varies with $\sigma(E_0^{\mathrm{fit}}) = 0.168\,\mathrm{eV}$ around its weighted mean $\langle E_0^{\mathrm{fit}} \rangle = (18\,573.679 \pm 0.009)\,\mathrm{eV}$. The chi-squared test yields $p = 0.92$, which means that the temporal endpoint evolution is compatible with a constant.

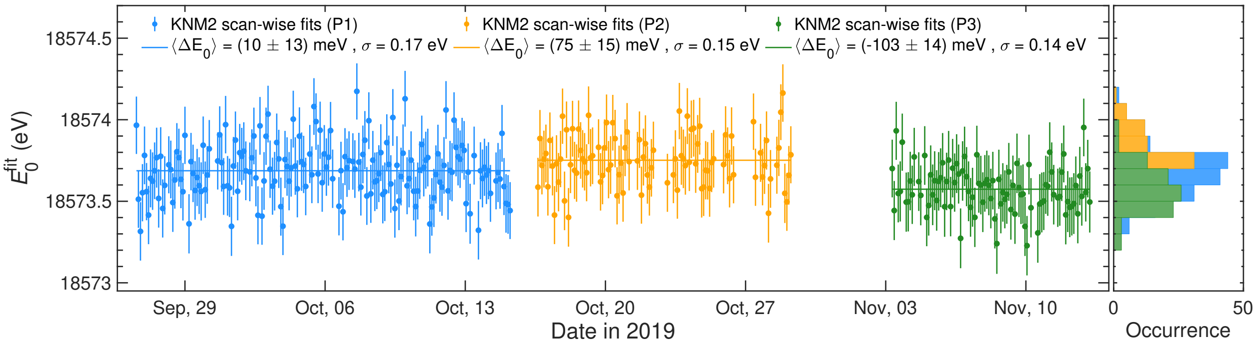

Figure 9.1: Scan-wise fit results of the effective endpoint as a function of live time in KNM2. The colors indicate the three different rear-wall periods. Within uncertainties, the endpoint is compatible with no time dependence. Key values concerning the temporal stability are summarized in table 9.1.

However, the rear-wall bias voltage was adjusted twice during KNM2 (see section 6.6.2), which should lead to three different source potentials and consequently to three different effective endpoints. The scan-wise fit results associated to the three rear-wall periods are highlighted in different colors in figure 9.1. The period-wise mean endpoints, summarized in table 9.1, differ up to 93 meV from each other. These endpoint differences agree within uncertainties with the relative source potential shifts[1], that were obtained from the rate monitor analysis in section 6.6.2.2. The runs test finds no significant deviation from random occurrence with $p_{\text{runs}} \geq 0.25$ for all rear-wall periods.

Data (sub-) set	$\langle E_0^{\text{fit}} \rangle$ (eV)	$\sigma(E_0^{\text{fit}})$ (eV)	p	p_{runs}
All golden scans	$18\,573.679 \pm 0.009$	0.168	0.92	0.25
Rear-wall period 1	$18\,573.689 \pm 0.013$	0.166	0.87	1.00
Rear-wall period 2	$18\,573.754 \pm 0.015$	0.152	0.94	0.38
Rear-wall period 3	$18\,573.576 \pm 0.014$	0.137	1.00	0.39

Table 9.1: The temporal stability of the fit endpoint is evaluated over the course of KNM2. Within uncertainties it is compatible with no time-dependence. The runs test attests no significant deviation from random occurrence. Moreover, the three rear-wall periods are examined individually. The period-wise mean endpoint differ significantly up 93 meV from each other.

9.4.2 Steady-state background rate

The fit results of the steady-state background rate are shown in figure 9.2 as a function of live time. The background rate significantly increased by (0.38 ± 0.04) mcps/day[2] over the course of KNM2. The average background rate is $\langle B_{\text{base}} \rangle = 220.1$ mcps. The runs test on the corrected rate yields $p_{\text{runs}} = 1.2\,\%$, which hints towards non random occurrence.

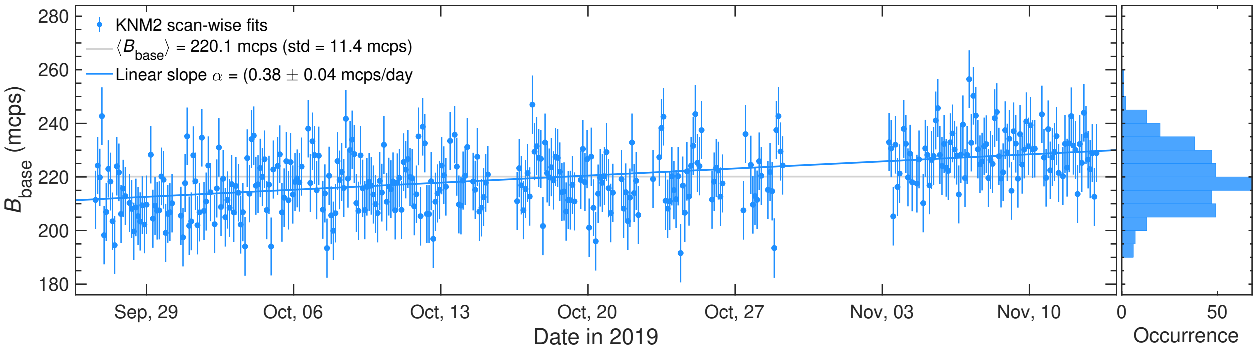

Figure 9.2: Scan-wise fit results on the steady-state background rate. The background rate increased over the course of KNM2 by (0.38 ± 0.04) mcps/day.

9.4.3 Signal normalization

The scan-wise signal normalization factor is displayed in figure 9.3. It varied by $\sigma(N_{\text{sig.}}) = 2\,\%$ over the course of KNM2. Its time evolution is compatible with a constant $p = 0.997$. Moreover, no pattern is visible, which is supported by $p_{\text{runs}} = 0.87$.

9.4.4 Goodness-of-fit

The temporal p-value evolution is depicted in figure 9.4. Large p-values occur more often than small ones. Only three out of 361 fits obtain a goodness-of-fit below the acceptance threshold of $p < 0.05$. Indeed, the Kolmogorow-Smirnow-Test rejects the (expected) uniform hypothesis. A possible reason for this could be that the

---

[1] A more positive source potential translates into a smaller endpoint, because the β-electrons are negatively charged. Therefore, the endpoint differences have to be compared to the *negative* source potential shifts.

[2] The time-wise slope is obtained from a linear fit. The goodness-of-fit is $p = 0.97$.

fit uncertainties are overestimated. Given that only statistical uncertainties and the Non-Poisson background rate over-dispersion are considered, this explanation seems unlikely.

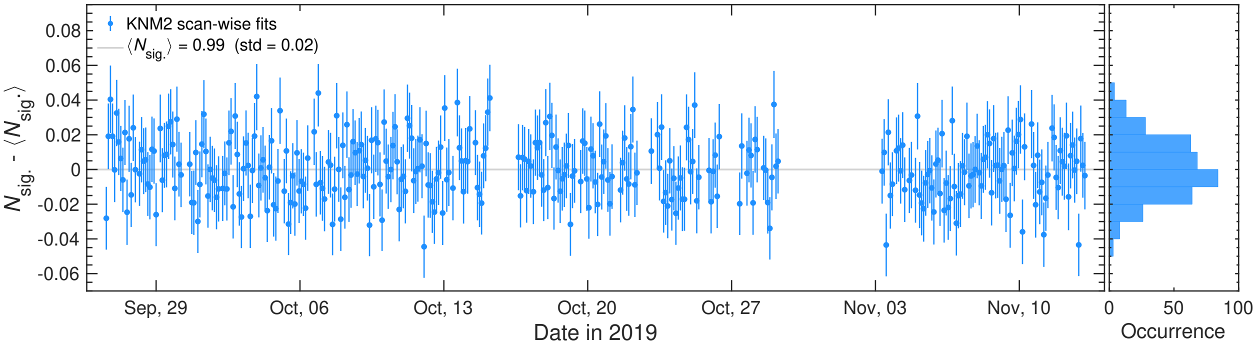

Figure 9.3: Scan-wise fit results of the signal normalization factor in KNM2. The time evolution is compatible with a constant.

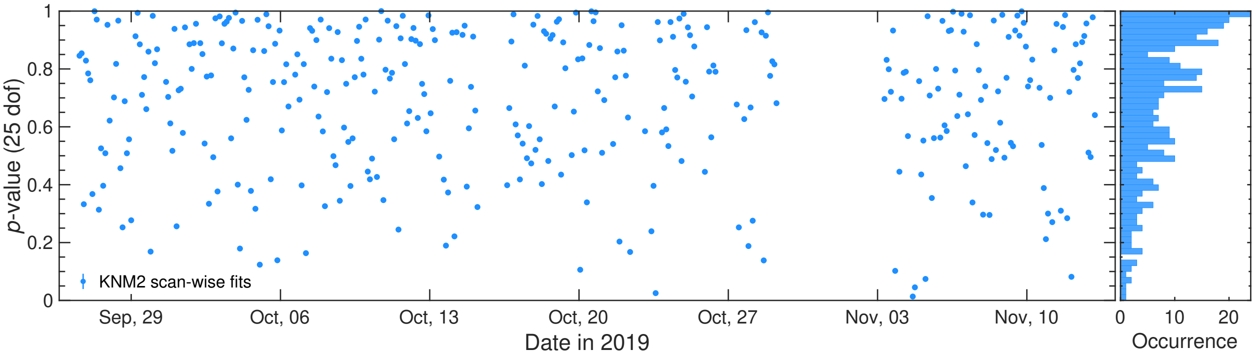

Figure 9.4: Temporal p-value evolution of the scan-wise fits. As can be seen in the right panel, the associated distribution does not follow a uniform distribution. Large p-values occur more often than small ones. However, no distinct non-random pattern is visible ($p_{\text{runs}} = 0.73$).

9.5 Baseline neutrino-mass analysis

This section presents the baseline analysis of the KNM2 campaign, which is a stacked multi-ring fit using four pseudo-rings. The fit is performed in the standard analysis interval. Statistical as well as systematic uncertainties are included. Best-fit parameters (section 9.5.1), chi-squared profile (section 9.5.2), fit parameter correlations (section 9.5.4) and improved upper limit (section 9.5.3) are discussed.

9.5.1 Best-fit result

The measured integral spectrum and the best-fit model are displayed in the top panel of figure 9.5. Data and model agree well with each other, which is mirrored by the good $p = 0.79$ ($\chi^2_{\mathrm{min}} = 87.3$ at 99 dof). The standardized residuals are displayed in the lower panels of figure 9.5 for each pseudo-ring. They exhibit no irregular pattern ($p_{\mathrm{runs}} \geq 0.25$ for all pseudo-rings). All residuals are smaller than 2.1σ. Thus, no outlier is observed.

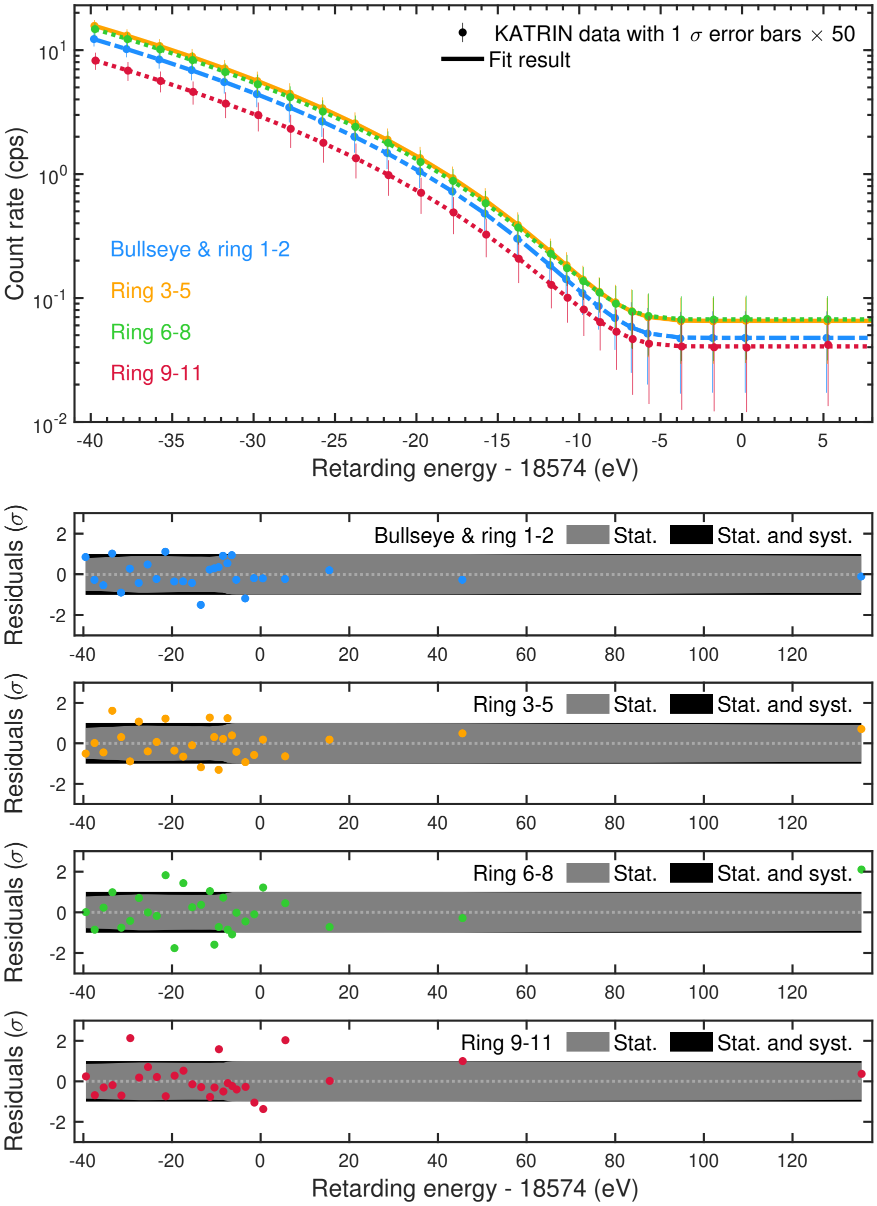

Figure 9.5: Multi-ring fit with four pseudo-rings to KNM2 data. **Top panel:** Overlay of data and best-fit model for each pseudo-ring. To improve the visibility, the (statistical) error bars are scaled by a factor of 50. **Bottom four panels:** The residuals for each pseudo-ring are normalized with the diagonal entry of the covariance matrix, that is used in the fit. All scan-steps have small residuals $< 2.1\sigma$. Moreover, the runs test does not find any suspicious patterns.

The multi-ring fit with four pseudo-rings comprises 13 free fit parameters: The physics parameter of interest, namely m_ν^2, is the same for all pseudo-rings. The nuisance parameters $\boldsymbol{\eta} = [E_0^{\text{fit}} + \Delta qU,\, B_{\text{base}},\, N_{\text{sig.}}]$ can take different values for each pseudo-ring. Due to technical reasons, the effective fit endpoint is split into a shared component E_0^{fit} and pseudo-ring-wise potential offsets ΔqU. The best-fit values are:

$$\begin{aligned} m_\nu^2 &= (0.26^{+0.33}_{-0.32})\,\text{eV}^2 && (9.1)\\ E_0^{\text{fit}} + \langle \Delta qU \rangle &= (18\,573.77 \pm 0.04)\,\text{eV} && (9.2)\\ \sum B_{\text{base}} &= (220.3 \pm 0.5)\,\text{mcps} && (9.3)\\ \langle N_{\text{sig.}} \rangle &= 0.987 \pm 0.003. && (9.4) \end{aligned}$$

Within uncertainties, m_ν^2 is compatible with zero. Best-fit value and its uncertainty are translated into an upper limit in section 9.5.3.
The $E_0^{\text{fit}} + \langle \Delta qU \rangle$ fit value is 0.04 eV larger than the KNM1 result. However, both values are compatible within uncertainties. Due to different source conditions in KNM2 and KNM1, the effective tritium endpoint could in principle differ between the first two measurement campaigns. However, large deviations $\mathcal{O}(1\,\text{eV})$ are not expected.

The ring-wise best-fit results are displayed in figure 9.6 and figure G.1. The effective fit endpoint exhibits a slight increase with increasing radial position. The fitted slope however is insignificant (1.6σ). As already seen in the background scan-step analysis in section 6.10.1, the steady-state background increases significantly as a function of radius. A linear fit finds an increase of $(0.144 \pm 0.004\,)$ mcps per pixel / pseudo-ring. The poor goodness-of-fit indicates that the radial pattern cannot be modeled well with a linear relation.

The signal normalization factor, displayed in figure G.1, exhibits no significant radial pattern. The fit values are compatible with a constant.

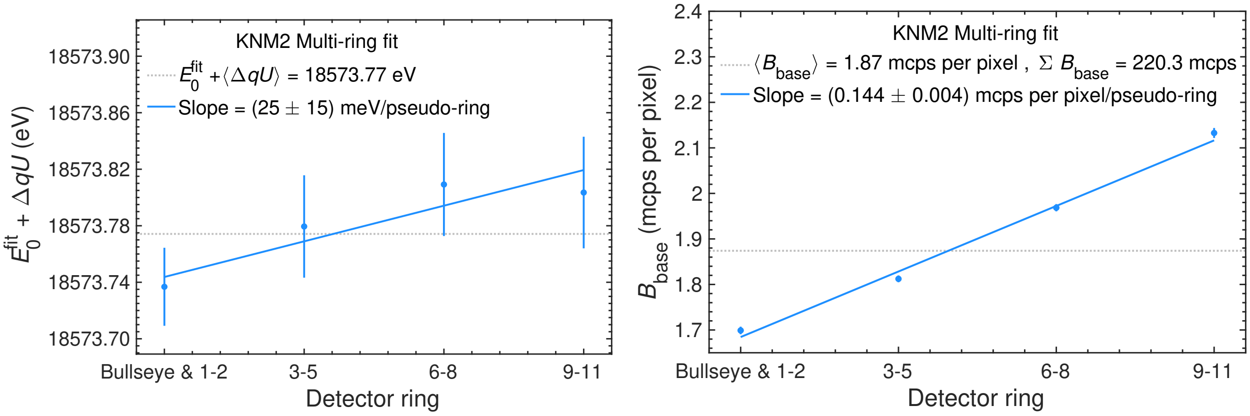

Figure 9.6: Pseudo-ring-dependent fit parameters in the KNM2 multi-ring fit with four pseudo-rings. **Left:** Effective fit endpoint with pseudo-ring-wise potential offsets. The effective endpoint is compatible with no radial dependence with $p_{\text{const}} = 0.34$. A linear fit yields a slight positive slope at low significance (1.6σ). **Right:** Steady-state background rate per pixel. B_{base} increases significantly as a function of radius with $(0.144 \pm 0.004\,)$ mcps per pixel / pseudo-ring. However, its radial distribution is also not compatible with a simple linear behavior.

9.5.2 Profile chi-squared

To cross check the best-fit result and uncertainties provided by the Minuit software using the Minos minimization algorithm, the profile chi-squared is calculated (see also section 8.5.2 for KNM1 profile). The chi-squared function is depicted in figure 9.7 for two cases: considering only statistical uncertainties (orange) and considering all uncertainties (blue). The m_ν^2 central value and uncertainty agree with the result from Minos in equation (9.1).

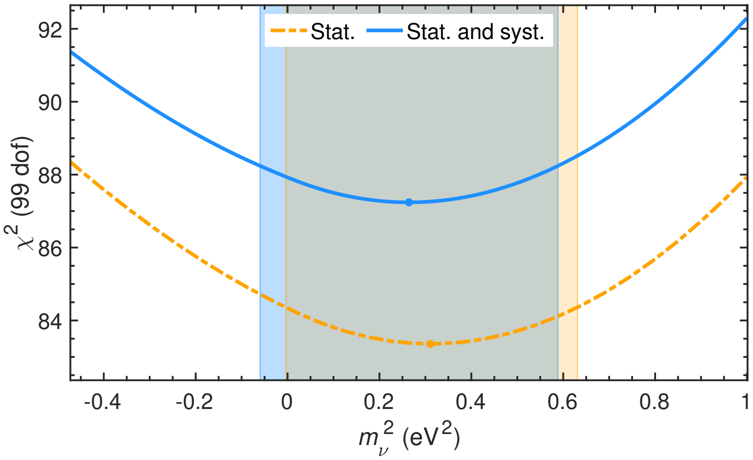

Figure 9.7: KNM2 chi-squared profile for multi-ring fit using statistical uncertainties (orange) and all uncertainties (blue). The 1σ uncertainties agree with the values from Minos.

9.5.3 Confidence belt and upper limit

The KNM2 sensitivity is not high enough to significantly determine the neutrino mass. Just like in KNM1 (section 8.5.3), it was decided before the unblinding that a confidence belt at 90 % C.L. will be calculated. Following the statistical methods in section 3.3.2, the Lokhov-Tkachov [82] and Feldman-Cousins [80] confidence belts are calculated with the MC twins. They are displayed in figure 9.8. The sensitivity at 90 % C.L., assuming $m_\nu^2 = 0\,\text{eV}^2$, is

$$m_\nu \leq 0.7\,\text{eV} \quad \text{(sensitivity)}. \tag{9.5}$$

This is the first time, that a direct neutrino-mass experiment could reach into the sub-eV sensitivity regime. The orange dotted lines in figure 9.8 mark the m_ν^2 baseline best-fit result and the resulting upper limits at 90 % C.L.

$$m_\nu \leq 0.9\,\text{eV} \quad \text{(Lokhov} - \text{Tkachov)} \tag{9.6}$$

$$m_\nu \leq 0.9\,\text{eV} \quad \text{(Feldman} - \text{Cousins)}. \tag{9.7}$$

Opposed to KNM1, the best-fit has a positive sign. Therefore, the LT and FC limits agree with each other. To date, this is the best upper limit on m_ν from a direct neutrino-mass measurement.

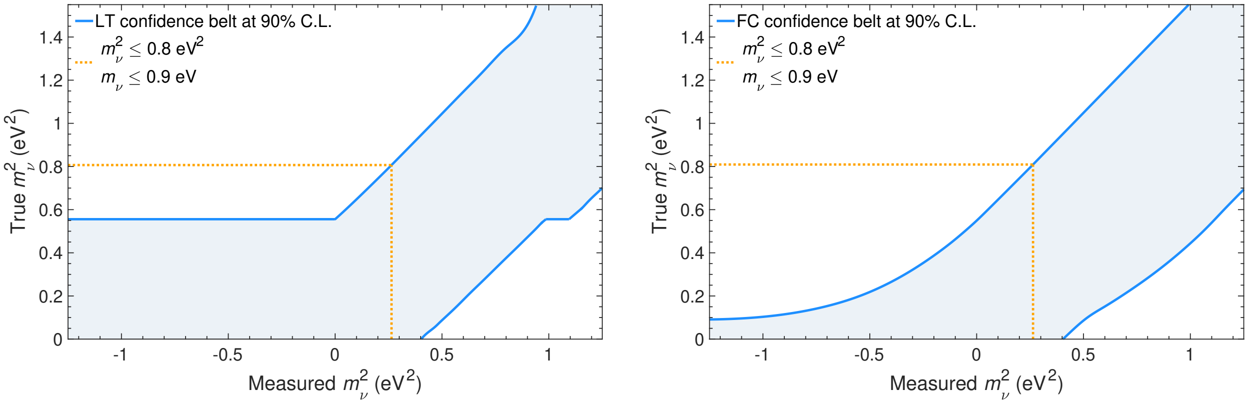

Figure 9.8: Neutrino-mass confidence belts at 90 % C.L. following the statistical strategies from LT [82] (**left**) and FC [80] (**right**). The neutrino-mass sensitivity at 90 % C.L. is $m_\nu \leq 0.7\,\text{eV}$. The orange lines highlight the KNM2 multi-ring best-fit result (equation (9.1)). Both limit-setting strategies yield the same upper limit $m_\nu \leq 0.9\,\text{eV}$ at 90 % C.L., rendering KNM2 the first direct neutrino-mass measurement that could reach into the sub-eV regime.

9.5.4 Fit parameter correlations

The correlation coefficients among the fit parameters are estimated by analyzing 2000 randomized KNM2 MC spectra. The KNM2 best-fit results are used as model inputs for their calculation. Statistical as well as systematic uncertainties are taken into account in the randomization process and in the fit. For simplicity, a uniform fit rather than a multi-ring fit is performed. By construction, the ring-wise fit parameter are fully correlated in a multi-ring fit. Therefore, no additional information can be gained in a multi-ring fit compared to the much faster uniform fit.

The fit results are displayed in figure 9.9. The histograms on the diagonal illustrate the KNM2 sensitivity to the respective fit parameter. The density scatter plots on the off-diagonal illustrate their correlations. The sample density is indicated by the coloring and ranges from low (dark blue) to high (yellow). The respective Pearson correlation coefficients are stated in the top left corners. Associated uncertainties are estimated via the bootstrapping technique.

As the interpretation is analogous to KNM1 (section 8.5.4), only differences between the two measurement campaigns are discussed further on. Due to different experimental conditions and systematic uncertainties, the parameter correlation are not expected to be identical in KNM1 and KNM2. Most notably and anticipated due to the increasing statistic, the correlation coefficient between m_ν^2 and E_0^{fit} is significantly reduced by 9 percentage points. According to the guideline offered by [104], it is now only considered as *high* instead of *very high*. The remaining considerable correlations coefficients only vary within a few percentage points or are compatible within uncertainties.

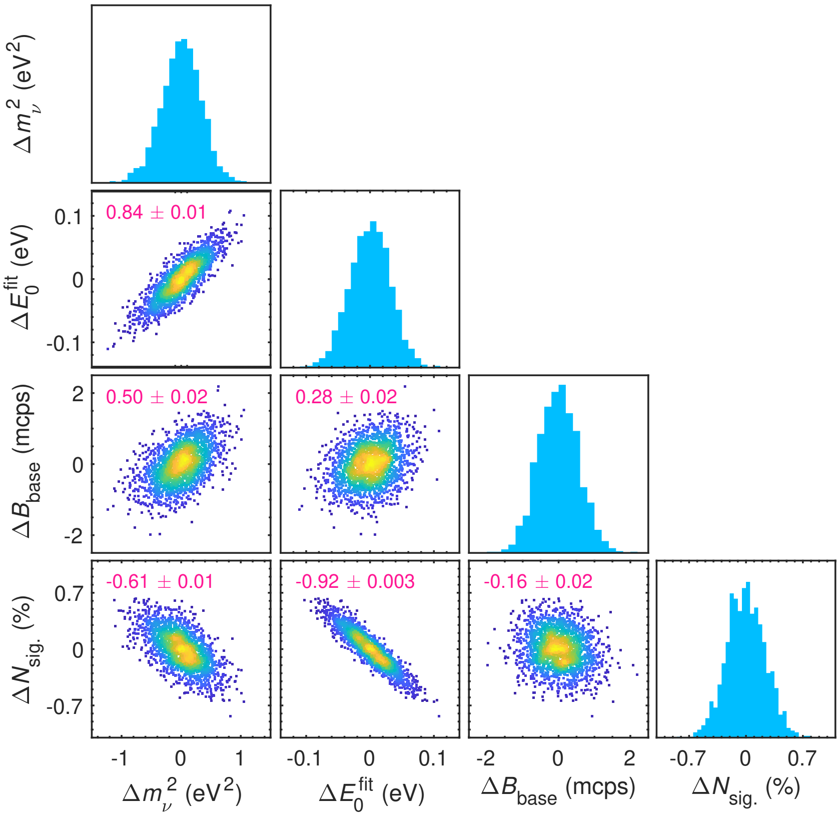

Figure 9.9: The Pearson correlation coefficient quantifies the linear relation between two fit parameters. It is estimated for all uniform fit parameters following the same technique as for KNM1 (section 8.5.4) using 2000 randomized KNM2 MC spectra. The fit-value distribution of each parameter is shown in the diagonal. Their correlations are illustrated on the off-diagonal by the scatter plots. The sample density is indicated by the color code ranging from low (dark blue) to high density (yellow). The Pearson correlation coefficient and its bootstrapping uncertainty are stated in the top left corners, respectively.

9.6 Comparison of pixel combination strategies

Different pixel combination strategies are applied to the KNM2 data and compared to each other. As demonstrated in section 9.2.2, all strategies are equally well justified due to the excellent electric and magnetic field homogeneity in the analyzing plane. The baseline neutrino-mass result presented in this section stems from a multi-ring fit, which has the advantage to be able to accommodate radial source potential differences in form of a pseudo-ring-wise qU-offset. However, no significant radial pattern was observed. The fit results of the different pixel combination strategies should thus be compatible with each other.

The m_ν^2 fit results are displayed in figure 9.10. A uniform fit, as well as multi-ring fits with four and twelve pseudo-rings, respectively, are considered. Indeed, the m_ν^2 best-fit values vary only $\Delta m_\nu^2 < 0.04\,\mathrm{eV}^2$ from each other. Translated into upper limits on m_ν at 90 % C.L., the deviations are as small as $\Delta m_\nu < 0.01\,\mathrm{eV}$. The small differences originate likely from the different parametrizations and numerical effects.

Based on this excellent agreement, most systematic investigations and sanity checks that follow are performed with a uniform fit, as it is less computational expensive. For reference, the uniform fit results are stated in appendix G.2.

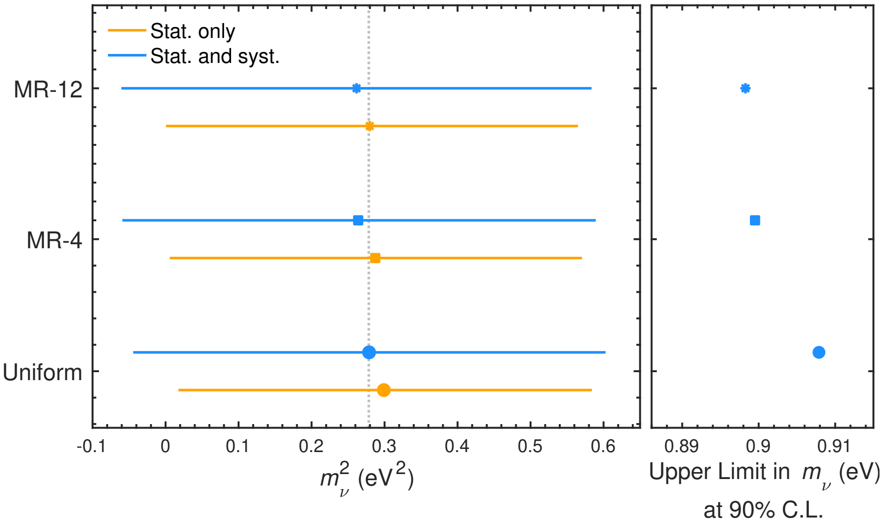

Figure 9.10: Overview of m_ν^2 best-fit values and m_ν-upper limit for different pixel combination strategies. The results from the different fits are in excellent agreement with each other.

9.7 Systematic uncertainty breakdown

The contribution of individual systematic effects σ_{syst}^i to the total m_ν^2 uncertainty budget is evaluated with the same method as in KNM1 (section 8.6). The uncertainty breakdown at 68.3 % C.L. for both data and twin is displayed in figure 9.11 using a multi-ring fit with four pseudo-rings. The associated covariance matrices are displayed in appendix E.7.

If only statistical uncertainties are included, the 1σ-neutrino-mass uncertainty is $\sigma_{\mathrm{stat}}(m_\nu^2) = 0.28\,\mathrm{eV}^2$. Including all (statistical and systematic) uncertainties, the neutrino-mass uncertainty increases to $\sigma_{\mathrm{tot}}(m_\nu^2) = 0.32\,\mathrm{eV}^2$. The (squared) difference (equation (8.8)) can be attributed to systematic uncertainties $\sigma_{\mathrm{syst}}(m_\nu^2) = 0.16\,\mathrm{eV}^2$. The KNM2 analysis is by far dominated by statistical uncertainties.

As in KNM1, the largest contribution to the systematic uncertainty budget is the Non-Poisson background rate over-dispersion. Moreover, second and third largest effect are the scan-step-time-dependent background rate and the uncertainty from the source potential distribution.

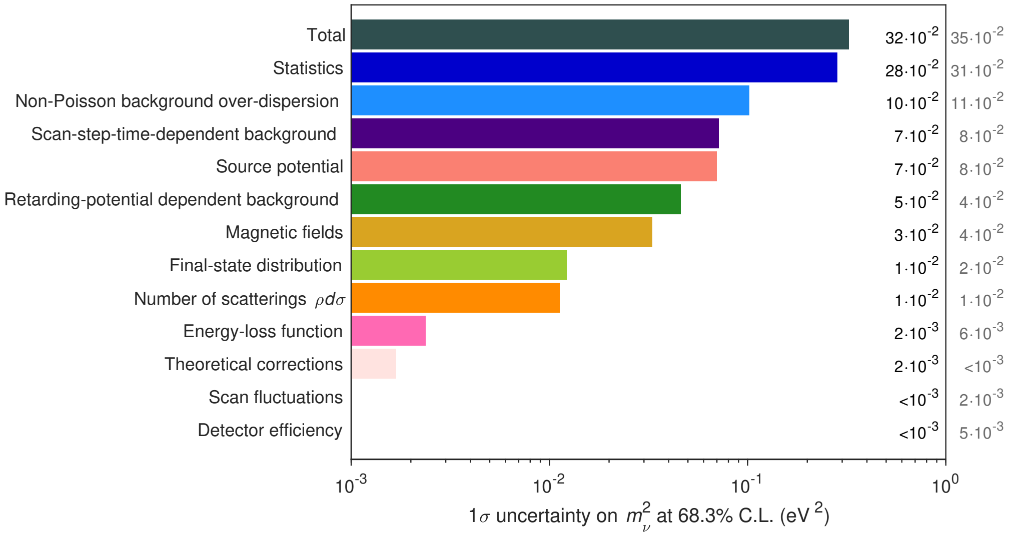

Figure 9.11: Neutrino-mass uncertainty breakdown for the KNM2 multi-ring fit with four pseudo-rings. Statistical uncertainties $\sigma_{\text{stat}}(m_\nu^2) = 0.28\,\text{eV}^2$ dominate over systematic uncertainties $\sigma_{\text{syst}}(m_\nu^2) = 0.16\,\text{eV}^2$. The influence of individual systematic effects on the m_ν^2 uncertainty is summarized above. The Non-Poisson background rate over-dispersion has the largest impact. The corresponding sensitivity values are given as reference on the right.

9.8 Radial-dependent neutrino mass

Being a physical constant, m_ν^2 is considered to be the same for all detector rings in the multi-ring fit in section 9.5.1. However, systematic effects, such as an unknown inhomogeneity of the source potential, are able to cause a radial m_ν^2 dependency if they are not accounted for in the spectral model. To investigate if such a significant systematic effect was missed, the detector rings are analyzed independently from each other. Each ring is fit with the standard four fit parameters (m_ν^2, E_0^{fit}, B_{base}, $N_{\text{sig.}}$). Statistical uncertainties and the uncertainty from the Non-Poisson background rate over-dispersion are taken into account. The m_ν^2 fit results are displayed in figure 9.12 as a function of detector ring. The remaining fit parameters are shown in appendix G.3 for reference.

No conspicuous structure of m_ν^2 as a function of detector ring is visible. A linear regression, fit to the m_ν^2 best-fit values, has only low significance (1.4σ). Within uncertainties, the radial m_ν^2 values are compatible with a constant function at $p = 0.13$. Thus, the existence of an overlooked systematic effect that would cause a significant radial neutrino dependency mass can be excluded.

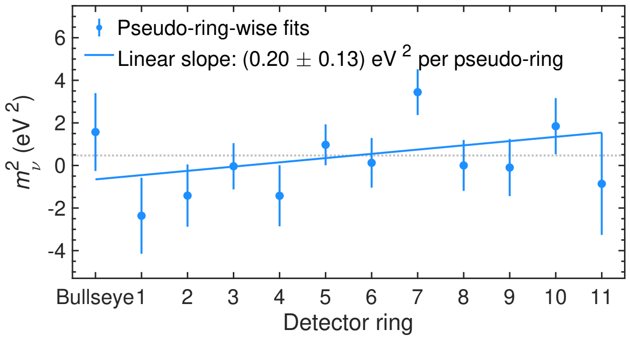

Figure 9.12: To investigate if a large systematic effect was overlooked in the KNM2 analysis, the ring-wise spectra are analyzed individually. The m_ν^2 best-fit values are shown here. The grey reference line corresponds to the associated weighted mean. The m_ν^2 best-fit values are compatible with no radial dependence at $p = 0.13$. The remaining fit parameters are presented in appendix G.3.

9.9 Alternative treatment of retarding-potential-dependent background rate

The systematic uncertainty on the retarding-potential dependency of the background rate is the fourth largest systematic effect in KNM2 with $\sigma_{\mathrm{syst}}(m_\nu^2) = 0.05\,\mathrm{eV}^2$ (figure 9.11). Its influence on the m_ν^2 uncertainty is mostly driven by the external constraint $\sigma(s_{qU}) = 4.74\,\mathrm{mcps/keV}$ (see appendix G.4), which stems from background measurements during FT. As discussed in section 6.10.4, its applicability to KNM2 is debatable. The alternative approach to account for a possible retarding-potential background rate dependency through a nuisance parameter is discussed in section 4.10.3. In the following, the concept is applied to the KNM2 data.

The introduction of s_{qU} as a nuisance parameter will affect the m_ν^2 best-fit result through their correlation. The latter is estimated by analyzing[3] 1000 randomized MC twin spectra. Each spectrum is fit twice: i) with unconstrained s_{qU} and ii) with fixed $s_{\mathrm{qU}} = 0\,\mathrm{mcps/keV}$. The best-fit results of case i) are displayed in figure 9.13. The resulting Pearson's correlation coefficient is $\rho(m_\nu^2, s_{\mathrm{qU}}) = -0.34 \pm 0.03$, which can be considered as low. Even though low, the correlation is expected to reduce the neutrino-mass sensitivity and to potentially change its best-fit value. The negative sign means that a positive background slope can be compensated to some extend by a smaller neutrino mass squared. Moreover, the differences in the m_ν^2 best-fit values between the case i) and case ii) are shown in appendix G.4. Deviations of $\sigma(\Delta m_\nu^2) = 0.06\,\mathrm{eV}^2$ can be expected. Proceeding to the data, the experimental spectrum is fit with s_{qU} as an additional nuisance parameter. A stacked uniform fit is performed considering statistical and systematic uncertainties. In order to not account for the retarding-potential dependency twice, the systematic effect is removed from the covariance matrix.

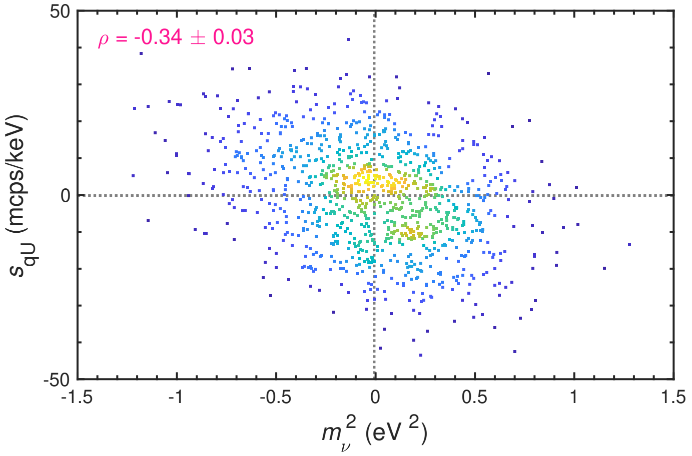

Figure 9.13: The correlation between m_ν^2 and s_{qU} is estimated by analyzing 1000 randomized MC simulations.

To first cross check the covariance matrix method applied in section 9.7, a Gaussian pull term is used according to equation (4.12) with $\sigma(s_{qU}) = 4.74\,\mathrm{mcps/keV}$. The best-fit value of s_{qU} is consistent with zero ($< 1\sigma$). Moreover, the systematic uncertainty contribution $\sigma_{\mathrm{syst}}(m_\nu^2) = 0.05\,\mathrm{eV}^2$ agrees as expected with the one from the covariance matrix method (figure 9.11).

Thereafter, the background slope is left unconstrained in the data analysis. The fit result is

$$m_\nu^2 = (0.08 \pm 0.36)\,\mathrm{eV}^2$$
$$s_{qU} = (24.2 \pm 12.3)\,\mathrm{mcps/keV}$$

---

[3] Stacked uniform fits in the standard analysis interval considering statistical uncertainties and the Non-Poisson background rate over-dispersion are performed.

A positive qU dependence of the background rate at moderate significance (2σ) is observed. Due to the negative correlation, the neutrino mass squared is shifted to smaller values. The difference to the standard uniform fit with fixed s_{qU} is $\Delta m_\nu^2 = -0.2\,\mathrm{eV}^2$, which is at the higher end of what can be expected. The influence of $\sigma(s_{qU})$ on the neutrino-mass uncertainty increases to $\sigma_\mathrm{syst}(m_\nu^2) = 0.16\,\mathrm{eV}^2$, rendering it the largest systematic uncertainty in the absence of an external constraint. This demonstrates that a strong and robust constraint on s_{qU} is essential for the neutrino-mass analysis.

9.10 Extended fit interval

Similar to KNM1, more scan-steps were recorded than eventually used for the KNM2 baseline analysis. As described in section 6.1, the full measurement interval consists of 38 scan-steps down to $qU - E_0 = -90\,\mathrm{eV}$. Not all data points were included in the neutrino-mass analysis, because most systematic uncertainties increase with increasing fit range. This concern in particular the final-state distribution, as the electronic ground state is known to a much higher precision than the electronic excited states and the electronic continuum. Refined calculations are on-going at the time of writing.

Analogous to KNM1 (section 8.8), an extension of the fit interval is investigated in terms of neutrino-mass sensitivity (section 9.10.1) and m_ν^2 best-fit result (section 9.10.2).

9.10.1 Fit-interval-dependent neutrino-mass sensitivity

The neutrino-mass-squared sensitivity as a function of fit interval is evaluated using the MC twins. The upper fit boundary is fixed to the largest retarding energy $qU - E_0 = 135\,\mathrm{eV}$. The lower fit boundary is scan-step-wise increased from $qU - E_0 = -90\,\mathrm{eV}$ to $qU - E_0 = -20\,\mathrm{eV}$, which results in 21 different fit intervals. The sensitivity values between the (discrete) lower fit boundaries are obtained through cubic spline interpolation. Figure 9.14 displays the 1σ sensitivity using the total uncertainty budget (blue). Further on, it is broken down into the contributions from statistical uncertainties (orange) and from systematic uncertainties (red). The systematics-only curve is calculated according to equation (8.8).

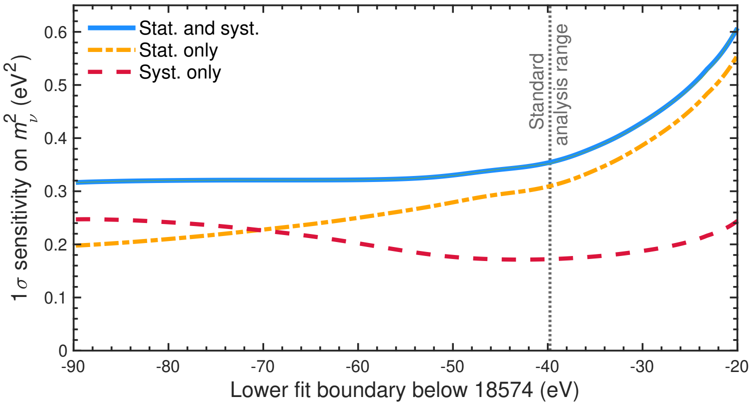

Figure 9.14: The neutrino-mass-squared sensitivity at 68.27 % C.L. is calculated from the MC twins for different fit intervals. While, the upper fit boundary is fixed to the largest retarding energy $qU - E_0 = 135\,\mathrm{eV}$, different lower fit boundaries are considered. The smaller the lower fit boundary, the more scan-steps are included. The sensitivity is evaluated twice: once considering the total uncertainty budget and once using only statistical uncertainties. The systematics-only contribution can then be calculated according to equation (8.8).

As already stated section 9.7, the m_ν^2 sensitivity in the standard analysis interval is dominated by statistical uncertainties with $\sigma_\mathrm{stat}(m_\nu^2) = 0.31\,\mathrm{eV}^2$. The latter can be significantly improved by including more scan-steps. If the full analysis interval is fit, $\sigma_\mathrm{stat}(m_\nu^2) = 0.20\,\mathrm{eV}^2$. In contrast to that, the systematic contribution increases slightly if the lower fit boundary is set to $-90\,\mathrm{eV}$ below E_0. The equilibrium between statistical and systematic uncertainties is reached at $qU - E_0 = -70\,\mathrm{eV}$. However, already for $qU - E_0 < -60\,\mathrm{eV}$, the improvement of adding another scan-step is negligible $\Delta\sigma_{\mathrm{stat}}(m_\nu^2) < 1 \times 10^{-3}\,\mathrm{eV}^2$.

9.10.2 Retarding-potential fit parameter dependencies

As described in section 8.8.2, unknown energy-dependent systematic effects can manifest themselves in energy-dependent best-fit values of m_ν^2. To search for the latter, the experimental spectrum is repeatedly fit with different fit intervals. The considered fit intervals are the same as in the sensitivity calculation in the previous section.

The m_ν^2 and E_0^{fit} fit results are displayed in figure 9.15. The remaining fit parameters and goodness-of-fits are shown in appendix G.5. The reference lines are anchored at the respective fit result in the standard analysis range.

Due to their high correlation, m_ν^2 and E_0^{fit} exhibit a similar retarding-potential-dependent pattern. The large majority of the fit intervals yield smaller m_ν^2 and E_0^{fit} values than the standard analysis interval. However, the runs test yields $p_{\mathrm{runs}} = 0.15$ for both parameters, attesting no significant deviation from random occurrence.

As explained in detail in section 8.8.2, the scan-step-wise fit results are strongly correlated among each other, as they are based on partly the same data. Thus, a quantitative evaluation of the fit-parameter stability is not straight forward. Similar to the analysis in KNM1, the expected retarding-potential-dependent difference to the fit result in the standard analysis range is calculated. This is achieved by analyzing 1000 randomized MC twins in the fit intervals of interest. The 1σ expectation band is illustrated in grey in figure 9.15. The fit results vary within the correlated expectation band.

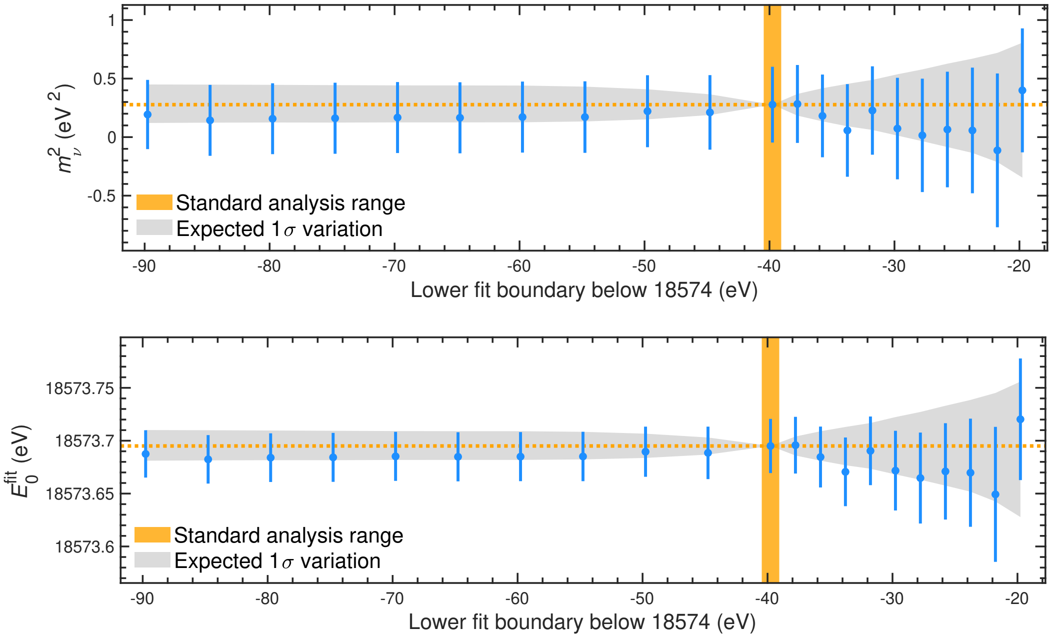

Figure 9.15: The data is analyzed in different fit intervals with a stacked uniform fit with systematic uncertainties. The lower fit boundary is varied, while the upper fit boundary is fixed to the largest retarding energy. The m_ν^2 and E_0^{fit} results are shown here. The remaining nuisance parametrs and goodness-of-fit are displayed in appendix G.5.

9.11 Alternative scan selection

As a sanity check, several sub-sets of the golden scan list are analyzed individually. The concept is identical to section 8.9. The alternative scan lists for KNM2 are given in appendix E.2. The m_ν^2 fit results are compared among each other and to the best fit from the golden scan selection in figure 9.16.

The alternative scan lists *Up scans* and *Down scans* comprise only scans that were recorded with time-wise increasing and decreasing retarding energies respectively. Being statistically uncorrelated, their m_ν^2 fit results agree within uncertainties. The same applies to the three alternative scan lists that group the golden scans according to the rear wall bias voltage U_{RW}. The central m_ν^2 values decrease monotonously with increasing U_{RW}. However, the slope obtained from a linear regression is not significant ($< 1\sigma$).

As described in figure 9.16, the comparison of all scan lists among each other is not straight forward, because they share partly the same data. Taking the correlation into account, a 1σ expectation band is calculated by randomly drawing 181 out of 361 golden scans. The results of all alternative scans lists lie within the expectation ($\leq 1.6\sigma$).

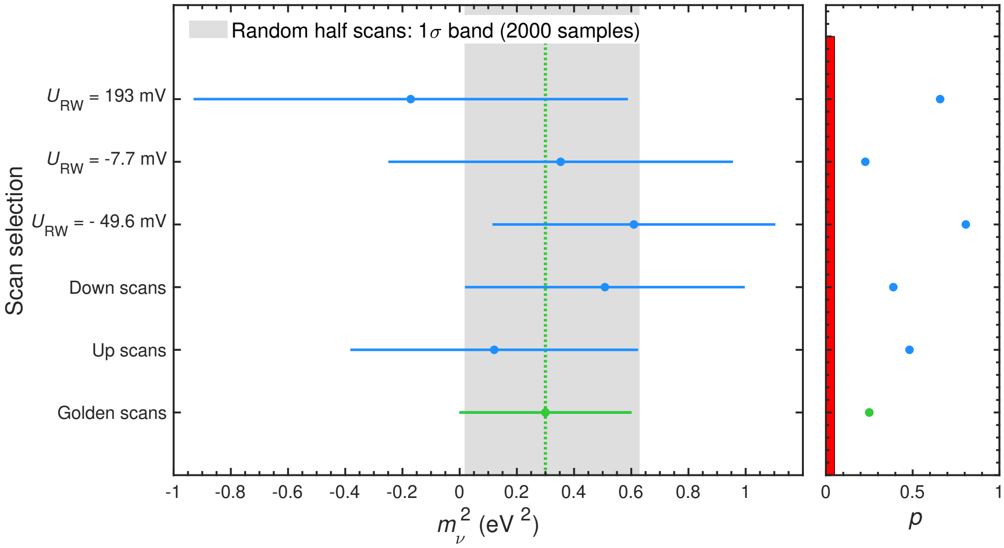

Figure 9.16: KNM2 alternative scan selections. Uniform fits are performed to each scan selection considering statistical uncertainties and the Non-Poisson background rate over-dispersion. The m_ν^2 results agree within uncertainties. Moreover, all fits yield good p-values (right panel) well above 5 % (red band).

9.12 Alternative pixel selection

As a sanity check, different pixel sub-sets within the golden pixel selection are analyzed. Each selection divides the FPD in two parts of roughly equal statistics: "Inner/Outer", "North/South", "East/West". The concept of this analysis is identical to section 8.10.1.

The neutrino-mass-squared results are displayed in figure 9.17. Northern and southern as well as Eastern and western halves agree very well with each other ($< 1\sigma$). The division into inner and outer pixels differ by 2σ from each other, which is still acceptable. The radial m_ν^2 dependence was investigated in section 9.8 in more detail using a finer radial resolution. No significant pattern could be found.

Moreover, the alternative pixel selections are compared to the expectation from 2000 random pixel lists. Each pixel list, containing a random sub-selection of 59 out of 117 golden pixels, is analyzed. The grey band in figure 9.17 corresponds to 1σ of the obtained m_ν^2 distribution. All alternative pixel selections agree with the expectation at $< 3\sigma$.

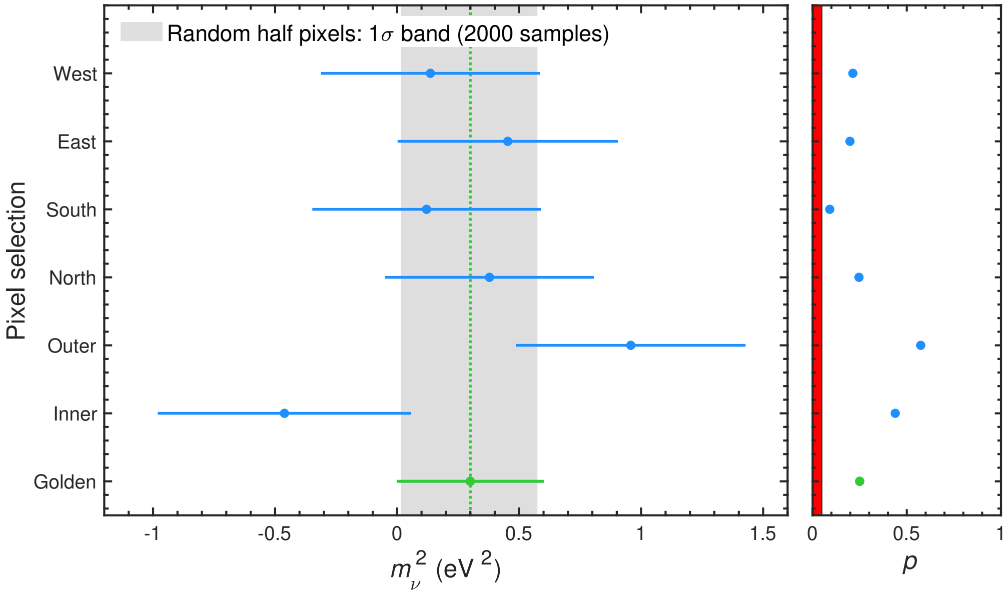

Figure 9.17: KNM2 alternative pixel selections. Uniform fits are performed to each pixel selection considering statistical uncertainties and the Non-Poisson background rate over-dispersion. The m_ν^2 fit results agree within uncertainties.

9.13 Statistical tests with CATS

The data set is further on tested for statistical anomalies. The diagnostics toolkit CATS [105] is used, which is based on local linearization of the chi-squared function. Systematic uncertainties are accounted for, as usual, with covariance matrices. For simplicity a uniform instead of a multi-ring fit is considered. The Cook's distance is evaluated in section 9.13.1. The influence of individual data points on the fit result is determined in section 9.13.2.

9.13.1 Cook's distance

The Cook's distance D is defined in section 8.11.1. It relates standardized residuals and leverages to detect influential data points. A scan-step with large D may distort the accuracy of the fit result and deserves further investigation. The scan-step-wise KNM2 values are displayed in figure 9.18. The critical regions with $D \geq 0.5$ and $D \geq 1$ are colored in blue and red, respectively. All standardized residuals lie within $< 3\sigma$, thus no outlier is observed. Like in KNM1, the leverages of all scan steps are low expect for the scan step with the smallest retarding energy $qU - E_0 = -40\,\text{eV}$. This data point is particularly sensitive to the overall signal normalization, because of its high statistics. As the agreement between model and data is excellent for this scan step, its Cook's distance is well outside the critical region.

To conclude, based on the Cook's distance no influential data points could be found.

9.13.2 Fits with excluded data points

The influence of individual data points on the fit results is evaluated analogous to KNM1 (section 8.11.2). The data is fit repeatedly, each time removing a different scan step from the analysis[4]. The m_ν^2 best-fit results as a function of excluded scan step are shown in figure 9.19. The fit uncertainties are not stated in the figure, because they are strongly correlated. Due to this correlation, the m_ν^2 values are expected to vary less than their fit uncertainty. For reference $\sigma(m_\nu^2) = 0.32\,\text{eV}^2$ in the standard analysis interval. The exact degree of variation could be calculated with randomized MC twins. Due to high computational cost, this was not done. Qualitative

---

[4] Stacked uniform with systematic uncertainties.

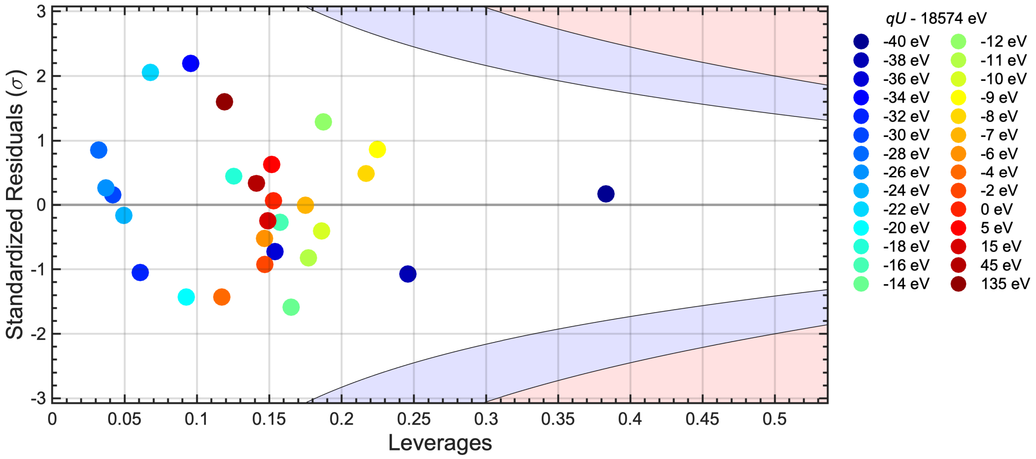

Figure 9.18: Standardized residuals as a function of leverage for the KNM2 uniform fit with systematic uncertainties. High Cook's distances, which are regions with large residual and high leverage, are highlighted: $D \geq 0.5$ and $D \geq 1$ are shaded in blue and red color respectively. All scan-steps are well outside the critical region.

statements, however, are still possible. The largest change is expected in the region that is most sensitive to m_ν^2, which is $qU - E_0 \approx -8\,\text{eV}$[5].

The differences to the baseline best-fit result are smaller than $\Delta m_\nu^2 = 0.12\,\text{eV}^2$, which is only a fraction of the overall 1σ m_ν^2 sensitivity. As expected, the largest differences can be found in the high m_ν^2 sensitivity region.

Interestingly, also the removal of the scan step in the background region at $qU - E_0 \approx 135\,\text{eV}$ induces a relative large change $\Delta m_\nu^2 = 0.10\,\text{eV}^2$. This scan step is very sensitive to the retarding-potential dependency of the background rate, which is known the be negatively correlated to m_ν^2. In this analysis the model uses $s_{\text{qU}} = (0.00 \pm 4.74)\,\text{mcps/keV}$. As the s_{qU} central value is fixed to zero in the model, the observed positive s_{qU} (section 9.9) is compensated by a more positive m_ν^2 value. If the considered scan step is removed, the observed s_{qU} is significantly reduced (figure 6.14). Thus, the m_ν^2 fit value is smaller compared to the baseline fit.

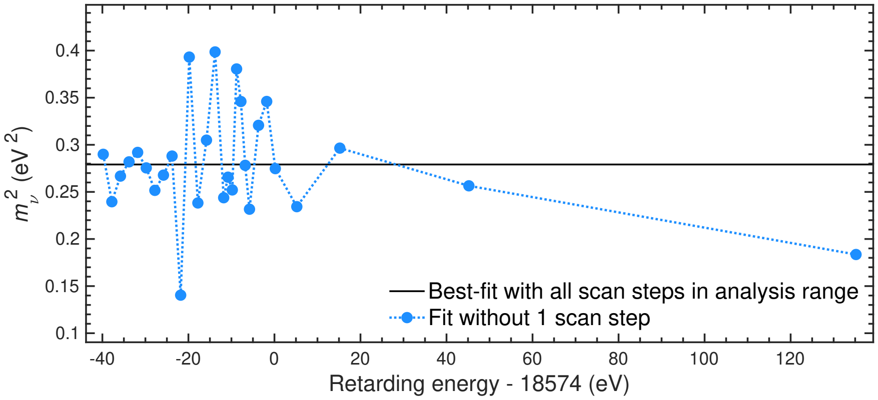

Figure 9.19: Neutrino mass squared fit result as a function of excluded data point. One scan step at a time is excluded from the stacked uniform analysis of the KNM2 data. The largest discrepancy to the baseline fit result is observed in the region around $qU - E_0 \approx -8\,\text{eV}$, that is most sensitive to m_ν^2. All differences are smaller than $\Delta m_\nu^2 = 0.12\,\text{eV}^2$, which is small compared to the overall sensitivity $\sigma(m_\nu^2) = 0.32\,\text{eV}^2$.

---

[5] Determined with the KNM2 MC twins in terms of maximal neutrino-mass signal for $m_\nu^2 = 0.1\,\text{eV}^2$

Chapter 10

Combined neutrino-mass analysis of KNM1 and KNM2

This chapter presents the combined neutrino-mass analysis of the first two measurement campaigns. The motivation is to exploit the full statistics of all available measurement campaigns to maximize the neutrino-mass sensitivity. In the case of KNM1 and KNM2, the combined sensitivity improves only slightly with respect to the KNM2 standalone analysis. Nevertheless, the combination of measurement campaigns will become very important in the future for the analysis of the final KATRIN data set, which will comprise $\mathcal{O}(20)$ measurement campaigns. Therefore, suitable combinations methods are investigated and tested for KATRIN.

This chapter is structured as follows: Firstly, the multi-campaign model and its configuration are presented in section 10.1. Secondly, two data combination methods are described in section 10.2. This is followed by an estimation of the combined sensitivity in section 10.3 and the combined data analysis in section 10.4.

10.1 Multi-campaign model

Due to different operational conditions, each measurement campaign has to be described with an individual experimental model. Campaign-wise response functions are necessary to account for the different experimental parameter values, such as the column density (22 % vs. 85 % of the nominal value). All campaign-wise settings are identical to the standalone configurations as stated in appendix C. For KNM1, the configuration from [96] is used. Both campaigns are described with a uniform stacked model.

The nuisance parameters are also expected to vary between the data sets. KNM2 was operated at a higher source activity and a lower background level compared to KNM1. Therefore, campaign-wise values for steady-state background rate and signal normalization are used. Even though the tritium endpoint is a physical constant, the effective fit endpoint is allowed to take different values for the respective measurement campaigns in order to account for different source potentials. The campaign-wise fit parameters (E_0^{fit}, $N_{\text{sig.}}$, B_{base}) are summarized in by $\boldsymbol{\eta}_{\text{knm1}}$ and $\boldsymbol{\eta}_{\text{knm2}}$ for the first and second measurement campaign, respectively. The neutrino-mass-squared is the only fit parameter, that is shared by both models.

10.2 Combination method

The choice of a suitable data combination strategy is largely influenced by the question whether the considered data sets are statistically uncorrelated or not. Systematic uncertainties, that affect both data sets in the same way, can induce campaign-wise correlations. However, both measurement campaigns are strongly dominated by statistical uncertainties, which are by nature uncorrelated. Therefore, KNM1 and KNM2 can be well approximated as statistically independent, which facilitates the combined analysis.

In the following, two analysis methods are presented: The combination via a combined fit (section 10.2.2) and via summation of the chi-squared profiles (section 10.2.2). If the data sets are uncorrelated as it is the case in this work, both methods are equivalent.

10.2.1 Combined fit

The combined fit is the most general method to analyze two (or more) measurement campaigns simultaneously. The combined chi-squared function can be written as

$$\chi^2(m_\nu^2, \boldsymbol{\eta}_{\mathrm{knm1}}, \boldsymbol{\eta}_{\mathrm{knm2}}) = (\boldsymbol{N}^{\mathrm{model}} - \boldsymbol{N}^{\mathrm{exp}})\mathbf{V}^{-1}(\boldsymbol{N}^{\mathrm{model}} - \boldsymbol{N}^{\mathrm{exp}})^T \tag{10.1}$$

with the multi-campaign model $\boldsymbol{N}^{\mathrm{model}}$ and the multi-campaign data set $\boldsymbol{N}^{\mathrm{exp}}$. The chi-squared minimization process is conducted as usual with the Minuit software using the Minos minimization algorithm. As usual, the fit uncertainties are derived from the profile chi-squared function $\chi^2(m_\nu^2) = \chi^2(m_\nu^2, \hat{\boldsymbol{\eta}}_{\mathrm{knm1}}, \hat{\boldsymbol{\eta}}_{\mathrm{knm2}})$. Systematic effects are incorporated in form of a multi-campaign covariance matrix V. This matrix comprises the regular KNM1 and KNM2 covariance matrices on its diagonal (northwest and southeast quadrants). If considered, campaign-wise correlations could be added on the off-diagonal (northeast and southwest quadrants). In the analysis at hand, all off-diagonal entries are set to zero.

10.2.2 Combination of chi-squared profiles

As the data sets can be considered as statistically independent, the combined profile chi-squared function can be rewritten as

$$\chi^2(m_\nu^2) = \chi^2(m_\nu^2, \hat{\boldsymbol{\eta}}_{\mathrm{knm1}}) + \chi^2(m_\nu^2, \hat{\boldsymbol{\eta}}_{\mathrm{knm2}}). \tag{10.2}$$

The chi-squared profiles can be first evaluated for each campaign separately, before they are combined through summation. Depending on the complexity of the multi-campaign model, that is required for section 10.2.1, this method can be significantly faster than the combined fit. The drawback is that campaign-wise correlations cannot be included with this combination method.

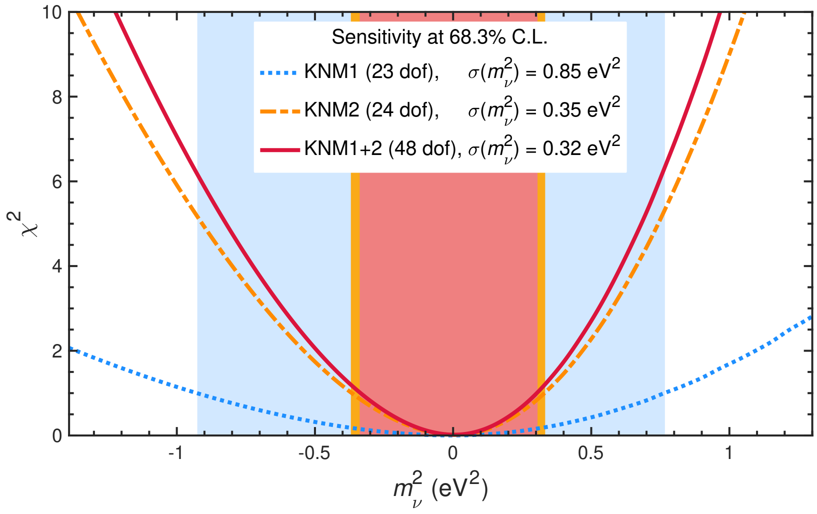

Figure 10.1: Sensitivity chi-squared profiles for KNM1 and KNM2 based on MC twins considering statistical and systematic uncertainties. The combined chi-squared profile is calculated as the sum of the standalone curves. The respective 1σ sensitivities are illustrated as colored bands around $m_\nu^2 = 0\,\mathrm{eV}^2$. The MC twin spectra are evaluated using a stacked uniform fit.

10.3 Combined sensitivity

A first estimation of the combined sensitivity can be obtained from the standalone 1σ neutrino-mass-squared sensitives $\sigma_{\mathrm{knm1}} = 0.85\,\mathrm{eV}^2$ and $\sigma_{\mathrm{knm2}} = 0.35\,\mathrm{eV}^2$ for KNM1 and KNM2, respectively. The combined sensitivity, calculated according to [106], is

$$\sigma_{\mathrm{combi.}}(m_\nu^2) \approx \sqrt{\left(\frac{1}{\sigma^2_{\mathrm{knm1}}} + \frac{1}{\sigma^2_{\mathrm{knm2}}}\right)^{-1}} \approx 0.32\,\mathrm{eV}^2. \tag{10.3}$$

Furthermore, the combination methods described in section 10.2 are applied to the MC twins. As expected, both strategies deliver the same 1σ sensitivity and coincide with the result from equation (10.3).

A graphical representation of the campaign-wise and combined sensitivities is provided in figure 10.1. The respective 1σ confidence intervals, for which the profile $\chi^2 \leq 1$, are illustrated as colored bands around $m_\nu^2 = 0\,\mathrm{eV}^2$. The combined sensitivity is only slightly better than the KNM2 standalone sensitivity, because KNM1 is much less sensitive than KNM2.

10.4 Combined neutrino-mass constraint

The combination methods of section 10.2 are applied to the KNM1 and KNM2 data sets. The overlay of data and best-fit model obtained by the combined fit is displayed in figure 10.2. The normalized residuals vary randomly within the expectation.

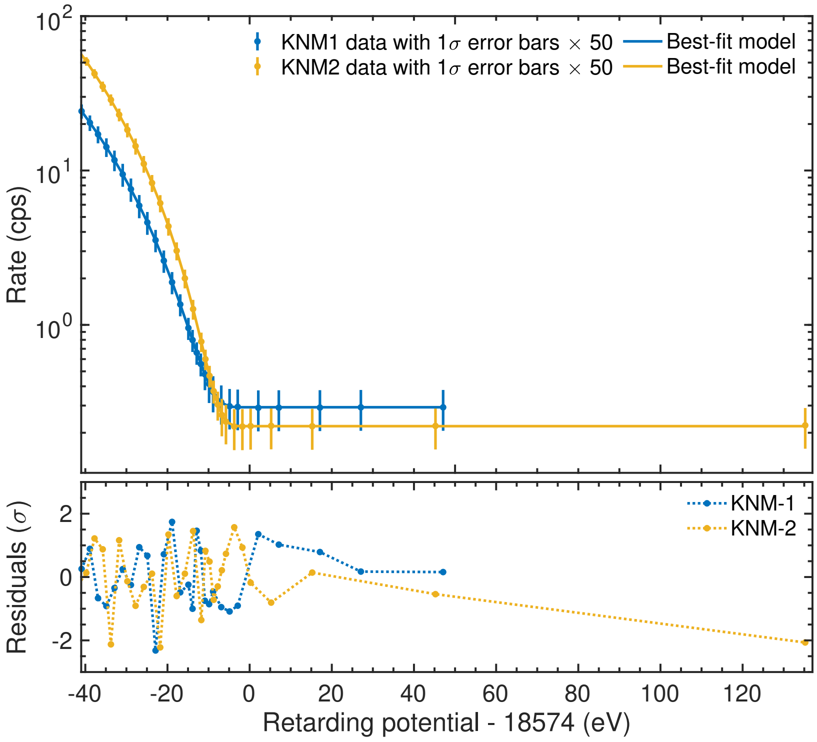

Figure 10.2: Result of the combined (stacked uniform) fit to KNM1 and KNM2. **Top:** Data and best-fit multi-campaign model. The statistical error bars are enhanced by a factor 50, as they would be not visible otherwise. **Bottom:** Normalized residuals of the combined fit. The agreement between data and best-fit multi-campaign model is very good. The residuals fluctuate randomly within the expectation.

The standalone and combined chi-squared profiles are depicted in figure 10.3. As expected, both methods give the same result:

$$m_\nu^2 = (0.10 \pm 0.31)\,\mathrm{eV}^2 \tag{10.4}$$

$$E_{0,\mathrm{knm1}}^{\mathrm{fit}} = (18\,573.79 \pm 0.02)\,\mathrm{eV} \tag{10.5}$$

$$E_{0,\mathrm{knm2}}^{\mathrm{fit}} = (18\,573.68 \pm 0.02)\,\mathrm{eV} \tag{10.6}$$

$$\chi^2_{\mathrm{min}} = 51.1\,(48\,\mathrm{dof}),\ p = 0.35 \tag{10.7}$$

The combined analysis can describe the data well, which is mirrored by the good goodness-of-fit $p = 0.35$[1]. The m_ν^2 best-fit value is compatible with zero. The combined analysis can constrain m_ν^2 better than the standalone analyses. Analogous to sections 8.5.3 and 9.5.3, the central value and uncertainty are translated into an upper limit at 90 % C.L.

$$m_\nu \leq 0.8\,\mathrm{eV} \qquad (\mathrm{FC\ and\ LT}). \tag{10.8}$$

Technicality, this is realized through summation of the χ^2 profiles for each test m_ν^2 value (section 3.3.2).

As both (campaign-wise) fit endpoints are strongly positive correlated with the neutrino mass squared, their respective uncertainties can be reduced compared to the standalone analyses. This is particularly the case for KNM1, for which the combined $\sigma(E_0^{\mathrm{fit}})$ is reduced by almost a factor of three compared to the standalone $\sigma(E_0^{\mathrm{fit}})$. Furthermore, the high correlation between m_ν^2 and E_0^{fit} also influences the (campaign-wise) E_0^{fit} best-fit values: For KNM1, the combined m_ν^2 best-fit value is larger than the standalone one. This is compensated for in the combined analysis by a larger fit endpoint $\Delta E_{0,\mathrm{knm1}}^{\mathrm{fit}} = 0.06\,\mathrm{eV}$. In KNM2, the opposite is observed: The combined m_ν^2 best-fit value is smaller than the standalone one, which is compensated by a smaller fit endpoint $\Delta E_{0,\mathrm{knm1}}^{\mathrm{fit}} = -0.04\,\mathrm{eV}$ compared to the standalone KNM2 result[2].

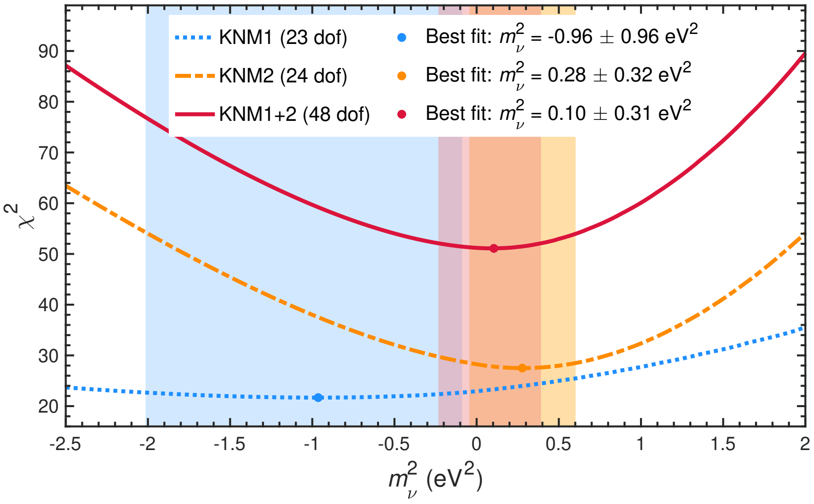

Figure 10.3: Standalone chi-squared profiles for KNM1 and KNM2 considering statistical and systematic uncertainties. The combined chi-squared profile is calculated according to section 10.2.2. The respective 1σ confidence regions are illustrated as colored bands around the respective best-fit values.

---

[1] The number of dof of the combined analysis is equivalent to the sum of the standalone dof increased by one unit, because m_ν^2 is shared by both data sets.

[2] The result of the combined analysis is compared to the stacked uniform result of KNM2 summarized in appendix G.2.

10.5 Data set compatibility: Parameter goodness-of-fit

The standard goodness-of-fit of the combined data analysis is the p-value in equation (10.7). It was pointed out by [107], that in some cases the p-value can be satisfyingly high even though the data sets are not compatible with each other. This can occur in cases when the chi-squared minima of the individual data sets are very low or when only few parameters are inferred from a large number of data points. The parameter goodness-of fit (PG), proposed by [107], circumvents this problem by defining a new test statistics $\hat{\chi}^2$.

$$\hat{\chi}^2 = \chi^2_{\mathrm{min,combi}} - \chi^2_{\mathrm{min,1}} - \chi^2_{\mathrm{min,2}} \tag{10.9}$$

with

$\chi^2_{\mathrm{min,1}} = 21.7\,(23\,\mathrm{dof})$	Minimum of KNM1 standalone analysis,
$\chi^2_{\mathrm{min,2}} = 27.5\,(24\,\mathrm{dof})$	Minimum of KNM2 standalone analysis,
$\chi^2_{\mathrm{min,combi}} = 51.1\,(48\,\mathrm{dof})$	Minimum of combined analysis.

It can be shown that $\hat{\chi}^2$ follows a χ^2-distribution with 1 dof (number of shared fit parameters), if the two data sets are statistical independent [107].

The parameter goodness-of-fit $\hat{p}$ is defined analog to the standard p-value:

$$\hat{p} = 1 - \int_0^{\hat{\chi}^2} \chi^2(x, \mathrm{dof} = 1)\, dx \tag{10.10}$$

The PG is further on calculated for the combined analysis of KNM1 and KNM2 using the definition above. The result is $\hat{p} = 0.17$, which demonstrates a good compatibility of KNM1 and KNM2 with respect to the shared m^2_ν parameter.

Chapter 11

Sterile-neutrino search of the first two measurement campaigns

This section presents the sterile-neutrino search from the first and second KATRIN measurement campaigns. The underlying data sets, introduced in chapters 5 and 6, are identical to the neutrino-mass analyses.

The sterile-neutrino search is conducted in the so-called $3\nu+1$ framework. As illustrated in figure 1.4, the electron energy spectrum is extended by one additional *sterile* branch, which is associated with a fourth neutrino mass eigenstate and its mixing to the electron flavor. The objective of this analysis is to infer constraints on m_4^2 and $|U_{e4}|^2$.

This chapter is structured as follows: First, the data combination strategy and model configuration are briefly summarized in section 11.1. Second, section 11.2 revises the statistical methods that are applied in the sterile-neutrino search. Thereafter, the correlation between active and sterile branches is addressed in section 11.3. As the correlation has a strong influence on the sterile-neutrino exclusion bounds, two complementary analysis cases are defined: Analysis case I) considers $m_\nu^2 = 0\,\mathrm{eV}^2$, whereas analysis case II) employs m_ν^2 as a nuisance parameter. The main results of the sterile-neutrino search are presented in section 11.4 based on simulations and in section 11.5 based on data. Thereafter, supplementary analyses are performed: Section 11.6 evaluates the m_ν^2 sensitivity in the presence of an eV-scale sterile neutrino. Section 11.7 investigates the influence of systematic effects on the sterile-neutrino search. Section 11.8 takes a deeper look into the tritium spectrum and presents exclusion contours for the full energy interval. The nonphysical parameter space is investigated in section 11.9, allowing for negative masses and mixings. At last, the validity of Wilks's theorem in the context of the sterile-neutrino analysis in KATRIN is discussed in section 11.10.

Most results presented in this chapter are published in [108] and [109] by the author of this thesis. Some of the following paragraphs are only slightly adapted from these publications.

11.1 Data combination, model configuration and blinding

The integral spectra within each measurement campaign are combined to a stacked uniform spectrum, respectively. The applicability of this data combination strategy was validated within the respective neutrino-mass analyses.

The spectral model is constructed in the $3\nu+1$ framework as introduced in section 1.4. Apart from the sterile-neutrino extension, the model configurations for the KNM1 and KNM2 sterile-neutrino searches are identical to the ones of the stacked uniform neutrino-mass analyses. For KNM1, the updated model configuration of the re-analysis (section 8.12) is used. Moreover, the same systematic uncertainty budgets as for the neutrino-mass analyses are considered. All input parameters are summarized in appendix C.

Similar to the neutrino-mass analyses, a blinding protocol (see chapter 7) was implemented. As the sterile-neutrino search was conducted after the unblinding of the neutrino-mass analysis, the model blinding through the FSD was no longer applied. Moreover, the model blinding was specifically developed to artificially bias the m_ν^2 best-fit value, but does not necessarily hide the best-fit in terms of $[m_4^2, |U_{e4}|^2]$. Therefore, the sterile-neutrino analysis was developed and tested on simulated spectra, so-called MC twins (see section 7.1) with the unmodified FSD. Only after three independent analysis teams, using different analysis codes, obtained consistent sensitivity estimates, the actual data analysis was performed without any subsequent modifications.

11.2 Sterile-neutrino analysis methods

The analysis methods of the sterile-neutrino search are based on the method of least-squares, presented in section 3.3. This section briefly summarizes how they are applied in the sterile-neutrino search.

11.2.1 Fit parameters

The fit parameters of the sterile-neutrino search are:

Physics parameters of interest:		$\boldsymbol{\Theta} = [m_4^2, \lvert U_{e4}\rvert^2]$,
Nuisance parameters:	Analysis case I)	$\boldsymbol{\eta} = [E_0^{\text{fit}}, B_{\text{base}}, N_{\text{sig}}]$,
	Analysis case II)	$\boldsymbol{\eta} = [m_\nu^2, E_0^{\text{fit}}, B_{\text{base}}, N_{\text{sig}}]$.

This results in 5 (analysis case I) and 6 (analysis case II) free fit parameters. Analysis case I), regarded as the main analysis, considers the hierarchical scenario $m_{1,2,3} \ll m_4$. This justifies setting m_ν^2 to zero, which is consistent with the lower limit derived from neutrino oscillations (0.009 eV [9]) within KATRIN's sensitivity.

11.2.2 Grid search

Sterile-neutrino constraints are inferred from a so-called grid search based on the method of least-squares in section 3.3.1. The two-dimensional profile chi-squared function $\chi^2(m_4^2, |U_{e4}|^2)$ is calculated on a grid of many $[m_4^2, |U_{e4}|^2]$ pairs: At each pair, the standard chi-squared function $\chi^2(m_4^2, |U_{e4}|^2, \boldsymbol{\eta})$ (equation (3.5)) is minimized with respect to the nuisance parameters $\boldsymbol{\eta}$. The two-dimensional exclusion contour is given by the set of parameter values $[\Delta\hat{m}_4^2, \Delta|\hat{U}_{e4}|^2]$, that fulfill equation (3.7). As the sterile-neutrino search has two physics parameters of interest, the chi-squared distribution with $N_k = 2$ dof has to be used. The contour curve is drawn at 95 % C.L. ($\Delta\chi^2_{\text{crit.}} = 5.99$), if not explicitly stated otherwise.

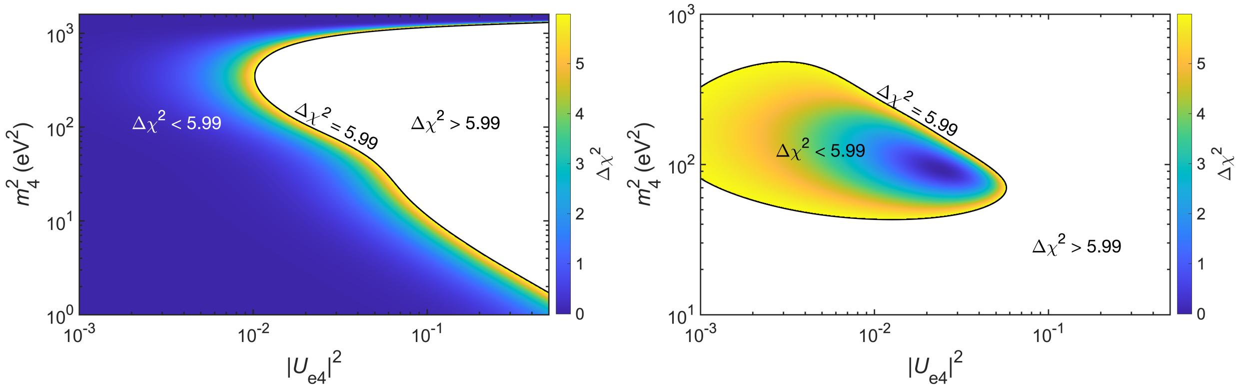

Figure 11.1: Profile chi-squared functions $\chi^2(m_4^2, |U_{e4}|)|^2$ based on simulations. The contours are drawn as black solid lines at 95 % C.L. **Left:** The simulated spectrum is based on the null hypothesis, i.e. no sterile neutrino. **Right:** The simulated spectrum is calculated with $m_4^2 \approx 90\,\text{eV}^2$ and $|U_{e4}|^2 \approx 0.02$. Both simulations are based on the statistics of the KNM2 data set for illustration.

Two profile chi-squared functions are illustrated in figure 11.1 based on a simulated spectrum with no sterile neutrino (left) and based on a simulated spectrum with $\hat{m}_4^2 \approx 90\,\mathrm{eV}^2$ and $|\hat{U}_{e4}|^2 \approx 0.02$ (right), respectively. The parameter space, for which $\Delta\chi^2 > 5.99$, is colored in white. This region can be excluded at 95 % confidence level. The remaining part of the parameter space with $\Delta\chi^2 \leq 5.99$ is the confidence region, which comprises $[\hat{m}_4^2, |\hat{U}_{e4}|^2]$. It is limited by the exclusion contour, displayed as a solid back line. The left figure illustrates a sterile-neutrino exclusion limit, which corresponds to an open contour. The right figure illustrates a sterile-neutrino signal, which corresponds to a closed contour.

The significance of the best-fit $[\hat{m}_4^2, |\hat{U}_{e4}|^2]$ with respect to the null hypothesis (no sterile neutrino) is given by the difference in chi-squared

$$\Delta\chi^2_{\mathrm{null}} = \chi^2_{\mathrm{null}} - \chi^2_{\mathrm{min}} \tag{11.1}$$

with

$$\chi^2_{\mathrm{null}} = \chi^2(m_4^2 = 0\,\mathrm{eV}^2, |U_{e4}|^2 = 0). \tag{11.2}$$

The significance in terms of chi-squared difference can be converted into a confidence level α according to equation (3.8) using $N_k = 2$ dof.

11.2.3 Choice of grid

The choice of grid points in the $[m_4^2, |U_{e4}|^2]$ parameter space depends on the analyzed data set. A typical grid comprises 50 × 50 logarithmically spaced parameter pairs with $m_4^2 \in [10^{-1}, 1600]\,\mathrm{eV}^2$ and $|U_{e4}|^2 \in [10^{-3}, 0.5]$. Grids with different grid sizes up to 100 × 100 are tested to guarantee full convergence of the grid search.

The mass m_4^2 is limited by the measurement range: KATRIN is only sensitive to $m_4^2 < (E_0 - \min(qU))^2$, because the onset of the sterile branch would occur at even smaller (not observed) retarding energies for larger m_4^2. For $m_4^2 < 0.1$, the peak of the sterile-neutrino signal in KATRIN is located at retarding energies, that are strongly dominated by background electrons.

The active-to-sterile mixing $|U_{e4}|^2 = 0.5$ is considered as maximal mixing: If both m_4^2 and m_ν^2 are unconstrained fit parameters (analysis case II), the active and sterile branches in the decay spectrum (equation (1.32)) are interchangeable: $(m_4^2, |U_{e4}|^2) \longleftrightarrow (m_\nu^2, 1 - |U_{e4}|^2)$. Consequently, no additional information can be gained by extending the active-to-sterile mixing beyond 0.5. However, in the analysis case I), $|U_{e4}|^2$ could be extended up to $|U_{e4}|^2 = 1$. In this case, the $3\nu + 1$ framework converges to the standard 3ν framework (see section 11.5.1). At the current KATRIN sensitivity, mixings smaller than $|U_{e4}|^2 < 10^{-3}$ cannot be observed.

11.2.4 Combined analysis

The combined sterile-neutrino analysis of KNM1 and KNM2 is conducted analogously to the combined neutrino-mass analysis in chapter 10. The same combination methods are used, namely either the addition of the campaign-wise profile chi-squared functions or the combined grid search (see section 10.2).

In the sterile-neutrino search, m_ν^2, m_4^2, and $|U_{e4}|^2$ are shared between the data sets. The remaining nuisance parameters $(E_0^{\mathrm{fit}}, B_{\mathrm{base}}, N_{\mathrm{sig}})$ are allowed to have campaign-wise values, as explained in section 10.1. The campaign-wise fit parameters are abbreviated as $\boldsymbol{\eta}_{\mathrm{knm1}}$ and $\boldsymbol{\eta}_{\mathrm{knm2}}$, respectively. The combined chi-squared function can thus be written as

$$\chi^2(m_4^2, |U_{e4}|^2, m_\nu^2, \boldsymbol{\eta}_{\mathrm{knm1}}, \boldsymbol{\eta}_{\mathrm{knm2}}) = \chi^2(m_4^2, |U_{e4}|^2, m_\nu^2, \boldsymbol{\eta}_{\mathrm{knm1}}) + \chi^2(m_4^2, |U_{e4}|^2, m_\nu^2, \boldsymbol{\eta}_{\mathrm{knm2}}). \tag{11.3}$$

In analysis case I), KNM1 and KNM2 do not share any common nuisance parameter, because m_ν^2 is fixed. The combined profile chi-squared function is thus simply given by the sum of the standalone profile chi-squared functions (equation (11.4)). In analysis case II), KNM1 and KNM2 share m_ν^2 as a common fit parameter. Therefore, the combined profile chi-squared function (equation (11.5)) has to be determined in a combined grid search, minimizing the chi-squared function in equation (11.3) with a multi-campaign model (see section 10.2.1).

The compatibility between data sets is evaluated with the parameter goodness-of-fit $\hat{p}$ [107], as introduced in section 10.5. This test quantifies the penalty of combining KNM1 and KNM2 in units of chi-squared compared to the standalone analyses. As opposed to the neutrino-mass analysis, $\hat{\chi}^2$ has to be compared with a chi-squared distribution with 2 dof (analysis case I) and 3 dof (analysis case II).

$$\text{Analysis case I):} \qquad \chi^2(m_4^2, |U_{e4}|^2) = \chi^2(m_4^2, |U_{e4}|^2, \hat{\boldsymbol{\eta}}_{\text{knm1}}) + \chi^2(m_4^2, |U_{e4}|^2, \hat{\boldsymbol{\eta}}_{\text{knm2}}) \tag{11.4}$$

$$\text{Analysis case II):} \qquad \chi^2(m_4^2, |U_{e4}|^2) = \chi^2(m_4^2, |U_{e4}|^2, \hat{m}_\nu^2, \hat{\boldsymbol{\eta}}_{\text{knm1}}) + \chi^2(m_4^2, |U_{e4}|^2, \hat{m}_\nu^2, \hat{\boldsymbol{\eta}}_{\text{knm2}}). \tag{11.5}$$

11.3 Correlation between active and sterile neutrino branches

The model spectrum in equation (1.32) consists of the weighted sum of two branches: the *active* branch with effective electron antineutrino mass m_ν^2 and the *sterile* branch with the fourth mass eigenstate m_4. The branches are weighted according to their mixing: $(1-|U_{e4}|^2)$ for the active branch and $|U_{e4}|^2$ for the sterile branch, respectively. Apart from the different neutrino masses and weights, the two branches are mathematically identical. Since m_ν^2 is small in the observed data and simulation, the two branches are degenerate in the case of small m_4^2 and large mixing $|U_{e4}|^2 \approx 0.5$.

To quantify this relation more generally, many model spectra $\mathbf{N}^{\text{model}}$ are simulated for several different values of $m_4^2, |U_{e4}|^2$ and $m_\nu^2 = 0\,\text{eV}^2$. The simulated spectra are based on the KNM2 MC twins. Each simulated spectrum is fit five times by varying m_4^2 stepwise by $\pm 1\,\text{eV}^2$ around the respective MC truths. The fits are optimized with respect to $\boldsymbol{\eta}$, keeping $|U_{e4}|^2$ fixed to its simulated value. For each $(m_4^2, |U_{e4}|^2)$-pair, the approximately linear relationship $m_\nu^2 = \alpha_{\text{slope}} \cdot m_4^2 + \text{const.}$ is determined in the vicinity of the MC truth. The linear slope α_{slope} serves as a proxy for the linear correlation between the two masses.

Figure 11.2 displays α_{slope} in the $(m_4^2, |U_{e4}|^2)$-parameter space. The smaller the active-to-sterile mixing is, the smaller the contribution of the sterile branch to the simulated spectrum is. For small $|U_{e4}|^2 < 0.01$, the slope is as small as $|\alpha_{\text{slope}}| < 0.01$. For small $m_4^2 \lesssim 30\,\text{eV}^2$, negative slope values are observed. For large $30\,\text{eV}^2 \lesssim m_4^2 \lesssim 1000\,\text{eV}^2$, the absolute magnitude of the slope is reduced and has a positive sign.

Due to the correlation between m_4^2 and m_ν^2, the exclusion curves vary significantly for different treatments of m_ν^2. Therefore, two complementary sterile-neutrino-analysis cases (see section 11.2.1) are considered in the following.

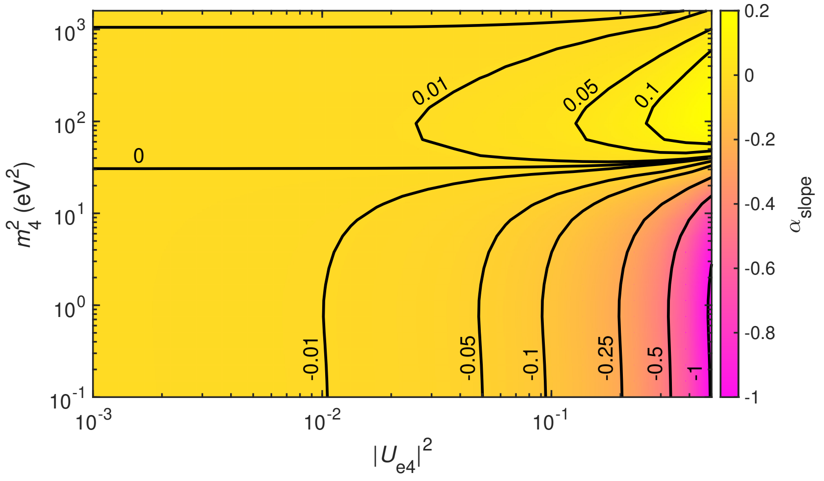

Figure 11.2: The correlation between active and sterile neutrino mass is approximated by a linear slope $m_\nu^2 = \alpha_{\text{slope}} \cdot m_4^2 + \text{const.}$ for various values of m_4^2 and $|U_{e4}|^2$ by analyzing simulated spectra. The color indicates the magnitude of α_{slope}. For small mixing $|U_{e4}|^2 < 0.01$, small slope values $|\alpha_{\text{slope}}| < 0.01$ are observed. For larger mixing $|U_{e4}|^2 > 0.01$ and small $m_4^2 \lesssim 30\,\text{eV}^2$, a strong negative correlation is found. For larger mixing $|U_{e4}|^2 > 0.01$ and larger $m_4^2 > 30\,\text{eV}^2$ a weaker positive correlation is found.

11.4 Sensitivity contours: Results on simulation

The sterile-neutrino sensitivities are obtained from a grid search on the respective MC twins, that mimic the actual data set with respect to all operational parameters. As outlined in section 7.1, the MC twins are Asimov spectra, which means that they are not statistically randomized. The Asimov sensitivity contours can therefore be considered as the mean sensitivity. The sensitivity contours are displayed in figure 11.3 at 95 % C.L. The curves in blueish color correspond to analysis case I) and the curves in reddish color correspond to analysis case II).

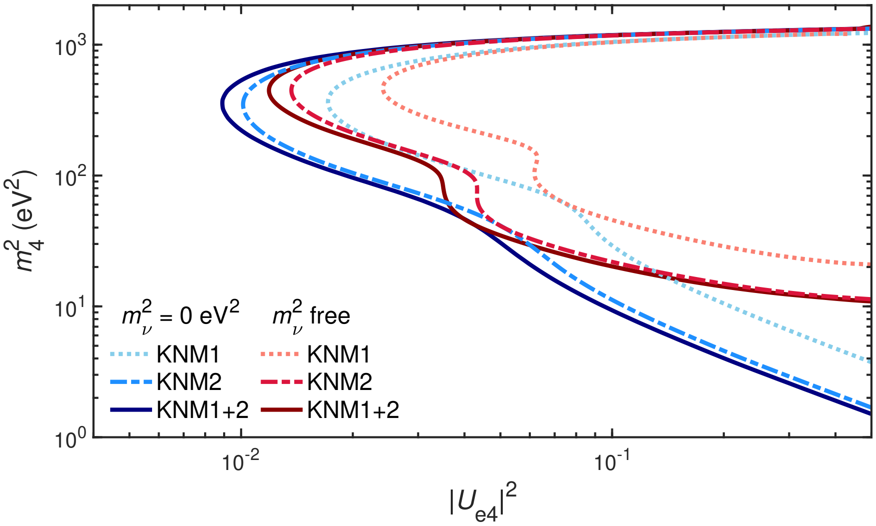

Figure 11.3: Sensitivity contours of the KNM1 and KNM2 standalone analyses and the combined analysis at 95 % C.L. The contour lines shaded in blue consider $m_\nu^2 = 0\,\mathrm{eV}^2$ (case I), whereas the exclusions shaded in red include m_ν^2 as an unconstrained fit parameter (case II). The sensitivity calculations are based on the respective MC twins, which consist of non-randomized, so-called Asimov, spectra. As no statistical fluctuations are added, the combined sensitivity of KNM1+2 is always higher than the standalone sensitivities.

11.4.1 Structure of sensitivity contours

As the analysis intervals of both data sets comprise only the last 40 eV of the β-spectrum, the sterile-neutrino searches are only sensitive to $m_4^2 < 1600\,\mathrm{eV}^2$. For all contours, the maximum sensitivity is located at $m_4^2 \simeq 400\,\mathrm{eV}^2$. For smaller m_4^2, the sensitivity decreases due to the reduction of the signal strength and the signal-to-background ratio. More details on this topic can be found in appendix H.1, where the influences of the background level on the sensitivity is investigated. For larger $m_4^2 > 400\,\mathrm{eV}^2$, the sensitivity rapidly drops as the influence of the sterile neutrino on the experimental β-spectrum shifts outside of the analysis interval.

11.4.2 Comparison of data sets

For both analysis cases, the KNM2 sensitivity contours are more stringed than the respective KNM1 contours, since the second measurement campaign comprises more measurement time and was operated at a higher source activity and a lower background level. Combining the statistical power of both data sets, the combined sensitivity contours potentially yield the best constraints.

11.4.3 Comparison of analysis cases

The sensitivity contours of analysis case I) are more stringent than the respective contours of analysis case II). On the one hand, this is due to the fact that at each point in the $[m_4^2,\ |U_{e4}|^2]$ parameter space, the fit in case II) has gained the freedom to find a best-fit value $\hat{m}_\nu^2$ that improves the profile chi-squared over $\chi^2(m_\nu^2 = 0\,\mathrm{eV}^2)$:

$$\chi^2_{\mathrm{II}}(\hat{m}_\nu^2) \leq \chi^2_{\mathrm{I}}(m_\nu^2 = 0\,\mathrm{eV}^2) \quad \forall \ [m_4^2, |U_{e4}|^2]. \tag{11.6}$$

On the other hand, the global minimum of the sensitivity chi-squared function χ^2_{min} is always located at the null hypothesis. Because of that and equation (11.6), in analysis case II) the critical chi-squared difference is reached only at larger $|U_{e4}|^2$ at a given m_4^2 than in analysis case I).

Comparing the respective sensitivity contours of analysis cases I) and II) in figure 11.3, it can be seen that the contours coincide at one particular $[m_4^2, |U_{e4}|^2]$ combination. At this point in the parameter space the fit in analysis case II) finds $\hat{m}_\nu^2 = 0\,\mathrm{eV}^2$, resulting in the same χ^2 as analysis case I).

The difference between analysis case I) and II) is most prominent for small $m_4^2 \lesssim 30\,\mathrm{eV}^2$. As discussed in section 11.3, high correlations between m_ν^2 and m_4^2 are observed at large mixings in this part of the parameter space. The larger the correlation coefficient, the better the fit at a given grid point in analysis case II) can compensate for a fixed m_4^2 value.

11.5 Exclusion contours: Results on data

No sterile-neutrino signal is observed. Thus, exclusion bounds in the $[m_4^2, |U_{e4}|^2]$ parameter space are calculated at 95 % C.L. with the grid search method. This section presents the contours from the standalone analyses of the KNM1 and KNM2 data sets and the combined exclusion. Analysis case I) is addressed in section 11.5.1, followed by analysis case II) in section 11.5.2.

An overview of all exclusion contours is given in figure 11.4. Moreover, the KNM1 and KNM2 standalone exclusion contours are compared in more detail in figures 11.5 and 11.6, respectively. The best-fit values are summarized in table 11.1.

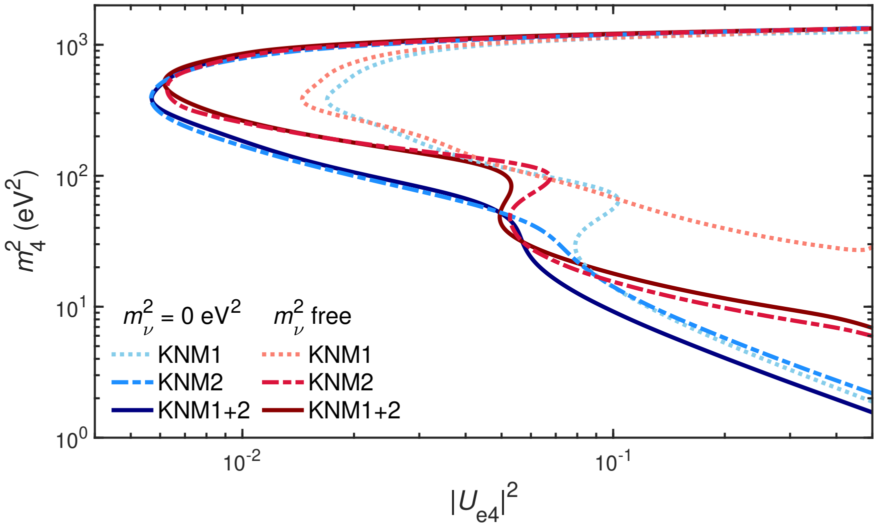

Figure 11.4: Exclusion contours of the KNM1 and KNM2 standalone analyses and the combined analysis at 95 % C.L. The contour lines shaded in blue consider $m_\nu^2 = 0\,\mathrm{eV}^2$ (case I), whereas the exclusions shaded in red include m_ν^2 as an unconstrained fit parameter (case II). Due to statistical fluctuations, some contours exhibit bump-shaped features in the region $30\,\mathrm{eV}^2 \lesssim m_4^2 \lesssim 100\,\mathrm{eV}^2$. The location of the $(m_4^2, |U_{e4}|^2)$ best-fit values, summarized in table 11.1, generally cause slightly weaker constraints in their vicinity compared to the sensitivity. For the same reason, the combined exclusion contour of KNM1+2 gives a weaker constraint in certain regions compared to KNM2 standalone exclusion contour.

Analysis case	Data set	m_4^2	$\lvert U_{e4}\rvert^2$	m_ν^2	$\chi^2_{\mathrm{min}}/\mathrm{dof}$	p	$\Delta\chi^2_{\mathrm{null}}$	Significance	$\hat{p}$
I	KNM1	77.5 eV^2	0.031	fixed	21.4/22	0.50	1.43	51.0 %	-
	KNM2	0.28 eV^2	1.0	fixed	27.5/23	0.24	0.74	31.0 %	-
	KNM1+2	59.9 eV^2	0.011	fixed	50.4/47	0.34	0.66	28.1 %	0.47
II	KNM1	21.8 eV^2	0.155	−5.3 eV^2	19.9/21	0.53	1.30	47.9 %	-
	KNM2	98.3 eV^2	0.027	1.1 eV^2	25.0/22	0.30	2.49	71.2 %	-
	KNM1+2	87.4 eV^2	0.019	0.57 eV^2	49.5/46	0.34	1.69	57.1 %	0.20

Table 11.1: Results of the KNM1 and KNM2 standalone and combined analyses. The first three rows correspond to analysis case I) with $m_\nu^2 = 0\,\mathrm{eV}^2$, whereas the last three rows show the results of analysis case II) with unconstrained m_ν^2. The first five columns show the best-fit parameter values (m_4^2, $|U_{e4}|^2$, m_ν^2) and the associated goodness of fits (χ^2_{bf}, p). Furthermore, the two following columns state the significance of the best fit over the no-sterile hypothesis in terms of χ^2 and confidence level. All observed sterile-neutrino signals are compatible with the no-sterile neutrino hypothesis; i.e., no significant spectral distortion at 95 % C.L. is found. The last column gives the parameter goodness of fit $\hat{p}$ for the combined analyses.

11.5.1 Analysis case I) $m_\nu^2 = 0\,\mathrm{eV}^2$

KNM1: The global chi-squared minimum $\chi^2_{\mathrm{min}} = 21.4\,(22\,\mathrm{dof}, p = 0.50)$ is found at the values $m_4^2 = 77.5\,\mathrm{eV}^2$, and $|U_{e4}|^2 = 0.031$. The significance of the best fit with respect to the null hypothesis is $\Delta\chi^2_{\mathrm{null}} = 1.43$. The best fit is therefore not significant at 95 % C.L.

The exclusion contour exhibits a bump-like feature in the vicinity of the best fit as illustrated in figure 11.5. Since it is caused by a statistical fluctuation, the structure is not visible in the corresponding sensitivity contour.

KNM2: The global minimum of the chi-squared function $\chi^2_{\mathrm{min}} = 27.5\,(23\,\mathrm{dof}, p = 0.24)$ is found at $m_4^2 = 0.28\,\mathrm{eV}^2$, and $|U_{e4}|^2 = 1.0$. The significance of the best fit with respect to the null hypothesis is $\Delta\chi^2_{\mathrm{null}} = 0.7$; i.e. the result is not statistically significant at 95 % C.L.

Even though not explicitly displayed in figure 11.6, the region $0.5 < |U_{e4}|^2 \leq 1$ is explored in analysis case I). As explained in section 11.2.3, active and sterile branches are not interchangeable in this region in case m_ν^2 is fixed. Thus, new solutions of the β-spectrum can be found beyond the maximal mixing $|U_{e4}|^2 > 0.5$.

The best fit being at the extreme active-to-sterile mixing $|U_{e4}|^2 = 1.0$ shows that the observed decay spectrum can be described best by only one branch with one associated free neutrino mass. As the active and sterile branches only differ in their neutrino mass and mixing nomenclature, the two branches are indistinguishable in the scenario at hand. However, since active-to-sterile mixing values of $|U_{e4}|^2 > 0.5$ are excluded by oscillation experiments [9], the results at hand are interpreted as signature from the active branch with free m_ν^2. Indeed, the best-fit value for m_4^2 coincides with the best-fit value of $m_\nu^2 = 0.28\,\mathrm{eV}^2$ that was found in the neutrino-mass analysis with the same FPD pixel combination strategy (appendix G.2).

KNM1 + KNM2 combined: The best fit of the combined analysis is located at $m_4^2 = 59.9\,\mathrm{eV}^2$, and $|U_{e4}|^2 = 0.011$ with $\chi^2_{\mathrm{min}} = 50.4$ (dof $= 47$, $p = 0.34$). The improvement with respect to the null hypothesis is not significant with $\Delta\chi^2_{\mathrm{null}} = 0.7$. To evaluate the compatibility between the two statistically independent data sets, the parameter goodness of fit is calculated according to section 11.2.4. A good agreement between the data sets is found $\hat{p} =$ 47 %.

Due to statistical fluctuations in both data sets, the combined exclusion improves for $m_4^2 \leq 50\,\mathrm{eV}^2$ compared to the KNM2 standalone result while providing slightly weaker constraints for $m_4^2 > 50\,\mathrm{eV}^2$. The KNM1 exclusion bounds are improved by the combined analysis for the entire mass range.

11.5.2 Analysis case II) with m_ν^2 free

The KNM1 and KNM2 standalone exclusion contours are shown figures 11.5 and 11.6, respectively, with the red solid lines corresponding to analysis case II). In addition, the isolines of the m_ν^2 fit values are included in the illustration as dotted light red lines. An isoline corresponds to a set of $(m_4^2, |U_{e4}|^2)$ pairs with equal fit value of m_ν^2. The combined exclusion contour of analysis case II) is included in the overview in figure 11.4.

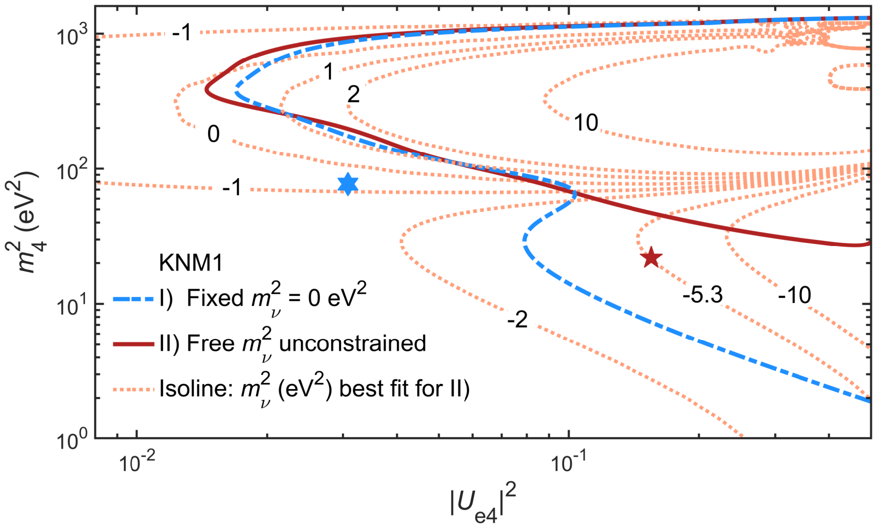

Figure 11.5: KNM1 data exclusion contours with I) fixed m_ν^2 and II) free m_ν^2. The m_ν^2 fit results within the grid search with free m_ν^2 are illustrated as isolines, i.e., $(m_4^2, |U_{e4}|^2)$ pairs with equal fit value of m_ν^2. The isolines are labeled with the corresponding value of m_ν^2 in eV^2. The location of the respective best fits are marked by star symbols.

KNM1: The global chi-squared minimum is found at $m_4^2 = 21.8\,\mathrm{eV}^2$ and $|U_{e4}|^2 = 0.155$ with a good $\chi^2 = 19.9\,(21\,\mathrm{dof}, p = 0.53)$. The best fit yields no significant improvement over the null hypothesis $\Delta\chi^2_{\mathrm{null}} = 1.30$.

For small active-to-sterile mixings $|U_{e4}|^2 < 10^{-2}$, the m_ν^2 fit values agree with the 1σ confidence region of the neutrino-mass analysis in section 8.12. However, the global best-fit value of m_ν^2 is largely negative $m_\nu^2 = -5.3\,\mathrm{eV}^2$. As discussed in section 11.6 at the example of KNM2, the m_ν^2 sensitivity is reduced in the $3\nu+1$ framework, if no external constraints on the active-to-sterile mixing are considered. Therefore, the negative m_ν^2 best-fit value is not considered significant.

The exclusion contour is similar to analysis case I) for $m_4^2 \lesssim 60\,\mathrm{eV}^2$. For smaller m_4^2, analysis case II) yields weaker constraints than case I) due to the high correlation between m_4^2 and m_ν^2, as expected.

KNM2: The best fit is found at $m_4^2 = 98.3\,\mathrm{eV}^2$, $|U_{e4}|^2 = 0.027$, and $m_\nu^2 = 1.1\,\mathrm{eV}^2$ with $\chi^2 = 25.0$ (dof = 22, $p = 0.30$). The best fit improves with respect to the null hypothesis by $\Delta\chi^2 = 2.5$, thus not reaching the $\Delta\chi^2$ threshold at 95 % C.L. for a significant result.

For small $m_4^2 \leq 40\,\mathrm{eV}^2$ and large $|U_{e4}|^2 \geq 0.04$, the fit finds negative m_ν^2 values of the same order of magnitude as m_4^2, reflecting the expected strong negative correlation between m_ν^2 and m_4^2. For small mixing, $|U_{e4}|^2 < 6 \cdot 10^{-3}$, the m_ν^2 fit values lie within the 1σ confidence region of the neutrino-mass analysis (chapter 9 and appendix G.2).

For most parts of the parameter space, analysis case II) yields weaker constraints than the case I) analysis, as expected. Different to the sensitivity contours, the case II) exclusion contour does not coincide with the case I) contour for fit values of $m_\nu^2 = 0\,\mathrm{eV}^2$ (located here at $m_4^2 \approx 30\,\mathrm{eV}^2$). Instead it yields a slightly stronger constraint on $|U_{e4}|^2$, because $\chi^2_{\text{min, II)}} < \chi^2_{\text{min, I)}}$.

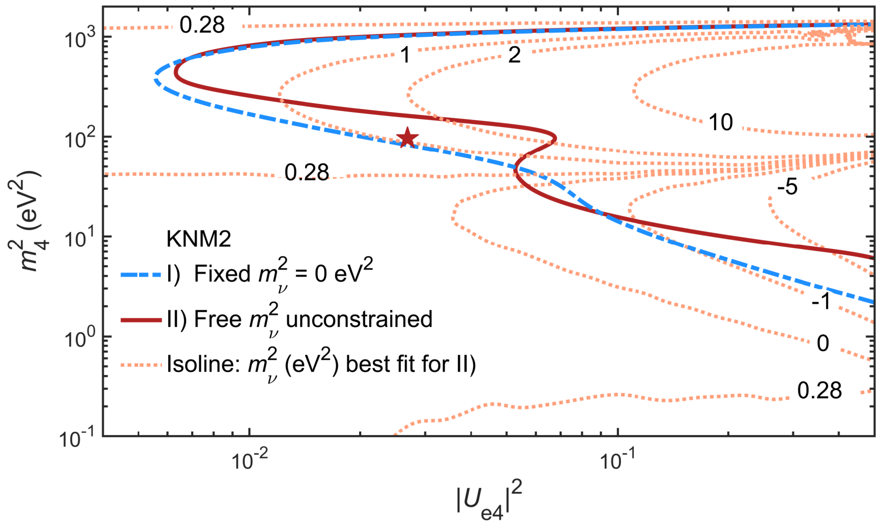

Figure 11.6: KNM2 data exclusion contours with I) fixed m_ν^2 and II) free m_ν^2. The m_ν^2 fit results within the grid search with free m_ν^2 are illustrated as isolines, i.e., $(m_4^2, |U_{e4}|^2)$ pairs with equal fit value of m_ν^2. The isolines are labeled with the corresponding value of m_ν^2 in eV^2. For small mixing $|U_{e4}|^2 < 6 \cdot 10^{-3}$, the neutrino-mass squared values lie within the 1σ confidence region of the neutrino-mass analysis (chapter 9), as expected. The location of the analysis case II) best fit is highlighted by a star symbol. The best fit of analysis case I) is not included in the plot, as it is located at the extreme active-to-sterile mixing $|U_{e4}|^2 = 1$ (see table 11.1). The contour for analysis case II) exhibits a bump-like structure in the vicinity of its best fit, which is caused by a statistical fluctuation.

KNM1 and KNM2 combined: The best fit of the combined exclusion in analysis case II) is found at $m_4^2 = 87.4\,\mathrm{eV}^2$, $|U_{e4}|^2 = 0.019$ and $m_\nu^2 = 0.57\,\mathrm{eV}^2$. The latter agrees within 1σ with the standard neutrino-mass analysis (chapter 10). The smallest chi-squared value is $\chi^2 = 49.9\,(46\,\mathrm{dof}, p = 0.34)$, which mirrors a good fit quality. It improves with respect to the null hypothesis by $\Delta\chi^2 = 1.7$, rendering the sterile-neutrino signal not significant at 95 % C.L. The compatibility between the data sets is determined to be good with $\hat{p} = 0.20$.

The combined exclusion improves over the KNM1 standalone analysis for all m_4^2. As already observed for analysis case I), the combined exclusion contours yields for some m_4^2 slightly weaker constraints than the KNM2 standalone result due to statistical fluctuations in both data sets.

11.5.3 Comparison of exclusion and sensitivity contours

Due to statistical fluctuations, it is expected that the sterile-neutrino constraints derived from data slightly differ from the sensitivity contours. Overall, the exclusion contours of the first two measurement campaigns (figure 11.4) agree well with the sensitivity estimated (figure 11.3). A direct comparison between the contours is provided in appendix H.2.

Moreover, a sensitivity band can be calculated by analyzing many randomized simulated spectra instead of a single simulated Asimov spectrum. It illustrates the deviation from the mean sensitivity contour, that is expected for an individual contour, that is based on a fluctuated spectrum. Likewise, it helps to evaluate in more detail if the exclusion contour derived from data varies more than expected from the mean sensitivity or not. As this calculation is rather computationally expensive, it is only conducted for the case I) analysis. For both data sets > 1500 simulated spectra are analyzed. These spectra are based on the respective MC twins, but are additionally randomized according to statistical and systematic uncertainties. For each simulated spectrum, a sensitivity contour is drawn at 95 % C.L. The standard deviation of the obtained sensitivity contours is called the 1σ-sensitivity band. The 1σ-sensitivity band for the combined analysis is compared to the mean Asimov sensitivity and the exclusion contour in figure 11.7. The corresponding illustrations for the standalone analyses are shown in appendix H.2. The difference between exclusion and sensitivity contours lies within the expectation for the KNM1 and KNM2 standalone analyses as well as for the combined analysis.

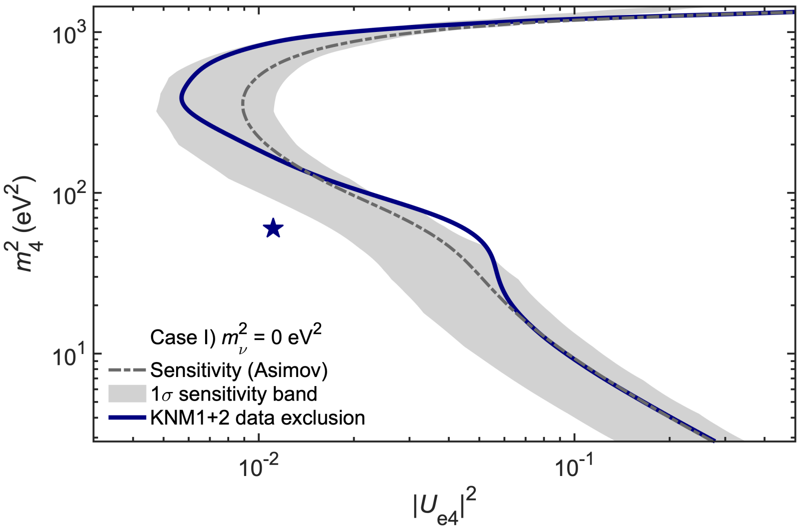

Figure 11.7: To estimate the expected degree of variations between Asimov sensitivity contours and exclusion contours, 1σ-sensitivity bands are calculated for the KNM1 and KNM2 standalone analyses (appendix H.2) as well as for the combined analysis (this figure). The sensitivity bands are derived from the analysis of > 1500 randomized MC spectra per measurement campaign. As the calculation is computationally expensive, only analysis case I) with $m_\nu^2 = 0\,\mathrm{eV}^2$ is considered. The combined exclusion contour agrees well with the sensitivity estimate.

11.5.4 Comparison to other experiments

To put this work into context, the case I) exclusion contours are compared to constraints from a selection of other experiments displayed in figure 11.8, focusing on sterile-neutrino searches in the electron disappearance channel. The KATRIN results improve on the constraints from the completed Mainz and Troitsk experiments for $m_4^2 \lesssim 300\,\mathrm{eV}^2$.

As short-baseline neutrino oscillation experiments are sensitive to different observables than β-decay experiments, the variables have to be transformed accordingly to relate the results. While KATRIN is directly sensitive to $|U_{e4}|^2$, sterile-neutrino oscillations are characterized by $\sin^2(2\theta_{ee}) = 4|U_{e4}|^2(1-|U_{e4}|^2)$. Moreover, the mass splitting can be written as $\Delta m_{41}^2 \approx m_4^2 - m_\nu^2$, which is valid within $2\times10^{-4}\,\mathrm{eV}^2$ [110]. For analysis case I), this approximation is equivalent to $\Delta m_{41}^2 \approx m_4^2$.

The KATRIN constraints are able to exclude the large Δm_{41}^2 solutions of the combined gallium experiments for $20\,\mathrm{eV}^2 \lesssim \Delta m_{41}^2 \lesssim 1000\,\mathrm{eV}^2$. Moreover, a considerable fraction of the reactor antineutrino anomaly for $50\,\mathrm{eV}^2 \lesssim \Delta m_{41}^2 \lesssim 1000\,\mathrm{eV}^2$ is challenged by the KATRIN results. The combined analysis of the first and second science runs disfavors the Neutrino-4 hint of a signal for $\sin^2(2\theta_{ee}) \gtrsim 0.4$ at 95 % C.L.

Furthermore, the results are compared to constraints from $0\nu\beta\beta$ experiments. If neutrinos are Majorana particles and $0\nu\beta\beta$ is triggered by light Majorana neutrino exchange, m_4 will contribute to the effective Majorana mass

$$\begin{aligned} m_{\beta\beta} &= |\sum_{i=1}^{4} U_{ei}^2 m_i| \\ &= |(1-|U_{e4}|^2)\sum_{i=1}^{3} U_{ei}^2 m_i + |U_{e4}|^2 e^{i\gamma} m_4| \end{aligned} \tag{11.7}$$

with a possible third Majorana phase $\gamma \in [-\pi, \pi]$. By limiting the active-neutrino contribution to $m_{\beta\beta}$ to the non-degenerate regime; i.e., between 0 and 0.005 eV (0.01 and 0.05 eV) for the normal (inverted) ordering, the current upper limit of $m_{\beta\beta}$ can be translated into constraints on sterile neutrinos. The conversion from the observable half-life to $m_{\beta\beta}$ depends on the nuclear matrix elements. As an illustration, the calculation with the nuclear matrix elements that result in the least stringent limit $m_{\beta\beta} < 0.16\,\text{eV}$ [20, 21] is selected. The width of the two gray exclusion bands in figure 11.8 reflects the uncertainties on the entries of the PMNS matrix and the unknown Majorana phases [9].

Moreover, the projected final KATRIN sensitivity is estimated. A net measurement time of 1000 days, a reduced background rate of 130 mcps for 117 active pixels and design model configurations [42] are assumed. The projected final sensitivity will improve the global sensitivity for $\Delta m^2_{41} \gtrsim 5\,\text{eV}^2$ and will provide complementary results to short-baseline oscillation experiments for smaller masses.

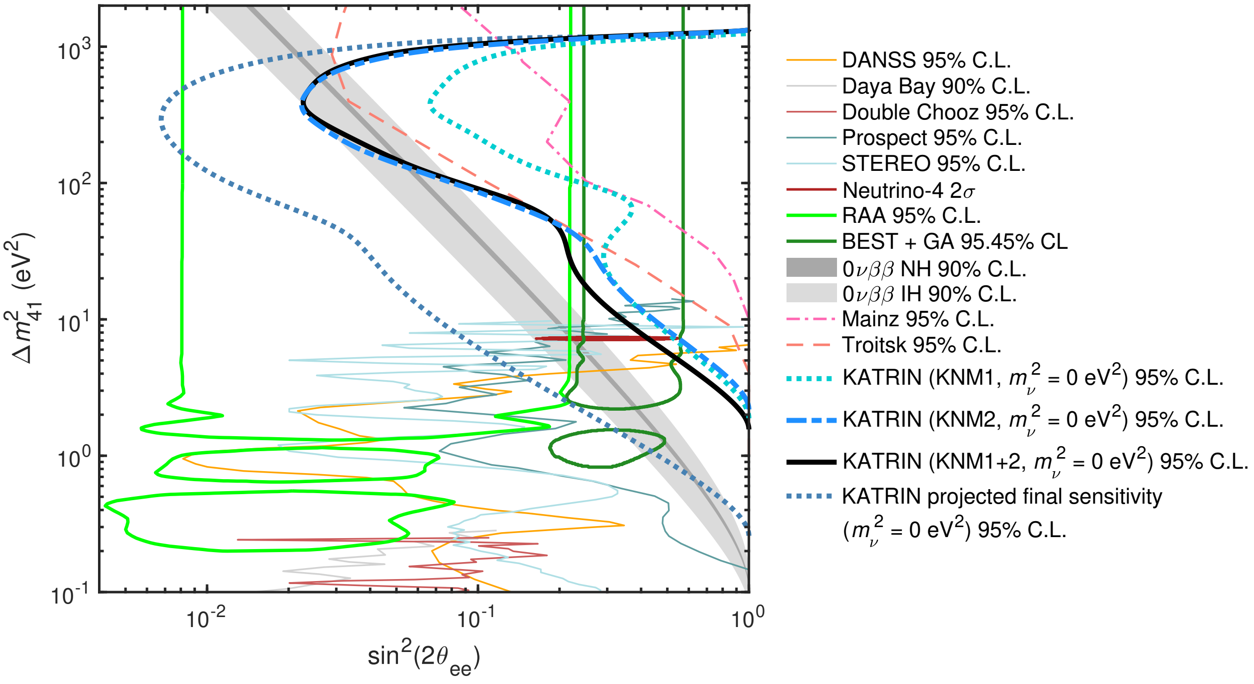

Figure 11.8: The 95 % C.L. KATRIN exclusion contours from the first two measurement campaigns with $m^2_\nu = 0\,\text{eV}^2$, standalone and combined, are shown. The final sensitivity was computed following the first measurement campaign while assuming 1000 live days and a reduced background of 130 mcps [108]. The second measurement campaign yields more stringent constraints than both Mainz [111] and Troitsk [112] experiments for $m^2_4 \lesssim 300\,\text{eV}^2$. Moreover, the large Δm^2_{41} solutions of the RAA and BEST+GA anomalies [27, 33] can be excluded to a great extent. The combined analysis is in tension with the positive results claimed by Neutrino-4 [34] for $\sin^2(2\theta_{ee}) \gtrsim 0.4$. Moreover, KATRIN data improves the exclusion bounds set by short-baseline oscillation experiments for $\Delta m^2_{41} \gtrsim 10\,\text{eV}^2$ [113–117]. Constraints from $0\nu\beta\beta$ with $m_{\beta\beta} < 0.16\,\text{eV}$ are shown as gray bands [9, 20, 21]

.

11.6 Neutrino-mass sensitivity in $3\nu + 1$ framework

As described in section 11.3, a sizable correlation between the effective electron antineutrino mass and the fourth mass eigenstate is observed. This relation results in weaker constraints on the active-to-sterile neutrino mixing when m^2_ν is included as a free fit parameter in the sterile-neutrino search (see section 11.5.2). Turning the analysis concept upside down, the $3\nu + 1$ model extension is expected to cause a reduction in m^2_ν sensitivity [118]. In the following, the m^2_ν sensitivity in the $3\nu{+}1$ framework is calculated at the example of the KNM2 standalone analysis.

For both data and MC twins, the chi-squared profiles are calculated as a function of m^2_ν, as displayed in figure 11.9.

For different fixed $m_\nu^2 \in [-1, 2.5]$ eV^2, a two-dimensional grid search over the $(|U_{e4}|^2, m_4^2)$ parameter space is performed, minimizing the chi-squared function with respect to all other nuisance parameters. The value $\chi^2(m_\nu^2)$ in the chi-squared profile corresponds to the global minimum found in the grid search with the respective fixed m_ν^2.

The global chi-squared minima for different fixed m_ν^2 values are displayed in appendix H.3. For $m_\nu^2 \leq 0\,\text{eV}^2$, the best fits are located at $m_4^2 < 2\,\text{eV}^2$ and large mixing $|U_{e4}|^2 \approx 0.5$. As m_ν^2 and m_4^2 are strongly correlated in this region (figure 11.2), the chi-squared profiles are flat. Assuming the existence of a sterile neutrino, this corresponds to a complete loss of sensitivity. The latter can be restored by using external constraints on m_4^2 or $|U_{e4}|^2$. Restricting $m_4^2 > 20\,\text{eV}^2$ or $|U_{e4}|^2 < 0.04$, lower and upper 1σ sensitivities on m_ν^2 have the same size. For $m_\nu^2 > 0\,\text{eV}^2$, the best fits are located at $10\,\text{eV}^2 < m_4^2 < 200\,\text{eV}^2$ and moderate mixings $\mathcal{O}(10^{-2})$. In this part of the parameter space, the correlation between the two masses is less pronounced. As a result, the 1σ uncertainty on m_ν^2 in the $3\nu + 1$ extension is only increased by a factor of 2 compared to the standard neutrino-mass analysis.

The neutrino-mass sensitivity in the $3\nu+1$ framework can be fully restored by limiting the active-to-sterile mixing to small values. For $|U_{e4}|^2 < 10^{-4}$, the sensitivity on m_ν^2 converges to the nominal one in the 3ν framework. Using the same constraint, central value and uncertainties of the standard neutrino-mass analysis in chapter 9 can be reproduced.

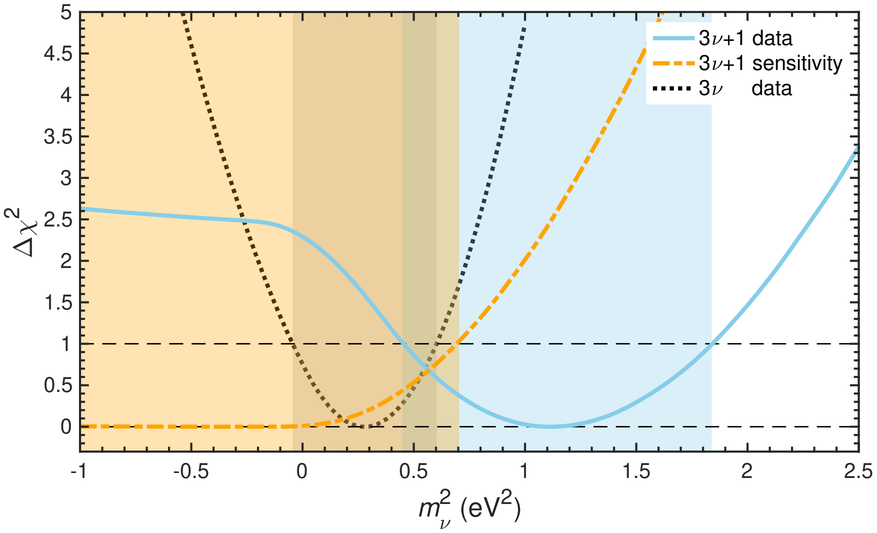

Figure 11.9: Central value and 1σ uncertainty on m_ν^2 within $3\nu + 1$ framework for data (blue) and simulation (orange). The uncertainty obtained within the 3ν framework is given in gray for comparison.

11.7 Influence of systematic uncertainties

The sterile-neutrino searches consider the same systematic effects as the respective neutrino mass analyses, summarized in appendix C. The influence of systematic uncertainties on the KNM1 and KNM2 contours is evaluated with the respective MC twin simulations considering $m_\nu^2 = 0\,\text{eV}^2$ (analysis case I). Two grid searches are performed on each stacked uniform twin spectrum: once considering only statistical uncertainties and once using the full covariance matrix that encodes statistical and all systematic uncertainties. The sensitivity contours with and without systematic uncertainties are displayed in appendix H.4 at 95 % C.L. For both data sets, systematic effects change the sensitivity contour only slightly.

To assess the influence of systematic uncertainties in a more quantitative way, a raster scan is performed: For fixed values of m_4^2, the sensitivity on $|U_{e4}|^2$ is calculated. Since m_4^2 is fixed in a raster scan, the number of degrees of freedom is reduced to 1. This means, that $\Delta\chi^2_\text{crit} = 1$ corresponds to a confidence level of 68.3 % or 1σ. This method allows the calculation of the *systematic-only* contribution:

$$\sigma_{\text{syst}} = \sqrt{\sigma^2_{\text{total}} - \sigma^2_{\text{stat}}} \tag{11.8}$$

with σ^2_{total} being the $|U_{e4}|^2$ sensitivity obtained from a raster scan with the full covariance matrix and σ^2_{stat} being the $|U_{e4}|^2$ sensitivity calculated from a raster scan considering only statistical uncertainties.

Figure 11.10 (bottom panel) displays σ_{syst} and σ_{stat} for KNM1 and KNM2. As the second measurement campaign has much more statistics than the first measurement campaign, its statistical $|U_{e4}|^2$ sensitivity is significantly better than the KNM1 sensitivity for all m_4^2. Different to that, the systematic-only contribution are similar for both measurement campaigns. Both measurement campaigns are statistics dominated in the analyzed energy range, with $\sigma^2_{\text{stat}}/\sigma^2_{\text{total}} > 0.5$ (top panel) for all considered values of m_4^2. The median relative contribution of the statistical uncertainty to the total $|U_{e4}|^2$ uncertainty budget at 68.3 % C.L., $(\sigma^2_{\text{stat}}/\sigma^2_{\text{total}})_{\text{median}}$, is as large as 99 % and 86 % for KNM1 and KNM2, respectively.

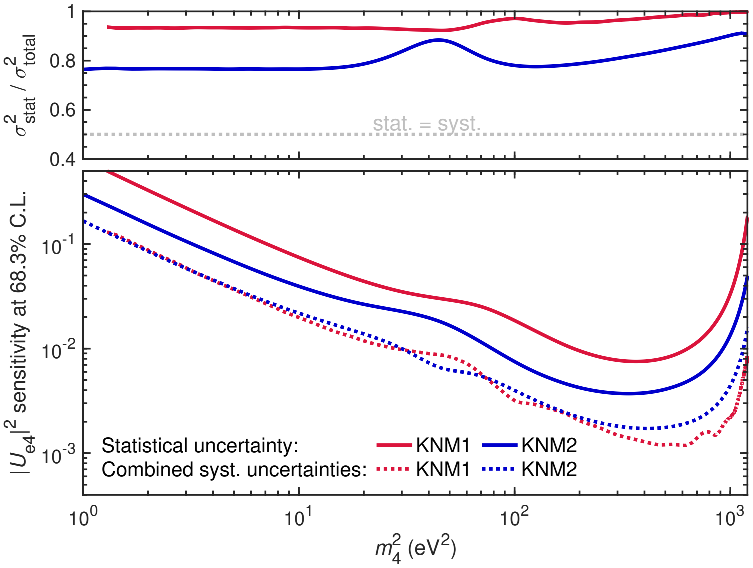

Figure 11.10: Comparison of statistical and systematic sensitivity on $|U_{e4}|^2$ at 68.3 % C.L. for KNM1 and KNM2. The sensitivities are obtained from raster scans for different fixed values of m_4^2. The solid curves in the lower panel correspond to the statistics-only contributions σ^2_{stat}, whereas the dotted curves illustrate the systematic-only contributions σ^2_{syst}. While KNM1 and KNM2 have similar systematic-only sensitivities, σ^2_{stat} is significantly better in KNM2 compared to KNM1. The ratio between statistical uncertainties and the total uncertainty budget is shown in the upper panel. Both measurement campaigns are dominated by statistical uncertainties, as $\sigma^2_{\text{stat}}/\sigma^2_{\text{total}} > 0.5$ for all m_4^2.

Furthermore, the influence of individual systematic effects is investigated at the example of KNM2. For each systematic effect, a raster scan considering only the respective systematic uncertainty on top of the statistical uncertainty is carried out. The systematics-only contributions σ_{syst} are displayed in figure 11.11 as a function of m_4^2 for all systematic effects in the KNM2 analysis. For $m_4^2 \leq 600\,\text{eV}^2$, the systematic effects are dominated by the non-Poisson rate distribution of the background, the scan-step-duration-dependent background, and source-potential variations. For larger $m_4^2 > 600\,\text{eV}^2$, all systematic contributions, except for the non-Poisson rate distribution of the background, rapidly increase. The largest systematic contribution for larger m_4^2 is given by the molecular final-state distribution. This can be explained by an increased uncertainty on the excited molecular states in this energy region. In table 11.2, the median relative contribution of each systematic effect is summarized, sorted by magnitude. The median is calculated using the same linearly spaced m_4^2 values for all systematic effects.

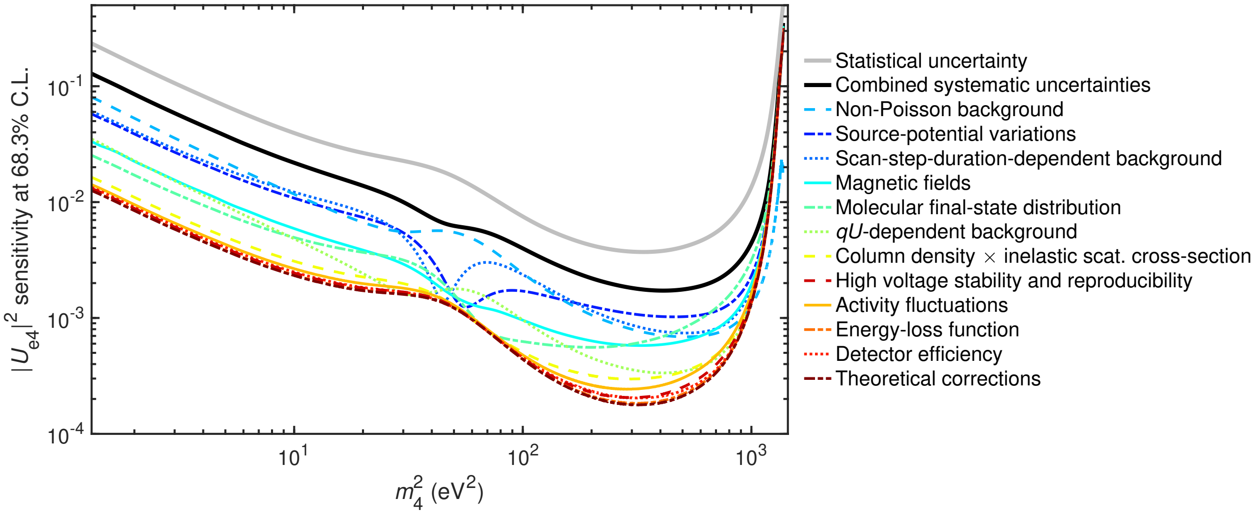

Figure 11.11: KNM2 sensitivity breakdown obtained from a simulated twin data set with $m_\nu^2 = 0\,\text{eV}^2$. The systematic-only contributions are extracted from raster scans for different fixed values of m_4^2 at 68.3 % C.L. For reference, also the statistics-only sensitivity and the combined sensitivity contributions on $|U_{e4}|^2$ are provided. Only the region $m_4^2 > 1\,\text{eV}$ is shown, since there is no sensitivity to the systematic-only contribution in small mass regions. The median relative contributions $(\sigma^2/\sigma^2_\text{total})_\text{median}$ are listed in table 11.2. All systematic effects are small compared to the statistical uncertainty. The statistical uncertainty even dominates over all systematic uncertainties combined, $\sigma^2_\text{stat}/\sigma^2_\text{total} > 0.5$ for all m_4^2.

Effect	$(\sigma^2/\sigma^2_\text{total})_\text{median}$
Statistical	0.86
Source-potential variations	0.06
Scan-step-duration-dependent background	0.04
Non-Poisson background	0.02
Magnetic fields	0.03
Molecular final-state distribution	0.05
qU-dependent background	0.01
Column density × inelastic scattering cross section	0.01
Detector efficiency	0.01
Activity fluctuations	< 0.01
Energy-loss function	< 0.01
High-voltage stability and reproducibility	< 0.01
Theoretical corrections	< 0.01
Total systematic uncertainty	0.14

Table 11.2: KNM2 breakdown of the relative sensitivities on $|U_{e4}|^2$, given as the median $(\sigma^2/\sigma^2_\text{total})_\text{median}$ over all m_4^2. The systematic effects are listed in descending order of the maximal uncertainty $\max(\sigma^2_\text{syst}/\sigma^2_\text{total})$. The systematic uncertainty inputs are those used in the neutrino-mass analysis (appendix C). The analysis is dominated by statistical uncertainties with $(\sigma^2_\text{stat}/\sigma^2_\text{total})_\text{median} > 0.5$.

11.8 Extension of the fit interval

All contour curves presented up to here are based on the standard analysis intervals, which extend down to 39 eV (KNM1) and 40 eV (KNM2) below the fit endpoint. An expansion of the fit interval is very beneficial for the sterile-neutrino search, as it increases the accessible parameter space for m_4^2. However, due to insufficient understanding of systematic uncertainties at high electron energy losses, the full measurement interval down to 93 eV (KNM1) and 90 eV (KNM2) below the fit endpoint was not selected as baseline result. Here, the same systematic uncertainties as in the standard analysis range are considered.

To investigate whether large unaccounted systematic effects appear at smaller retarding energies, a supplementary analysis is performed taking all scan steps into account. In addition, the full-range exclusion contours demonstrate the potential benefit of a larger fit interval for KATRIN's sterile-neutrino search. However, because of the aforementioned reasons, the exclusion contours in this section have to treated with caution. A more robust analysis would require a comprehensive review of the systematic uncertainty budget.

The full-range exclusion contours at 95 % C.L. are displayed in figure 11.12 for analysis case I) and figure H.6 for analysis case II) alongside the respective contours in the standard analysis intervals. An overview of the best-fit results and their significances is provided in table H.1. As discussed previously, the full-range exclusion contours extend to larger masses compared to the standard analysis interval. The KNM1 contour is closed in both analysis cases, which corresponds to a sterile-neutrino signal at 95 % C.L. However, an open exclusion contour can be drawn at 99 % C.L. The KNM1 best fits of both analysis cases are located at similar large masses $m_4^2 \approx 4000\,\mathrm{eV}^2$ and moderate mixings $|U_{e4}|^2 \approx 0.014$. As the signal cannot be reproduced in the KNM2 analysis, it stems likely from a statistical fluctuation or an unaccounted systematic effect. Moreover, this region is already excluded by the sterile-neutrino search of the Troitsk experiment [112] at 95 % C.L., displayed in figure H.7. The combined KNM1 and KNM2 analysis is presented in figure H.7 for analysis case I). It yields an open exclusion contour at 95 % C.L. and improves upon the constrains from Mainz [111] for $m_4^2 \lesssim 6000\,\mathrm{eV}^2$ and upon the constraints from Troitsk for $m_4^2 \lesssim 2000\,\mathrm{eV}^2$.

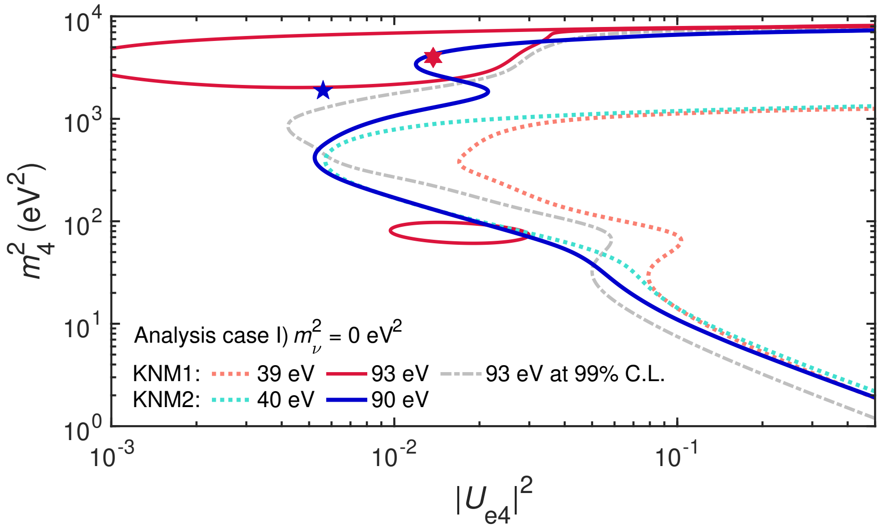

Figure 11.12: Analysis case I) contour curves considering the full measurement interval of KNM1 and KNM2. If not explicitly stated otherwise, the contours are drawn at 95 % C.L. The positive signal at 95 % in KNM1 stems likely from a statistical fluctuation or an unaccounted systematic effect. Moreover, the closed contour opens at 99 % C.L., as illustrated by the gray dash-dotted line.

11.9 Nonphysical parameter space

Moreover, supplementary analyses are performed on the KNM1 and KNM2 data sets for both analysis cases allowing the sterile-neutrino parameters to take nonphysical values: $m_4^2 \in [-40\,\mathrm{eV}^2, +40\,\mathrm{eV}^2]$, $|U_{e4}|^2 \in [-0.5, 1]$. The resulting two-dimensional chi-squared profiles, depicted in figures H.11 and H.12, can be divided into four quadrants. The north-east quadrant is considered to be the physical quadrant. The remaining three quadrant are considered to be nonphysical, as they would formally correspond to tachyonic sterile neutrinos ($m_4^2 < 0\,\mathrm{eV}^2$) or negative tritium decay rates ($|U_{e4}|^2 < 0$).

No significant sterile neutrino is found in the nonphysical parameter space. Even though the global chi-squared minimum is often found outside the physical region, the improvement in terms of χ^2_{min} with respect to the physical region is insignificant (≤ 2.7) for all considered cases.

11.10 Test of Wilks's theorem

The confidence regions presented in this work are constructed with grid searches. In this process, the asymptotic behavior of the chi-squared test statistic is utilized as formulated by Wilks's theorem to avoid costly Monte Carlo simulations. In this section, the applicability of Wilks's theorem is validated with Monte Carlo methods for different exemplary Monte Carlo truths. The hypothesis test that determines whether a grid point is compatible with the best-fit hypothesis H_1 or not is based on the $\Delta\chi^2$ test statistics

$$\Delta\chi^2 = \chi^2(H_0) - \chi^2(H_1). \tag{11.9}$$

In the grid search, H_0 is set to the $[m_4^2, |U_{e4}|^2]$ values of the respective grid point while fixing H_1 to the global best fit. According to Wilks's theorem, $\Delta\chi^2$ converges to a chi-squared distribution with 2 dof in the large sample limit if H_0 is true. The application of Wilks's theorem dramatically facilitates the sterile-neutrino analysis, because it provides the threshold value $\Delta\chi^2_{\mathrm{crit}} = 5.99$, above which a grid point H_0 is considered incompatible with H_1 at 95 % C.L. If Wilks's theorem was not applicable, the probability density function of the $\Delta\chi^2$ test statistics had to be calculated with Monte Carlo methods for each grid point, which would be an enormous computational effort. However, it was pointed out by [38] using the example of neutrino oscillation experiments, that the unjustified application of Wilks's theorem can lead to inaccurate confidence regions or even to a falsely claimed discovery. Therefore, the applicability of Wilks's theorem in the sterile-neutrino analysis in KATRIN is investigated in detail in the following.

The usage Wilks's theorem can be justified by numerically calculating the probability density functions of the $\Delta\chi^2$ function with MC methods and comparing the result to the prediction from Wilks.

As a first step, $\mathcal{O}(10^3)$ randomized tritium spectra are simulated using statistical and systematic uncertainties. The spectral model configurations are the same as for the MC twins. Secondly, each sample spectrum is analyzed with the grid search method and $m_\nu^2 = 0\,\mathrm{eV}^2$ (analysis case I). For each sample grid, $\Delta\chi^2$ is calculated according to equation (11.9) with H_0 being the MC truth and H_1 being the global best fit of the respective sample. The locations of the best fits in the $[m_4^2, |U_{e4}|^2]$ plane are displayed in figure H.8 at the example of KNM2-like MC simulations with $H_0 = [m_4^2 = 0\,\mathrm{eV}^2\ , |U_{e4}|^2 = 0]$. The histogram of $\Delta\chi^2$, shown in figure H.9 (left), is then compared to a chi-squared distribution with 2 dof. The critical $\Delta\chi^2$ value for 95 % C.L. can then be retrieved from the cumulative probability density function, illustrated in figure H.9 (right).

The procedure is carried out for both data sets and different MC truths. The corresponding figures for KNM1 and different MC truths are provided in appendix H.6. The null hypothesis with $H_0 = [m_4^2 = 0\,\mathrm{eV}^2\ , |U_{e4}|^2 = 0]$ is, by definition, the boundary physics case. As it can be realized with an infinite number of sterile parameter pairs with $|U_{e4}| = 0$ and arbitrary m_4^2, a hypothetical deviation from Wilks's theorem is anticipated to be most prominent here. The results for all MC truths and data sets are summarized in table 11.3. The numerical $\Delta\chi^2_{\mathrm{crit}}$ values are in good agreement to the prediction from Wilks's theorem. The uncertainties on $\Delta\chi^2_{\mathrm{crit}}$ are estimated with the bootstrapping method.

Furthermore, the impact on the exclusion contour is estimated at the example of KNM2 assuming that the numerically calculated $\Delta\chi^2_{\mathrm{crit}}$ values of table 11.3 are representative for all grid points. The exclusion curve at 95 % C.L.

is drawn 3 times with 3 different threshold values: 1) $\Delta\chi^2_{\mathrm{crit}} = 5.99$ (Wilks's theorem), 2) $\Delta\chi^2_{\mathrm{crit}} = 6.31 \pm 0.30$ (Numerical values from null hypothesis) and 3) $\Delta\chi^2_{\mathrm{crit}} = 6.69 \pm 0.27$ (Numerical values from a sterile-neutrino hypothesis). The resulting exclusion curves as well as their 1σ-uncertainty bands are displayed in figure H.10. The contour differ only very little from one another.

In conclusion, the numerically calculated threshold values $\Delta\chi^2_{\mathrm{crit}}$ and the respective coverages agree well with the prediction of Wilks's theorem for both data sets and all MC truths considered. Moreover, using the $\Delta\chi^2_{\mathrm{crit}}$ obtained in this work instead of Wilk's theorem results only in a small shift of the exclusion curve. The application of Wilk's theorem is therefore justified for the sterile-neutrino search in KATRIN.

Data set	MC truth		$\Delta\chi^2_{\mathrm{crit}}$ at 95 %C.L.
	m_4^2	$\lvert U_{e4}\rvert^2$	
KNM1	0 eV^2	0	5.92 ± 0.26
KNM2	0 eV^2	0	6.31 ± 0.30
KNM2	92.7 eV^2	0.024	6.69 ± 0.27
KNM2	20 eV^2	0.07	6.30 ± 0.22

Table 11.3: The critical chi-squared difference, which corresponds to 95 % C.L., is numerically calculated by analyzing simulated MC spectra for KNM1 and KNM2. For KNM2, two sterile-neutrino hypotheses are investigated in addition to the null hypothesis. The resulting $\Delta\chi^2_{\mathrm{crit}}$ agree within uncertainties to the predicition of Wilks ($\Delta\chi^2_{\mathrm{crit}} = 5.99$). The underlying $\Delta\chi^2$ distributions are displayed in figure 11.13 and appendix H.6.

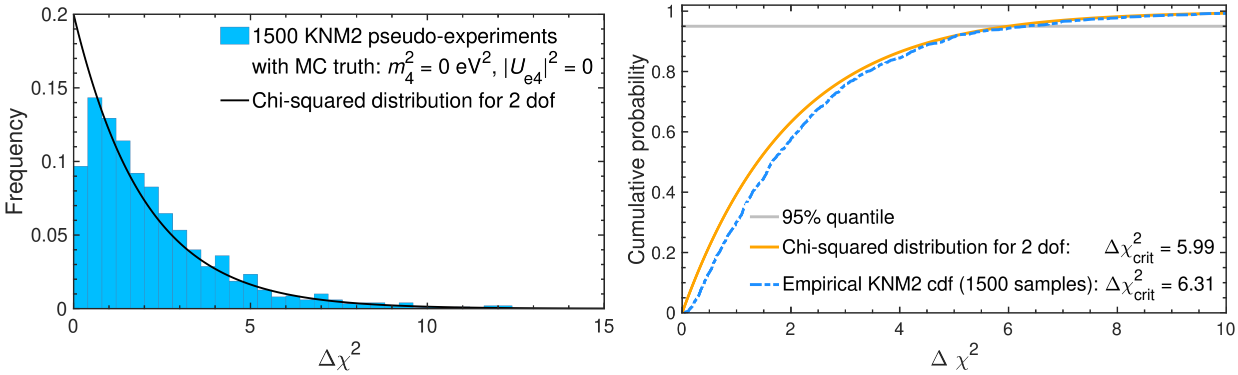

Figure 11.13: Test of Wilks's theorem for the KNM2 sterile-neutrino analysis considering the null hypothesis. **Left:** $\Delta\chi^2$ is calculated for each simulated sample spectrum according to equation (11.9). The MC truth is the null hypothesis with $m_4^2 = 0\,\mathrm{eV}^2$ and $|U_{e4}|^2 = 0$. The black solid line corresponds to the expectation from Wilks's theorem. **Right:** The empirical cumulative density function is calculated from the $\Delta\chi^2$ samples in the left figure. The 95 % quantile corresponds to $\Delta\chi^2_{\mathrm{crit}} = 6.31 \pm 0.30$, which is in good agreement with Wilks prediction. The uncertainty is estimated with the boot-strapping method. The corresponding figures for KNM1 and other MC truths are given in appendix H.6.

Chapter 12

Summary and Conclusion

This thesis is dedicated to the analyses of the first two measurement campaigns of the KATRIN experiment. In terms of effective electron antineutrino mass, a world-best upper limit below the sub-eV level could be reached. Moreover, to exploit the full physics potential of the KATRIN experiment, a search for light sterile neutrinos was conducted.

After a nearly 20-year-long journey from design to commissioning, the KATRIN experiment took its first neutrino-mass data in spring 2019 ("KNM1"). In total, 274 tritium scans were recorded, which accumulate to a net measurement time of 23 days. The first measurement campaign was the first operation at high tritium purity ($> 95\,\%$), which is one of the most important prerequisites to achieve considerable neutrino-mass sensitivity. The source activity was eventually limited to $2.5 \times 10^{10}\,\mathrm{Bq}$ (25 % design value), as initial radio-chemical reactions between tritium molecules and surfaces in the source system required the operation at reduced column density. An energy-independent background rate of 290 mcps was observed, which exceeds the design value many times over and currently limits the statistical sensitivity. Overall, an excellent stability of all operational parameters could be achieved, for some parameters even exceeding the design requirements.

The second measurement campaign ("KNM2") followed in fall 2019 and comprised 361 tritium scans and 29 net measurement days. No longer limited to operate in the burn-in configuration, the column density could be increased and an unprecedented source activity of $9.5 \times 10^{10}\,\mathrm{Bq}$ could be reached. Moreover, the background rate was reduced by 25 % with respect to KNM1, due to improved vacuum conditions in the main spectrometer.

Neutrino-mass analysis

The first two measurement campaigns are analyzed with respect to the neutrino mass, which is the main objective of KATRIN. The neutrino-mass results that were obtained in the scope of this thesis were published in [23, 65, 96, 101].

A least-squares fit to the KNM1 spectral data yields $m_\nu^2 = (-0.96^{+0.88}_{-1.05})\,\mathrm{eV}^2$. Within uncertainties, the result is consistent with no neutrino mass. However, it adds to a long list of direct neutrino-mass experiments, that inferred a negative best-fit value of m_ν^2. Even though nonphysical, negative m_ν^2 values are allowed in the calculation of the decay spectrum. Neither prior assumption on m_ν^2, nor artificial modification of the phase space are made. Thorough investigations were carried out to search for unaccounted systematic effects that could be responsible for a negative m_ν^2 bias. None were found. Consequently, the result is interpreted as a 1σ statistical fluctuation into the nonphysical mass regime. Taking the physical boundary $m_\nu > 0\,\mathrm{eV}$ into account, the KNM1 best-fit result is translated into an upper limit of $m_\nu \leq 1.1\,\mathrm{eV}$ at 90 % C.L., which coincides with the experimental sensitivity.

Thanks to an increased source activity and a reduced background level, the KNM2 sensitivity could be greatly improved to $m_\nu \leq 0.7\,\mathrm{eV}$ at 90 % C.L. The spectral analysis of the KNM2 data set infers $m_\nu^2 = (0.26^{+0.33}_{-0.32})\,\mathrm{eV}^2$. Like in KNM1, the best-fit value is consistent with no neutrino mass. The result translates into an upper limit of $m_\nu \leq 0.9\,\mathrm{eV}$ (90 % C.L.). Combining the first two measurement campaigns, an improved upper limit of $m_\nu \leq 0.8\,\mathrm{eV}$

(90 % C.L.) can be obtained. Reaching for the first time in the sub-eV regime, the first two KATRIN results mark a milestone in the direct neutrino-mass search.

The influences of statistical and systematic effects on the neutrino-mass are investigated in detail. Both data sets are strongly dominated by statistical uncertainties: The total uncertainty budget at 68.27 % C.L. in KNM1 amounts to $\sigma_{\mathrm{tot}}(m_\nu^2) = 0.97\,\mathrm{eV}^2$, from which the vast majority can be attributed to statistical uncertainties with $\sigma_{\mathrm{stat}}(m_\nu^2) = 0.93\,\mathrm{eV}^2$. A similar observation is made for KNM2. The total budget uncertainty of $\sigma_{\mathrm{tot}}(m_\nu^2) = 0.32\,\mathrm{eV}^2$ is governed by statistical uncertainties with $\sigma_{\mathrm{stat}}(m_\nu^2) = 0.28\,\mathrm{eV}^2$. Moreover, the influence of individual systematic effects is evaluated. For both campaigns, the largest contribution to the systematic m_ν^2 uncertainty stems from the Non-Poisson background rate over-dispersion. As the latter effectively increases the relative statistical uncertainty on the steady-state background rate, it is expected to become less relevant in future measurement campaigns.

The baseline fit intervals in KNM1 and KNM2 comprise data points down to 39 eV and 40 eV below the tritium endpoint, respectively. Even though an extension of the range would have been beneficial in terms of statistical m_ν^2 sensitivity, the narrow energy interval was selected over wider one, because systematic effects become more relevant for larger electron-energy losses. This concerns in particular the uncertain high-energy part of the final-state distribution, for which refined calculations were ongoing at the time of the analysis. However, both measurement campaigns recorded additional data points at retarding energies down to 93 eV (KNM1) and 90 eV (KNM2) below the endpoint. The sensitivity equilibrium between statistical and known systematic effects is only found at the full measurement range for KNM1 and at 70 eV below E_0 for KNM2. Moreover, the data sets are analyzed using the full energy range. No significant energy dependence in terms of m_ν^2, which would point towards unaccounted systematic effects, is found.

In both measurement campaigns, 117 out of 148 slightly different FPD pixels were selected and jointly analyzed. However, different pixel combination strategies were applied: In KNM1, all selected pixels were combined to a single uniform spectrum. This was possible due to an excellent spatial homogeneity of the electric and magnetic fields in the source and the analyzing plane. In KNM2, the selected pixels were grouped into four pseudo-rings. The pseudo-rings were fit with a shared m_ν^2 value and individual nuisance parameters. The latter include ring-wise source potential offsets ΔqU to account for a possible radial dependency. The multi-ring fit, however, revealed only small ring-wise differences $\Delta qU < 100\,\mathrm{meV}$. Different pixel combination strategies applied to the KNM2 data yield consistent results with $\Delta m_\nu^2 < 0.04\,\mathrm{eV}^2$.

Moreover, various sub-sets within the standard pixel selection are analyzed independently, allowing for individual m_ν^2 values. An unexpected radial or angular pattern in m_ν^2 would hint toward an unaccounted systematic effect. The data sets are divided into 4 and 12 (pseudo-) rings for KNM1 and KNM2, respectively. While in KNM1 the fitted m_ν^2 values tend to decrease with FPD radius, the opposite is observed for KNM2. In both cases the radial pattern is insignificant ($< 2\sigma$) and therefore attributed to statistical fluctuations. Moreover, the pixels are grouped according to their azimuth angle on the FPD. For the KNM2 data set, no angular m_ν^2 dependence is observed. In KNM1, however, an asymmetry between the north-eastern quarter and the remaining FPD is observed at 2.3σ significance. As no physical effect is known that could explain such a pattern and the asymmetry is not observed in KNM2, it likely stems from a statistical fluctuation.

To further search for missed systematic effects, several sub-sets of the golden tritium scan selection are analyzed independently. The scans are grouped by scanning strategy ("upward/downward"), temporal occurrence ("first/middle/last third") or operational parameters (e.g. rear wall bias voltage). No significant m_ν^2 dependence is observed.

With hundreds of scheduled measurement days ahead, KATRIN will further improve its statistics by a factor of 50. Extensive investigations of systematic effects are in progress to reduce the already small systematic uncertainties even more. Moreover, a novel operation mode, called "shifted analysis plane", achieved a reduction of the background rate by a factor of 2. Combining all three characteristics (high-statistics, small systematic uncertainties and a low background), the KATRIN experiments targets a m_ν^2 sensitivity close to its design value around 0.2-0.3 eV (90 %) C.L. by 2025.

Sterile-neutrino analysis

Accumulating anomalies in short-baseline neutrino oscillation experiments, that could be resolved with the existence of eV-scale sterile neutrinos, triggered a huge experimental effort. In this thesis, a search for light sterile neutrinos in the KATRIN experiment was conducted using the same data as for the neutrino-mass analysis. Considering the $3\nu+1$ framework, the spectral model is extended by a sterile decay branch, which is characterized by a fourth neutrino mass eigenstate m_4^2 and its mixing to the electron flavor $|U_{e4}|^2$. The signature of a sterile neutrino in KATRIN is a kink-like spectral distortion, that is most prominent at electron energies around $E_0 - m_4$. Limited by the energy range, the analysis is sensitive to $m_4^2 \lesssim 1600\,\mathrm{eV}^2$. Given the statistics of the first two measurement campaigns, mixings down to $|U_{e4}|^2 \gtrsim 6 \times 10^{-3}$ are accessible.

The search for sterile neutrinos with the KATRIN experiment provides an independent test of the short-baseline neutrino oscillation anomalies. Being based exclusively on the *shape* of the β-spectrum, the analysis is robust and independent of any normalization effects, such as the absolute source activity. Moreover, KATRIN is influenced by a different set of systematic effects than neutrino-oscillation experiments.

No sterile-neutrino signal is observed at 95 % C.L. Thus, exclusion contours are calculated instead. The obtained constraints on the active-to-sterile mixing improve upon the results from previous tritium β-decay experiments. Moreover, a significant fraction of the large Δm_{41}^2 solutions of the reactor and gallium anomalies can be excluded. Furthermore, the claimed sterile-neutrino signal of the Neutrino-4 collaboration is disfavored at 95 % C.L. by the KATRIN data for $\sin^2(2\theta_{ee}) \gtrsim 0.4$. The sterile-neutrino constraints, that were derived in the frame of this thesis, are published in [108] and in [109][1].

In a supplementary analysis, the nonphysical parameter space was explored allowing m_4^2 and $|U_{e4}|^2$ to take negative values. No significant improvement of the goodness-of-fit with respect to the physical parameter space was found.

Furthermore, the coverage of the calculated confidence regions was validated with extensive Monte Carlo simulations. The applicability of Wilks' theorem could be confirmed at several representative sterile-neutrino hypothesis.

The impact of systematic effects on the sterile-neutrino search is evaluated. Both data sets are strongly dominated by statistical uncertainties for all considered m_4^2 values. The median relative contribution of statistical uncertainties to the total $|U_{e4}|^2$ uncertainty budget $(\sigma^2_{\mathrm{stat}}/\sigma^2_{\mathrm{total}})_{\mathrm{median}}$ amounts to 99 % and 86 % for KNM1 and KNM2, respectively. Whereas the influence of systematics uncertainties on $|U_{e4}|^2$ is comparable between the measurement campaigns, statistical uncertainties in KNM2 are significantly smaller compared to KNM1.

Furthermore, different treatments of m_ν^2 in the $3\nu+1$ framework are investigated. The main analysis case I), presented above, considers the hierarchical scenario $m_{1,2,3} \ll m_4$, which justifies fixing m_ν^2 to $0\,\mathrm{eV}^2$. In a complementary analysis case II), m_ν^2 is allowed to vary freely as an unconstrained nuisance parameter. The case II) generally yields weaker constraints on m_4^2 and $|U_{e4}|^2$ than case I), due to the correlation between the active and the sterile decay branches. For small $m_4^2 \lesssim 30\,\mathrm{eV}^2$ values, a negative correlation between m_ν^2 and m_4^2 is observed with increasing absolute strength for increasing $|U_{e4}|^2$. Indeed, the difference between the analysis cases in terms of exclusion contours is most pronounced for small sterile masses. For larger m_4^2 values, the correlation is less pronounced and has a positive sign. Assuming the existence of a light sterile neutrino, the correlation also translates into a reduction in m_ν^2 sensitivity by a factor of 2 compared to the neutrino-mass analysis in the 3ν framework. By constraining the sterile neutrino mass or mixing, the nominal sensitivity can be restored.

For the same reasons as in the neutrino-mass analysis, the baseline sterile-neutrino search is restricted to the relatively narrow analysis interval. In the case of the sterile-neutrino search, the extension to the full measurement range is extremely beneficial as it opens the door to larger m_4^2 values up to $\lesssim 8600\,\mathrm{eV}^2$. However, the results have to be regarded with caution due to ongoing investigations of systematic effects that occur at large electron energy losses. Indeed, the analysis of the KNM1 data set considering the full measurement interval produces a closed contour at 95 % C.L. However, the associated best-fit result can be excluded by the open KNM2 exclusion contour (95 % C.L.) for the full interval. Due to the aforementioned reasons, it is rather doubtful that the KNM1 full-range result is the signature of an actual sterile neutrino rather than a neglected systematic effect.

---

[1] as corresponding author

The sterile-neutrino analysis of future KATRIN measurement campaigns will provide a crucial input to resolve the gallium and reactor antineutrino anomalies at large Δm^2_{41}. Moreover, it will provide complementary results to short-baseline oscillation experiments for small $\Delta m_{41} \lesssim 10\,\mathrm{eV}$ and will soon test the entire Neutrino-4 signal region.

Appendix A

KATRIN Experiment

A.1 Energy-dependent scattering cross section

The cross section $\sigma_{\text{inel.}}$ characterizes the inelastic scattering between electrons and tritium molecules. The scattering probabilities section 2.2.2.2 depend the product $\rho d \sigma_{\text{inel.}}$, which can be directly measured in KATRIN. Therefore, only the energy dependence of the $\sigma_{\text{inel.}}$ is needed as an external input. This work uses the high-energy Born approximation based calculation from [119–121]:

$$\sigma_{\text{inel.}} = \frac{4\pi a_0^2}{T/R_{\text{H}}} \cdot \left[M_{\text{tot}}^2 \cdot \ln\left(4 c_{\text{tot}} \frac{T}{R} \right) - 0.01 \right] \tag{A.1}$$

with the parameters:

Bohr radius:	$a_0^2 = 28.003 \times 10^{-18}\,\text{cm}^2$
Non-relativistic kinetic electron energy	$T = \frac{1}{2} m_e \beta^2 = \frac{1}{2} m_e \left(1 - \frac{m_e^2}{(m_e + E)^2} \right)$
Rydberg energy	$R_{\text{H}} = 13.606\,\text{eV}$
Expectation value [122]	$M_{\text{tot}} = 1.536$ for T_2
Subdominant parameter [121]	$c_{\text{tot}} = 1.18$

The energy-dependent scattering cross sections is displayed in figure A.1 using the formula and parameter values above. For an electron energy around to the tritium endpoint, $\sigma_{\text{inel.}}(18\,574\,\text{eV}) = 3.64 \times 10^{-18}\,\text{cm}^{-2}$. The uncertainty is estimated to be 0.5 % [65].

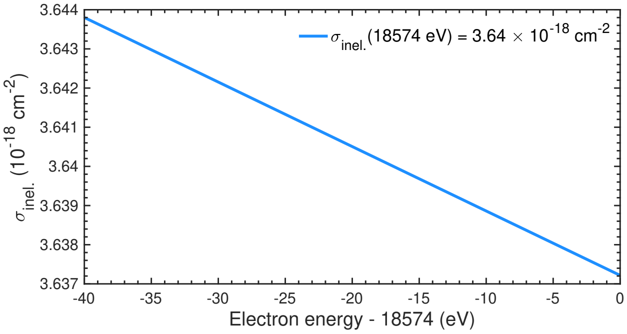

Figure A.1: Inelastic scattering cross section as a function of electron energy.

A.2 Energy-loss function parameter

The energy-loss function (section 2.2.2.2) is measured *in-situ* in KATRIN. All details on the measurement and analysis can be found in [48, 49, 68]. As the analysis was refined several times and new data was recorded, the energy-loss parameter values used in this work slightly differ from those published in [68]. Thus, they are explicitly stated in the table A.1. An ionization threshold energy of $E_i = 15.487\,\mathrm{eV}$ (T_2) is used in both cases. The parameters are correlated among each other. The correlations have to be taken into account when propagating the parameter uncertainties to the integral spectrum. The correlation matrices is are stated in table A.2 and table A.3.

Parameter	Analysis from May 2019[123]	Analysis from April 2020 [72]
a_1 (eV^{-1})	0.0314 ± 0.0013	0.0323 ± 0.0011
a_2 (eV^{-1})	0.2982 ± 0.0009	0.2960 ± 0.0006
a_3 (eV^{-1})	0.0765 ± 0.0004	0.0760 ± 0.0004
μ_1 (eV)	11.9359 ± 0.0091	11.9160 ± 0.0077
μ_2 (eV)	12.8267 ± 0.0023	12.8042 ± 0.0019
μ_3 (eV)	14.9726 ± 0.0048	14.9658 ± 0.0037
σ_1 (eV)	0.1797 ± 0.0080	0.1825 ± 0.0065
σ_2 (eV)	0.4708 ± 0.0024	0.4692 ± 0.0020
σ_3 (eV)	0.8700 ± 0.0134	0.8999 ± 0.0117

Table A.1: Best-fit parameter values of the energy-loss function from dedicated energy-loss function measurements. The parametrization in equation (2.22) is used. The analysis is described in [68].

	a_1	μ_1	σ_1	a_2	μ_2	σ_2	a_3	μ_3	σ_3
a_1	1.0000	0.4151	0.2559	0.1481	0.4824	-0.6544	-0.1250	-0.1877	0.2397
μ_1	0.4151	1.0000	0.7570	-0.0801	0.5475	-0.4265	-0.0416	-0.0866	0.0974
σ_1	0.2559	0.7570	1.0000	0.0311	0.5271	-0.5938	-0.1015	-0.1492	0.2029
a_2	0.1481	-0.0801	0.0311	1.0000	0.1303	-0.3499	0.1409	-0.2060	-0.1779
μ_2	0.4824	0.5475	0.5271	0.1303	1.0000	-0.2469	0.2393	0.0547	-0.3041
σ_2	-0.6544	-0.4265	-0.5938	-0.3499	-0.2469	1.0000	0.3221	0.3387	-0.5643
a_3	-0.1250	-0.0416	-0.1015	0.1409	0.2393	0.3221	1.0000	-0.4451	-0.8799
μ_3	-0.1877	-0.0866	-0.1492	-0.2060	0.0547	0.3387	-0.4451	1.0000	0.0154
σ_3	0.2397	0.0974	0.2029	-0.1779	-0.3041	-0.5643	-0.8799	0.0154	1.0000

Table A.2: Parameter correlation matrix for measurement in May 2019[123].

	a_1	μ_1	σ_1	a_2	μ_2	σ_2	a_3	μ_3	σ_3
a_1	1.0000	0.4155	0.2506	0.1299	0.5049	-0.6496	-0.1091	-0.1884	0.2159
μ_1	0.4155	1.0000	0.7680	0.1115	0.5677	0.4204	0.0295	0.0847	0.0765
σ_1	0.2506	0.7680	1.0000	0.0106	0.5426	0.5791	0.0829	0.1536	0.1737
a_2	0.1299	0.1115	0.0106	1.0000	0.1606	0.3728	0.1884	0.0609	0.2204
μ_2	0.5049	0.5677	0.5426	0.1606	1.0000	0.2501	0.2336	0.0990	0.3162
σ_2	-0.6496	0.4204	0.5791	0.3728	0.2501	1.0000	0.3088	0.3785	0.5447
a_3	-0.1091	0.0295	0.0829	0.1884	0.2336	0.3088	1.0000	0.4198	0.8864
μ_3	-0.1884	0.0847	0.1536	0.0609	0.0990	0.3785	0.4198	1.0000	0.0294
σ_3	0.2159	0.0765	0.1737	0.2204	0.3162	0.5447	0.8864	0.0294	1.0000

Table A.3: Parameter correlation matrix for measurement in April 2020[72].

Appendix B

Pixel combination

The basic pixel combinations are presented in section 3.2.2 and displayed in figure 3.1. Sometimes it can be beneficial to arrange the pixels in larger groups to improve the statistics within each group. Fur this purpose, two or more groups are combined. All pixel combinations, that are used throughout this work in addition to the ones in section 3.2.2, are summarized in tables B.1 to B.3 and visualized in figure B.1.

Ring	Pixel numbers	Pseudo-ring	Pixel numbers	Halves	Pixel numbers
0 (bullseye)	0 – 3	1	0 – 27	Inner	0 – 63
1	4 – 15				
2	16 – 27				
3	28 – 39	2	28 – 63		
4	40 – 51				
5	52 – 63				
6	64 – 75	3	64 – 99	Outer	64 – 147
7	76 – 87				
8	88 – 99				
9	100 – 111	4	100 – 147		
10	112 – 123				
11	124 – 135				
12	136 – 147				

Table B.1: Radial pixel lists. To search for a radial pattern, e.g. in terms of m_ν^2, the FPD pixels can be grouped according to their radial position in rings or pseudo-rings. Different levels of granularity are available in Samak. The pixel lists include all FPD pixels. Applied to a specific data set, the overlap of the respective golden pixel list has to be considered.

Halves	Pixel numbers
Northern half	0, 1, 5 − 10, 16 − 21, 28 − 33, 40 − 45, 52 − 57, 64 − 69, 76 − 81, 88 − 93, 100 − 105, 112 − 117, 124 − 129, 136 − 141
Southern half	2 − 4, 11 − 15, 22 − 27, 34 − 39, 46 − 51, 58 − 63, 70 − 75, 82 − 87, 94 − 99, 106 − 111, 118 − 123, 130 − 135, 142 − 147
Eastern half	0, 3 − 7, 14 − 18, 25 − 30, 37 − 42, 49 − 54, 61 − 66, 73 − 78, 85 − 90, 97 − 102, 109 − 114, 121 − 126, 133 − 138, 145 − 147
Western half	1, 2, 8 − 13, 19 − 24, 31 − 36, 43 − 48, 55 − 60, 67 − 72, 79 − 84, 91 − 96, 103 − 108, 115 − 120, 127 − 132, 139 − 144

Table B.2: Alternative pixel lists. As a sanity check, the FPD pixels can be grouped into two parts. The pixel lists include all FPD pixels. Applied to a specific data set, the overlap of the respective golden pixel list has to be considered.

Slice	Angle	Pixel numbers	Pseudo-slice	⟨Angle⟩
0	0°	7, 31, 55, 79, 103, 127	1	15°
1	15°	18, 42, 66, 90, 114, 138		
2	30°	6, 30, 54, 78, 102, 126		
3	45°	0, 17, 41, 65, 89, 113, 137	2	60°
4	60°	5, 29, 53, 77, 101, 125		
5	75°	16, 40, 64, 88, 112, 136		
6	90°	4, 28, 52, 76, 100, 124	3	105°
7	105°	27, 51, 75, 99, 123, 147		
8	120°	15, 39, 63, 87, 111, 135		
9	135°	3, 26, 50, 74, 98, 122, 146	4	150°
10	150°	14, 38, 62, 86, 110, 134		
11	165°	25, 49, 73, 97, 121, 145		
12	180°	13, 37, 61, 85, 109, 133	5	195°
13	195°	24, 48, 72, 96, 120, 144		
14	210°	12, 36, 60, 84, 108, 132		
15	225°	2, 23, 47, 71, 95, 119, 143	6	240°
16	240°	11, 35, 59, 83, 107, 131		
17	255°	22, 46, 70, 94, 118, 142		
18	270°	10, 34, 58, 82, 106, 130	7	285°
19	285°	21, 45, 69, 93, 117, 141		
20	300°	9, 33, 57, 81, 105, 129		
21	315°	1, 20, 44, 68, 92, 116, 140	8	330°
22	330°	8, 32, 56, 80, 104, 128		
23	345°	19, 43, 67, 91, 115, 139		

Table B.3: Angular pixel lists. To search for an angular pattern, e.g. in terms of m_ν^2, the FPD pixels can be grouped according to their azimuth angle in slices or pseudo-slices. Different levels of granularity are available in Samak. The pixel lists include all FPD pixels. Applied to a specific data set, the overlap of the respective golden pixel list has to be considered.

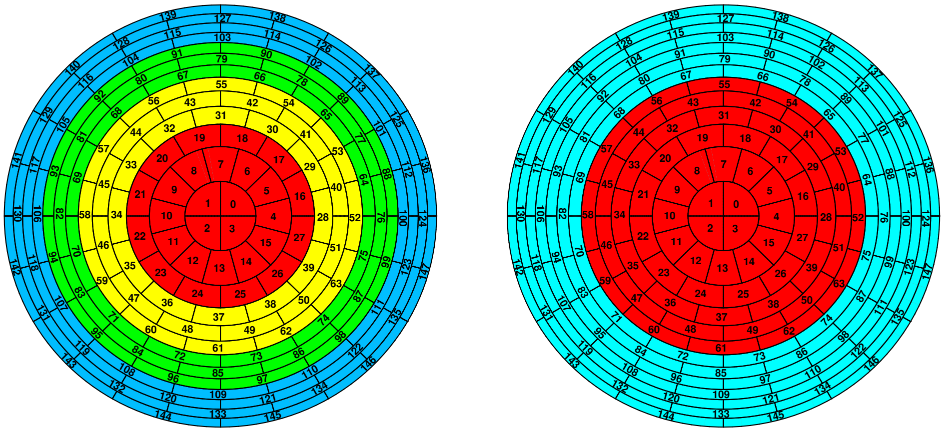

(a) Radial groups with four pseudo-rings

(b) Inner/outer halves

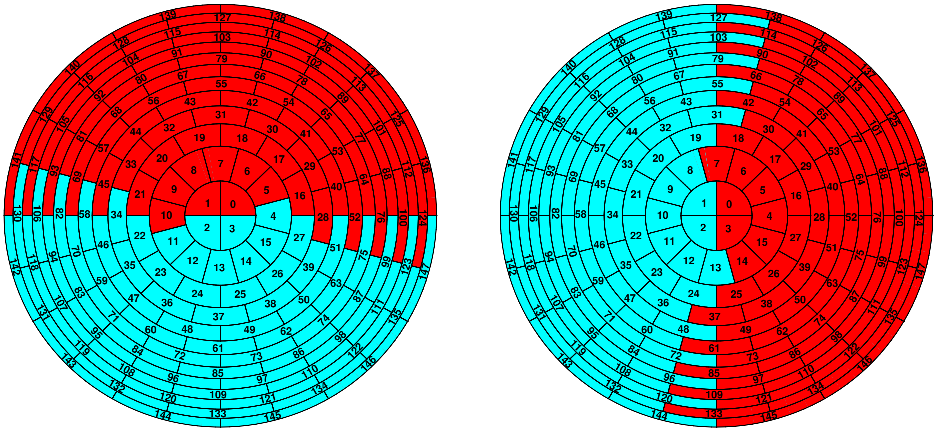

(c) Northern/southern halves

(d) Eastern/western halves

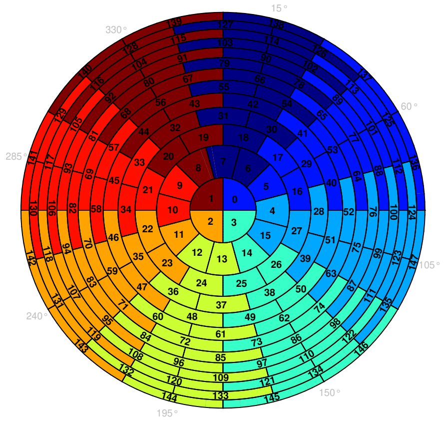

(e) Azimuthal groups with eight pseudo-slices

Figure B.1: Display of different FPD pixel combinations. To enhance the statistics, the pixel-wise tritium spectra can be combined into groups.

Appendix C

Overview Tables of KNM1 and KNM2 Campaigns

Parameter	**KNM1**	**KNM2**
Campaign period	2019, April - May	2019, September - November
Analysis interval[1]	$[E_0 - 39\,\text{eV}, E_0 + 47\,\text{eV}]$	$[E_0 - 40\,\text{eV}, E_0 + 135\,\text{eV}]$
Number of β-scans	274	361
Number of scan-steps per β-scan	27	28
Net measurement time (hours)	521.7	694.3
Number of counts	2.03×10^6	4.31×10^6
Signal	1.48×10^6	3.76×10^6
Background	0.55×10^6	0.55×10^6

Table C.1: Scan overview for KNM1 and KNM2. All values refer to the respective analysis interval and the golden data selection.

	KNM1 original [96]	KNM1 Re-analysis	KNM2
Theoretical corrections	Only radiative	Only radiative	Only radiative
Doppler Effect	included	included	included
Final-state distribution	KNM1 [65]	KNM2 [23]	KNM2 [23]
Elastic scattering	neglected	neglected	neglected
Inel. scattering cross section	energy-dependent	energy-dependent	energy-dependent
Max. order of scatterings	7	7	7
Energy-loss function (see appendix A.2)	[123]	[72]	[72]
Synchrotron radiation	included	included	included
Non-isotropic transmission	neglected	included	included
Scan-step-time background	neglected	$2.2\,\mu$cps/s	$3\,\mu$cps/s
Source potential broadening	not observed	not observed	$\sigma^2_{\text{plasma}} = 0.015\,\text{eV}^2$

Table C.2: Model configuration for KNM1 and KNM2. The original KNM1 configuration is the baseline KNM1 analysis presented in this work. A re-analysis was performed after the first publication in [96] with slightly updated settings, presented also in section 8.12.

---

[2] Only considered in the re-analysis

Parameter	KNM1		KNM2	
	Value	Uncertainty	Value	Uncertainty
Average source parameters				
Activity	2.46×10^{10} Bq	–	9.46×10^{10} Bq	–
Relative activity fluctuations within scan	0.006 % (error of the mean)		0.002 % (error of the mean)	
Column density ρd	$1.11 \times 10^{17}\,\mathrm{cm}^{-2}$	0.85 %	$4.23 \times 10^{17}\,\mathrm{cm}^{-2}$	0.25 %
Atomic tritium purity ε_T	97.56 %		98.63 %	
Molecular fraction c_{T_2}	95.26 %		97.34 %	
Molecular fraction c_HT	3.53 %		2.27 %	
Molecular fraction c_DT	1.08 %		0.31 %	
Temperature T_source	30.1 K		30.1 K	
Rear wall bias voltage U_rw	[−183, −149] mV		[−49.6, −7.7, 193] mV	
Effective source potential broadening σ^2_plasma	not considered		$0.015\,\mathrm{eV}^2$	$0.016\,\mathrm{eV}^2$
Energy-loss shift parameter Δ_{10}	not considered		0 meV	61 meV
Average retarding potentials				
Pre-spectrometer	−10 kV	–	−10 kV	–
Main-spectrometer	Scan-step dependent, see analysis interval in table C.1: $U \approx -18.6$ kV			
Inner electrode offset	−200 V	–	−200 V	–
Post-acceleration	10 kV	–	10 kV	–
Average magnetic fields				
B_source	2.52 T	2.5 %	2.52 T	1.7 %
B_ana	6.31×10^{-4} T	1.0 %	6.31×10^{-4} T	1.0 %
B_max	4.23 T	0.2 %	4.24 T	0.1 %
Focal plane detector				
Active pixel	117	–	117	–
Mean efficiency ϵ_FPD	> 95 %	0.1 %	> 95 %	0.1 %
ROI	[14-32] keV	–	[22-32] keV	–
Average backgrounds				
Steady-state background rate	292 mcps	0.7 mcps	220 mcps	0.5 mcps
Non-Poisson factor $f^2_\mathrm{Non-Poisson}$	6.4 %	–	11.2 %	–
Signal-to-background equilibrium	$qU - E_0 = -12$ eV	–	$qU - E_0 = -9$ eV	–
Retarding-potential dependence s_qU	0 mcps/keV	15 mcps/keV	0 mcps/keV	4.74 mcps/keV
Scan-step-time dependence s_time	$2.2\,\mu\mathrm{cps/s}^2$	$4.3\,\mu\mathrm{cps/s}^2$	$3.0\,\mu\mathrm{cps/s}$	$3.0\,\mu\mathrm{cps/s}$

Table C.3: Overview of the key experimental parameters in KNM1 and KNM2. The values are averaged over all golden scans and golden pixels of the respective measurement campaign.

Appendix D

First measurement campaign

D.1 Golden scan list

KNM1 included 274 scans in the final analysis. The first 19 scans (51410 - 51442) were recorded at $U_{\mathrm{rw}} = -183\,\mathrm{mV}$ whereas the rear wall bias voltage was set to $U_{\mathrm{rw}} = -149\,\mathrm{mV}$ for the remaining 255 scans. The full scan list is found below.

51410 51411 51412 51413 51414 51415 51416 51417 51418 51419 51420 51421 51422 51423 51424 51425 51426 51441 51442 51443 51444 51446 51447 51448 51449 51450 51451 51452 51453 51454 51455 51456 51457 51458 51459 51460 51461 51462 51463 51464 51465 51466 51467 51468 51469 51470 51472 51473 51474 51475 51476 51477 51478 51479 51480 51481 51486 51487 51488 51489 51490 51491 51492 51493 51494 51495 51496 51497 51498 51499 51500 51501 51502 51503 51516 51517 51521 51522 51523 51524 51525 51526 51527 51528 51529 51530 51531 51532 51533 51534 51535 51536 51537 51538 51539 51540 51541 51542 51543 51544 51545 51546 51547 51548 51549 51550 51551 51552 51553 51554 51555 51556 51557 51558 51559 51560 51561 51562 51563 51564 51565 51566 51579 51580 51581 51582 51583 51584 51585 51586 51639 51640 51641 51642 51643 51644 51645 51646 51647 51651 51652 51653 51654 51655 51656 51657 51658 51659 51660 51664 51665 51669 51670 51671 51672 51673 51674 51675 51676 51677 51678 51679 51680 51681 51682 51683 51684 51685 51686 51687 51688 51689 51690 51692 51693 51694 51695 51696 51701 51703 51704 51705 51706 51707 51708 51709 51822 51823 51824 51825 51826 51827 51828 51829 51830 51831 51832 51833 51834 51835 51836 51837 51838 51839 51840 51841 51842 51843 51844 51845 51846 51847 51848 51849 51850 51851 51852 51853 51854 51855 51856 51857 51858 51859 51860 51870 51871 51872 51873 51874 51875 51876 51879 51880 51881 51882 51883 51884 51885 51886 51887 51888 51889 51890 51891 51892 51893 51894 51895 51898 51908 51909 51910 51911 51912 51913 51919 51920 51921 51922 51923 51924 51925 51926 51927 51928 51929 51930 51931 51932 51933 51934 51935 51936

D.2 Alternative scan lists

As a sanity check, several alternative scan lists are investigated. These lists are subselections from the golden scan list.

Up scans

This alternative scan list contains all scans, whose scan-steps are recorded in upward direction. In this context, upward means from small to large (absolute) main-spectrometer voltages. The scan-step at $U = -18\,535\,\mathrm{V}$ was consequently measured *before* the scan-step at $U = -18\,621\,\mathrm{V}$. This scan list comprises the following 140 scans:

51410 51412 51414 51416 51418 51420 51422 51424 51426 51441 51443 51447 51449 51451 51453 51455 51457 51459 51461 51463 51465 51467 51469 51473 51475 51477 51479 51481 51486 51488 51490 51492

51494 51496 51498 51500 51502 51516 51517 51521 51523 51525 51527 51529 51531 51533 51535 51537 51539 51541 51543 51545 51547 51549 51551 51553 51555 51557 51559 51561 51563 51565 51580 51582 51584 51586 51639 51641 51643 51645 51647 51651 51653 51655 51657 51659 51664 51669 51671 51673 51675 51677 51679 51681 51683 51685 51687 51689 51693 51695 51701 51703 51705 51707 51709 51822 51824 51826 51828 51830 51832 51834 51836 51838 51840 51842 51844 51846 51848 51850 51852 51854 51856 51858 51860 51870 51872 51874 51876 51880 51882 51884 51886 51888 51890 51892 51894 51898 51908 51910 51912 51920 51922 51924 51926 51928 51930 51932 51934 51936

Down scans

This alternative scan list contains all scans, whose scan-steps are recorded in downward direction. In this context, downwards means from large to small (absolute) main-spectrometer voltages. The scan-step at $U = -18\,535\,\mathrm{V}$ was consequently measured *after* the scan-step at $U = -18\,621\,\mathrm{V}$. This scan list comprises the following 134 scans:

51411 51413 51415 51417 51419 51421 51423 51425 51442 51444 51446 51448 51450 51452 51454 51456 51458 51460 51462 51464 51466 51468 51470 51472 51474 51476 51478 51480 51487 51489 51491 51493 51495 51497 51499 51501 51503 51522 51524 51526 51528 51530 51532 51534 51536 51538 51540 51542 51544 51546 51548 51550 51552 51554 51556 51558 51560 51562 51564 51566 51579 51581 51583 51585 51640 51642 51644 51646 51652 51654 51656 51658 51660 51665 51670 51672 51674 51676 51678 51680 51682 51684 51686 51688 51690 51692 51694 51696 51704 51706 51708 51823 51825 51827 51829 51831 51833 51835 51837 51839 51841 51843 51845 51847 51849 51851 51853 51855 51857 51859 51871 51873 51875 51879 51881 51883 51885 51887 51889 51891 51893 51895 51909 51911 51913 51919 51921 51923 51925 51927 51929 51931 51933 51935

First third

This alternative scan list contains all scans within the first third all the golden scan list. The following 92 scans are included:

51410 51411 51412 51413 51414 51415 51416 51417 51418 51419 51420 51421 51422 51423 51424 51425 51426 51441 51442 51443 51444 51446 51447 51448 51449 51450 51451 51452 51453 51454 51455 51456 51457 51458 51459 51460 51461 51462 51463 51464 51465 51466 51467 51468 51469 51470 51472 51473 51474 51475 51476 51477 51478 51479 51480 51481 51486 51487 51488 51489 51490 51491 51492 51493 51494 51495 51496 51497 51498 51499 51500 51501 51502 51503 51516 51517 51521 51522 51523 51524 51525 51526 51527 51528 51529 51530 51531 51532 51533 51534 51535 51536

Middle third

This alternative scan list contains all scans within the middle third all the golden scan list. The following 91 scans are included:

51707 51708 51709 51822 51823 51824 51825 51826 51827 51828 51829 51830 51831 51832 51833 51834 51835 51836 51837 51838 51839 51840 51841 51842 51843 51844 51845 51846 51847 51848 51849 51850 51851 51852 51853 51854 51855 51856 51857 51858 51859 51860 51870 51871 51872 51873 51874 51875 51876 51879 51880 51881 51882 51883 51884 51885 51886 51887 51888 51889 51890 51891 51892 51893 51894 51895 51898 51908 51909 51910 51911 51912 51913 51919 51920 51921 51922 51923 51924 51925 51926 51927 51928 51929 51930 51931 51932 51933 51934 51935 51936

Last third

This alternative scan list contains all scans within the last third all the golden scan list. The following 91 scans are included:

51537 51538 51539 51540 51541 51542 51543 51544 51545 51546 51547 51548 51549 51550 51551 51552 51553 51554 51555 51556 51557 51558 51559 51560 51561 51562 51563 51564 51565 51566 51579 51580

51581 51582 51583 51584 51585 51586 51639 51640 51641 51642 51643 51644 51645 51646 51647 51651
51652 51653 51654 51655 51656 51657 51658 51659 51660 51664 51665 51669 51670 51671 51672 51673
51674 51675 51676 51677 51678 51679 51680 51681 51682 51683 51684 51685 51686 51687 51688 51689
51690 51692 51693 51694 51695 51696 51701 51703 51704 51705 51706

$\sigma(\rho d) < 1$

This alternative scan list contains all scans whose column density (ρd) lies within 1σ around the mean value. The following 214 scans are included:

51410 51411 51412 51413 51414 51415 51416 51417 51418 51419 51420 51421 51422 51423 51424 51425
51426 51441 51442 51443 51444 51446 51447 51448 51449 51450 51451 51452 51453 51454 51455 51456
51457 51458 51459 51460 51461 51462 51463 51464 51465 51466 51467 51468 51469 51470 51472 51473
51474 51475 51476 51477 51478 51479 51480 51481 51486 51487 51488 51489 51490 51491 51492 51493
51494 51495 51496 51497 51498 51523 51524 51525 51526 51527 51528 51529 51530 51531 51532 51533
51534 51535 51536 51537 51538 51539 51540 51541 51542 51543 51544 51545 51546 51580 51581 51582
51583 51584 51585 51586 51639 51655 51656 51657 51658 51659 51660 51664 51665 51677 51678 51679
51680 51681 51682 51683 51684 51685 51686 51703 51704 51705 51706 51707 51708 51709 51822 51823
51824 51825 51826 51827 51828 51829 51830 51831 51832 51833 51834 51835 51836 51837 51838 51839
51840 51841 51842 51843 51844 51845 51846 51847 51848 51849 51850 51851 51852 51853 51854 51855
51856 51857 51858 51859 51860 51870 51871 51872 51873 51874 51875 51876 51879 51880 51881 51882
51883 51884 51885 51886 51887 51888 51889 51890 51891 51892 51893 51894 51895 51898 51908 51909
51910 51911 51912 51913 51919 51920 51921 51922 51923 51924 51925 51926 51927 51928 51929 51930
51931 51932 51933 51934 51935 51936

$\sigma(\rho d) > 1$

This alternative scan list contains all scans whose column density (ρd) is more than 1σ away from the mean value. The following 60 scans are included:

51499 51500 51501 51502 51503 51516 51517 51521 51522 51547 51548 51549 51550 51551 51552 51553
51554 51555 51556 51557 51558 51559 51560 51561 51562 51563 51564 51565 51566 51579 51640 51641
51642 51643 51644 51645 51646 51647 51651 51652 51653 51654 51669 51670 51671 51672 51673 51674
51675 51676 51687 51688 51689 51690 51692 51693 51694 51695 51696 51701

High ϵ_T

This alternative scan list contains all scans whose tritium purity (ϵ_T) is smaller than the median ϵ_T. The following 137 scans are included:

51410 51411 51412 51413 51414 51415 51416 51417 51418 51419 51420 51421 51422 51423 51424 51425
51426 51441 51442 51443 51444 51446 51447 51448 51449 51450 51451 51452 51453 51454 51455 51456
51457 51458 51459 51460 51461 51462 51463 51464 51465 51466 51467 51468 51469 51470 51472 51473
51474 51475 51476 51477 51478 51479 51480 51481 51486 51487 51488 51489 51490 51491 51492 51493
51494 51495 51496 51497 51498 51499 51500 51501 51502 51503 51516 51517 51521 51522 51523 51524
51525 51526 51527 51528 51529 51530 51531 51532 51533 51534 51535 51536 51537 51538 51539 51540
51541 51542 51543 51544 51545 51546 51547 51548 51549 51550 51551 51552 51553 51554 51555 51557
51558 51559 51560 51647 51651 51652 51653 51654 51664 51665 51669 51670 51671 51672 51675 51676
51678 51682 51683 51688 51695 51701 51703 51704 51705

Low ϵ_T

This alternative scan list contains all scans whose tritium purity (ϵ_T) is larger than the median ϵ_T. The following 137 scans are included:

51556 51561 51562 51563 51564 51565 51566 51579 51580 51581 51582 51583 51584 51585 51586 51639 51640 51641 51642 51643 51644 51645 51646 51655 51656 51657 51658 51659 51660 51673 51674 51677 51679 51680 51681 51684 51685 51686 51687 51689 51690 51692 51693 51694 51696 51706 51707 51708 51709 51822 51823 51824 51825 51826 51827 51828 51829 51830 51831 51832 51833 51834 51835 51836 51837 51838 51839 51840 51841 51842 51843 51844 51845 51846 51847 51848 51849 51850 51851 51852 51853 51854 51855 51856 51857 51858 51859 51860 51870 51871 51872 51873 51874 51875 51876 51879 51880 51881 51882 51883 51884 51885 51886 51887 51888 51889 51890 51891 51892 51893 51894 51895 51898 51908 51909 51910 51911 51912 51913 51919 51920 51921 51922 51923 51924 51925 51926 51927 51928 51929 51930 51931 51932 51933 51934 51935 51936

$U_{\mathrm{RW}} = -183\,\mathrm{meV}$

This alternative scan list contains all scans with rear wall bias voltage $U_{\mathrm{RW}} = -183\,\mathrm{meV}$. The following 19 scans are included:

51410 51411 51412 51413 51414 51415 51416 51417 51418 51419 51420 51421 51422 51423 51424 51425 51426 51441 51442

$U_{\mathrm{RW}} = -149\,\mathrm{meV}$

This alternative scan list contains all scans with rear wall bias voltage $U_{\mathrm{RW}} = -149\,\mathrm{meV}$. The following 255 scans are included:

51443 51444 51446 51447 51448 51449 51450 51451 51452 51453 51454 51455 51456 51457 51458 51459 51460 51461 51462 51463 51464 51465 51466 51467 51468 51469 51470 51472 51473 51474 51475 51476 51477 51478 51479 51480 51481 51486 51487 51488 51489 51490 51491 51492 51493 51494 51495 51496 51497 51498 51499 51500 51501 51502 51503 51516 51517 51521 51522 51523 51524 51525 51526 51527 51528 51529 51530 51531 51532 51533 51534 51535 51536 51537 51538 51539 51540 51541 51542 51543 51544 51545 51546 51547 51548 51549 51550 51551 51552 51553 51554 51555 51556 51557 51558 51559 51560 51561 51562 51563 51564 51565 51566 51579 51580 51581 51582 51583 51584 51585 51586 51639 51640 51641 51642 51643 51644 51645 51646 51647 51651 51652 51653 51654 51655 51656 51657 51658 51659 51660 51664 51665 51669 51670 51671 51672 51673 51674 51675 51676 51677 51678 51679 51680 51681 51682 51683 51684 51685 51686 51687 51688 51689 51690 51692 51693 51694 51695 51696 51701 51703 51704 51705 51706 51707 51708 51709 51822 51823 51824 51825 51826 51827 51828 51829 51830 51831 51832 51833 51834 51835 51836 51837 51838 51839 51840 51841 51842 51843 51844 51845 51846 51847 51848 51849 51850 51851 51852 51853 51854 51855 51856 51857 51858 51859 51860 51870 51871 51872 51873 51874 51875 51876 51879 51880 51881 51882 51883 51884 51885 51886 51887 51888 51889 51890 51891 51892 51893 51894 51895 51898 51908 51909 51910 51911 51912 51913 51919 51920 51921 51922 51923 51924 51925 51926 51927 51928 51929 51930 51931 51932 51933 51934 51935 51936

D.3 Golden pixel list

KNM1 included 117 out of 148 FPD pixels in the final analysis. The associated pixel numbers are:

0 1 2 3 4 5 6 7 8 9 10 11 12 13 14 15 16 17 18 19 20 21 22 23 24 25 26 27 28 29 30 31 32 33 34 35 36 37 38 39 40 41 42 43 44 45 46 47 48 49 50 51 52 53 54 55 56 57 58 59 60 61 62 63 64 65 66 67 68 69 70 71 72 73 74 75 76 77 78 79 80 81 82 83 84 85 86 87 88 89 90 91 92 93 94 95 96 101 102 103 104 105 106 107 108 109 113 114 115 116 117 118 119 120 131 132 133

D.4 Pseudo-ring statistics

To search for radial dependence in terms of m_ν^2, the FPD pixels are grouped into four pseudo-rings.

Pseudo-ring	FPD rings	Number of active pixels	Number of signal electrons
1	Bullseye & 1 − 2	28	3.58×10^5
2	3 − 5	36	4.50×10^5
3	6 − 8	33	4.28×10^5
4	9 − 11	20	2.54×10^5

Table D.1: KNM1 Pseudo-ring-wise statistics. To investigate a possible radial dependence of the fit parameter, the bullseye and the 11 active FPD rings are grouped according to appendix B into 4 pseudo-rings with approximately the same statistics.

D.5 Covariance matrices

The covariance matrices used in the spectral analyses of the KNM1 data set are shown in figures D.1 to D.10 using the systematic uncertainties in table C.3 as input. The left panels visualize the respective fractional covariance matrix, calculated according to equation (3.19). The right panels state the correlation coefficients, that described the correlation between scan steps.

Most systematic effects, such as the final-state distribution, influence only the signal electrons. The respective (fractional) covariance matrices are therefore zero for bins above the tritium endpoint. In these cases, the correlation coefficient cannot be calculated and the associated bins are colored in grey in the correlation matrix. Moreover, in some case the fractional covariance matrix contains relatively large entries for bins just below the endpoint, because the expected number of counts is small compared to the systematic uncertainty. To improve the visibility, the respective bins are colored in grey.

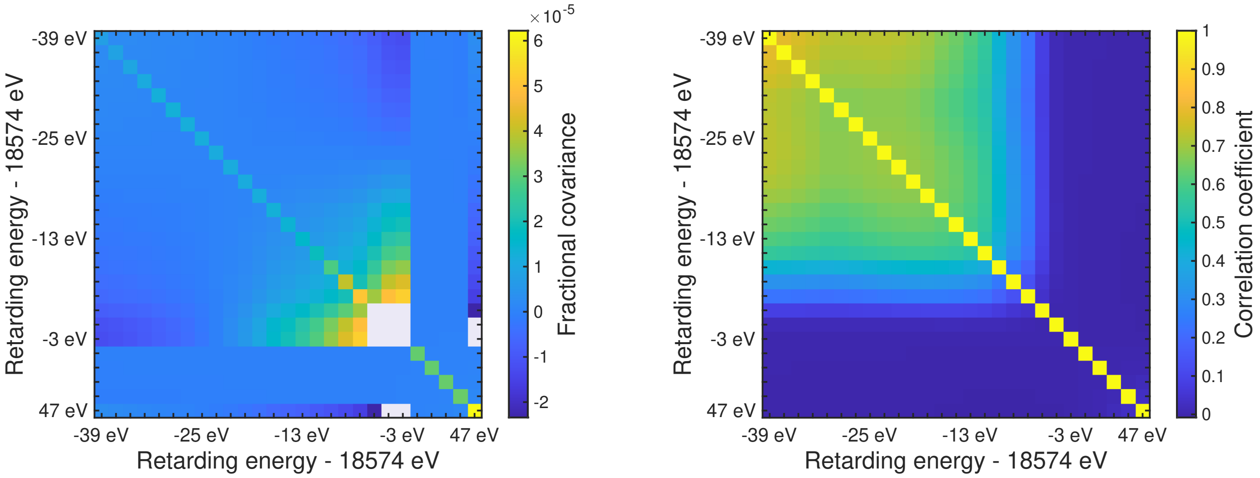

Figure D.1: KNM1 total covariance matrix inclduing statistical and all systematic uncertainties (left) and correlation matrix (right).

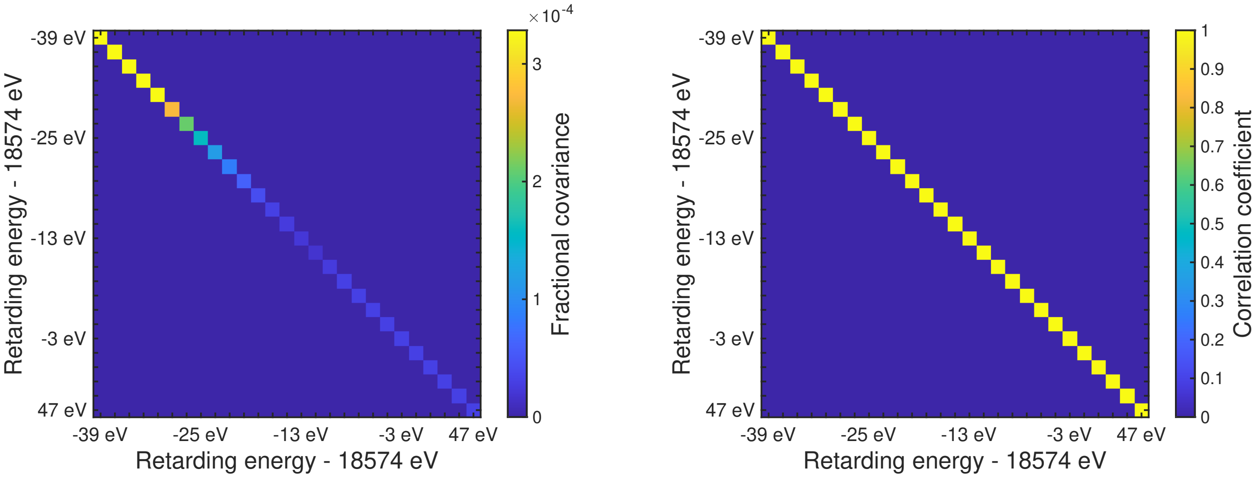

Figure D.2: KNM1 background rate (Non-Poisson) covariance matrix (left) and correlation matrix (right).

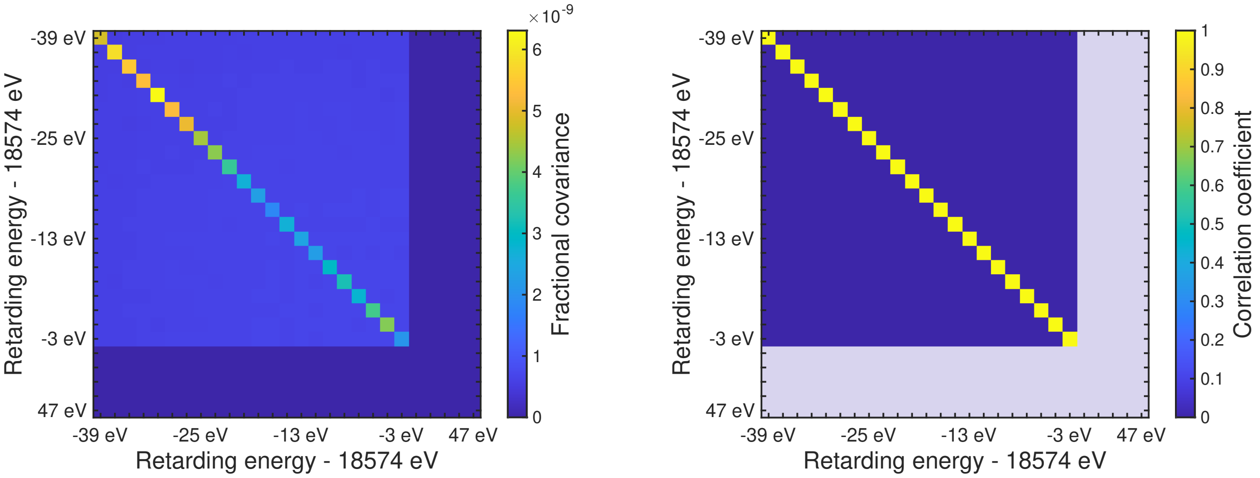

Figure D.3: KNM1 scan fluctuations covariance matrix (left) and correlation matrix (right).

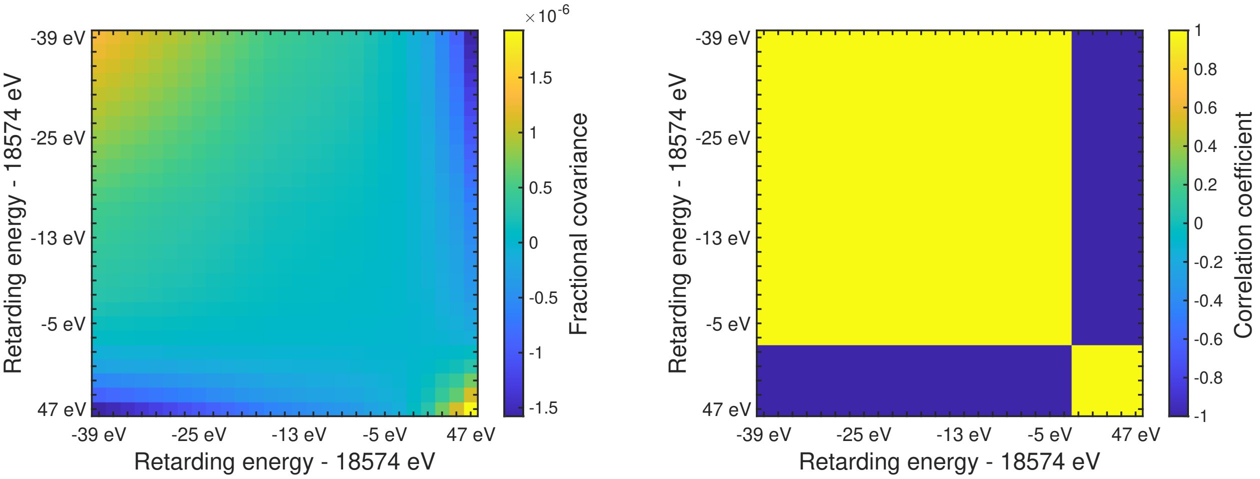

Figure D.4: KNM1 retarding-potential-dependent background covariance matrix (left) and correlation matrix (right).

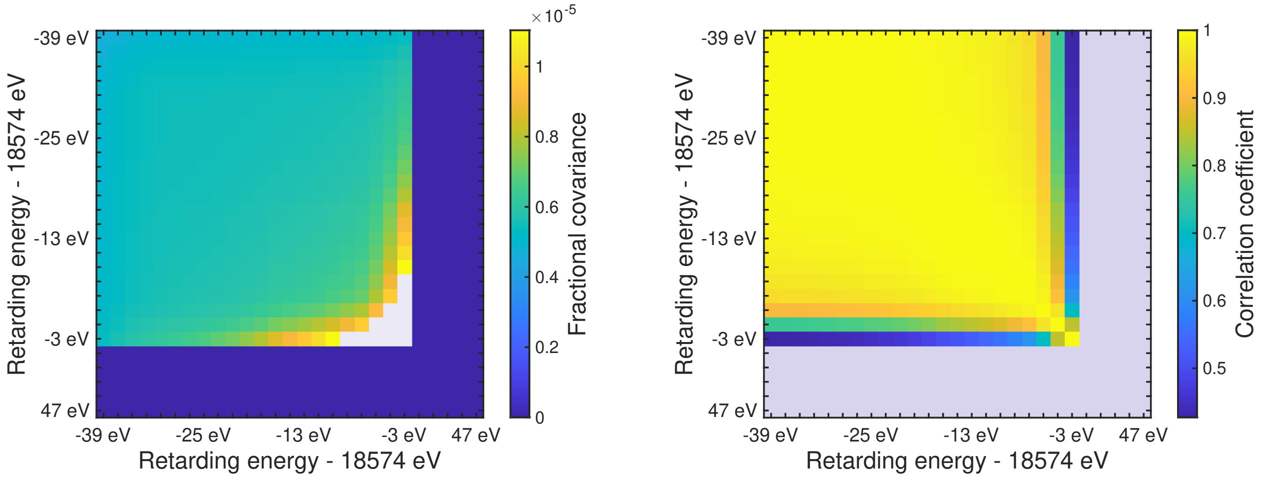

Figure D.5: KNM1 final-state distribution covariance matrix (left) and correlation matrix (right).

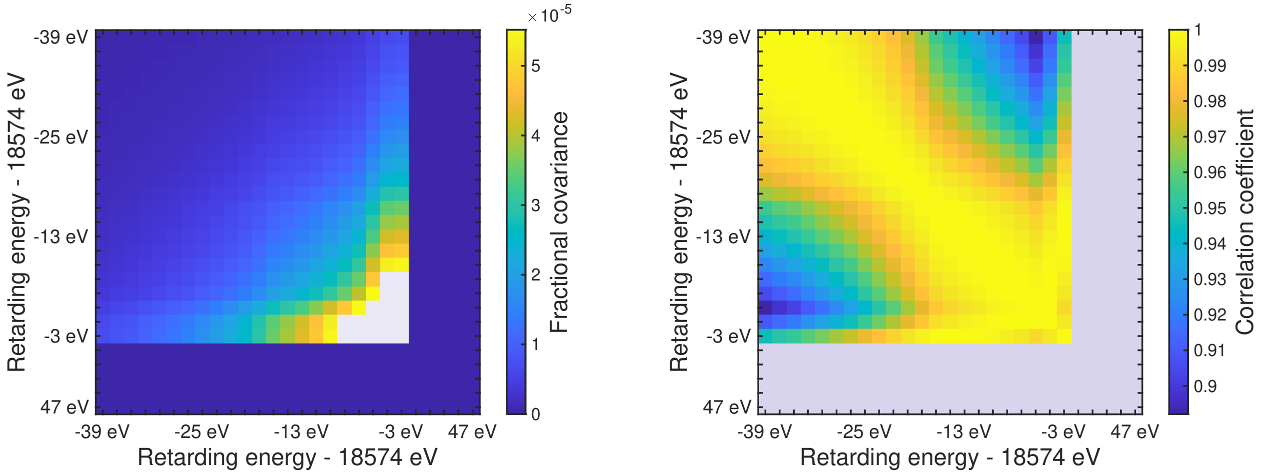

Figure D.6: KNM1 magnetic fields covariance matrix (left) and correlation matrix (right).

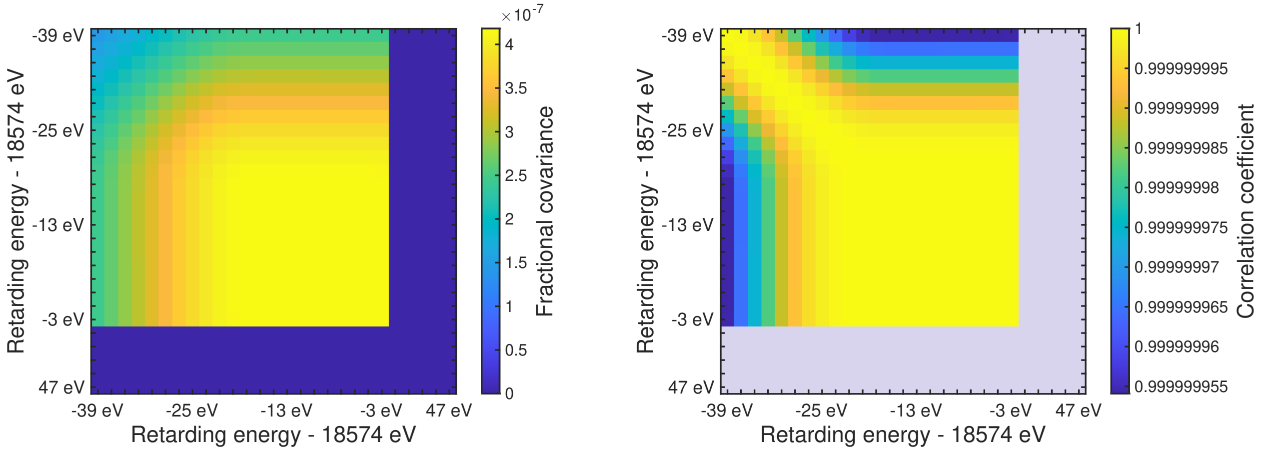

Figure D.7: KNM1 number of scatterings covariance matrix (left) and correlation matrix (right).

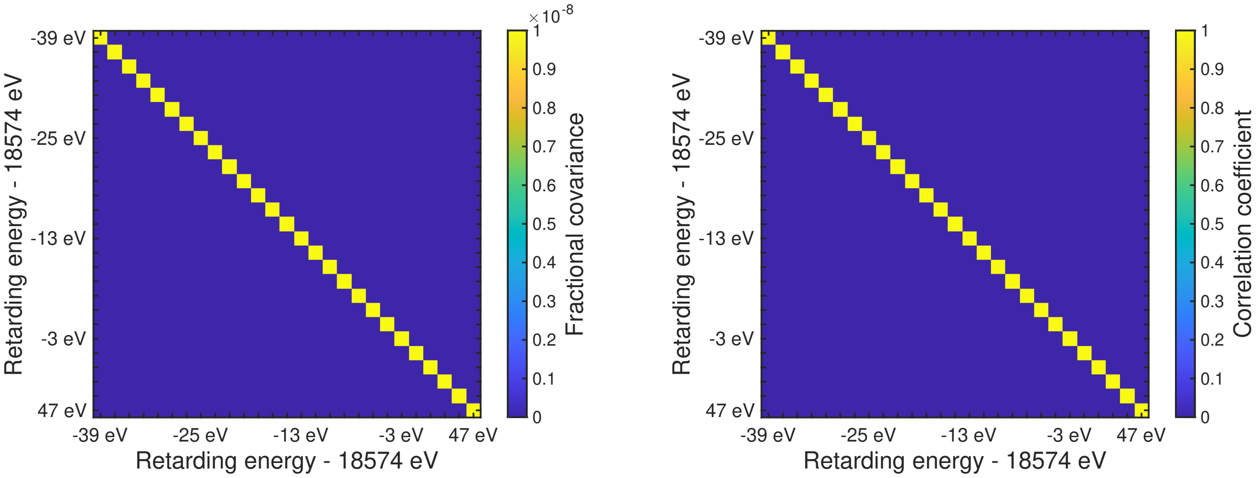

Figure D.8: KNM1 focal plane detector efficiency covariance matrix (left) and correlation matrix (right).

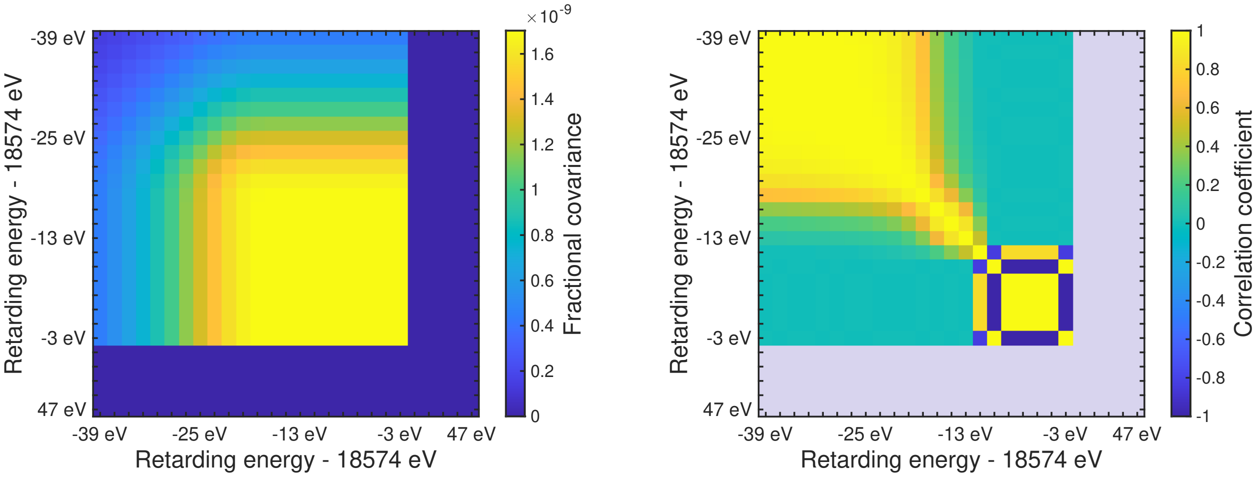

Figure D.9: KNM1 energy-loss function covariance matrix (left) and correlation matrix (right).

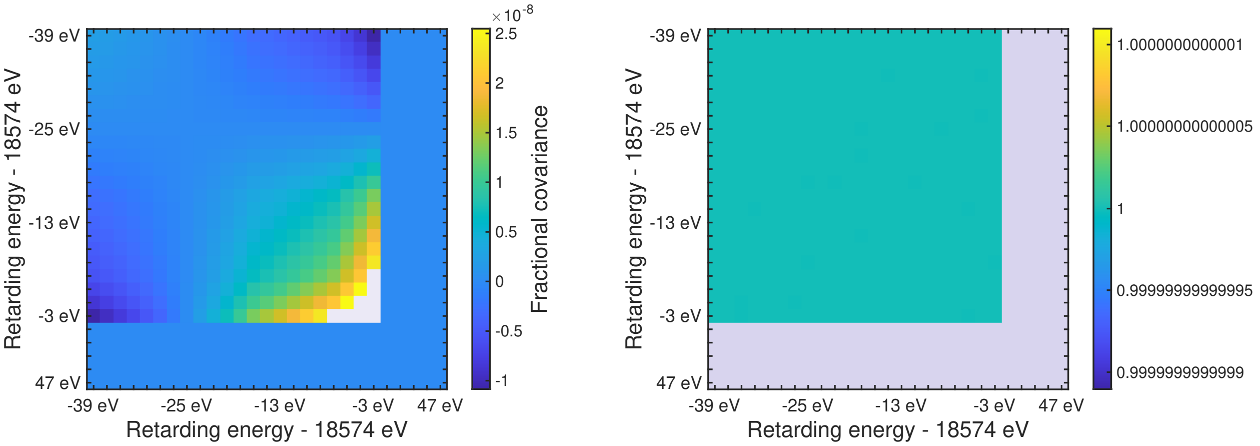

Figure D.10: KNM1 theoretical corrections covariance matrix (left) and correlation matrix (right).

Appendix E

Second measurement campaign

E.1 Golden scan list

The golden scan list comprises 361 tritium scans with stable run conditions. The KATRIN internal scan numbers are:

56160 56161 56162 56163 56164 56165 56166 56167 56168 56169 56170 56171 56172 56173 56174 56176 56177 56178 56179 56180 56181 56182 56183 56184 56186 56187 56188 56189 56190 56191 56192 56193 56194 56195 56196 56268 56269 56270 56271 56272 56273 56274 56275 56276 56277 56278 56279 56280 56281 56282 56284 56285 56286 56287 56288 56289 56290 56291 56292 56293 56294 56301 56302 56303 56304 56305 56306 56307 56308 56309 56310 56311 56312 56313 56314 56315 56316 56317 56319 56320 56321 56322 56323 56324 56325 56326 56327 56328 56329 56330 56333 56334 56335 56336 56337 56338 56341 56342 56343 56344 56345 56346 56347 56348 56349 56350 56351 56352 56353 56354 56355 56356 56357 56358 56359 56360 56361 56362 56363 56364 56365 56366 56367 56368 56369 56370 56379 56380 56381 56382 56383 56384 56385 56386 56387 56388 56389 56390 56391 56392 56393 56394 56395 56396 56397 56398 56399 56400 56401 56402 56403 56404 56405 56406 56407 56409 56412 56413 56414 56415 56416 56417 56418 56472 56473 56474 56475 56476 56477 56478 56479 56560 56561 56562 56563 56564 56565 56566 56575 56576 56577 56578 56579 56580 56581 56582 56583 56584 56585 56586 56587 56588 56589 56590 56591 56592 56593 56594 56595 56598 56599 56600 56601 56602 56603 56604 56605 56606 56607 56608 56609 56610 56611 56612 56613 56621 56622 56623 56624 56625 56626 56627 56628 56629 56636 56639 56640 56641 56642 56643 56644 56645 56646 56647 56648 56654 56655 56656 56657 56658 56659 56660 56661 56662 56663 56664 56669 56670 56671 56672 56673 56674 56684 56685 56688 56689 56690 56691 56692 56693 56706 56707 56708 56709 56710 56711 56712 56713 57015 57016 57017 57018 57019 57020 57022 57023 57024 57025 57026 57035 57036 57038 57039 57040 57041 57042 57043 57044 57045 57046 57047 57048 57049 57050 57051 57052 57053 57054 57055 57056 57057 57058 57059 57060 57061 57062 57068 57069 57070 57071 57072 57073 57074 57075 57076 57077 57078 57079 57080 57081 57082 57083 57084 57085 57086 57087 57088 57089 57090 57091 57092 57093 57094 57095 57096 57103 57104 57105 57106 57107 57108 57109 57110 57111 57120 57121 57122 57123 57124 57125 57126 57127 57128 57129 57130 57131 57132 57133 57134 57135 57136

E.2 Alternative scan lists

As a sanity check several alternative scan lists are analyzed separately.

Up scans

This alternative scan list contains all scans, whose scan-steps are recorded in upward direction. In this context, upward means from small to large (absolute) main-spectrometer voltages. The scan-step at $U = -18\,534\,\mathrm{V}$ was consequently measured *before* the scan-step at $U = -18\,709\,\mathrm{V}$. This scan list comprises the following 187 scans:

56160 56162 56164 56166 56168 56170 56172 56174 56177 56178 56180 56182 56184 56187 56188 56190 56192 56194 56196 56269 56271 56273 56275 56277 56279 56281 56284 56286 56288 56290 56292 56294 56302 56304 56306 56308 56310 56312 56314 56316 56319 56322 56324 56326 56329 56333 56335 56336 56338 56342 56344 56346 56348 56350 56353 56354 56356 56358 56360 56362 56364 56366 56368 56370 56380 56382 56384 56386 56388 56390 56392 56394 56396 56398 56400 56402 56404 56406 56407 56412 56414 56416 56418 56473 56475 56477 56479 56561 56563 56565 56575 56577 56579 56580 56582 56584 56586 56588 56590 56592 56594 56595 56599 56601 56603 56604 56605 56607 56609 56611 56613 56622 56624 56626 56628 56636 56640 56642 56644 56646 56648 56655 56657 56659 56661 56663 56669 56671 56673 56684 56688 56690 56692 56706 56708 56710 56712 57015 57017 57019 57022 57024 57026 57036 57039 57040 57042 57044 57046 57048 57050 57052 57054 57056 57057 57059 57061 57068 57070 57072 57073 57075 57077 57079 57081 57083 57085 57087 57088 57090 57092 57094 57096 57104 57105 57107 57109 57111 57121 57122 57124 57126 57128 57130 57132 57134 57136

Down scans

This alternative scan list contains all scans, whose scan-steps are recorded in downward direction. In this context, downwards means from large to small (absolute) main-spectrometer voltages. The scan-step at $U = -18\,534\,\mathrm{V}$ was consequently measured *after* the scan-step at $U = -18\,709\,\mathrm{V}$. This scan list comprises the following 174 scans:

56161 56163 56165 56167 56169 56171 56173 56176 56179 56181 56183 56186 56189 56191 56193 56195 56268 56270 56272 56274 56276 56278 56280 56282 56285 56287 56289 56291 56293 56301 56303 56305 56307 56309 56311 56313 56315 56317 56320 56321 56323 56325 56327 56328 56330 56334 56337 56341 56343 56345 56347 56349 56351 56352 56355 56357 56359 56361 56363 56365 56367 56369 56379 56381 56383 56385 56387 56389 56391 56393 56395 56397 56399 56401 56403 56405 56409 56413 56415 56417 56472 56474 56476 56478 56560 56562 56564 56566 56576 56578 56581 56583 56585 56587 56589 56591 56593 56598 56600 56602 56606 56608 56610 56612 56621 56623 56625 56627 56629 56639 56641 56643 56645 56647 56654 56656 56658 56660 56662 56664 56670 56672 56674 56685 56689 56691 56693 56707 56709 56711 56713 57016 57018 57020 57023 57025 57035 57038 57041 57043 57045 57047 57049 57051 57053 57055 57058 57060 57062 57069 57071 57074 57076 57078 57080 57082 57084 57086 57089 57091 57093 57095 57103 57106 57108 57110 57120 57123 57125 57127 57129 57131 57133 57135

Rear-wall period 1: $U_{\mathrm{RW}} = -49.6\,\mathrm{meV}$

This alternative scan list contains all scans with rear wall bias voltage $U_{\mathrm{RW}} = -49.6\,\mathrm{meV}$. The following 171 scans are included:

56160 56161 56162 56163 56164 56165 56166 56167 56168 56169 56170 56171 56172 56173 56174 56176 56177 56178 56179 56180 56181 56182 56183 56184 56186 56187 56188 56189 56190 56191 56192 56193 56194 56195 56196 56268 56269 56270 56271 56272 56273 56274 56275 56276 56277 56278 56279 56280 56281 56282 56284 56285 56286 56287 56288 56289 56290 56291 56292 56293 56294 56301 56302 56303 56304 56305 56306 56307 56308 56309 56310 56311 56312 56313 56314 56315 56316 56317 56319 56320 56321 56322 56323 56324 56325 56326 56327 56328 56329 56330 56333 56334 56335 56336 56337 56338 56341 56342 56343 56344 56345 56346 56347 56348 56349 56350 56351 56352 56353 56354 56355 56356 56357 56358 56359 56360 56361 56362 56363 56364 56365 56366 56367 56368 56369 56370 56379 56380 56381 56382 56383 56384 56385 56386 56387 56388 56389 56390 56391 56392 56393 56394 56395 56396 56397 56398 56399 56400 56401 56402 56403 56404 56405 56406 56407 56409 56412 56413 56414 56415 56416 56417 56418 56472 56473 56474 56475 56476 56477 56478 56479

Rear-wall period 2: $U_{\mathrm{RW}} = -7.7\,\mathrm{meV}$

This alternative scan list contains all scans with rear wall bias voltage $U_{\mathrm{RW}} = -7.7\,\mathrm{meV}$. The following 97 scans are included:

56560 56561 56562 56563 56564 56565 56566 56575 56576 56577 56578 56579 56580 56581 56582 56583 56584 56585 56586 56587 56588 56589 56590 56591 56592 56593 56594 56595 56598 56599 56600 56601

56602 56603 56604 56605 56606 56607 56608 56609 56610 56611 56612 56613 56621 56622 56623 56624 56625 56626 56627 56628 56629 56636 56639 56640 56641 56642 56643 56644 56645 56646 56647 56648 56654 56655 56656 56657 56658 56659 56660 56661 56662 56663 56664 56669 56670 56671 56672 56673 56674 56684 56685 56688 56689 56690 56691 56692 56693 56706 56707 56708 56709 56710 56711 56712 56713

Rear-wall period 3: $U_{\mathrm{RW}} = 193.0\,\mathrm{meV}$

This alternative scan list contains all scans with rear wall bias voltage $U_{\mathrm{RW}} = 193.0\,\mathrm{meV}$. The following 93 scans are included:

57015 57016 57017 57018 57019 57020 57022 57023 57024 57025 57026 57035 57036 57038 57039 57040 57041 57042 57043 57044 57045 57046 57047 57048 57049 57050 57051 57052 57053 57054 57055 57056 57057 57058 57059 57060 57061 57062 57068 57069 57070 57071 57072 57073 57074 57075 57076 57077 57078 57079 57080 57081 57082 57083 57084 57085 57086 57087 57088 57089 57090 57091 57092 57093 57094 57095 57096 57103 57104 57105 57106 57107 57108 57109 57110 57111 57120 57121 57122 57123 57124 57125 57126 57127 57128 57129 57130 57131 57132 57133 57134 57135 57136

E.3 Golden pixel list

The golden pixel list contains 117 out of 148 pixels. The pixel numbers are stated below and visualized in figure 6.2.
0 1 2 3 4 5 6 7 8 9 10 11 12 13 14 15 16 17 18 19 20 21 22 23 24 25 26 27 28 29 30 31 32 33 34 35 36 37 38 39 40 41 42 43 44 45 46 47 48 49 50 51 52 53 54 55 56 57 58 59 60 61 62 63 64 65 66 67 68 69 70 71 72 73 74 75 76 77 78 79 80 81 82 83 84 85 86 87 88 89 90 91 92 93 94 95 96 99 101 102 103 104 105 106 107 108 109 114 115 116 117 118 119 120 131 132 133

E.4 Rate monitor analysis

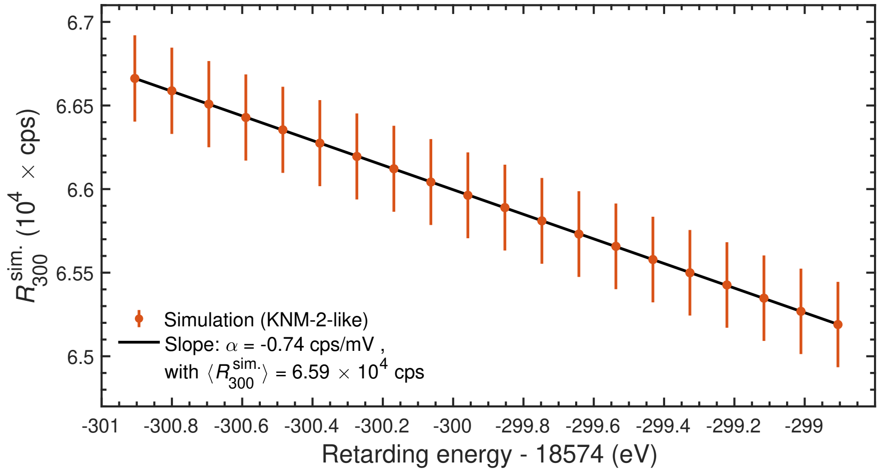

Figure E.1: Simulation of rate monitor point R_{300} at $qU - E_0 = -300\,\mathrm{eV}$ with KNM2-like settings. The rate-to-potential relation is approximated by a linear model in the vicinity of ±1 eV. A fit finds a slope of $\alpha = -0.74\,\mathrm{cps/mV}$ at an average rate $\langle R_{300} \rangle = 6.59 \times 10^4\,\mathrm{cps}$. This relation is used in section 6.6.2 to translate shifts and drifts in terms of rate into an meV-equivalent.

E.5 Retarding potential

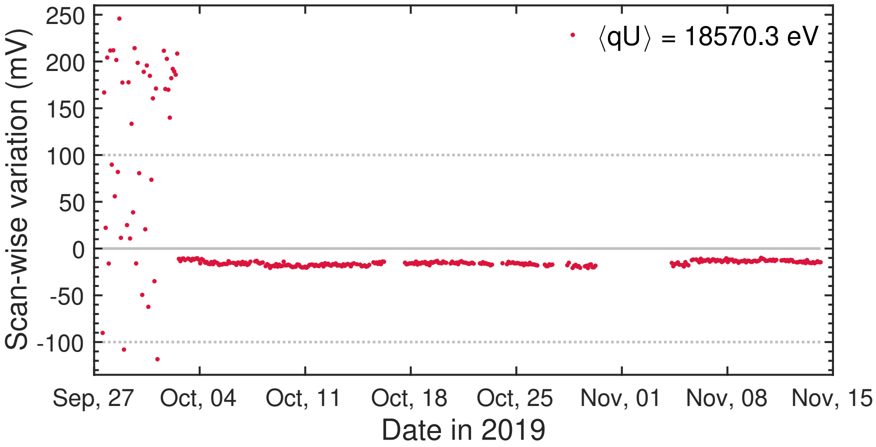

Figure E.2: Retarding potential as a function of time for the high-voltage set point $\langle qU \rangle = 18\,570\,\mathrm{V}$ in KNM2. Its reproducibility ($\sigma(qU) = 55\,\mathrm{mV}$) was significantly worse than for all other set points ($\langle \sigma(qU) \rangle = 10\,\mathrm{mV}$). The problem was addressed during data taking and eliminated on October 2. Considering all scans after scan number 56 277, the retarding potential at $\langle qU \rangle = 18\,570\,\mathrm{V}$ varied as little as $\sigma(qU) = 2\,\mathrm{mV}$.

E.6 Background

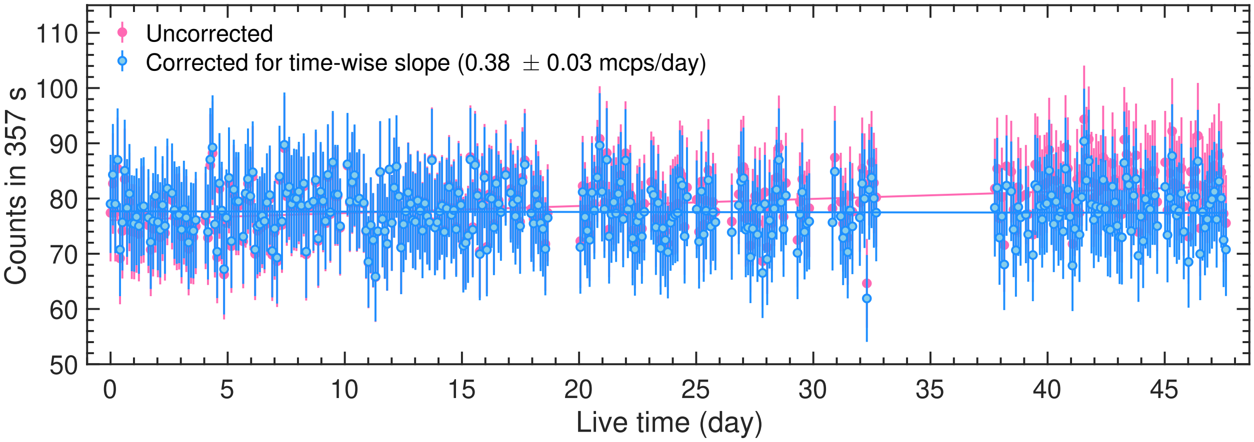

Figure E.3: Correction of the time-wise background slope in KNM2.

E.7 Covariance matrices

The multiring covariance matrices used in the spectral analyses of the KNM2 data set are shown in figures E.4 to E.15 using the systematic uncertainties in table C.3 as input. Four pseudo-rings are considered. The left panels visualize the respective fractional covariance matrix, calculated according to equation (3.19). The right panels state the correlation coefficients, that described the correlation between scan steps. Some bins are colored in grey for better visibility, as described in appendix D.5.

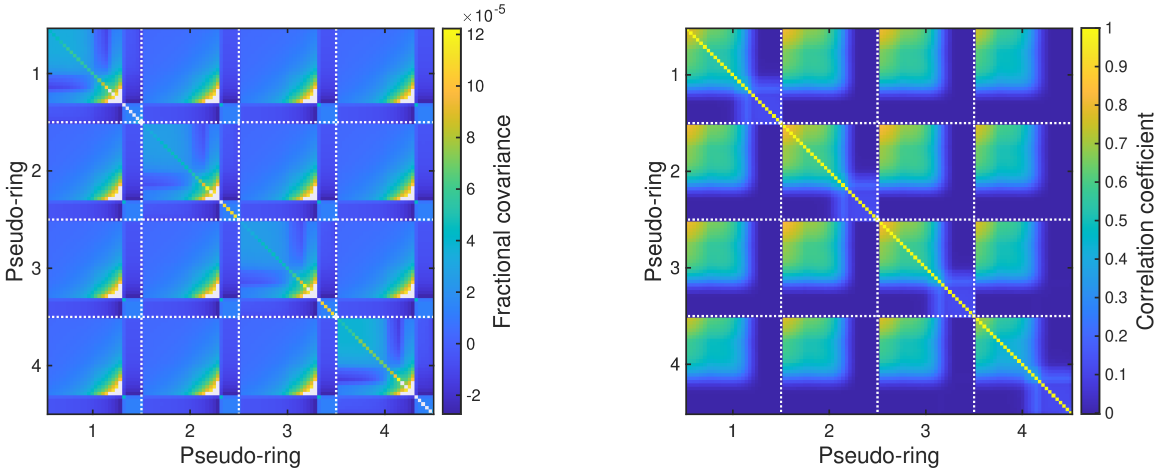

Figure E.4: KNM2 total covariance matrix inclduing statistical and all systematic uncertainties (left) and correlation matrix (right).

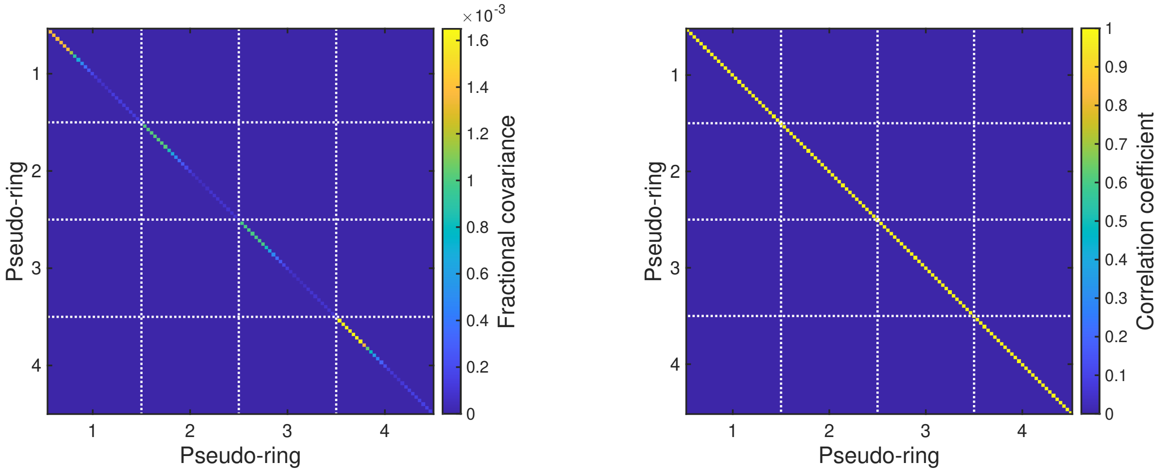

Figure E.5: KNM2 background rate (Non-Poisson) covariance matrix (left) and correlation matrix (right).

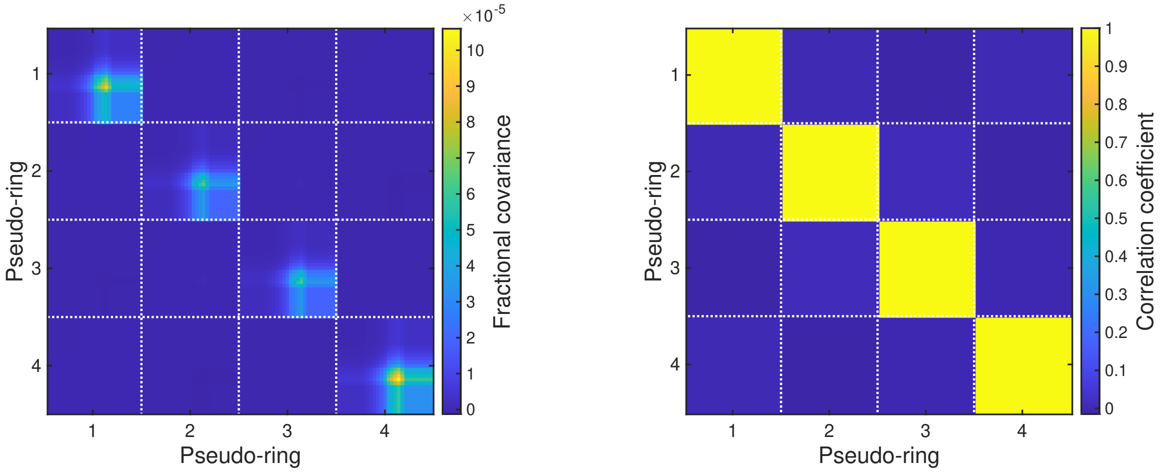

Figure E.6: KNM2 scan-step-time-dependent background covariance matrix (left) and correlation matrix (right).

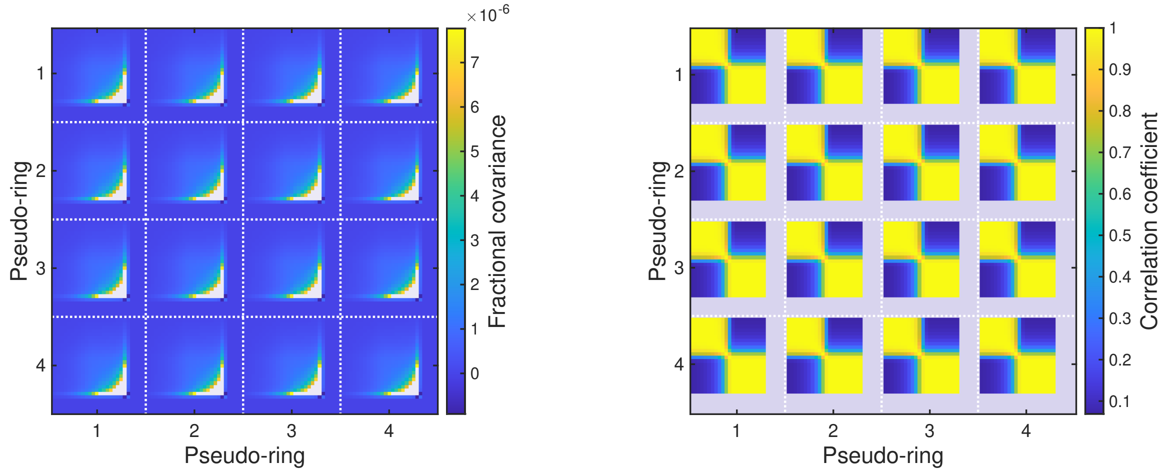

Figure E.7: KNM2 source potential covariance matrix (left) and correlation matrix (right).

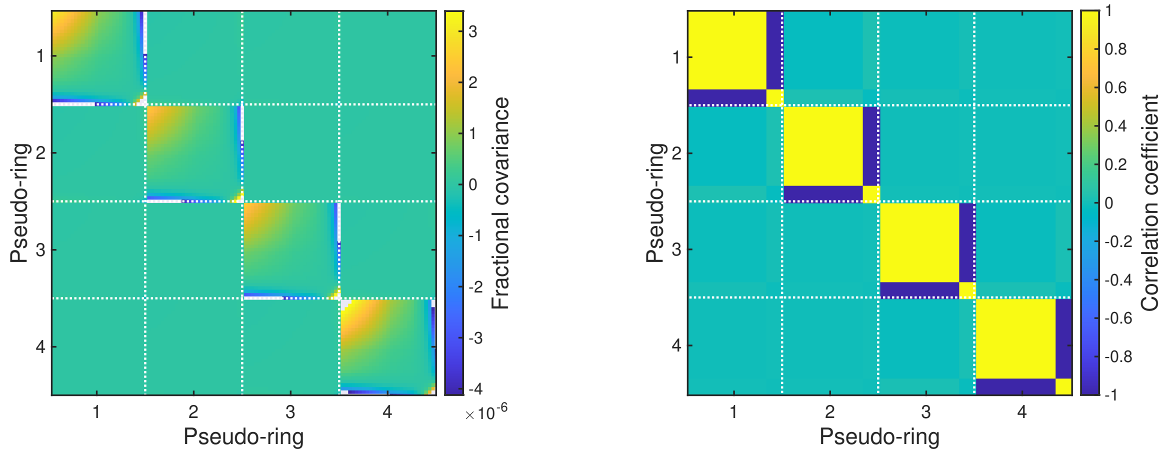

Figure E.8: KNM2 retarding-potential-dependent background covariance matrix (left) and correlation matrix (right).

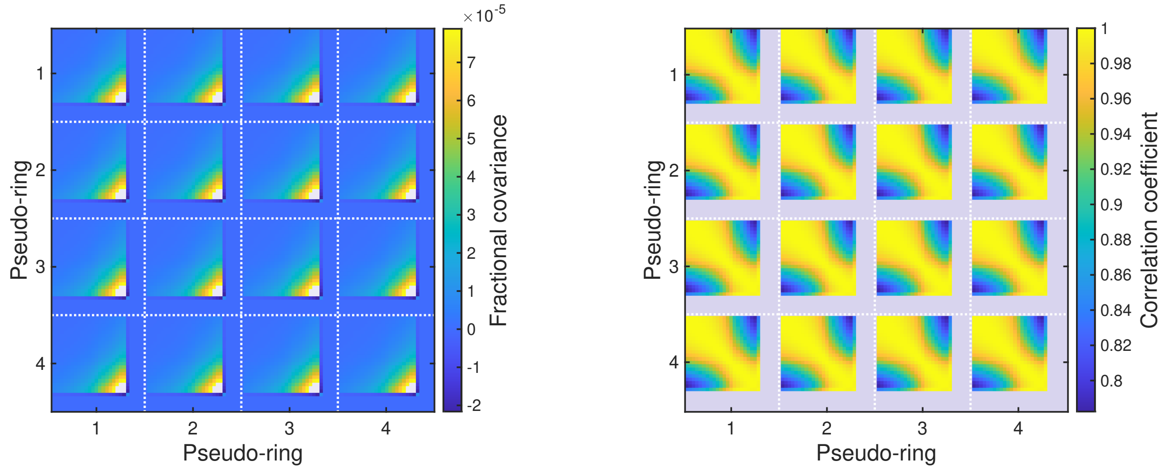

Figure E.9: KNM2 magnetic fields covariance matrix (left) and correlation matrix (right).

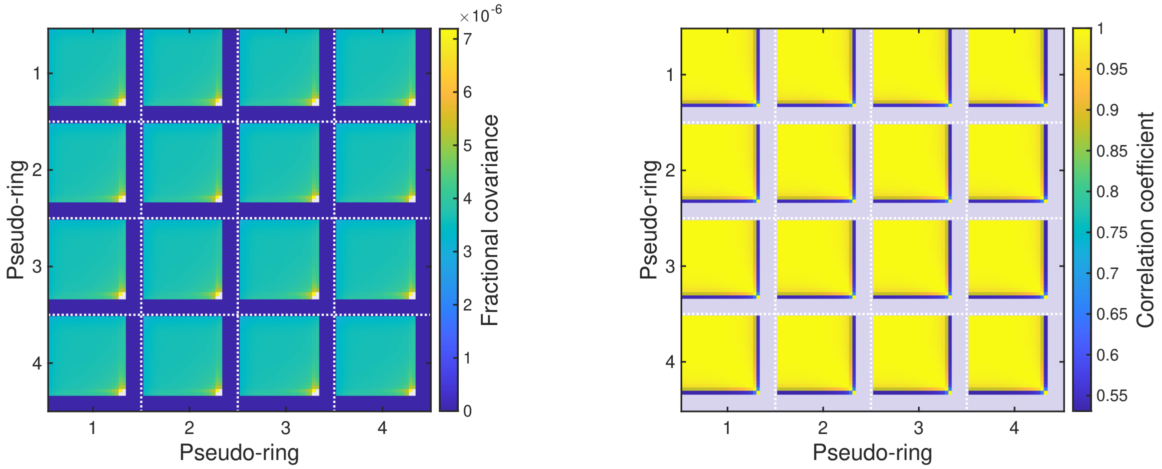

Figure E.10: KNM2 final-state distribution covariance matrix (left) and correlation matrix (right).

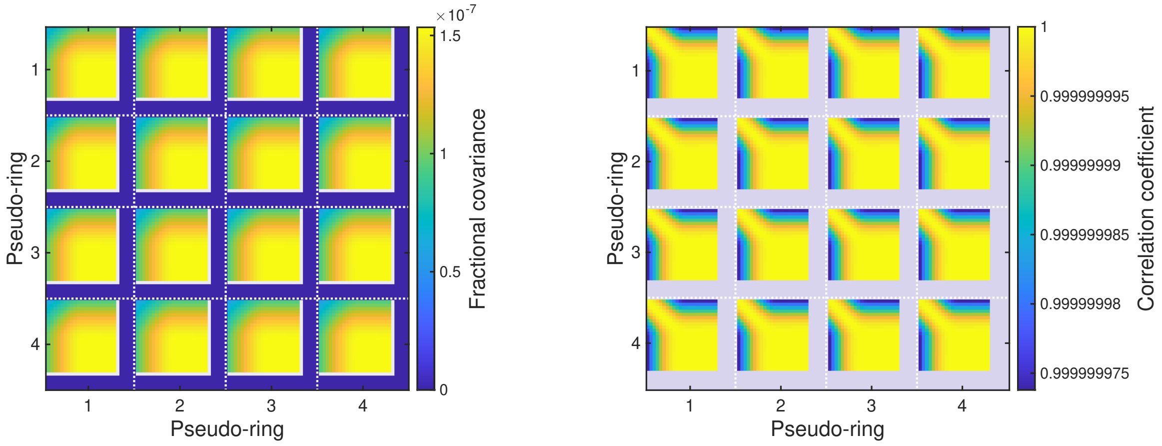

Figure E.11: KNM2 number of scatterings covariance matrix (left) and correlation matrix (right).

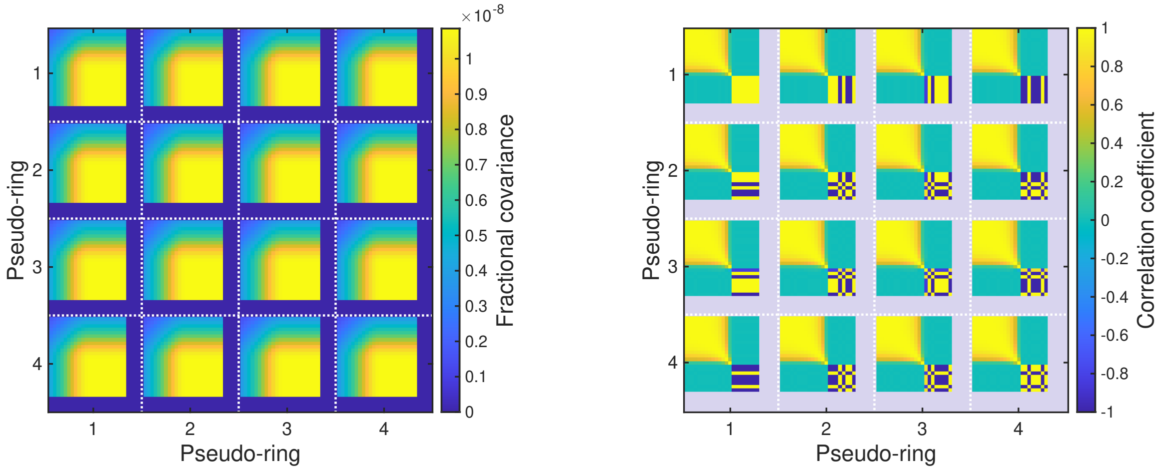

Figure E.12: KNM2 energy-loss function covariance matrix (left) and correlation matrix (right).

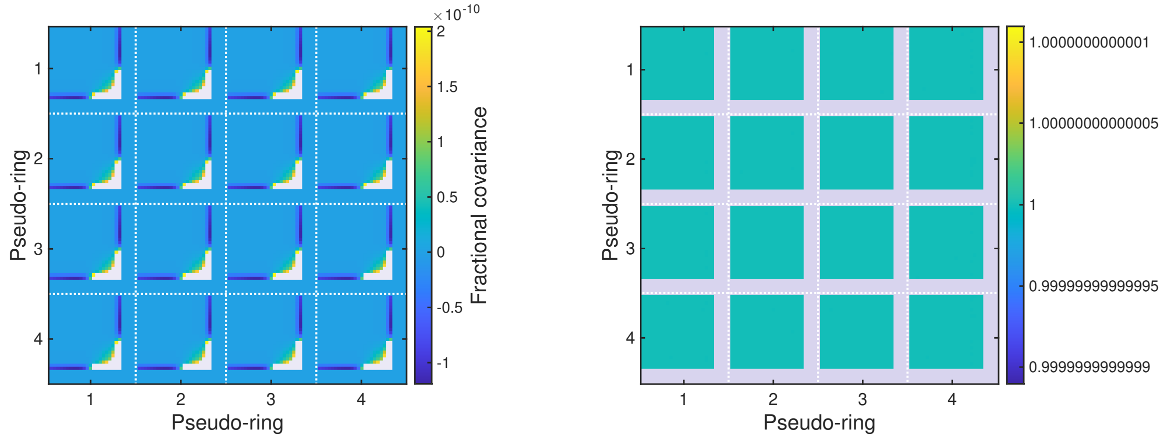

Figure E.13: KNM2 theoretical corrections covariance matrix (left) and correlation matrix (right).

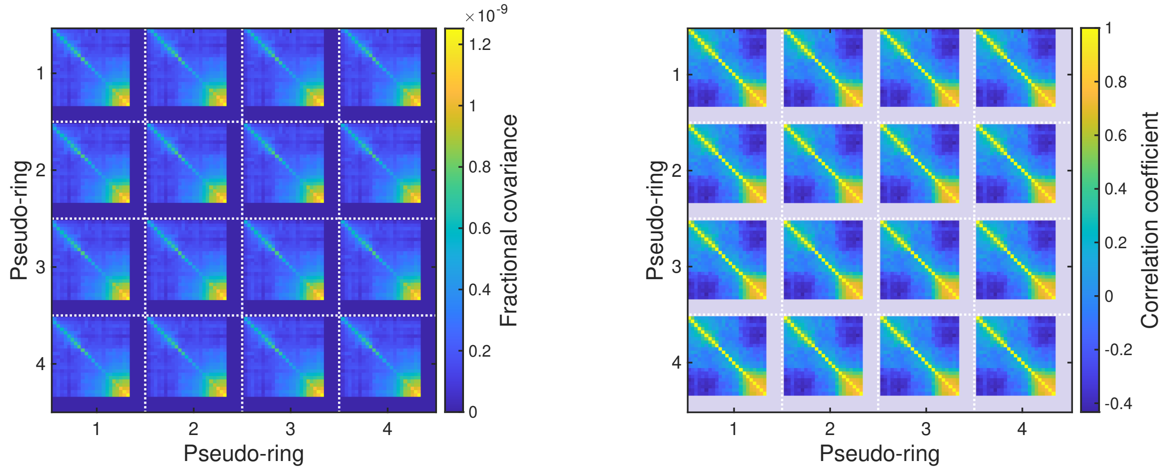

Figure E.14: KNM2 scan fluctuations covariance matrix (left) and correlation matrix (right).

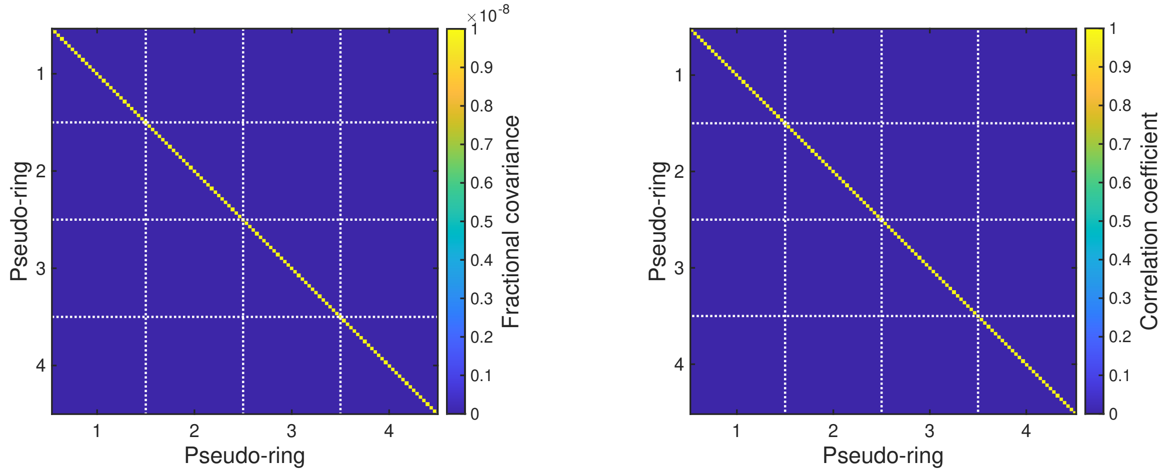

Figure E.15: KNM2 focal plane detector efficiency covariance matrix (left) and correlation matrix (right).

Appendix F

Neutrino-mass analysis of KNM1

F.1 Retarding potential fit parameter dependencies

Retarding potential dependence of steady-state background B_{base}, signal normalization $N_{\text{sig.}}$ and p-value. The remaining fit parameters, m_ν^2 and E_0^{fit} are discussed in detail in section section 8.8.

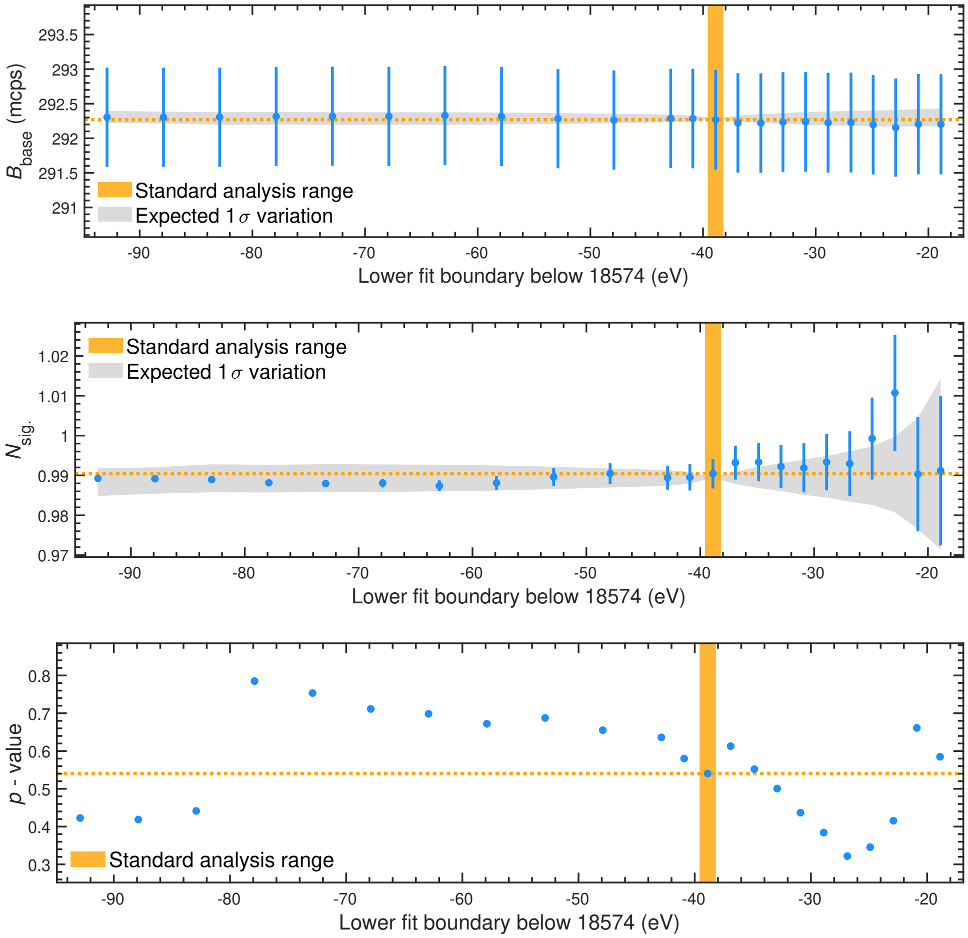

Figure F.1: Best-fit results of the fit parameter as a function of lower fit boundary. Statistical and systematic uncertainties.

F.2 Azimuthal fit parameter dependencies

To investigate the east-west asymmetry in m_ν^2 in the KNM1 data analysis, the FPD are grouped into slices with similar azimuth angle (section 8.10.2). The fit results of the nuisance parameters are displayed in figure F.2. As presented in section 8.5.4, the neutrino mass has a very high positive and a moderate negative correlation with the fit endpoint and the signal normalization, respectively. The fit results of E_0^{fit} thus exhibit a similar azimuthal pattern as m_ν^2, whereas the $N_{\text{sig.}}$ best-fit values show the inverse pattern. The background per number pixels, being only weakly correlated with m_ν^2, features a different behavior. The southwest detector area ($\theta = 135°$) is significantly lower than the uniform result.

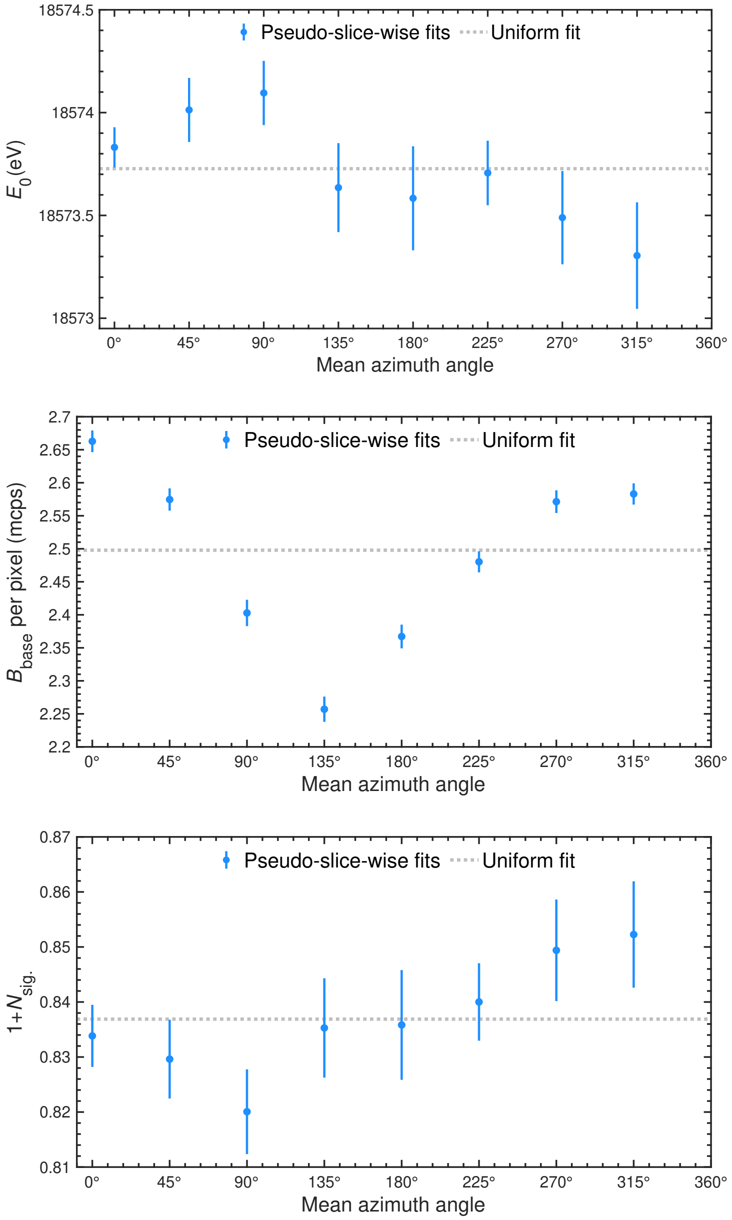

Figure F.2: KNM1 best-fit results of the nuisance parameters as a function of azimuth angle. The associated best-fit values for m_ν^2 are displayed in figure 8.15.

F.3 Neutrino-mass imprint in the integral spectrum

The signature of m_ν^2 in the *differential* tritium β-spectrum is visualized in figure 1.3 in a 5 eV-wide energy window below the endpoint. In practice, however, experimental effects, such the background level or the energy resolution influence the strength of the neutrino-mass imprint in the *integral* spectrum. The neutrino-mass signal strength is defined as the ratio of model spectra with and without nonzero m_ν^2 value

$$\frac{\mathbf{N}^{\text{model}}(m_\nu^2)}{\mathbf{N}^{\text{model}}(m_\nu^2 = 0\,\text{eV}^2)} \tag{F.1}$$

and is depicted in figure F.3 for KNM1 and KNM2 in the standard analysis interval. KNM2 was operated at a higher signal strength and lower background level than KNM1. Consequently, the expected neutrino-mass signal is more prominent in KNM2 than in KNM1. Due to the improved signal-to-background ratio, the KNM2 neutrino-mass signal peaks at larger retarding energies than in KNM1.

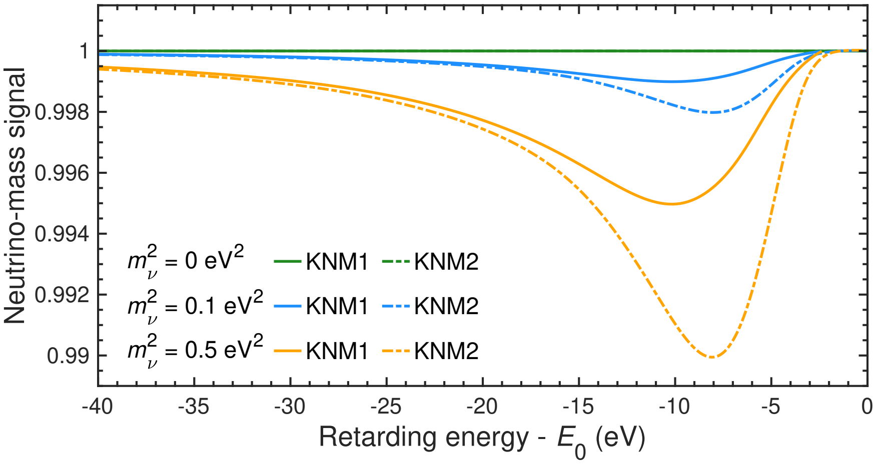

Figure F.3: Expected neutrino-mass imprint in the integral spectrum for KNM1 and KNM2 for different values of m_ν^2.

Appendix G

Neutrino-mass analysis of KNM2

G.1 Signal normalization in multi-ring fit

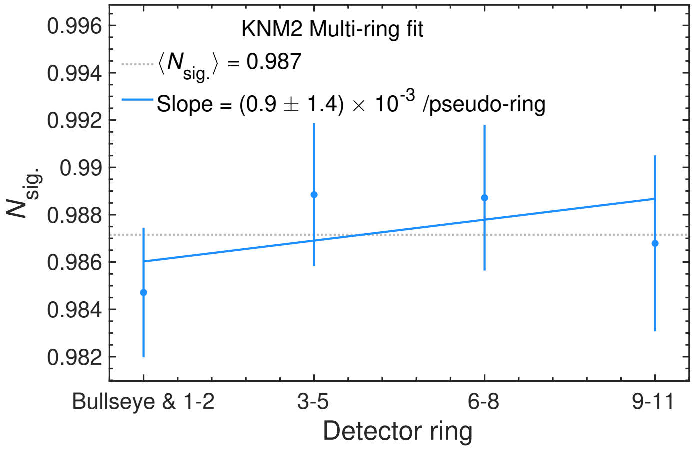

Figure G.1: Pseudo-ring-dependent signal normalization factor in the KNM2 multi-ring fit with four pseudo-rings. N_{sig} is compatible with no radial dependence with $p_{\mathrm{const}} = 0.71$.

G.2 Fit result using uniform pixel segmentation

The KNM2 uniform fit in the standard analysis range including statistical and systematic uncertainties is:

$$\begin{aligned} m_\nu^2 &= (0.28 \pm 0.32)\,\mathrm{eV}^2 \\ E_0^{\mathrm{fit}} &= (18\,573.69 \pm 0.02)\,\mathrm{eV} \\ B_{\mathrm{base}} &= (220.3 \pm 0.5)\,\mathrm{mcps} \\ N_{\mathrm{sig.}} &= 0.986 \pm 0.002 \\ \chi^2_{\mathrm{min}} &= 27.5\,(24\,\mathrm{dof}). \end{aligned}$$

G.3 Radial fit parameter dependencies

The neutrino-mass is a physical constant and is therefore by nature the same of all FPD detector rings. To search for unknown systematic effects, that lead to a radial neutrino-mass dependence, a ring-wise analysis is performed.

In contrast to the multi-ring analysis in section 9.5.1, the neutrino-mass is allowed to have different values for the individuals rings. The radial distribution of the nuisance parameters are shown in figure G.2. Effective tritium endpoint and signal normalization are constant within uncertainties. The background rate exhibits, as expected, a significant increase as a function of detector radius. The results are compatible to the results in section 9.5.1 with uniform m_ν^2.

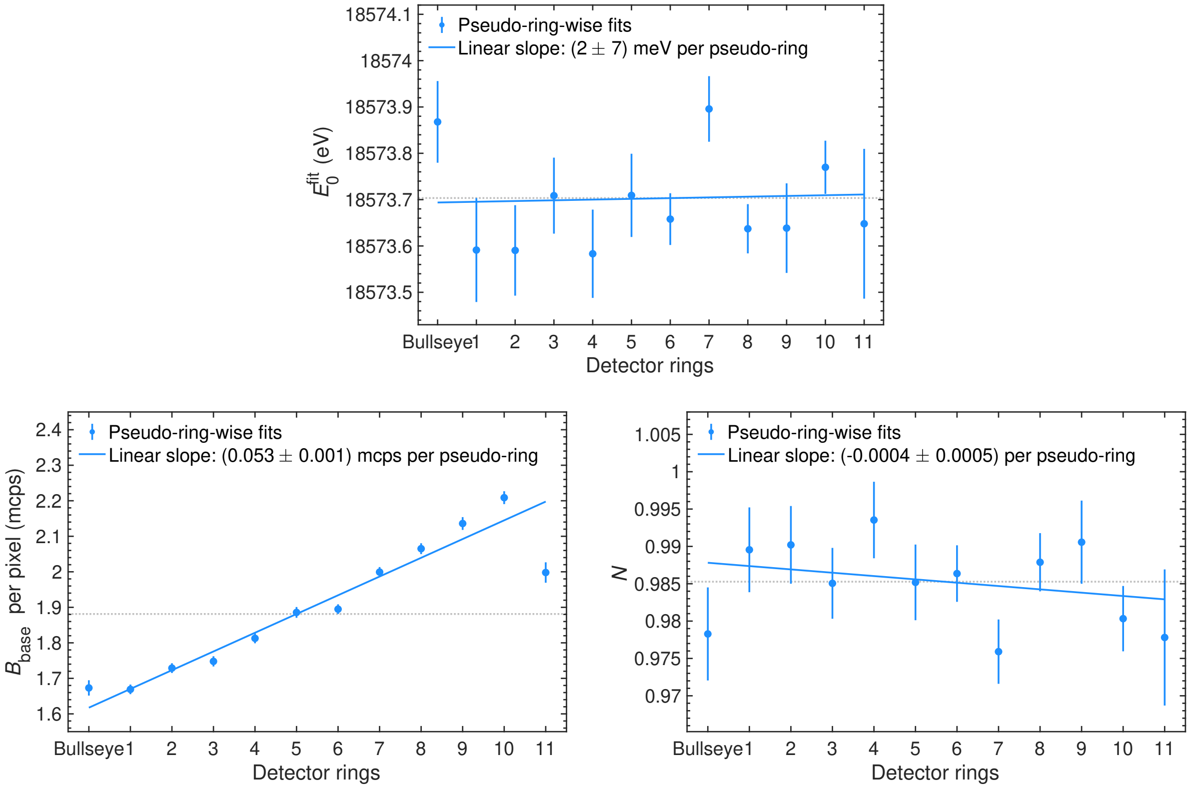

Figure G.2: Ring-wise analysis of KNM2 data. Grey reference line is respective weighted mean. **Top** Endpoint. The linear fit yields a very small radial slope at low significance 1.9σ. **Bottom left:** Background rate per pixel increases as a function of radii. The radial dependence cannot be described well with a linear function ($p < 1 \times 10^{-9}$). **Bottom right:** Signal normalization. Linear slope has only low significance 1.3σ. Pattern is compatible with a no radial dependence at $p = 0.27$.

G.4 Alternative treatment of retarding-potential-dependent background rate

Expected change of best-fit result

In a complementary analysis, the KNM2 data are fit with s_{qU} (retarding-potential-dependent background slope) as a nuisance parameter (section 9.9). Due to the correlation between m_ν^2 and s_{qU}, the fit result and the uncertainty is expected to change. To estimate the expected change randomized MC twins are fit twice: Once with $s_{\mathrm{qU}} = 0\,\mathrm{mcps/keV}$ and once with free s_{qU}. The difference

$$\Delta m_\nu^2 = m_\nu^2\ (\text{free } s_{\mathrm{qU}}) - m_\nu^2\ (\text{fixed } s_{\mathrm{qU}}) \tag{G.1}$$

is shown in figure G.3. As both analyses are bias-free, the median $\Delta m_\nu^2 = 0\,\mathrm{eV}^2$.However, deviations of $\sigma(\Delta m_\nu^2) = 0.06\,\mathrm{eV}^2$ are expected. In some fits, the central m_ν^2 values even differed up to $0.2\,\mathrm{eV}^2$.

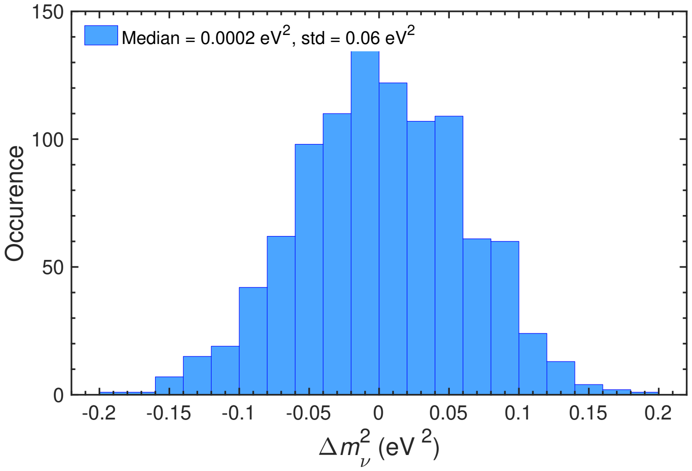

Figure G.3: Expected influence of retarding-potential-dependent background rate on fit result. Randomized MC twins are analyzed twice: Once with fixed retarding-potential background slope and one with free retarding-potential background slope. The differences of m^2_ν best-fit value (equation (G.1)) are shown.

Neutrino-mass uncertainty as a function of retarding-energy-dependent background slope constraint

External constraints $\sigma(s_{\mathrm{qU}})$ can be included in the fit in form of a pull term according to equation (4.12). Uniform fits to the data with different $\sigma(s_{\mathrm{qU}})$ are performed. The 1σ systematic uncertainty on m^2_ν as a function of $\sigma(s_{\mathrm{qU}})$ is displayed in figure G.4. The stronger (smaller) the constraint, the smaller is the systematic uncertainty on m^2_ν. If s_{qU} is left unconstrained in the fit ($\chi^2_{\mathrm{pull}} = 0$), the systematic uncertainty on m^2_ν increases to $\sigma(m^2_\nu) = 0.16\,\mathrm{eV}^2$.

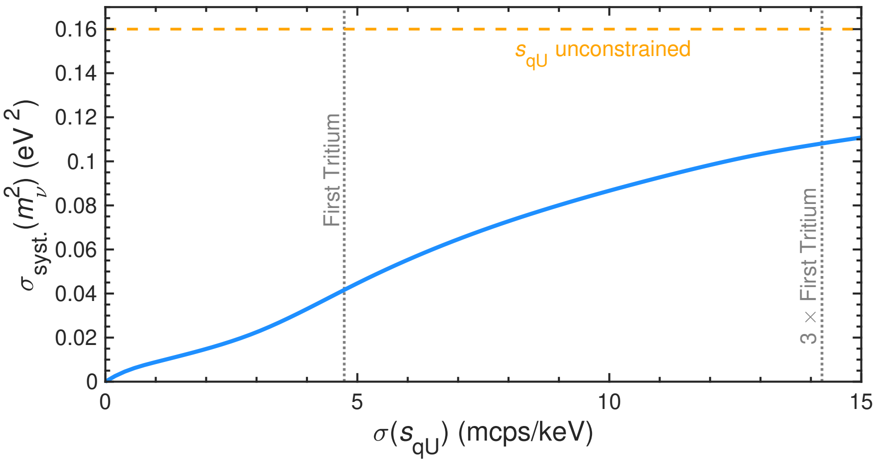

Figure G.4: KNM2 neutrino-mass uncertainty as a function of retarding-energy-dependent background slope constraint. The uncertain retarding-potential dependency of the background rate propagates into a systematic uncertainty on m^2_ν at 68.3 % C.L. The influence on m^2_ν is evaluated by fitting the data with s_{qU} as a fit parameter, which is constrained with a Gaussian pull term with $\sigma(s_{\mathrm{qU}})$. The one-fold and threefold FT constraints are illustrated as grey dotted reference lines. They were used in the KNM2 and KNM1 neutrino-mass analysis respectively. The systematic uncertainty contribution that arises when s_{qU} is unconstrained in the KNM2 fit, amounts to $\sigma(m^2_\nu) = 0.16\,\mathrm{eV}^2$.

G.5 Retarding potential fit parameter dependencies

Retarding potential dependence of steady-state background B_{base}, signal normalization $N_{\mathrm{sig.}}$ and p-value. The remaining fit parameters, m_ν^2 and E_0^{fit} are discussed in detail in section section 9.10.

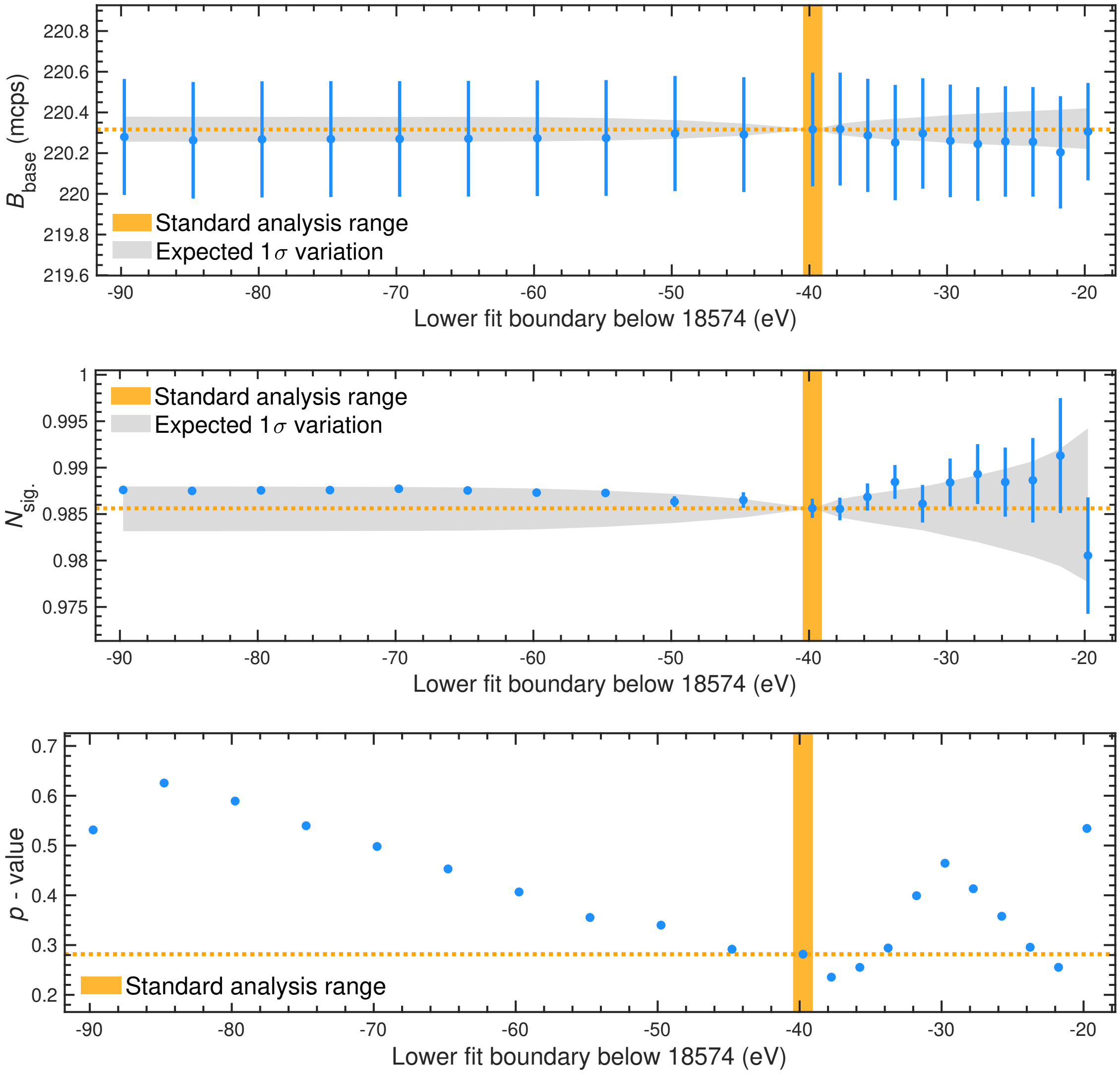

Figure G.5: Retarding-potential dependent fit parameter for KNM2 stacked uniform fit with systematics.

Appendix H

Sterile Neutrino Search

H.1 Influence of background level on sterile-neutrino search

The influence of the background rate is evaluated with simulated KNM2-like spectra without statistical fluctuations. Different steady-state background rates are assumed between 0 mcps and 200 mcps. The sensitivity contours, drawn at 95 % C.L., are displayed in figure H.1. The lower the background rate, the smaller active-to-sterile mixings can be excluded. In KNM2, the scan steps that are most sensitive to $m_4^2 < 100\,\mathrm{eV}^2$ are dominated by background electrons (see section 6.10.3). Thus, the improvement in sensitivity caused by the background reduction is most prominent for small masses.

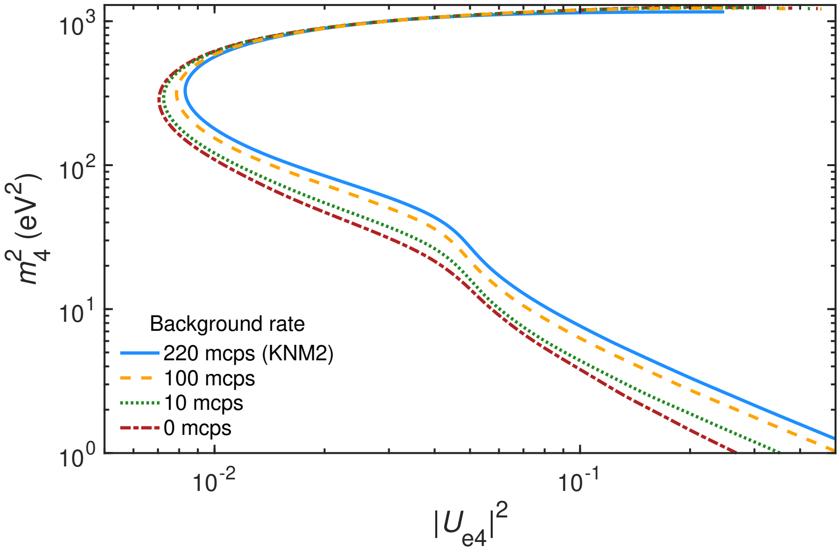

Figure H.1: Sensitivity contours at 95 % C.L. based on KNM2-like simulations with different steady-background levels. The lower the background rate, the more stringent are the sterile-neutrino constraints.

H.2 Comparison of exclusion and sensitivity contour

As described in section 11.5.3, 1σ sensitivity bands at 95 % C.L. for analysis case I) are calculated based on randomized MC twins. The exclusion contours of the KNM1 and KNM2 standalone analyses are compared to the respective mean (Asimov) sensitivity and the associated sensitivity bands in figure H.2. The corresponding display for the combined analysis is shown in figure 11.7. All exclusion contours agree well with the sensitivity estimates.

A direct comparison between exclusion and sensitivity for analysis case II) is given in figure H.3. Also for analysis case II), the exclusion contours agree well with their respective sensitivity estimate. As expected, moderate difference are visible, in particular in the vicinity of the respective best fits.

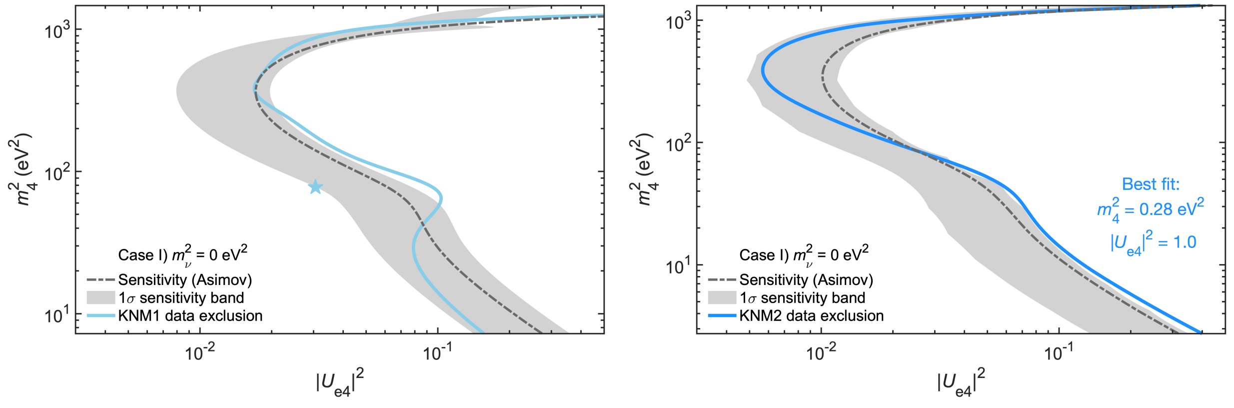

(a) KNM1 (b) KNM2

Figure H.2: To evaluate the agreement between exclusion and mean sensitivity contours in more detail for analysis case I), 1σ-sensitivity bands are calculated at 95 % C.L. as described in section 11.5.3 for the KNM1 and KNM2 standalone analyses. The exclusion contours differ from the Asimov sensitivity contours within the expectation.

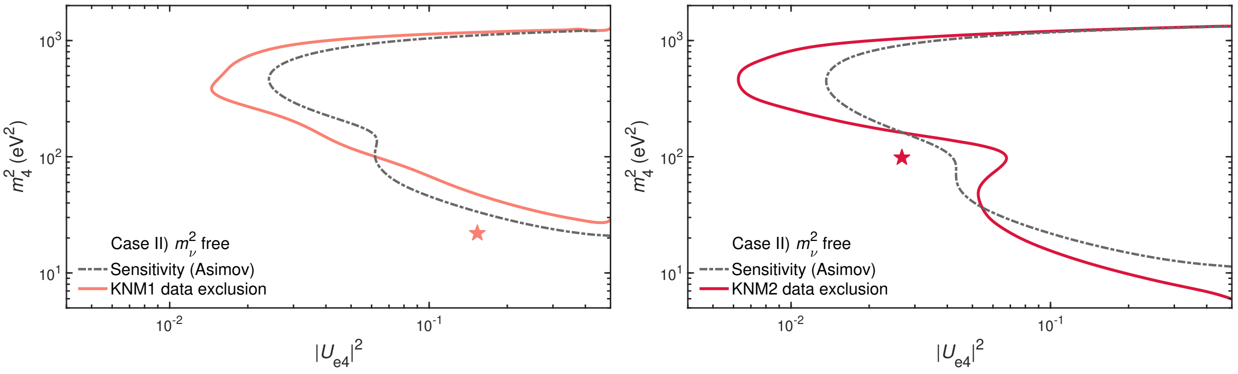

(a) KNM1 (b) KNM2

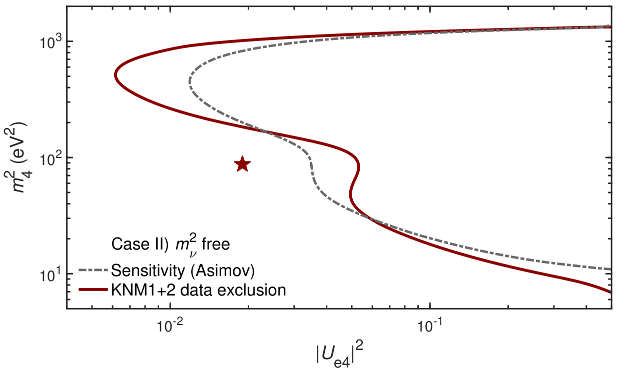

(c) KNM1 and KNM2 combined

Figure H.3: Comparison between (Asimov) sensitivity and exclusion contour in analysis case II) at 95 % C.L.

H.3 Neutrino-mass sensitivity in $3\nu + 1$ framework

The hypothetical existence of eV-scale sterile neutrinos affects the sensitivity to m_ν^2, if no external constraints on the active-to-sterile mixing are consulted. In appendix H.3, the m_ν^2 sensitivity is calculated in the $3\nu + 1$ framework by performing grid searched on data and MC twins for different fixed values of m_ν^2. The m_ν^2 sensitivity can be then retrieved from the resulting chi-squared profile. Figure H.4 shows the best-fit locations in the $[m_4^2, |U_{e4}|^2]$ parameter space for 36 different fixed neutrino mass squared values $m_\nu^2 \in [-1, 2.5]$ eV^2.

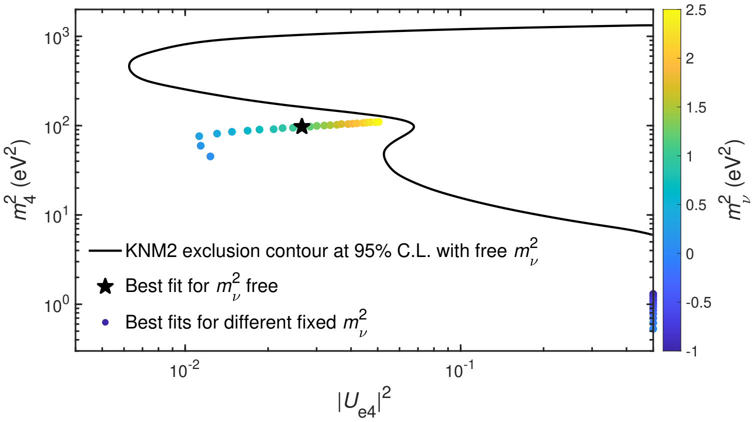

Figure H.4: To obtain the profile chi-squared function $\chi^2(m_\nu^2)$ in the 3ν+1 framework, grid searches are performed on the data with different fixed $m_\nu^2 \in [-1, 2.5]$. The respective best fits of the grid searches are displayed as filled points. Their colors indicate the fixed m_ν^2 value.

H.4 Influence of systematic uncertainties

The influence of systematic uncertainties on the sterile-neutrino contours is evaluated with (Asimov) MC twin spectra. For each simulated spectrum, two grid searches are performed: The first considers only statistical uncertainties and the second considers statistical and all systematic uncertainties. The sensitivity contours are depicted at 95 % C.L. in figure H.5. If systematic uncertainties are included, the grid searches yield slightly weaker constraints compared to the statistics-only sensitivity contours. However, the influence is small for both data sets.

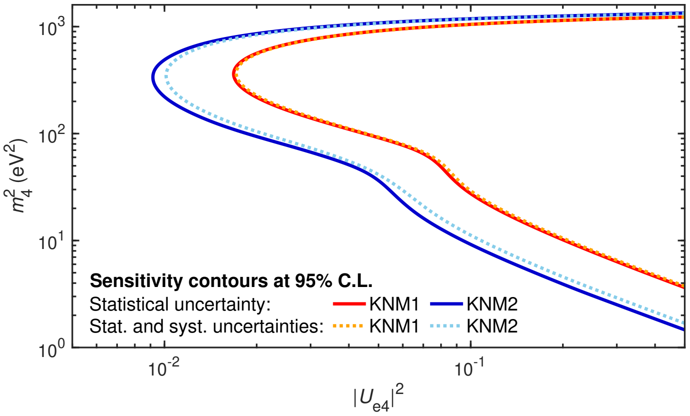

Figure H.5: Sensitivity contours at 95 % C.L. for KNM1 and KNM2 analysis case I). The solid lines result from grid searches considering only statistical uncertainties. The dotted lines are calculated with the total uncertainty budget of statistical and systematic uncertainties. The influence of systematic uncertainties on the sensitivity contour is small for both data sets.

H.5 Extension of the fit interval

As a supplement analysis, the KNM1 and KNM2 data is analyzed for sterile neutrinos using the full measurement interval. The same systematic uncertainty budget as for the standard analysis interval is used. The results are discussed in section 11.8. The contour curves at 95 % C.L. for analysis case II) are given in figure H.6. Moreover, the combined KNM1 and KNM2 analysis is compared to KATRIN predecessor experiments in figure H.7. The best-fit results and their significances are summarized in table H.1.

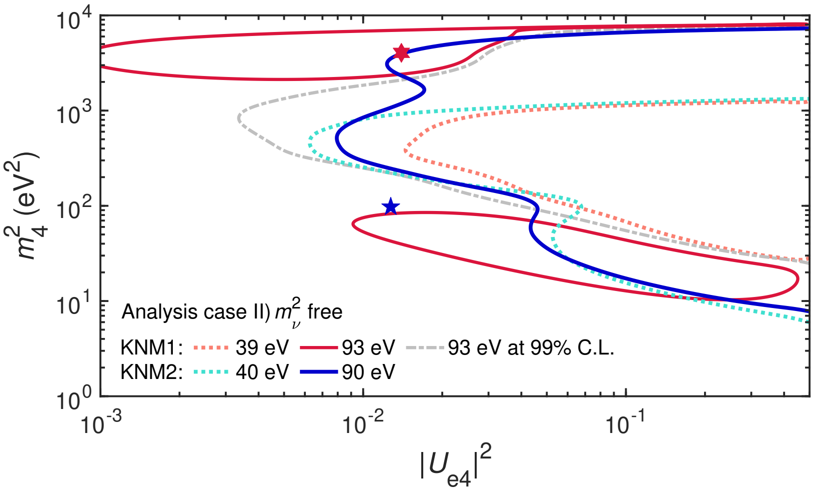

Figure H.6: Analysis case II) contour curves considering the full measurement interval of KNM1 and KNM2. If not explicitly stated otherwise, the contours are drawn at 95 % C.L. The positive signal at 95 % of the KNM1 vanishes stems likely from a statistical fluctuation or unaccounted systematic effect. Moreover, the closed contour open for 99 % C.L., illustrated by the gray dash-dotted line.

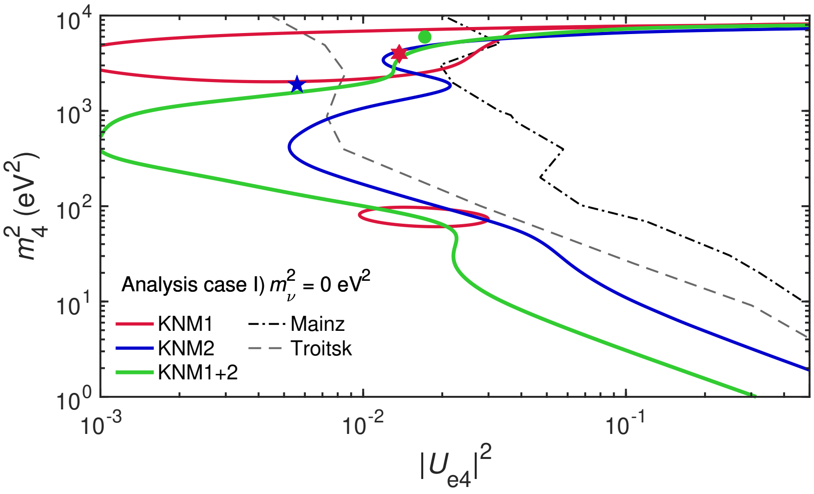

Figure H.7: Combined KNM1 and KNM2 contours at 95 % C.L. for analysis case I) considering the full measurement interval. The combined exclusion curve improves with respect to Mainz [111] for $m_4^2 \lesssim 6000\,\text{eV}^2$ and with respect to Troitsk [112] for $m_4^2 \lesssim 2000\,\text{eV}^2$.

Analysis case	Dataset	m_4^2	$\|U_{e4}\|^2$	m_ν^2	χ^2_{min}/dof	p	$\Delta\chi^2_{\mathrm{null}}$	Significance	$\hat{p}$
I	KNM1	3986 eV^2	0.014	fixed	29.2/34	0.70	6.72	96.5 %	-
	KNM2	1886 eV^2	0.006	fixed	32.4/33	0.50	3.62	83.6 %	-
	KNM1+2	5963 eV^2	0.017	fixed	63.9/69	0.65	5.17	92.4 %	0.10
II	KNM1	4042 eV^2	0.014	−0.68 eV^2	28.5/33	0.69	6.81	96.7 %	-
	KNM2	97.7 eV^2	0.013	0.56 eV^2	31.8/32	0.48	0.81	33.4 %	-

Table H.1: Best-fit results of the KNM1 and KNM2 sterile-neutrino searches for the full measurement interval.

H.6 Test of Wilks's theorem

The applicability of Wilk's theorem is tested for the KNM1 and KNM2 statistics. Following the procedure in section 11.10, the critical chi-squared difference for 95 % C.L. is numerically calculated for different MC truths. The $\Delta\chi^2$ distributions are sampled by analyzing randomized tritium spectra, based on the respective MC truths. The position of the global chi-squared minimum of each each sample is shown in figure H.8 for the Null hypothesis. The $\Delta\chi^2$ probability density functions and the associated cumulative probability density functions are displayed in figure H.9.

The influence of $\Delta\chi^2_{\mathrm{crit}}$ on the KNM2 exclusion contour (analysis case I) is illustrated in figure H.10. The exclusion curves drawn for different numerical $\Delta\chi^2_{\mathrm{crit}}$ values (see table 11.3) are only slightly shifted compared to the exclusion contour assuming Wilks's theorem.

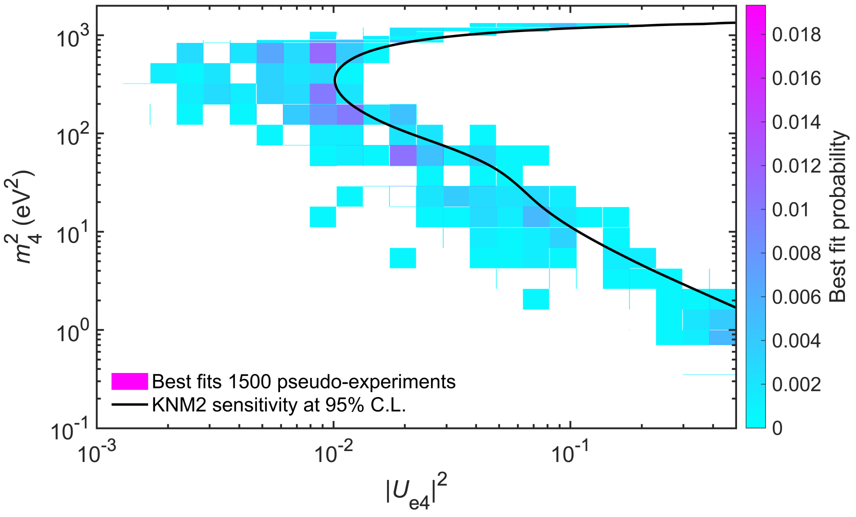

Figure H.8: Positions of best fits from grid search on 1500 randomized KNM2-like tritium spectra. The MC truth is $m_4^2 = 0\,\mathrm{eV}^2$,$|U_{e4}|^2 = 0$. The black solid line is the sensitivity curve, obtained with Asimov twins, at 95 % C.L.

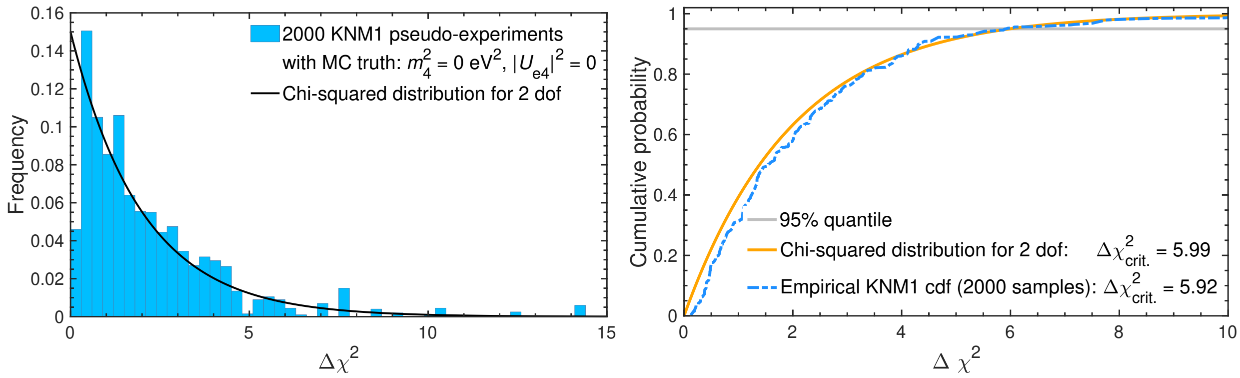

(a) KNM1, MC truth: $m_4^2 = 0\,\text{eV}^2$ and $|U_{e4}|^2 = 0$ (b) KNM1, MC truth: $m_4^2 = 0\,\text{eV}^2$ and $|U_{e4}|^2 = 0$

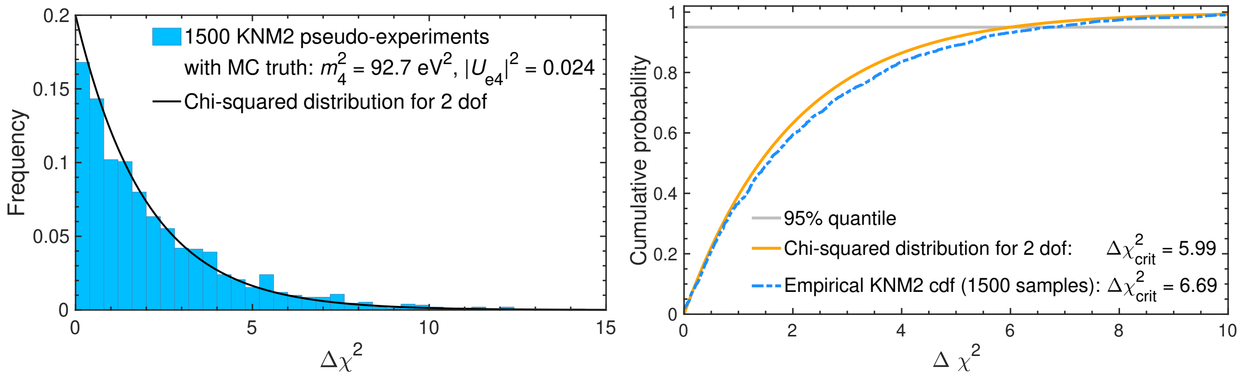

(c) KNM2, MC truth: $m_4^2 = 92.7\,\text{eV}^2$ and $|U_{e4}|^2 = 0.024$ (d) KNM2, MC truth: $m_4^2 = 92.7\,\text{eV}^2$ and $|U_{e4}|^2 = 0.024$

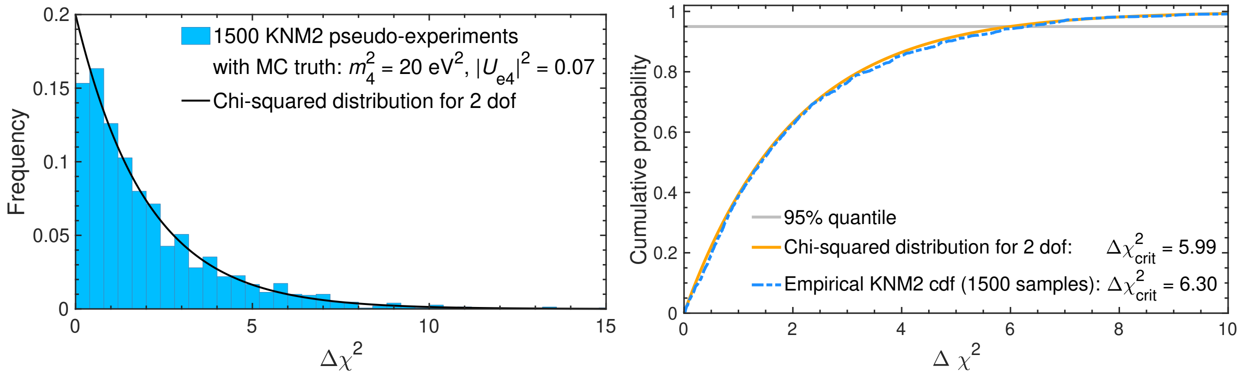

(e) KNM2, MC truth: $m_4^2 = 20\,\text{eV}^2$ and $|U_{e4}|^2 = 0.07$ (f) KNM2, MC truth: $m_4^2 = 20\,\text{eV}^2$ and $|U_{e4}|^2 = 0.07$

Figure H.9: Test of Wilks's theorem **Left:** $\Delta\chi^2$ is calculated for $\mathcal{O}(10^3)$ simulated sample spectra according to equation (11.9). The respective MC truths are stated in the captions. The black solid lines correspond to the expectation from Wilks's theorem, respectively. **Right:** The empirical cumulative density function is calculated from the $\Delta\chi^2$ samples. The 95 % quantile corresponds to $\Delta\chi^2_{\text{crit}}$. Its is estimated with the boot-strapping method.

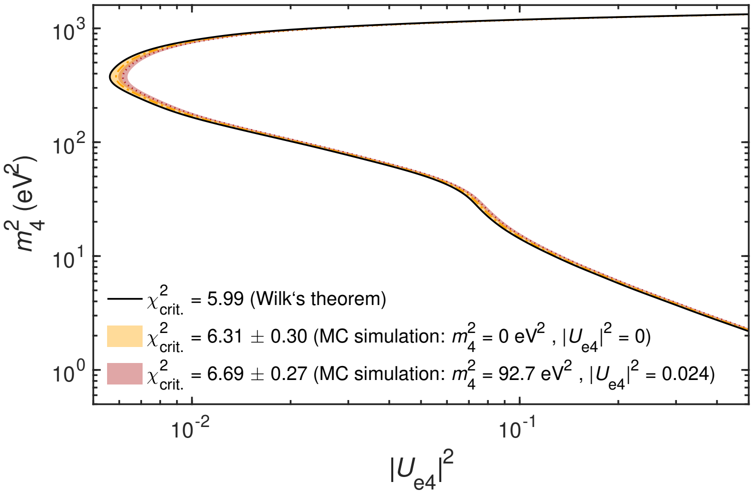

Figure H.10: The threshold value $\Delta\chi^2_{\text{crit}}$ that corresponds to 95 % C.L. is numerically calculated for two exemplary grid points. The impact on the exclusion contour is demonstrated assuming that the numerically calculated $\Delta\chi^2_{\text{crit}}$ is representative for the entire parameter space considered. The orange dashed-dotted line corresponds to contour with $\Delta\chi^2_{\text{crit}}$ from the MC simulation, in which the Null hypothesis is set as MC truth. Since the numerical threshold value is larger than the predicted one, the exclusion curve is shifted towards larger mixings. The orange area illustrates the 1 σ uncertainty on $\Delta\chi^2_{\text{crit}}$. The red dotted line and area show the exclusion curve using $\Delta\chi^2_{\text{crit.}}$ from a sterile-neutrinos hypothesis simulation. The two colorful contour curves are to be compared with the black solid line, which is the exclusion curve assuming Wilks's theorem. The shift of the exclusion curve is small.

H.7 Nonphysical parameter space

In a supplementary analysis, the $[m_4^2, |U_{e4}|^2]$ parameter space is extended to negative values. Grid searches are performed in four quadrants to obtain the respective profile chi-squared functions. The results for analysis case I) are shown in figure H.11 for KNM1 and KNM2, respectively. The corresponding display for analysis case II) is provided in figure H.12. The best fit within each quadrant is marked with a star symbol with the global best fit for all quadrants being highlighted in red color. If no improvement over to the Null hypothesis could be found, no best fit is given. No significant sterile-neutrino signal could be observed in the nonphysical parameter space.

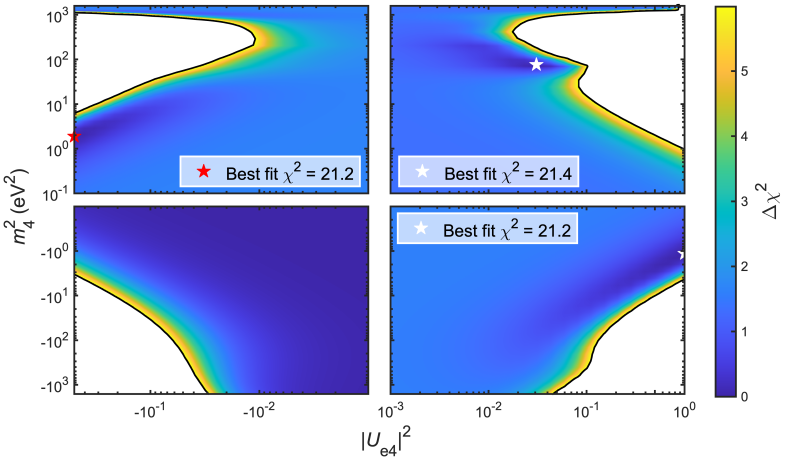

(a) KNM1 with $\chi^2_{\text{null}} = 22.8\,(24\,\text{dof})$

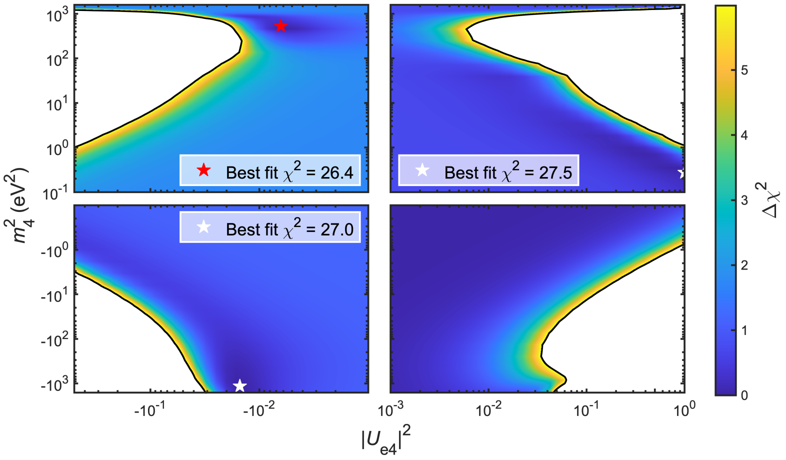

(b) KNM2 with $\chi^2_{\text{null}} = 28.2\,(25\,\text{dof})$

Figure H.11: Chi-squared profiles for the physical and non-physical parameter space for analysis case I) (fixed m_ν^2). As a sanity check, the modeled sterile-neutrino signal is extended to nonphysical values of m_4^2 and $|U_{e4}|^2$. The north-east quadrant corresponds to the physical region. The best fit of each quadrant is marked with a star symbol. The global best fit is highlighted in red. In case $\chi^2_{\text{min}} \geq \chi^2_{\text{null}}$, no best fit is given.

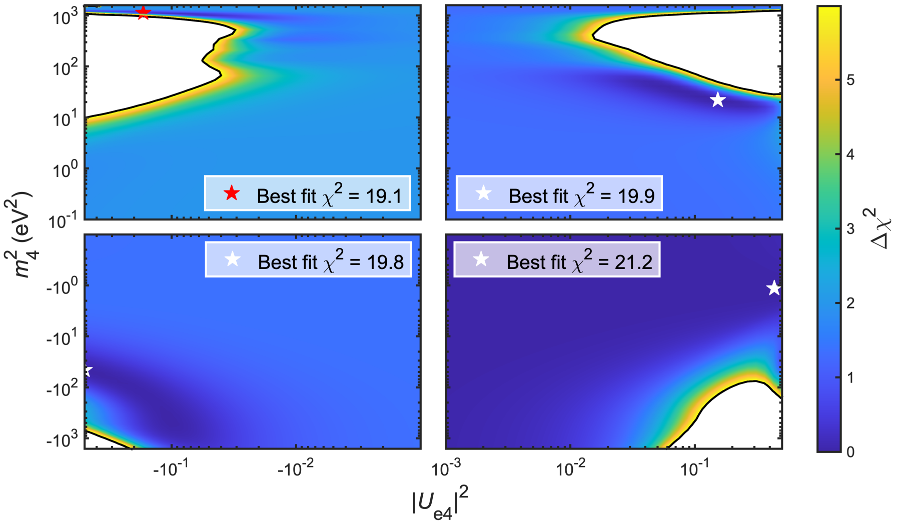

(a) KNM1 with $\chi^2_{\text{null}} = 21.2\,(23\,\text{dof})$

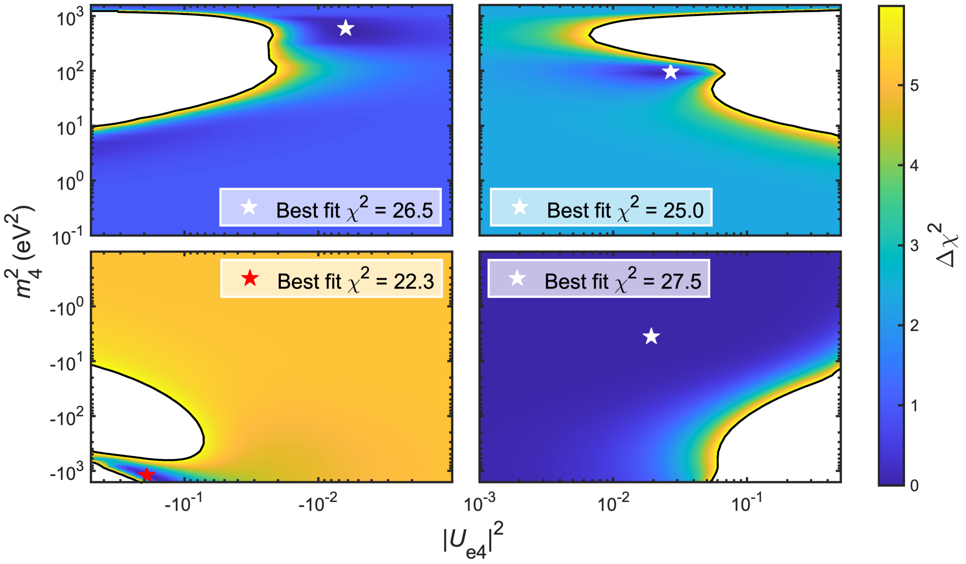

(b) KNM2 with $\chi^2_{\text{null}} = 27.5\,(24\,\text{dof})$

Figure H.12: Chi-squared profiles for the physical and non-physical parameter space for analysis case II) (free m_ν^2). As a sanity check, the modeled sterile-neutrino signal is extended to nonphysical values of m_4^2 and $|U_{e4}|^2$. The north-east quadrant corresponds to the physical region. The best fit of each quadrant is marked with a star symbol. The global best fit is highlighted in red. In case $\chi^2_{\text{min}} \geq \chi^2_{\text{null}}$, no best fit is given.

List of Acronyms

Samak	Simulation and Analysis with MATLAB for KATRIN
KATRIN	KArlsruhe TRItium Neurino
TDR	KATRIN Design Report
MTD	measurement time distribution
WGTS	windowless gaseous tritium source
FPD	focal plane detector
LARA	LAser RAman spectroscopy
ROI	region of interest
FSD	final state distribution
MC	Monte Carlo
DPS	differential pumping system
CPS	cryogenic pumping system
KNM1	KATRIN neutrino mass run 1
KNM2	KATRIN neutrino mass run 2
KNM3	KATRIN neutrino mass run 3
FT	First Tritium (campaign)
FBM	Forward beam monitor
MAC	Magnetic Adiabatic Collimation
TLK	Tritium Laboratory Karlsruhe
dof	degree(s) of freedom
HV	high voltage
PG	parameter goodness-of-fit
LT	Lokhov and Tkachov
FC	Feldman and Cousins
PMNS	Pontecorvo–Maki–Nakagawa–Sakata
C.L.	confidence level

p.d.f. probability density function

SNO Sudbury Neutrino Observatory

PMT Photomultiplier tube

RAA Reactor antineutrino anomaly

GA Gallium anomaly

BEST Baksan Experiment on Sterile Transitions

GALLEX Gallium-Experiment

SAGE Soviet–American Gallium Experiment

LSND Liquid Scintillator Neutrino Detector

MiniBooNE Mini Booster Neutrino Experiment

KARMEN Karlsruhe Rutherford Medium Energy Neutrino

List of Figures

1.1 Two-flavor neutrino oscillations . . . 6
1.2 Experimental signature of neutrinoless double β-decay . . . 9
1.3 Signature of the neutrino mass in tritium β-decay spectrum . . . 11
1.4 Signature of sterile neutrinos in tritium β-decay spectrum . . . 13
1.5 LSND and MiniBooNE sterile-neutrino anomalies . . . 15

2.1 Schematic view of the KATRIN experiment . . . 18
2.2 Working principle of a MAC-E filter . . . 21
2.3 Final-state distribution of different tritium isotopologues . . . 24
2.4 Response function . . . 26
2.5 Transmission function . . . 28
2.6 Angular dependence of inelastic scattering probabilities . . . 28
2.7 Energy-loss function . . . 30

3.1 Overview of basic FPD pixel combinations . . . 35
3.2 Profile chi-squared function and probability density function . . . 38
3.3 Feldman and Cousins $\Delta\chi^2$ ordering principle . . . 39
3.4 Illustration of different confidence-belt-construction techniques . . . 40

4.1 Theoretical correction to the standard Fermi-function . . . 43
4.2 Illustration of the systematic uncertainty on the final-state distribution . . . 44
4.3 Illustration of longitudinal plasma parameters . . . 46
4.4 Integral spectra for different tritium isotopologues . . . 49
4.5 Systematic uncertainty on the energy-loss function . . . 49

5.1 KNM1 measurement-time distribution . . . 53
5.2 KNM1 golden pixel selection . . . 54
5.3 KNM1 time evolution of tritium purity and isotopologue concentrations . . . 55
5.4 KNM1 time evolution of the column density . . . 56
5.5 KNM1 scan-step-wise source activity variations . . . 57
5.6 KNM1 high-voltage reproducibility . . . 58
5.7 KNM1 pixel-wise electric and magnetic potentials in the analyzing plane . . . 59
5.8 KNM1 pixel-wise background rate . . . 60
5.9 KNM1 background count distribution . . . 60
5.10 KNM1 signal-to-background ratio . . . 61
5.11 KNM1 retarding-potential-dependent background . . . 62
5.12 KNM1 retarding-potential dependency of the background rate . . . 62

6.1 KNM2 measurement-time distribution . . . 63
6.2 KNM2 golden pixel selection . . . 64
6.3 KNM2 time evolution of tritium purity and isotopologue concentrations . . . 65
6.4 KNM2 time evolution of the column density . . . 66
6.5 KNM2 scan-step-wise source activity variations . . . 67
6.6 KNM2 time evolution of the rate monitor point . . . 68

6.7 KNM2 period-wise energy broadening based on the rate monitor point . . . 70
6.8 KNM2 global energy broadening based on the rate monitor point . . . 71
6.9 KNM2 high-voltage reproducibility . . . 73
6.10 KNM2 pixel-wise electric and magnetic potentials in the analyzing plane . . . 73
6.11 KNM2 pixel-wise background rate . . . 74
6.12 KNM2 background count distribution . . . 75
6.13 KNM2 signal-to-background ratio . . . 76
6.14 KNM2 retarding-potential-dependent background . . . 76

7.1 Illustration of Monte Carlo twin scan . . . 80

8.1 KNM1 validation of scan combination . . . 82
8.2 KNM1 validation of pixel combination . . . 83
8.3 KNM1 time evolution of the nuisance parameters: E_0^{fit}, B_{base} ,N_{sig} . . . 84
8.4 KNM1 time evolution of the p-value of the scan-wise fits . . . 85
8.5 KNM1 best fit: Spectrum and residuals . . . 86
8.6 KNM1 profile chi-squared function . . . 87
8.7 KNM1 confidence belt and upper limit . . . 88
8.8 KNM1 fit parameter correlations . . . 89
8.9 KNM1 systematic uncertainty breakdown . . . 90
8.10 KNM1 radial fit parameter dependencies . . . 91
8.11 KNM1 neutrino-mass sensitivity for extended fit intervals . . . 92
8.12 KNM1 m_ν^2 and E_0^{fit} fit results for different fit intervals . . . 93
8.13 KNM1 alternative scan selections . . . 94
8.14 KNM1 alternative pixel selections . . . 95
8.15 KNM1 azimuthal neutrino-mass dependence . . . 96
8.16 KNM1 influential data points and Cook's distance . . . 97
8.17 KNM1 influential data point and excluded data points . . . 98
8.18 KNM1 re-analysis with an updated model configuration . . . 99

9.1 KNM2 time evolution of the fit endpoint . . . 102
9.2 KNM2 time evolution of the steady-state background rate . . . 103
9.3 KNM2 time evolution of the signal normalization . . . 104
9.4 KNM2 time evolution of the goodness-of-fit . . . 104
9.5 KNM2 best fit: Spectrum and residuals . . . 105
9.6 KNM2 pseudo-ring-dependent fit parameters in multi-ring analysis . . . 106
9.7 KNM2 profile chi-squared function . . . 107
9.8 KNM2 confidence belt and upper limit . . . 107
9.9 KNM2 fit parameter correlations . . . 108
9.10 KNM2 best-fit results for different pixel combination strategies . . . 109
9.11 KNM2 systematic uncertainty breakdown . . . 110
9.12 KNM2 radial neutrino-mass dependency . . . 110
9.13 KNM2 correlation between neutrino-mass and retarding-potential-dependent background rate . . . 111
9.14 KNM2 neutrino-mass sensitivity for extended fit intervals . . . 112
9.15 KNM2 m_ν^2 and E_0^{fit} fit results for different fit intervals . . . 113
9.16 KNM2 alternative scan selections . . . 114
9.17 KNM2 alternative pixel selections . . . 115
9.18 KNM2 influential data points and Cook's distance . . . 116
9.19 KNM2 influential data points and excluded data points . . . 116

10.1 Combined sensitivity chi-squared profile of KNM1 and KNM2 . . . 118
10.2 Combined best-fit of KNM1 and KNM2 . . . 119
10.3 Combined data chi-squared profile of KNM1 and KNM2 . . . 120

11.1 Illustration of different two-dimensional profile chi-squared functions in sterile-neutrino analysis . 124
11.2 Correlation between active and sterile neutrino mass 126
11.3 Overview of sterile-neutrino sensitivity contours for KNM1 and KNM2 127
11.4 Overview of sterile-neutrino exclusion contours for KNM1 and KNM2 128
11.5 KNM1 data exclusion contours with m^2_ν fit values 130
11.6 KNM2 data exclusion contours with m^2_ν fit values 131
11.7 Comparison of exclusion and sensitivity contours for combined analysis 132
11.8 Comparison of KATRIN sterile-neutrino constraints to other experiments 133
11.9 Neutrino-mass sensitivity and fit result in $3\nu+1$ framework 134
11.10 Comparison of statistical and systematic sensitivity on $|U_{e4}|^2$ for KNM1 and KNM2 135
11.11 Breakdown of systematic uncertainties on $|U_{e4}|^2$ for KNM2 136
11.12 Exclusion contours using the extended fit interval for $m^2_\nu = 0\,\mathrm{eV}^2$ 137
11.13 Validation of Wilks's theorem: Chi-squared distributions 139

A.1 Energy dependence of inelastic scattering cross section 145

B.1 Alternative FPD pixel combinations 149

D.1 KNM1 total covariance matrix 157
D.2 KNM1 Non-Poisson background rate covariance matrix 158
D.3 KNM1 scan fluctuations covariance matrix 158
D.4 KNM1 retarding-potential-dependent background covariance matrix 158
D.5 KNM1 final-state distribution covariance matrix 159
D.6 KNM1 magnetic fields covariance matrix 159
D.7 KNM1 number of scatterings covariance matrix 159
D.8 KNM1 focal plane detector efficiency covariance matrix 160
D.9 KNM1 energy-loss function covariance matrix 160
D.10 KNM1 theoretical corrections covariance matrix 160

E.1 KNM2-like simulation of retarding-potential dependency of the rate monitor point 163
E.2 KNM2 time evolution of retarding potential for $\langle qU\rangle = 18\,570\,\mathrm{V}$ 164
E.3 KNM2 time-wise background slope correction 164
E.4 KNM2 total covariance matrix 165
E.5 KNM2 Non-Poisson background rate covariance matrix 165
E.6 KNM2 scan-step-time-dependent background covariance matrix 165
E.7 KNM2 source potential covariance matrix 166
E.8 KNM2 retarding-potential-dependent background covariance matrix 166
E.9 KNM2 magnetic fields covariance matrix 166
E.10 KNM2 final-state distribution covariance matrix 167
E.11 KNM2 number of scatterings covariance matrix 167
E.12 KNM2 energy-loss function covariance matrix 167
E.13 KNM2 theoretical corrections covariance matrix 168
E.14 KNM2 scan fluctuations covariance matrix 168
E.15 KNM2 focal plane detector efficiency covariance matrix 168

F.1 KNM1 $B_{\mathbf{base}}$, N_{sig} fit results and p-value for different fit intervals 169
F.2 KNM1 best-fit results all nuisance parameters as a function of azimuth angle 170
F.3 Expected neutrino-mass imprint in the integral spectrum for KNM1 and KNM2 171

G.1 KNM2 pseudo-ring-dependent signal normalization in multi-ring analysis 173
G.2 KNM2 radial fit parameter dependency 174
G.3 Expected influence of retarding-potential-dependent background rate on fit result in KNM2 175
G.4 KNM2 neutrino-mass uncertainty as a function of retarding-energy-dependent background slope constraint 175

G.5 KNM2 $B_{\mathbf{base}}$, N_{sig} fit results and p-value for different fit intervals . . . 176

H.1 Sensitivity contours based on KNM2-like simulations with different steady-background levels . . . 177
H.2 Comparison of exclusion and sensitivity contours considering $m_\nu^2 = 0\,\mathrm{eV}^2$ . . . 178
H.3 Comparison of exclusion and sensitivity contours considering m_ν^2 as a nuisance parameter . . . 178
H.4 Neutrino-mass sensitivity in $3\nu + 1$ framework: Locations of best fit as a function of m_ν^2 . . . 179
H.5 Influence of systematic uncertainties on the sensitivity contour for KNM1 and KNM2 . . . 179
H.6 Exclusion contours using the extended fit interval considering m_ν^2 as a nuisance parameter . . . 180
H.7 Combined exclusion contours using the extended fit interval for $m_\nu^2 = 0\,\mathrm{eV}^2$. . . . 180
H.8 Validation of Wilks's theorem: positions of best fits . . . 181
H.9 Validation of Wilks's theorem: Numerical chi-squared distributions for several representative MC truths . . . 182
H.10 Validation of Wilks's theorem: Influence of numerical $\Delta\chi^2_{\mathrm{crit}}$ on exclusion contour . . . 183
H.11 Chi-squared profiles for the physical and non-physical parameter space for $m_\nu^2 = 0\,\mathrm{eV}^2$ . . . 184
H.12 Chi-squared profiles for the physical and non-physical parameter space considering m_ν^2 as a nuisance parameter . . . 185

List of Tables

2.1 Average inelastic scattering probabilities . . . 29

3.1 Baseline fit parameters . . . 36

6.1 KNM2 Difference of period-wise mean rate of rate monitor point . . . 69
6.2 KNM2 effective global broadening based on the rate monitor point . . . 71

9.1 KNM2 average fit endpoint for different rear-wall periods . . . 103

11.1 Overview of best-fit results in the $3\nu+1$ framework for KNM1 and KNM2 . . . 129
11.2 Breakdown of systematic uncertainties on $|U_{e4}|^2$ for KNM2 . . . 136
11.3 Validation of Wilks's theorem: Numerical critical chi-squared difference . . . 139

A.1 Parameter values of energy-loss function . . . 146
A.2 Correlation of energy-loss function parameters for measurement in May 2019 . . . 146
A.3 Correlation of energy-loss function parameters for measurement in April 2020 . . . 146

B.1 Radial pixel lists . . . 147
B.2 Alternative pixel lists . . . 148
B.3 Angular pixel lists . . . 148

C.1 Scan overview for KNM1 and KNM2 . . . 151
C.2 Model configuration for KNM1 and KNM2 . . . 151
C.3 Overview of the key experimental parameters in KNM1 and KNM2 . . . 152

D.1 KNM1 pseudo-ring-wise β-electron statistics . . . 157

H.1 Overview of best-fit results in the $3\nu+1$ framework considering the full range . . . 181

Bibliography

[1] L. Schlüter. Development of New Methods to Include Systematic Effects in the First Tritium Data Analysis and Sensitivity Studies of the KATRIN Experiment. Master's thesis, Technical University of Munich and Max-Planck-Institute for Physics, 2019. URL `https://www.katrin.kit.edu/publikationen/SchlueterLisaMSc19%20(1).pdf`.

[2] J Chadwick. Intensitätsverteilung im magnetischen Spectrum der β-Strahlen von radium B + C. *Verhandl. Dtsc. Phys. Ges.*, 16:383, 1914. URL `https://cds.cern.ch/record/262756`.

[3] W. Pauli. Open letter to the group of radioactive people at the Gauverein meeting in Tübingen. CERN Pauli letter collection, 12 1930. URL `https://cds.cern.ch/record/83282/files/meitner_0393.pdf`.

[4] E. Fermi. Versuch einer Theorie der β-Strahlen. *Zeitschrift für Physik*, 88(3), 03 1934. doi:10.1007/BF01351864.

[5] C.L. Cowan Jr., F. Reines, F.B. Harrison, H. W. Kruse, and A. D. McGuire. Detection of the Free Neutrino: a Confirmation. *Science*, 124, 07 1956. doi:10.1126/science.124.3212.103.

[6] G. Danby, J-M. Gaillard, K. Goulianos, L. M. Lederman, N. Mistry, M. Schwartz, and J. Steinberger. Observation of high-energy neutrino reactions and the existence of two kinds of neutrinos. *Phys. Rev. Lett.*, 9, 07 1962. doi:10.1103/PhysRevLett.9.36.

[7] Kodama *et al.* (DONUT Collaboration). Observation of tau neutrino interactions. *Phys. Lett. B*, 504(3): 218–224, 2001. doi:10.1016/S0370-2693(01)00307-0.

[8] Decamp *et al.* (ALEPH Collaboration). A precise determination of the number of families with light neutrinos and of the Z boson partial widths. *Phys. Lett. B*, 235(3):399–411, 1990. ISSN 0370-2693. doi:10.1016/0370-2693(90)91984-J.

[9] P. A. Zyla et al. Review of Particle Physics. *PTEP*, 2020(8):083C01, 2020. doi:10.1093/ptep/ptaa104.

[10] B. Pontecorvo. Inverse β processes and nonconservation of lepton charge. *Zhur. Eksptl'. i Teoret. Fiz.*, 34, 1 1958. URL `https://www.osti.gov/biblio/4349231`.

[11] V. Gribov and B. Pontecorvo. Neutrino astronomy and lepton charge. *Phys. Lett. B*, 28(7):493–496, 1969. ISSN 0370-2693. doi:10.1016/0370-2693(69)90525-5.

[12] Z. Maki, M. Nakagawa, and S. Sakata. Remarks on the Unified Model of Elementary Particles. *Progress of Theoretical Physics*, 28(5):870–880, 11 1962. doi:10.1143/PTP.28.870.

[13] B. Povh, K. Rith, C. Scholz, F. Zetsche, and W. Rodejohann. *Particles and Nuclei - An Introduction to the Physical Concepts*. Springer Berlin, Heidelberg, 2015. doi:10.1007/978-3-662-46321-5.

[14] C. Giunti and C. W. Kim. *Particles and Nuclei - An Introduction to the Physical Concepts*. Oxford University Press, 2007. doi:10.1093/acprof:oso/9780198508717.001.0001.

[15] R. Davis, D. S. Harmer, and K. C. Hoffman. Search for Neutrinos from the Sun. *Phys. Rev. Lett.*, 20, 05 1968. doi:10.1103/PhysRevLett.20.1205.

[16] Cleveland, B. T. and Daily, T. and Davis, R. and Distel, J. R. and Lande, K. and Lee, C. K. and Wildenhain, P. S. and Ullman, J. Measurement of the Solar Electron Neutrino Flux with the Homestake Chlorine Detector. *Astrophy. J.*, 496(1):505–526, 03 1998. doi:10.1086/305343.

[17] Ahmad *et al.* (SNO collaboration). Measurement of the rate of $\nu_e + d \rightarrow p + p + e^-$ interactions produced by ^8B solar neutrinos at the Sudbury Neutrino Observatory. *Phys. Rev. Lett.*, 87:071301, 07 2001. doi:10.1103/PhysRevLett.87.071301.

[18] S. R. Elliott, A. A. Hahn, and M. K. Moe. Direct evidence for two-neutrino double-beta decay in ^{82}Se. *Phys. Rev. Lett.*, 59, 11 1987. doi:10.1103/PhysRevLett.59.2020.

[19] A. Giuliani and A. Poves. Neutrinoless double-beta decay. *Adv. High Energy Phys.*, page 857016, 2012. doi:10.1155/2012/857016.

[20] Gando *et al.* (KamLAND-Zen Collaboration). Search for Majorana Neutrinos near the Inverted Mass Hierarchy Region with KamLAND-Zen. *Phys. Rev. Lett.*, 117(8):082503, 2016. doi:10.1103/PhysRevLett.117.082503.

[21] Agostini *et al.* (GERDA Collaboration). Final Results of GERDA on the Search for Neutrinoless Double-β Decay. *Phys. Rev. Lett.*, 125:252502, 12 2020. doi:10.1103/PhysRevLett.125.252502.

[22] W. Klaus and G. Altarelli. *Neutrino Mass*. Springer Tracts in Modern Physics. Springer, 12003. ISBN 978-3-540-40328-9.

[23] Aker *et al.* (KATRIN Collaboration). Direct neutrino-mass measurement with sub-electronvolt sensitivity. *Nat. Phys.*, 18(2):160–166, 2022. doi:10.1038/s41567-021-01463-1.

[24] R.R. Volkas. Introduction to sterile neutrinos. *Prog. Part. Nucl. Phys.*, 48(1):161–174, 2002. ISSN 0146-6410. doi:https://doi.org/10.1016/S0146-6410(02)00122-9.

[25] S. Böser, C. Buck, C. Giunti, J. Lesgourgues, L. Ludhova, S. Mertens, A. Schukraft, and M. Wurm. Status of light sterile neutrino searches. *Prog. Part. Nucl. Phys.*, 111:103736, 2020. ISSN 0146-6410. doi:https://doi.org/10.1016/j.ppnp.2019.103736.

[26] S. Gariazzo, C. Giunti, M. Laveder, Y. F. Li, and E.M. Zavanin. Light sterile neutrinos. *J. Phys. G: Nucl. Part. Phys.*, 43(3):033001, 03 2015. doi:10.1088/0954-3899/43/3/033001.

[27] G. Mention, M. Fechner, Th. Lasserre, Th. A. Mueller, D. Lhuillier, M. Cribier, and A. Letourneau. The Reactor Antineutrino Anomaly. *Phys. Rev. D*, 83:073006, 2011. doi:10.1103/PhysRevD.83.073006.

[28] V. Kopeikin, M. Skorokhvatov, and O. Titov. Reevaluating reactor antineutrino spectra with new measurements of the ratio between ^{235}U and ^{239}Pu β spectra. *Phys. Rev. D*, 104:L071301, 10 2021. doi:10.1103/PhysRevD.104.L071301.

[29] K. Schreckenbach, H.R. Faust, F. von Feilitzsch, A.A. Hahn, K. Hawerkamp, and J.L. Vuilleumier. Absolute measurement of the beta spectrum from ^{235}U fission as a basis for reactor antineutrino experiments. *Phys. Lett. B*, 99(3):251–256, 1981. ISSN 0370-2693. doi:10.1016/0370-2693(81)91120-5.

[30] Hampel *et al.* (GALLEX Collaboration). GALLEX solar neutrino observations: results for GALLEX IV. *Phys. Lett. B*, 447(1):127–133, 1999. doi:10.1016/S0370-2693(98)01579-2.

[31] Hampel *et al.* (GALLEX Collaboration). Final results of the ^{51}Cr neutrino source experiments in GALLEX. *Phys. Lett. B*, 420(1):114–126, 1998. doi:10.1016/S0370-2693(97)01562-1.

[32] Abdurashitov *et al.* (SAGE Collaboration). Measurement of the solar neutrino capture rate with gallium metal. III. Results for the 2002–2007 data-taking period. *Phys. Rev. C*, 80:015807, 07 2009. doi:10.1103/PhysRevC.80.015807.

[33] Barinov *et al.* (BEST Collaboration). Results from the Baksan Experiment on Sterile Transitions (BEST). *Phys. Rev. Lett.*, 128:232501, 06 2022. doi:10.1103/PhysRevLett.128.232501.

[34] Serebrov *et al.* (NEUTRINO-4 Collaboration). First Observation of the Oscillation Effect in the Neutrino-4 Experiment on the Search for the Sterile Neutrino. *JETP Letters*, 109(4):213–221, 2019. doi:110.1134/S0021364019040040.

[35] Serebrov *et al.* (NEUTRINO-4 Collaboration). Search for sterile neutrinos with the Neutrino-4 experiment and measurement results. *Phys. Rev. D*, 104:032003, 08 2021. doi:10.1103/PhysRevD.104.032003.

[36] C. Giunti, Y.F. Li, C.A. Ternes, and Y.Y. Zhang. Neutrino-4 anomaly: Oscillations or fluctuations? *Phys. Lett. B*, 816:136214, 2021. ISSN 0370-2693. doi:10.1016/j.physletb.2021.136214.

[37] M. V. Danilov and N. A. Skrobova. Comment on "Analysis of the Results of the Neutrino-4 Experiment on the Search for the Sterile Neutrino and Comparison with Results of Other Experiments". *JETP Letters*, 112: 452–454, 2020. doi:10.1134/S0021364020190066.

[38] M. Agostini and B. Neumair. Statistical Methods Applied to the Search of Sterile Neutrinos. *Eur. Phys. J. C*, 80(8):750, 2020.

[39] Aguilar *et al.* (LSND Collaboration). Evidence for neutrino oscillations from the observation of $\overline{\nu}_e$ appearance in a $\overline{\nu}_\mu$ beam. *Phys. Rev. D*, 64:112007, 11 2001. doi:10.1103/PhysRevD.64.112007.

[40] Aguilar-Arevalo *et al.* (MiniBooNE Collaboration). Significant Excess of Electronlike Events in the MiniBooNE Short-Baseline Neutrino Experiment. *Phys. Rev. Lett.*, 121(22), 11 2018. ISSN 1079-7114. doi:10.1103/physrevlett.121.221801.

[41] Armbruster*et al.* (KARMEN Collaboration). Upper limits for neutrino oscillations $\overline{\nu}_\mu \rightarrow \overline{\nu}_e$ from muon decay at rest. *Phys. Rev. D*, 65:112001, 06 2002. doi:10.1103/PhysRevD.65.112001.

[42] Angrik *et al.* (KATRIN Collaboration). KATRIN design report 2004. Technical report, Forschungszentrum, Karlsruhe, 2005. URL `https://publikationen.bibliothek.kit.edu/270060419`. Tech. Report.

[43] Aker *et al.* (KATRIN collaboration). The Design, Construction, and Commissioning of the KATRIN Experiment. *JINST*, 16(08):T08015, 2021. doi:10.1088/1748-0221/16/08/t08015.

[44] L. Köllenberger (KIT). KATRIN beam line drawing, 2021. leonard.koellenberger@kit.edu.

[45] L. Kuckert. *The Windowless Gaseous Tritium Source of the KATRIN Experiment - Characterisation of Gas Dynamical and Plasma Properties*. PhD thesis, Karlsruhe Institute of Technology, 2016. URL `https://publikationen.bibliothek.kit.edu/1000065077`.

[46] F. R. Friedel. *Ion and plasma systematics during the first KATRIN neutrino mass measurements*. PhD thesis, Karlsruher Institut für Technologie, 2020. URL `https://publikationen.bibliothek.kit.edu/1000126837`.

[47] M. Röllig, F. Priester, M. Babutzka, J. Bonn, L. Bornschein, G. Drexlin, S. Ebenhoech, E. Otten, M. Steidl, and M. Sturm. Activity monitoring of a gaseous tritium source by beta induced X-ray spectrometry. *Fusion Eng. Des.*, 01 2012. doi:10.1016/j.fusengdes.2012.11.001.

[48] L. Schimpf. *Characterisation of energy loss processes of 18.6 keV electrons inside the windowless tritium source of KATRIN*. PhD thesis, Karlsruhe Institute of Technology, 2021. URL `https://publikationen.bibliothek.kit.edu/1000131810`.

[49] R. Sack. *Measurement of the energy loss of 18.6 keV electrons on deuterium gas and determination of the tritium Q-value at the KATRIN experiment*. PhD thesis, WWU Münster, 2020. URL `https://nbn-resolving.de/urn:nbn:de:hbz:6-59069498754`.

[50] C. Köhler. Determination of the Column Density in the KATRIN Beamline with Electrons from the Photo-Electric Source. Master's thesis, Technical University of Munich and Max-Planck-Institute for Physics, 2019. URL `https://publications.mppmu.mpg.de/2019/MPP-2019-357/FullText.pdf`.

[51] Kleesiek *et al.* β-Decay spectrum, response function and statistical model for neutrino mass measurements with the KATRIN experiment. *Eur. Phys. J. C*, 79(3):204, 2019. doi:10.1140/epjc/s10052-019-6686-7.

[52] L. Kuckert, F. Heizmann, G. Drexlin, F. Glück, M. Hötzel, M. Kleesiek, F. Sharipov, and K. Valerius. Modelling of gas dynamical properties of the katrin tritium source and implications for the neutrino mass measurement. *Vacuum*, 158:195–205, 2018. ISSN 0042-207X. doi:https://doi.org/10.1016/j.vacuum.2018.09.036.

[53] M. Sturm. *Aufbau und Test des Inner-Loop-Systems der Tritiumquelle von KATRIN*. PhD thesis, Karlsruhe Institute of Technology, 2010. URL `https://publikationen.bibliothek.kit.edu/1000019355`.

[54] M. Arenz *et al.* (KATRIN Collaboration). The KATRIN superconducting magnets: overview and first performance results. *JINST*, 13(08):T08005–T08005, aug 2018. doi:10.1088/1748-0221/13/08/t08005.

[55] S. Lukić, B. Bornschein, L. Bornschein, G. Drexlin, A. Kosmider, K. Schlösser, and A. Windberger. Measurement of the gas-flow reduction factor of the KATRIN DPS2-F differential pumping section. *Vacuum*, 86(8): 1126–1133, 2012. doi:https://doi.org/10.1016/j.vacuum.2011.10.017.

[56] C. Röttele. Tritium suppression factor of the KATRIN transport section. 2019. URL `https://publikationen.bibliothek.kit.edu/1000096733`.

[57] K. Urban. Application of a TRISTAN Silicon Drift Detector as Forward Beam Monitor in KATRIN. Master's thesis, Technical University of Munich and Max-Planck-Institute for Physics, 2019. URL `https://www.katrin.kit.edu/publikationen/Urban_Korbinian_19.pdf`.

[58] V. M. Lobashev and P. E. Spivak. A method for measuring the anti-electron-neutrino rest mass. *Nucl. Instrum. Methods A*, 240:305–310, 1985. doi:10.1016/0168-9002(85)90640-0.

[59] A. Picard et al. A solenoid retarding spectrometer with high resolution and transmission for keV electrons. *Nucl. Instrum. Methods Phys. Res. B*, 63(3):345–358, 1992. doi:10.1016/0168-583X(92)95119-C.

[60] K. Hugenberg. Design of the electrode system of the KATRIN main spectrometer. Dipolma thesis, WWU Münster, 2008. URL `https://www.uni-muenster.de/Physik.KP/AGWeinheimer/theses/Diplom_Karen_Hugenberg.pdf`.

[61] Amsbaugh *et al.* Focal-plane detector system for the KATRIN experiment. *Nuclear Instruments and Methods in Physics Research Section A: Accelerators, Spectrometers, Detectors and Associated Equipment*, 778:40–60, 2015. ISSN 0168-9002. doi:https://doi.org/10.1016/j.nima.2014.12.116.

[62] Kraus *et al.* (Mainz collaboration). Final results from phase II of the Mainz neutrino mass searchin tritium β-decay. *Eur. Phys. J. C*, 40(4):447–68, 2005. doi:10.1140/epjc/s2005-02139-7.

[63] Aseev *et al.* (Troitsk collaboration). Upper limit on the electron antineutrino mass from the Troitsk experiment. *Phys. Rev. D*, 84:112003, 2011. doi:10.1103/PhysRevD.84.112003.

[64] A. Saenz, S. Jonsell, and P. Froelich. Improved Molecular Final-State Distribution of HeT$^+$ for the β-Decay Process of T_2. *Phys. Rev. Lett.*, 84:242–245, 2000. doi:10.1103/PhysRevLett.84.242.

[65] Aker *et al.* (KATRIN Collaboration). Analysis methods for the first KATRIN neutrino-mass measurement. *Phys. Rev. D*, 104:012005, 2021. doi:10.1103/PhysRevD.104.012005.

[66] D. H. Wilkinson. Small terms in the beta-decay spectrum of tritium. *Nucl. Phys. A*, 526(1):131–140, 1991. ISSN 0375-9474. doi:10.1016/0375-9474(91)90301-L.

[67] Aseev *et al.* Energy loss of 18 keV electrons in gaseous T and quench condensed D films. *Eur. Phys. J. D*, 10:39–52, 03 2000. doi:10.1007/s100530050525.

[68] Aker *et al.* (KATRIN Collaboration). Precision measurement of the electron energy-loss function in tritium and deuterium gas for the KATRIN experiment. *Eur. Phys. J. C*, 81(7):579, 2021. doi:10.1140/epjc/s10052-021-09325-z.

[69] N. Trost. *Modeling and measurement of Rydberg-State mediated Background at the KATRIN Main Spectrometer*. PhD thesis, Karlsruhe Institute of Technology, 2018. URL `https://publikationen.bibliothek.kit.edu/1000090450`.

[70] Abdurashitov *et al.* Electron scattering on hydrogen and deuterium molecules at 14–25 keV by the "Troitsk nu-mass" experiment. *Phys. Part. Nucl. Lett.*, (6):892–899, 2017. doi:https://doi.org/10.1134/S1547477117060024.

[71] Y. Kim, J. P. Santos, and F. Parente. Extension of the binary-encounter-dipole model to relativistic incident electrons. *Phys. Rev. A*, 62:052710, 2000. doi:10.1103/PhysRevA.62.052710.

[72] V. Hannen, C. Rodenbeck, R. Sack, and L. Schimpf. Energy-loss function measurement with KATRIN, April 2020. URL `https://nuserv.uni-muenster.de:8443/katrin-git/KATRIN-eloss/-/tree/master/parameters/KNM2/t2-eloss_parameterization_v3`.

[73] S. Groh. *Modeling of the response function and measurement of transmission properties of the KATRIN experiment*. PhD thesis, Karlsruhe Institute of Technology, 2015. URL `https://publikationen.bibliothek.kit.edu/1000046546`.

[74] D. Furse. Kassiopeia: a modern, extensible C++ particle tracking package. 19(5):053012, may 2017. doi:10.1088/1367-2630/aa6950.

[75] A. K. Schaller. *Characterization and mitigation of the background in KATRIN*. PhD thesis, Technical University of Munich, 2020. URL `https://mediatum.ub.tum.de/doc/1553598/1553598.pdf`.

[76] Aker *et al.* (KATRIN Collaboration). Suppression of Penning discharges between the KATRIN spectrometers. *Eur. Phys. J. C*, 80(9):821, 2020. doi:10.1140/epjc/s10052-020-8278-y.

[77] M. Kleesiek. *A Data-Analysis and Sensitivity-Optimization Framework for the KATRIN Experiment*. PhD thesis, Karlsruhe Institute of Technology, 2014. URL `https://publikationen.bibliothek.kit.edu/1000043301`.

[78] S. S. Wilks. The Large-Sample Distribution of the Likelihood Ratio for Testing Composite Hypotheses. *Annals Math. Statist.*, 9(1):60–62, 1938. doi:10.1214/aoms/1177732360.

[79] J. Neyman. A selection of early statistical papers of J. Neyman. 1967.

[80] G. J. Feldman and R. D. Cousins. Unified approach to the classical statistical analysis of small signals. *Phys. Rev. D*, 57:3873–3889, 1998. doi:10.1103/PhysRevD.57.3873.

[81] T. M. Karbach. Feldman-Cousins Confidence Levels - Toy MC Method. 2011. doi:10.48550/ARXIV.1109.0714.

[82] A. V. Lokhov and F. V. Tkachov. Confidence intervals with a priori parameter bounds. *Phys. Part. Nuclei*, 46 (3):347–365, 2015. doi:10.1134/S1063779615030089.

[83] W. Stoeffl and D. J. Decman. Anomalous Structure in the Beta Decay of Gaseous Molecular Tritium. *Phys. Rev. Lett.*, 75:3237–40, 10 1995. doi:10.1103/PhysRevLett.75.3237.

[84] R. G. H. Robertson, T. J. Bowles, G. J. Stephenson, D. L. Wark, J. F. Wilkerson, and D. A. Knapp. Limit on $\bar{\nu}_e$ mass from observation of the β-decay of molecular tritium. *Phys. Rev. Lett.*, 67:957–60, 8 1991. doi:10.1103/PhysRevLett.67.957.

[85] O. Fackler, B. Jeziorski, W. Kołos, H. J. Monkhorst, and K. Szalewicz. Accurate Theoretical β-Decay Energy Spectrum of the Tritium Molecule and Its Neutrino Mass Dependence. *Phys. Rev. Lett.*, 55:1388–1391, 1985. doi:10.1103/PhysRevLett.55.1388.

[86] L. I. Bodine, D. S. Parno, and R. G. H. Robertson. Assessment of molecular effects on neutrino mass measurements from tritium β decay. *Phys. Rev. C*, 91:035505, 2015. doi:10.1103/PhysRevC.91.035505.

[87] R. G. H. Robertson. Internal communication. 2018.

[88] M. B. Machatschek. *A Phenomenological Theory of KATRIN Source Potential Systematics and its Application in Krypton-83m Calibration Measurements*. PhD thesis, Karlsruhe Institute of Technology, 2020. URL `https://publikationen.bibliothek.kit.edu/1000132391`.

[89] R. Ostertag. Investigation of Plasma Effects in the KATRIN Source with $^{83\mathrm{m}}$Kr. Master's thesis, Karlsruhe Institute of Technology, 2020. URL `https://www.katrin.kit.edu/downloads/mth_ostertag.pdf`.

[90] Aker *et al.* (KATRIN Collaboration). Quantitative Long-Term Monitoring of the Circulating Gases in the KATRIN Experiment Using Raman Spectroscopy. *Sensors*, 20(17), 2020. doi:10.3390/s20174827.

[91] A. Beglarian, E. Ellinger, N. Haußmann, K. Helbing, S. Hickford, U. Naumann, H.-W. Ortjohann, M. Steidl, J. Wolf, and S. Wüstling. Forward Beam Monitor for the KATRIN experiment. *JINST*, 17(03), 2022. doi:10.1088/1748-0221/17/03/t03002.

[92] Arenz *et al.* (KATRIN Collaboration). Calibration of high voltages at the ppm level by the difference of 83mKr conversion electron lines at the KATRIN experiment. *Eur. Phys. J. C*, 78(5):368, 2018. doi:10.1140/epjc/s10052-018-5832-y.

[93] F. Block. Characterisation of the Backgrounds in the KATRIN experiment. Master's thesis, Karlsruhe Institute of Technology, 2018. URL `https://www.katrin.kit.edu/publikationen/mth_fblock.pdf`.

[94] S. Welte, E. Fanghänel, S. Fischer, F. Kramer, T. L. Le, M. Sturm, and N. Tuchscherer. Experimental Performance Test of Key Components of the KATRIN Outer Tritium Loop. *Fusion Science and Technology*, 71(3): 316–320, 2017. doi:10.1080/15361055.2017.1291233.

[95] A. C. Marsteller. *Characterization and Optimization of the KATRIN Tritium Source*. PhD thesis, Karlsruhe Institute of Technology, 2020. URL `https://publikationen.bibliothek.kit.edu/1000127553`.

[96] Aker *et al.* (KATRIN collaboration). Improved Upper Limit on the Neutrino Mass from a Direct Kinematic Method by KATRIN. *Phys. Rev. Lett.*, 123:221802, 11 2019. doi:10.1103/PhysRevLett.123.221802.

[97] M. B. Machatschek, F. Friedel, F. Glück, M. Klein, and M. Schlösser. Plasma Investigations during KNM1 (short version on krypton measurement only). Katrin internal Analysis Report, Karlsruhe Institute of Technology, 2019. URL `https://ikp-katrin-wiki.ikp.kit.edu/katrin/images/3/39/GKrS_KNM1_report_v1.0.pdf`.

[98] M. G. Erhard. *Influence of the magnetic field on the transmission characteristics and the neutrino mass systematic of the KATRIN experiment*. PhD thesis, Karlsruhe Institute of Technology, 2016. URL `1https://publikationen.bibliothek.kit.edu/1000065003`.

[99] S. Enomoto. Detector systematics. *KATRIN Analysis Workshop*, 2019. URL `https://ikp-katrin-wiki.ikp.kit.edu/katrin/images/0/0c/190715-Detector-Sanshiro.pdf`.

[100] Fränkle *et al.* Katrin background due to surface radioimpurities. *Astropart. Phys.*, 138:102686, 2022. doi:https://doi.org/10.1016/j.astropartphys.2022.102686.

[101] L. Schlüter, T. Lasserre, and *et al.* First neutrino mass measurement with the KATRIN experiment. *J. Phys.: Conf. Ser.*, 1468(1):012180, 2020. doi:10.1088/1742-6596/1468/1/012180.

[102] J. V. Bradley. *Distribution-Free Statistical Tests*. Prentice-Hall, 1968.

[103] B. A. Murtagh and M. A. Saunders. Minos 5.51 user's guide. Technical report, Stanford University, 2003. URL `https://stanford.edu/group/SOL/guides/minos551.pdf`.

[104] D. E. Hinkle, W. Wiersma, and S. G. Jurs. *Applied statistics for the behavioral sciences*. Houghton Mifflin College Division, 2003. ISBN 978-0618124053.

[105] G. Mention. Linear and locally linearized χ^2 with systematics and regression diagnostics (Version 1.30). Technical report, CEA Saclay, 2013.

[106] G. Cowan. *Statistical Data Analysis*. Oxford science publications. Clarendon Press, 1998. ISBN 9780198501558.

[107] M. Maltoni and T. Schwetz. Testing the statistical compatibility of independent data sets. *Phys. Rev. D*, 68: 033020, Aug 2003. doi:10.1103/PhysRevD.68.033020. URL `https://link.aps.org/doi/10.1103/PhysRevD.68.033020`.

[108] Aker *et al.* (KATRIN Collaboration). Bound on 3+1 Active-Sterile Neutrino Mixing from the First Four-Week Science Run of KATRIN. *Phys. Rev. Lett.*, 126(9):091803, 2021. doi:10.1103/PhysRevLett.126.091803.

[109] Aker *et al.* (KATRIN Collaboration). Improved eV-scale sterile-neutrino constraints from the second KATRIN measurement campaign. *Phys. Rev. D*, 105:072004, 2022. doi:10.1103/PhysRevD.105.072004.

[110] C. Giunti, Y.F. Li, and Y.Y. Zhang. *J. High Energy Phys.*, 05:61, 2020.

[111] C. Kraus, A. Singer, K. Valerius, and C. Weinheimer. Limit on sterile neutrino contribution from the Mainz Neutrino Mass Experiment. *Eur. Phys. J. C*, 73(2):2323, 2013. doi:10.1140/epjc/s10052-013-2323-z.

[112] A. I. Belesev et al. An upper limit on additional neutrino mass eigenstate in 2 to 100 eV region from 'Troitsk nu-mass' data. *JETP Lett.*, 97:67–69, 2013. doi:10.1134/S0021364013020033.

[113] Andriamirado *et al.* (PROSPECT Collaboraton). Improved short-baseline neutrino oscillation search and energy spectrum measurement with the PROSPECT experiment at HFIR. *Phys. Rev. D*, 103(3):032001, 2021. doi:10.1103/PhysRevD.103.032001.

[114] Mikhail Danilov. Recent results of the DANSS experiment. *PoS*, EPS-HEP2019:401, 2020. doi:10.22323/1.364.0401.

[115] Adamson *et al.* Improved Constraints on Sterile Neutrino Mixing from Disappearance Searches in the MINOS, MINOS+, Daya Bay, and Bugey-3 Experiments. *Phys. Rev. Lett.*, 125(7):071801, 2020. doi:10.1103/PhysRevLett.125.071801.

[116] Abrahão *et al.* (Double Chooz Collaboration). Search for Signatures of Sterile Neutrinos with Double Chooz. 9 2020.

[117] Almazán *et al.* (STEREO Collaboration). Improved sterile neutrino constraints from the STEREO experiment with 179 days of reactor-on data. *Phys. Rev. D*, 102(5):052002, 2020. doi:10.1103/PhysRevD.102.052002.

[118] Anna Sejersen Riis and Steen Hannestad. Detecting sterile neutrinos with katrin like experiments. *Journal of Cosmology and Astroparticle Physics*, 2011(02):011–011, Feb 2011. ISSN 1475-7516. doi:10.1088/1475-7516/2011/02/011. URL `http://dx.doi.org/10.1088/1475-7516/2011/02/011`.

[119] M. Inokuti. Inelastic Collisions of Fast Charged Particles with Atoms and Molecules—The Bethe Theory Revisited. *Rev. Mod. Phys.*, 43:297–347, 1971. doi:10.1103/RevModPhys.43.297.

[120] J. W. Liu. Total Inelastic Cross Section for Collisions of H_2 with Fast Charged Particles. *Phys. Rev. A*, 7: 103–109, 1973. doi:10.1103/PhysRevA.7.103.

[121] J. W. Liu. Total cross sections for high-energy electron scattering by h_2 $({}^1\Sigma_g^+)$, n_2 $({}^1\Sigma_g^+)$, and o_2 $({}^3\Sigma_g^-)$. *Phys. Rev. A*, 35:591–597, 1987. doi:10.1103/PhysRevA.35.591.

[122] P. Weck, B. Joulakian, and P. A. Hervieux. Fivefold differential cross section of fast $(e, 2e)$ ionization of H_2, D_2, and T_2 by a Franck-Condon approach. *Phys. Rev. A*, 60:3013–3019, 1999. doi:10.1103/PhysRevA.60.3013.

[123] V. Hannen, C. Rodenbeck, R. Sack, and L. Schimpf. Energy-loss function measurement with KATRIN, May 2019. URL `https://nuserv.uni-muenster.de:8443/katrin-git/KATRIN-eloss/-/tree/master/code/KNM1`.

Acknowledgments

I would like to thank all the people who supported me during my PhD and thereby contributed to its success.

THIERRY LASSERRE It was a pleasure to work with you! Thank you for sharing your invaluable expertise and for giving me the freedom to develop and test my ideas. I consider myself very lucky to have had such a great mentor.

SUSANNE MERTENS Thank you for giving me the opportunity to pursue a PhD in KATRIN and supporting me along the way. Your encouragement and persistent belief in me helped a great deal.

MARTIN SLEZÁK, CHRISTIAN KARL and all members of the FITRIUM analysis team I appreciate our fruitful discussions on the neutrino-mass analyses, which demonstrate that team work is possible while maintaining a healthy competition in the unblinding process.

CHRISTOPH KÖHLER I'd like to thank you for our discussions on sterile neutrinos, column density and other KATRIN-related topics. Big thanks for helping me - alongside with **CYNTHIA GLAS** - to produce the public outreach video on KATRIN data analysis. Lastly, I also want to thank you for fostering my education in *good* movies by organizing the container movie nights.

LEONARD KÖLLENBERGER Thank you for the productive and uncomplicated collaboration in the sterile-neutrino analysis and the subsequent paper writing.

FABIAN KELLERER Thanks for equipping SAMAK with tools to search for the relic neutrino background and for interesting discussions on local overdensities.

KATRIN group in Karlsruhe I'd like to thank the analysis group at KIT, in particular **MAGNUS SCHLÖSSER**, for pleasant collaboration meetings and analysis workshops.

KATRIN and TRISTAN group in Munich A special thank you goes to all current and past members of the KATRISTAN group, who made my time at the Max Planck Institute memorable. I'm grateful that I could work alongside so many talented people in such a pleasant atmosphere. For sure, my PhD experience would not have been the same without you guys and our numerous social activities and ice cream breaks.

IMRPS and fellow PhD students I'd like to thank the IMPRS of the Max Planck Institute for Physics for organizing the amazing *Young Scientist Workshops* at castle Ringberg and for providing me with the opportunity to present and discuss my research. I also thank all fellow PhD students at the institute, with whom I could share the highs and lows of PhD life or simply have a good time at lake Tegernsee.

Finally, I want to thank my **parents** for their continuous support beyond the academic world and **Tim Brunst** for being the pillar that I can always rely on.